

CFD Study of Surface Roughness Effects on the Thermo-
Elastohydrodynamic Lubrication Line Contact Problem

Thesis submitted for the degree of
Doctor of Philosophy
at the University of Leicester

by

Sutthinan Srirattayawong
Engineering Department
University of Leicester

May 2014

**CFD Study of Surface Roughness Effects on the Thermo-
Elastohydrodynamic Lubrication Line Contact Problem**

Abstract

This research investigates the effect of surface roughness on Thermo-Elastohydrodynamic Lubrication (TEHL) by Computational Fluid Dynamics (CFD). Traditionally, the Reynolds equation has been used to describe the flow of a lubricant for the TEHL problem, but this approach has some limitations. To overcome these, CFD is used in this research, as an alternative to solving the Reynolds equation.

The commercial software packages ANSYS ICEM CFD 13.0 and ANSYS FLUENT 13.0 are employed to solve the Navier-Stokes equations. User-defined functions (UDFs) for the heat generated in the lubricant film, the density and the viscosity of lubricant, and the elastic deformation of the cylindrical roller bearing are created for this particular research. For viscosity, the lubricant is modelled as a non-Newtonian fluid based on the Ree-Eyring model. A number of CFD models are created under different conditions to predict the flow characteristics in the TEHL line contact problem, including the pressure distribution, the temperature distribution, the film thickness, and the friction coefficient. The effect of surface roughness is considered in the CFD models.

The predicted results from the CFD models and the Reynolds equation are compared. The pressure distribution and the film thickness of both models are found to be in agreement. The simulation results show that the surface roughness affects significantly for the behaviour of fluid film lubrication problems, especially in the thin film case. It is found that the pressure profile at the centre of the contact area directly relates to the roughness amplitude. Furthermore, the CFD models can model the elastic deformation of cylinders of different materials, which is another advantage of the CFD approach over the Reynolds equation.

Acknowledgements

I would like to express my appreciation and gratitude to Dr. Shian Gao for all his assistance and guidance as research supervisor over the past years. I would also like to thank to my co-supervisor Professor Hongbiao Dong for his support and constructive suggestions. A special thanks to Dr. Aldo Rona for all his feedback and useful suggestions.

My appreciation goes to the NTN Company for providing a cylindrical roller bearing sample and to Mr. Graham Clark who helped and supported me to measure the surface roughness of the cylindrical roller bearing. This work is funded through the Ministry of Science and Technology of Thailand, grant number ST_2968. Their support is thankfully acknowledged.

Lastly, I am indebted to my family for all their help and support and to my parents who kept my inspiration and encouragement.

Contents

Cover	i
Acknowledgements	iii
Contents	iv
List of Figures	vii
List of tables	xiii
Nomenclatures	xiv
Chapter 1 Introduction.....	1
1.1 Context.....	1
1.2 Literature review.....	4
1.3 Aims and objectives	8
Chapter 2 Elastohydrodynamic Lubrication	10
2.1 Introduction	10
2.2 The Reynolds equation	10
2.3 The film thickness equation.....	14
2.4 The force balance equation.....	16
2.5 Rheology	17
2.5.1 Newtonian fluid	18
2.5.2 Non-Newtonian fluids.....	19
2.6 The density equation.....	22
2.7 Energy equation	23
Chapter 3 Surface Roughness	25
3.1 Introduction	25
3.2 Surface texture characterization.....	25
3.2.1 The nature of surfaces.....	25
3.2.2 Surface texture parameters	26
3.2.3 Abbott-Firestone curve	30
3.3 Filters	32

3.4 Measurement of Surface Roughness	36
3.4.1 Surface roughness of the bearing case in the azimuthal direction	40
3.4.2 Surface roughness of the bearing case in the axial direction...	41
3.4.3 Surface roughness of the roller in the azimuthal direction	42
3.4.4 Surface roughness of the roller in the axial direction	43
3.5 Generation of surface roughness	46
3.6 Roughness and the EHL problem	49
Chapter 4 The Computation Fluid Dynamics	50
4.1 Introduction	50
4.2 The governing equations.....	50
4.2.1 The continuity equation	51
4.2.2 The momentum equation	52
4.2.3 The energy equation	53
4.3 Cavitation model	56
4.4 The discretized equations	58
4.5 Shear stress at wall	61
4.6 Numerical scheme	62
4.6.1 SIMPLE algorithm.....	64
4.6.2 PISO algorithm	65
Chapter 5 The CFD Models for the EHL Problem	67
5.1 Introduction	67
5.2 The application of the CFD to the EHL problem.....	67
5.2.1 The modelling geometry	67
5.2.2 Boundary conditions and initial condition	68
5.2.3 Model meshing and solver	69
5.2.4 Dynamic mesh	74
5.2.5 User-Defined Functions	75

5.3 Mesh dependence test.....	75
5.4 Validation of the CFD approach	81
5.5 The simulation models	84
5.5.1 Roller and plate contact	85
5.5.2 Two rollers contact.....	86
Chapter 6 CFD Model for Roller and Plate Contact.....	89
6.1 Introduction	89
6.2 Influence of non-Newtonian fluid	90
6.3 Influence of lubricant viscosity.....	96
6.4 Influence of surface speed	99
6.5 Influence of the normal load	103
6.6 Influence of material properties	106
6.7 Thermal effects	110
Chapter 7 The CFD Model for Two Rollers Contact	124
7.1 Introduction	124
7.2 Influence of material properties	124
7.2.1 Two rollers contact ($R_1=R_2$)	125
7.2.2 Two cylinders contact ($R_1 \neq R_2$)	133
7.3 Influence of the roughness parameters.....	141
7.4 Thermal effects	152
Chapter 8 Conclusion and Future Work.....	155
8.1 Conclusion	155
8.2 Further research recommendations	157
Appendix 1: List of published papers and papers on process.	161
Appendix 2: UDF codes for CFD model parameters	162
Appendix 3: Numerical solver for the Reynolds equation.....	173
Appendix 4: Temperature at the solid surfaces	175
Appendix 5: Flow charts for the Reynolds equation and the CFD model ..	177
References.....	179

List of Figures

Figure 1-1: A typical Stribeck curve [1].....	2
Figure 1-2: A typical cylindrical roller bearing [2].....	2
Figure 1-3: Dimensionless pressure (P) and film thickness (H) distributions of a typical EHL problem.	4
Figure 2-1: The acting forces on a fluid element [35].	11
Figure 2-2: EHL film shape [35, 42].....	15
Figure 2-3: The rotational viscometer [48].....	17
Figure 2-4: The standard cup to measure the viscosity of fluids using a rotational viscometer [48].	17
Figure 2-5: Schematic of Newton's postulate [49].	18
Figure 2-6: The relation of shear stress and shear strain rate for different types of fluids [54].....	19
Figure 3-1: The actual surface profile of a solid component [47].....	26
Figure 3-2: A schematic of the roughness parameter, R_a	27
Figure 3-3: Different profiles of surface roughness with the same R_a value [74].	28
Figure 3-4: Relationship between the height profile and the cumulative PDF of surface roughness [75].....	28
Figure 3-5: Schematic of variance skewness [75].	29
Figure 3-6: Representing distribution curve with variance kurtosis [75].	30
Figure 3-7: Abbott-Firestone curve [83].....	31
Figure 3-8: Representing the depth distribution histogram and the Abbott-Firestone curve.	32
Figure 3-9: The influence of the cut-off values on waviness and roughness profiles using the Gaussian filter. Measured primary surface roughness (blue line), long wavelength waviness profile (red line), filtered roughness profile (green line).....	34
Figure 3-10: Representative scheme for reflecting of light with smooth and rough surfaces [93].	36

Figure 3-11: Schematic of the optical surface profile [94].....	37
Figure 3-12: Surtronic 3+ [92].	38
Figure 3-13: Schematic of the working principle of a stylus profilometer [97]....	38
Figure 3-14: Comparison of the surface measurements between stylus A and B.	38
Figure 3-15: Error due to stylus tip radius [98]	39
Figure 3-16: The sample of a cylindrical roller bearing for measuring the surface texture.	39
Figure 3-17: The stylus is moved tangentially over the surface of the bearing case.	40
Figure 3-18: The surface texture of the bearing case in the azimuthal direction.	41
Figure 3-19: The stylus is moved axially along the surface of the bearing case.	41
Figure 3-20: The surface texture of the bearing case in the axial direction.	42
Figure 3-21: The stylus is moved across the surface of the cylindrical roller. ...	43
Figure 3-22: The surface texture of the cylindrical roller in the tangential direction.	43
Figure 3-23: The stylus is moved axially on the surface of the cylindrical roller.	44
Figure 3-24: The surface texture of the cylindrical roller in the axial direction...	44
Figure 3-25: The depth distribution histogram and Abbott-Firestone curve measured in sections 3.4.1(a), 3.4.2 (b), 3.4.3(c) and 3.4.4 (d), respectively. ..	46
Figure 4-1: The cavitation phenomenon at the outlet region of point contact [130].	57
Figure 4-2: Schematic of a discretized computational domain.	61
Figure 4-3: Schematic of a staggered grid arrangement.	64
Figure 5-1: The analytical model for EHL line contact problem.	68
Figure 5-2: Creating geometry and meshing.	69
Figure 5-3: The static pressure in the fluid film at the contact zone.	71
Figure 5-4: Two types of CFD model meshes for the EHL problem.	72
Figure 5-5: Schematic representation of the mesh refinement process.	76
Figure 5-6: A CFD model for an EHL problem.	78
Figure 5-7: Pressure distribution using different mesh sizes (smooth surface).	79

Figure 5-8: Film thickness using different mesh sizes (smooth surface).	79
Figure 5-9: Pressure distribution using different mesh sizes (rough surface).	80
Figure 5-10: Film thickness using different mesh sizes (rough surface).	80
Figure 5-11: The CFD model used to compare with the Reynolds equation.	81
Figure 5-12: Comparison of dimensionless pressure (P) and film thickness (H) distributions between the CFD model and the Reynolds equation. (W=1.8182×10 ⁻⁵ , U=7.2727×10 ⁻¹² and G=3500).	83
Figure 5-13: The relationship between dimensionless pressure distribution (P) and the volume fraction along the non-dimensional Hertzian contact zone length x/b, where b is the half-width of Hertzian contact (0.14263 mm).	84
Figure 5-14: The comparison schematic of the EHL problem for cylinders contact between the Reynolds equation (Model 1) and the CFD models (Models 2 and 3).	87
Figure 5-15: The CFD model 2 for predicting two cylinders contact ($R_1 = R_2$).	88
Figure 5-16: The CFD model 3 for predicting two cylinders contact ($R_1 \neq R_2$).	88
Figure 6-1: The relationship between the undeformed gap (h_o) and the pressure generated (time dependent).	90
Figure 6-2: Comparison of pressure distributions between Newtonian and non-Newtonian fluids when $SRR = 0$ and 1.	91
Figure 6-3: Comparison of film thicknesses between Newtonian and non-Newtonian fluids when $SRR = 0$ and 1.	93
Figure 6-4: Effect of surface roughness on pressure distribution at $SRR = 0$ and 1 for non-Newtonian fluid.	93
Figure 6-5: Effect of non-Newtonian fluid on viscosity (Pa·s) at $SRR = 0$, 1 and 2 for smooth (a, c and e) and rough (b, d and f) surfaces.	94
Figure 6-6: Effect of viscosity on pressure distribution (smooth surface).	96
Figure 6-7: Effect of viscosity on film thickness (smooth surface).	97
Figure 6-8: Effect of viscosity on pressure distribution (rough surface).	97
Figure 6-9: Effect of viscosity on pressure distribution (rough surface).	98
Figure 6-10: Effect of velocity on pressure distribution (smooth surface).	100
Figure 6-11: Effect of velocity on film thickness (smooth surface).	100
Figure 6-12: Effect of velocity on pressure distribution (rough surface).	101
Figure 6-13: Effect of velocity on film thickness (rough surface).	101

Figure 6-14: Effect of loads (N/m) on pressure distribution (smooth surface).	104
Figure 6-15: Effect of loads (N/m) on oil film thickness (smooth surface).	104
Figure 6-16: Effect of loads (N/m) on pressure distribution (rough surface)....	105
Figure 6-17: Effect of loads (N/m) on oil film thickness (rough surface).	105
Figure 6-18: Effect of material properties on the pressure distribution (smooth surfaces).	108
Figure 6-19: Effect of material properties on the film thickness (smooth surfaces).	108
Figure 6-20: Effect of material properties on the pressure distribution (rough surfaces).	109
Figure 6-21: Effect of material properties on the film thickness (rough surfaces).	110
Figure 6-22: Maximum temperature when wall thickness is increased.	111
Figure 6-23: Comparison of pressure distributions at $SRR = 0, 1$ and 2 between the isothermal and thermal cases (smooth surfaces).....	113
Figure 6-24: Comparison of film thicknesses at $SRR = 0, 1$ and 2 between the isothermal and thermal cases (smooth surfaces).....	114
Figure 6-25: Effect of surface roughness on iso-levels of temperature (K) at $SRR = 0, 1$ and 2 (Left: smooth surface; Right: rough surface).....	115
Figure 6-26: Effect of surface roughness on pressure distribution at $SRR = 0, 1$ and 2	116
Figure 6-27: Effect of surface roughness on film thickness at $SRR = 0, 1$ and 2	116
Figure 6-28: Effect of surface roughness on velocity magnitude iso-levels (m/s) at $SRR = 0, 1$ and 2 (Left: smooth surface; Right: rough surface).....	117
Figure 6-29: Effect of surface roughness on the iso-levels of viscosity ($\text{Pa}\cdot\text{s}$) at $SRR = 0, 1$ and 2 (Left: smooth surface; Right: rough surface).....	118
Figure 6-30: Effect of surface roughness on velocity gradients (s^{-1}).	120
Figure 6-31: Effect of surface roughness on pressure gradients ($\text{Pa}\cdot\text{m}^{-1}$).	121
Figure 6-32: Effect of surface roughness on viscosity of lubricant ($\text{Pa}\cdot\text{s}$).	121
Figure 6-33: Effect of surface roughness on temperature field (K).	122
Figure 7-1: Material effects on the pressure distributions and the deformed cylinder surfaces (smooth surface).	125

Figure 7-2: Material effects on the pressure distributions and the deformed cylinder surfaces (smooth surface).	126
Figure 7-3: Material effects on the pressure distributions and the deformed cylinder surfaces (smooth surface).	126
Figure 7-4: Material effects on the pressure distributions and the deformed cylinder surfaces (smooth surface).	127
Figure 7-5: Comparison of the pressure distribution (top cylinder) among different material contacts.	127
Figure 7-6: Comparison of the material effects on the pressure distributions between CFD model 1 and CFD model 2 from Table 5-4.	129
Figure 7-7: Material effects on the pressure distributions and on the deformed cylinder surface (rough surface).	130
Figure 7-8: Material effects on the pressure distributions and on the deformed cylinder surface (rough surface).	130
Figure 7-9: Material effects on the pressure distributions and on the deformed cylinder surface (rough surface).	131
Figure 7-10: Material effects on the pressure distributions and on the deformed cylinder surface (rough surface).	131
Figure 7-11: The pressure distributions and profiles of cylinders ($E_1=E_2$).	134
Figure 7-12: The pressure distributions and profiles of cylinders ($E_1<E_2$).	134
Figure 7-13: The pressure distributions and profiles of cylinders ($E_1>E_2$).	135
Figure 7-14: The pressure distributions when $E_1<E_2$ and $E_1>E_2$ with the CFD model 3.	136
Figure 7-15: Comparison of the deformations when top and bottom cylinders are brass – ceramic and ceramic – brass.	136
Figure 7-16: Comparison of the pressure profiles among models 1, 2 and 3.	138
Figure 7-17: Comparison of the film thickness among models 1, 2 and 3.	139
Figure 7-18: Pressure distribution and film thickness (iron – iron).	139
Figure 7-19: Pressure distribution and film thickness (brass – ceramic).	140
Figure 7-20: Pressure distribution and film thickness (ceramic-brass).	140
Figure 7-21: Surface roughness profiles when R_a is increased.	143
Figure 7-22: Influence of kurtosis on the surface roughness profiles.	144
Figure 7-23: Influence of skewness on the surface roughness profiles.	144

Figure 7-24: Effect of surface roughness when the top cylinder is rough (Profile 1).....	145
Figure 7-25: Effect of surface roughness when the top cylinder is rough (Profile 2).....	145
Figure 7-26: Effect of surface roughness when the top cylinder is rough (Profile 3).....	146
Figure 7-27: Effect of surface roughness when the top cylinder is rough (Profile 4).....	146
Figure 7-28: Effect of surface roughness when the top cylinder is rough (Profile 5).....	147
Figure 7-29: Effect of surface roughness when the top cylinder is rough (Profile 6).....	147
Figure 7-30: Effect of surface roughness when the top cylinder is rough (Profile 7).....	148
Figure 7-31: Effect of surface roughness on pressure distributions when the average roughness (R_a) is increased.	148
Figure 7-32: Effect of surface roughness on pressure distributions when the kurtosis (R_{ku}) value is varied ($R_{ku}=3$, $R_{ku}>3$ and $R_{ku}<3$).....	149
Figure 7-33: The effects of surface roughness on pressure distribution when the value of skewness is 0, -0.70 and 0.72, respectively.	149
Figure 7-34: Comparison of pressure distributions between models 1 and 3..	153
Figure 7-35: Comparison of (a-b) temperature distribution (K), (c-d) viscosity (Pa·s), and (e-f) velocity (m/s) between smooth (left) and rough surfaces (right).	154
Figure 8-1: Schematic simulation between fluid and solid mechanics.....	159

List of tables

Table 3-1: Calculated surface roughness parameters.....	45
Table 5-1: The common parameters [137].	70
Table 5-2: The mesh independence test.....	78
Table 5-3: Common parameters [144]	82
Table 5-4: The CFD models for each contact.....	85
Table 6-1: Properties of materials [149, 150]	107
Table 6-2: The materials of the top and bottom rollers.....	107
Table 6-3: Common parameters	112
Table 7-1: Comparison of the maximum pressure and film thickness of the CFD models 1 and 2.....	132
Table 7-2: Effect of material on two cylinders contact ($R_1 \neq R_2$).....	133
Table 7-3: The roughness parameters for profiles 1 to 7 ($\Delta x = 0.5 \mu\text{m}$)	142
Table 7-4: The average oil film thickness and friction coefficient	150

Nomenclatures

Roman symbols

A	Area (m^2)
b	Half-width of Hertzian contact
C_p	Specific heat capacity ($\text{J} \cdot \text{kg}^{-1} \cdot \text{K}^{-1}$)
E	Young's modulus of elasticity (Pa)
E'	Effective elastic modulus (Pa)
h	Film thickness (m)
\bar{h}	Sensible enthalpy ($\text{J} \cdot \text{kg}^{-1}$)
H	Dimensionless film thickness
H_0	Dimensionless minimum film thickness
G	Dimensionless material parameter, $G = \alpha E'$
\mathbf{I}	Unit tensor
k	Thermal conductivity ($\text{W} \cdot \text{m}^{-1} \cdot \text{K}^{-1}$)
L	A sampling length (m)
m_0	Viscosity index (Power law model)
\dot{m}	Mass flow rate per unit span ($\text{kg} \cdot (\text{ms})^{-1}$)
p	Pressure (Pa)
p_h	Maximum Hertzian pressure (Pa)
P	Dimensionless pressure
R	Radius of roller bearing (m)
$R(i)$	Surface roughness profile (m)
R'	Effective radius of curvature (m)
R_a	Average roughness (μm)
R_q	Root mean square roughness (μm)
R_{ku}	Kurtosis
R_{sk}	Skewness

SRR	Slide to roll ratio, $SRR = 2 u_1 - u_2 /(u_1 + u_2)$
S_T	Total heat sources ($W \cdot m^{-3}$)
t	Time, (s)
t^*	Dimensionless time
T	Temperature (K)
u_1, u_2	Velocities of roller and plate respectively, in x direction ($m \cdot s^{-1}$)
u_m	Average velocity ($m \cdot s^{-1}$)
\mathbf{u}	Vector velocity ($m \cdot s^{-1}$)
U	Dimensionless velocity
v	Velocity in the y direction ($m \cdot s^{-1}$)
V_{ch}	Characteristic velocity ($m \cdot s^{-1}$)
w	Load ($N \cdot m^{-1}$)
W	Dimensionless load
x, y, z	Coordinates (m)
X, Y, Z	Dimensionless coordinates

Greek symbols

α	Pressure-viscosity coefficient of lubricant ($m^2 \cdot N^{-1}$)
α_i	Volume fraction of phase i
β	Temperature-viscosity coefficient of lubricant (K^{-1})
Γ	Diffusion coefficient
$\dot{\gamma}$	Shear strain rate tensor (s^{-1})
$\dot{\gamma}_{eq}$	The second invariant of the strain-rate tensor (s^{-1})
ε	Thermal expansivity of lubricant (K^{-1})
$\mu_{Roeland}$	Roelands viscosity ($Pa \cdot s$)
$\mu_{Houpert}$	Houpert viscosity ($Pa \cdot s$)
μ_{Eyring}	Ree-Eyring viscosity ($Pa \cdot s$)
$\mu_{Carreau}$	Carreau viscosity ($Pa \cdot s$)
λ	A time constant (s)

λ_c	Cut-off wavelength of a filter (mm)
μ	Viscosity of fluid (Pa·s)
μ_f	Friction coefficient
ν	Poisson's ratio
ξ	Relative coordinates (m)
ρ	Density (kg·m ⁻³)
τ	Shear stress (N·m ⁻²)
ϑ	Relaxation factor
ϕ	An intensive property of the flow

Subscripts

a	Average
c	The zero shear strain rate viscosity
l	Liquid phase
m	Mixture phase
0	At atmospheric pressure condition
v	Vapour phase
f	Fluid
1	The bottom solid (plate)
2	The top solid (cylinder)

Superscripts

n	The flow index (Power law model)
new	New parameter
old	Current parameter
z	Pressure viscosity index
T	Transpose of matrix

Chapter 1

Introduction

1.1 Context

Lubrication systems have received much interest over the years as they are the lifeblood of all mechanical machines. Lubrication techniques can help reduce friction force, as well as prevent and reduce the wear that can occur on all contacting and moving parts.

In order to improve the efficiency of a lubrication system, the behaviours and mechanics of fluid film lubrication must be explored and understood. Typically, fluid film lubrication can be divided into four categories according to load and friction coefficient, as shown by a typical Stribeck curve in Figure 1-1.

The first type of lubrication in the Stribeck curve is thick full fluid lubrication or hydrodynamic lubrication (HD), that can generate the necessary pressure to carry a load when two surfaces are in sliding motion. The film thickness of the HD lubrication is usually between 20-100 μm and the maximum pressure between 2 MPa - 5 MPa. The friction occurring in the fluid film is high as the oil film for a HD lubrication is very thick. The torque initially required to rotate the shaft for the HD lubrication is also high. In addition, a HD lubrication system is also complex and needs routine maintenance. In spite of these disadvantages, hydrodynamic lubrication can carry heavy loads and has a long service life. This lubrication type is only applied in large machinery, such as the plain bearing in generators or turbine machines.

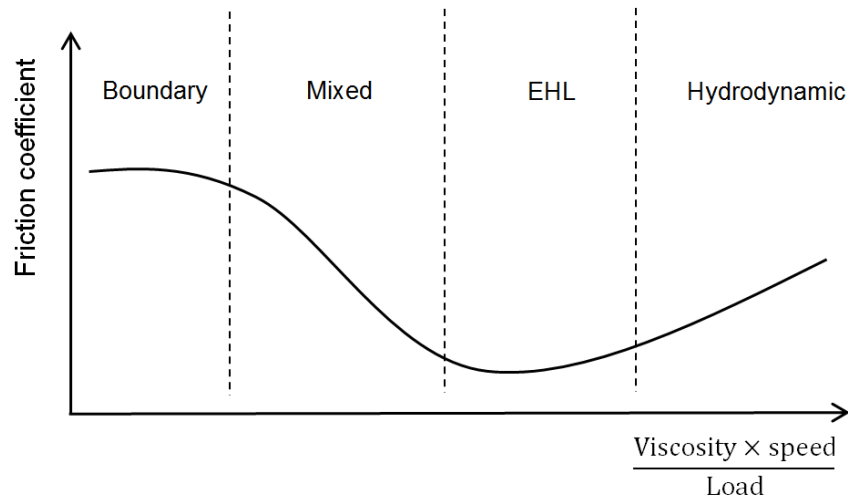


Figure 1-1: A typical Stribeck curve [1].

The second lubrication type is elastohydrodynamic lubrication (EHL). This lubrication is also full film, similar to the first type, but thinner, and pressure can be generated in pure rolling conditions without sliding. The generated pressure of EHL is extremely high and can cause the elastic deformation of solids. EHL also attracts more attention from researchers and has been continuously developed. In general, this viscous fluid film lubrication is commonly used in small and medium machines as it has less friction, smaller than hydrodynamic lubrication, and requires less maintenance. A common application of this fluid film lubrication is shown in Figure 1-2.



Figure 1-2: A typical cylindrical roller bearing [2].

The third type is mixed lubrication. Although similar to EHL, it involves the partial contact of asperities between both surfaces as the lubricant film is lower than the surface roughness. Direct contact can cause more wear and higher friction force, which is also the main cause of machinery breakdown. This lubrication can occur during lubricant starvation or overload conditions.

The fourth and final type is boundary lubrication. This type of lubrication occurs when a machine is starting or stopping, as the speed of the moving parts is very slow causing a discontinuous fluid film over their surface. This lubrication is likely to be a dry contact that has a higher friction and rate of wear than other types of lubrication.

The characteristics of lubrication, as described above, depend on fluid film thickness and the pressure generated in the thin fluid film. As a result, the influence of surface roughness on fluid film lubrication should be considered, as surface roughness has significant effects on friction force [3]. If the film thickness of the lubricant is lower than the peaks of surface roughness, a direct contact of both surfaces will occur, leading to a high friction coefficient as well as high wear rate. The influence of surface roughness on fluid film lubrication problems, however, is quite complex and is very difficult to investigate by using an experimental method. Therefore, a numerical approach is often sought to address such a problem. Understanding the effects of surface roughness on thin fluid lubrication is necessary for improving and analysing fluid film lubrication problems.

EHL is defined as a thin film lubrication, which takes into consideration the elastic deformation of materials under high pressure. An EHL model is developed from hydrodynamic lubrication by accounting for the elastic deflection in the film thickness equation. Conventionally, the viscous fluid flow in EHL problems has been represented by the Reynolds equation [4], developed by integrating the Navier-Stokes equations across the film thickness. In the past decade, the Reynolds equation has been improved by combining film thickness with the viscosity equation, the density equation, the energy equation, and the load balance for investigating EHL problems [5-7].

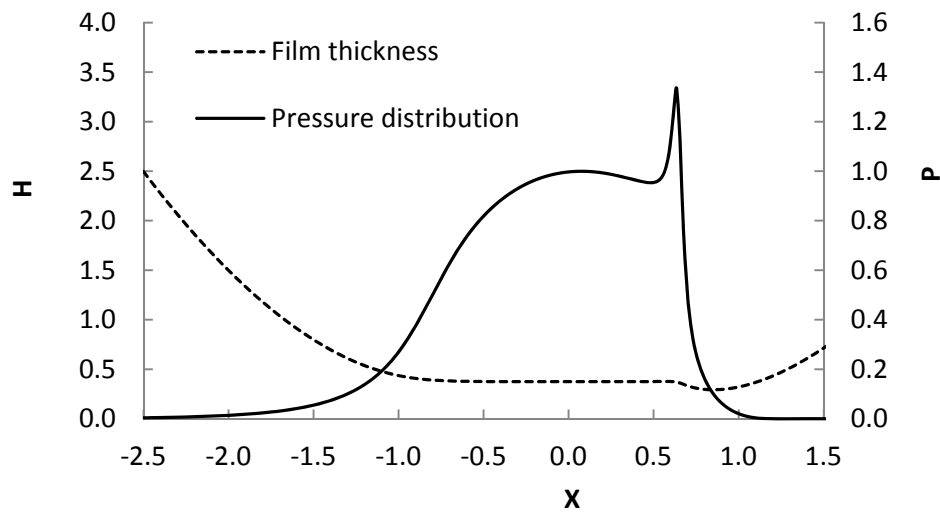


Figure 1-3: Dimensionless pressure (P) and film thickness (H) distributions of a typical EHL problem.

1.2 Literature review

Fluid film lubrication has gained widespread attention since 1886, when Osborne Reynolds [4] published his famous equation that is now known as the ‘Reynolds equation’ which governs the generation of pressure in a thin viscous fluid film. The Reynolds equation can be used to predict the characteristics of a laminar flow for the Newtonian fluid in a hydrodynamics lubrication problem, such as the pressure distribution and film thickness upon the contact area, as shown in Figure 1-3.

In 1916, Martin [8] presented an application of the Reynolds equation on the gears contact problem. To simplify the problem, the lubricant used was assumed to be incompressible, isoviscous, and the gears were considered to be smooth rigid bodies. Under these assumptions, Martin [8] predicted the minimum film thickness of the lubricant at the contact centre ($X=0$). However, the minimum film thickness was found to be smaller than the asperity of surface roughness. This result cannot be used to explain the real physics of gear contact, as the gears can still work for a long time with very little wear.

The contact surface becomes deformed under a heavy load and the properties of the bulk material should be considered in the evaluation of contact mechanics. Hertz [9, 10] studied the elastic deformation of solids in dry contact and proposed the elasticity theory which determines the resultant stresses between two spherical bodies. Hertz theory of elastic contact is widely accepted and considered to be the foundation of the study of deformation for non-conformal contacts.

Since 1939, the elastic deformation of solids [11] and the viscosity-pressure effects [12] have been applied to the Reynolds equation by Ertel [13] and Grubin [14]. By employing an analytical solution, they found that the minimum oil film thickness obtained is larger than the average surface roughness of the gear surfaces. It can be seen that the deformation of the solid surface and the viscosity-pressure effect are significant for fluid film lubrication behaviour. These applications on fluid film lubrication problems are widely known as 'elastohydrodynamic lubrication' (EHL).

In 1951, Petrusevich [15] was the first to solve the EHL line contact problem under steady state conditions by a numerical method. The numerical solution predicted the presence of a second maximum pressure peak. According to the pressure profile obtained, the pressure increases gradually at the lubricant inlet region of contact, reaches a pressure maximum, and then slightly drops after passing the contact centre. It then rapidly spikes, as illustrated in Figure 1-3. It can be observed that the pressure spike occurs at the minimum film thickness position. This feature is known as the 'Petrusevich Pressure Spike'.

Many numerical techniques have been proposed to calculate the Reynolds equation, which is a non-linear differential equation. In 1959, Dowson and Higginson [16] used a numerical method (inverse method) to solve EHL problems with the Newtonian fluid and isothermal conditions. This method is mainly suitable for highly loaded cases. By observing the experiment of Dyson et al. [17], measuring oil film thickness, it was found that isothermal EHL analysis could not be used to predict film thickness when this is significantly decreased at high rolling speeds.

In 1962, Dowson [18] presented an analytical method derived from the combination of lubricant properties (density and viscosity) and the classic Reynolds equation. The modified Reynolds equation is known as the 'generalized Reynolds equation' and can be used to predict viscous fluid film lubrication problems in a more realistic way than the previous deterministic models, which assumed isothermal conditions. By including thermal effects, the model deriving from the generalized Reynolds equation can describe the thermal effects on hydrodynamic lubrication problems [19]. In addition, in 1967, Cheng [7] investigated the influence of viscous shear heating at the inlet region and found that it was significant to the reduction of the oil film thickness.

In 1976, Hamrock and Dowson [20] showed how Gauss-Seidel relaxation can be applied to the iterative method for solving the EHL point contact problem. The Gauss-Seidel technique is successful when applied to the EHL line contact problem, but takes a long time to converge in a point contact problem. Later, in 1983, Okamura [21] suggested the use of the Newton-Raphson method for solving the Reynolds equation. It was found that the Newton-Raphson method is a powerful numerical technique for solving the Reynolds equation and is much faster than previous techniques.

In 1987, Lubrecht [22, 23] suggested the use of the multilevel technique, a multi-scale approach designed to speed up significantly the numerical procedure for solving EHL problems. This method was developed and designed to solve differential equations and reduce the simulation time. Following Lubrecht's work, a number of faster numerical evaluation techniques were proposed to reduce the simulation time, such as adaptive meshing, multigrid-multilevel and multilevel multi-integration [24, 25].

The surface roughness effect on the thin fluid film problem has been continuously studied since the first rough surface model based on stochastic theory was presented by Christensen in 1969 [26]. It was found that the influence of surface roughness on the hydrodynamic problem depends on the type of roughness. Subsequently, many mathematical models were proposed to predict the influence of surface roughness on the fluid film lubrication problem.

For example, in 1978, Patir and Cheng [27] studied the effect of surface roughness on hydrodynamic lubrication problems by creating a general roughness pattern model. This model is useful but cannot deal with real roughness that is non-isotropic.

In 1992, Venner and Napel [28] studied the effects of surface roughness on the EHL problem. They determined the roughness profile by measuring the actual surface of the material, as surface texture significantly influences both pressure profile and film thickness. Later, in 2001, Zhu and Hu [29] studied the effects of surface roughness on the EHL and mixed lubrication problems with circular contact. The simulation results indicated that the average film thickness in the case of rough surfaces was slightly thicker than in the case of smooth surfaces.

In 2002, a commercial computational fluid dynamic (CFD) code, based on the momentum equation, the continuity equation and the energy equation, was used by Almqvist et al. [30] to simulate an EHL line contact problem. They compared the solutions to an EHL problem solved both by the Reynolds equation and by the contemporary CFD techniques used in commercial CFD software. The results from both methods were in good agreement. A small deviation, however, was found in the case of thin film thickness [31]. In 2008, Almqvist and Larsson [32] developed an EHL model with CFX4, commercial CFD package, which considered the effects of temperature, surface roughness and time dependence. In this model, the fluid is considered to be non-Newtonian and the upper surface is assigned a sinusoidal roughness, while the lower plate is defined as a smooth surface. The results showed that temperature and surface roughness bear an influence on pressure and film thickness. However, the pattern from real surface roughness was not represented by the sinusoidal model.

In 2008, Hartinger et al. [33] presented a CFD model of the thermo-elastohydrodynamic lubrication (TEHL) line contact problem. The shear in thin film was studied in the CFD model and compared with the Reynolds equation approach. The free package OPENFOAM was employed to solve the TEHL problem. The cavitation effect, which is not modelled by the Reynolds equation,

was considered by modifying the momentum computation as a function of pressure to include the effect of lubricant density. The results from the Reynolds equation and the CFD model are similar, with the exception of a small difference between the pressure predictions of the two methods observed in the case of high viscosity.

Recently, Bruyere et al. (2011) [34] presented a CFD model and a full elastic model for an EHL sliding line contact problem. They proposed an approach for solving the Navier-Stokes equations, in which a finite-element method was used to solve the discretized equation of the Navier-Stokes equations. The results obtained indicated that the friction in the contact region has the dominant effect on the heat generated in the lubricant at the inlet region.

It can be seen from the above literature review that the study of the thin film lubrication problems has been continually developed. There are many assumptions in the generalised Reynolds equation. For example, the deformation term in the film thickness equation is calculated by using the effective elastic modulus instead of the Young's modulus of solids. In addition, the effective radius or the average radius of curvature of rollers is employed to represent the radii of both geometries for a two rollers configuration. These parameters will affect the results obtained, as the thin fluid film problem is very complex. These observations have led to the use in this project of a CFD model, instead of the Reynolds equation, to simulate and analyse EHL problems.

1.3 Aims and objectives

The aim of this study is to develop further CFD techniques for predicting and analysing the characteristics of the TEHL line contact problem. Three CFD models are designed to study the viscous fluid flow in a small gap for the contact between a cylinder and a flat plate, cylinders of equal radii ($R_1=R_2$), and cylinders of unequal radii ($R_1<R_2$).

The first model will be designed for the contact between a cylinder and a plate. This model will be used to investigate the influence of some key parameters on the characteristics of the TEHL line contact problem. A combination of viscosity, load, velocity, and material properties will be simulated under smooth and rough surfaces conditions. The effect of modelling viscosity either as a Newtonian fluid and a non-Newtonian fluid will be investigated. Furthermore, the influence of thermal effects on the viscosity and density of the selected lubricant will be considered, in the place of isothermal conditions.

The second and third models will be designed for predicting the contact conditions between infinite-length (two dimensional) cylinders. Cylinders with the same radius of contact will be investigated in the second CFD model and the contact between subsequently the cylinders of different radius will be studied in the third CFD model. Both CFD models will be employed to study the distorted film thickness shape when the material elastic deformation and radius of each cylinder are applied directly to them. The deformation on each cylinder from the second and third CFD models will be compared with that from the first CFD model (roller and plate contact). More importantly, the influence of surface roughness on the thin fluid film will be studied in all three CFD models. The measured real surface profile will be used in the first and second CFD models, while stochastically generated surface profiles will be employed in the third CFD model. The aim is for behaviour predicted by the TEHL problem through the CFD simulation using more accurate models to be more like the reality.

The objectives of this research are:

1. To create and develop predictive models for the TEHL line contact problem by using CFD techniques.
2. To study the effects of real surface roughness on the TEHL line contact problem by using the developed CFD models.
3. To compare the effects of surface roughness on the TEHL line contact problem between predictions from CFD models.

Chapter 2

Elastohydrodynamic Lubrication

2.1 Introduction

In this chapter, a brief introduction to the theory of the Reynolds equation for elastohydrodynamic lubrication (EHL) is presented. Other equations employed, such as the film thickness equation, the density equation, the viscosity equation and the load balance equation are also described. Viscosity models for both Newtonian fluid and non-Newtonian fluid are defined. After that, the elastic deformation in the film thickness equation, which depends upon pressure generation and Young's modulus of elasticity, is explained. Finally, the energy equation used to compute the temperature rise in the oil film at the contact area is described.

2.2 The Reynolds equation

Typically, the macroscopic behaviour of fluid in motion can be modelled by the Navier-Stokes equations, which describe the motion of the fluid and the relationship between velocity and fluid stress in the element of fluid. In 1886, Reynolds [4] derived a simplified form of the Navier-Stokes equations to model the pressure distribution in a thin fluid film by integrating the Navier-Stokes equations across the film thickness. The Reynolds equation, based on the conservation of mass, has a partial differential equation form. In this equation, the lubricant is assumed to be a Newtonian and incompressible fluid. In 1962, Dowson [18] developed the theory for a general Reynolds equation further by

considering the effects of viscosity changes across the film thickness. The following assumptions were made:

- The weight of the fluid is negligible.
- The viscous fluid flow is considered to be laminar.
- The lubricant is considered to be a Newtonian fluid.
- There is no-slip surface between the solid and the fluid.
- Surface tension and the inertia of the fluid are negligible when compared with viscous forces.
- The pressure is constant across the film thickness ($\frac{\partial p}{\partial z} = 0$).

For simplicity, Dawson [16] specified further assumptions in the derivation of the generalised Reynolds equation - i.e. shear stress and velocity gradients are applied only perpendicularly to the direction of the fluid flow. An element of fluid with applied forces is depicted in Figure 2-1.

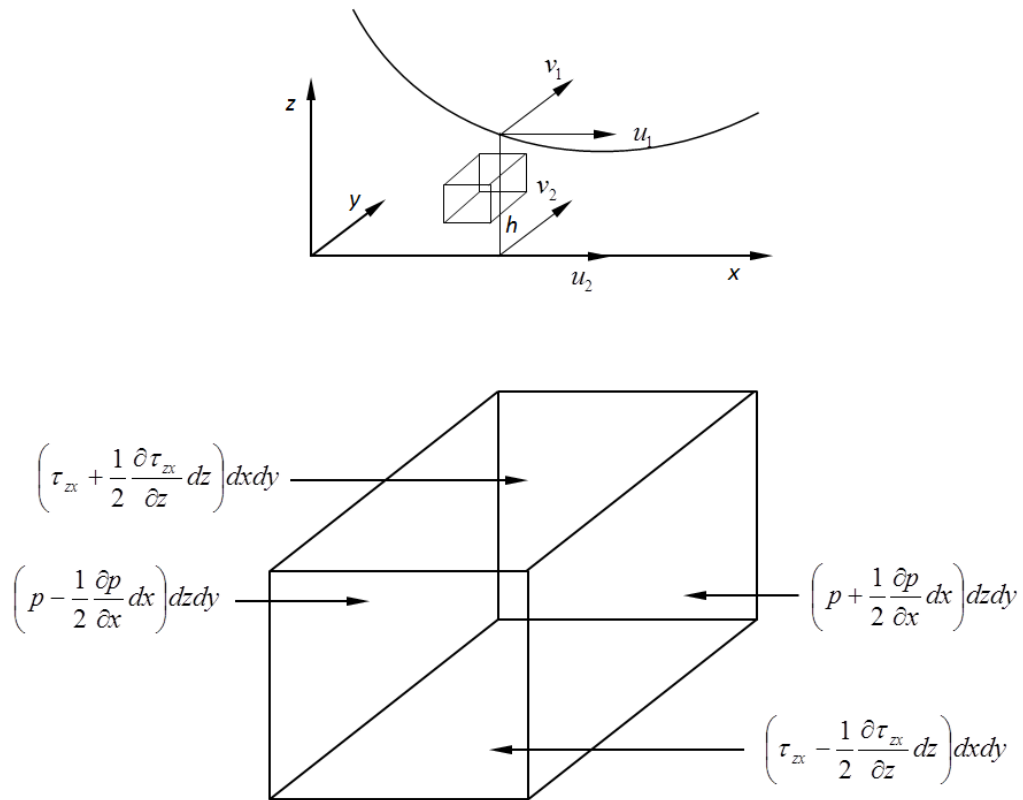


Figure 2-1: The acting forces on a fluid element [35].

If the shear stresses and velocity gradients in the x and y directions are considered negligible, the relation between pressure and stress can be written as [5]:

$$\begin{aligned}\sum F_x &= 0 \\ \frac{\partial \tau_{zx}}{\partial z} &= \frac{\partial p}{\partial x}\end{aligned}\quad (2.1)$$

Similarly,

$$\begin{aligned}\sum F_y &= 0 \\ \frac{\partial \tau_{zy}}{\partial z} &= \frac{\partial p}{\partial y}\end{aligned}\quad (2.2)$$

According to Newton's law of viscosity:

$$\begin{aligned}\tau_{zx} &= \mu \frac{\partial u}{\partial z} \\ \tau_{zy} &= \mu \frac{\partial v}{\partial z}\end{aligned}\quad (2.3)$$

Substituting equation (2.3) into equations (2.1) and (2.2) gives:

$$\frac{\partial}{\partial z} \left(\mu \frac{\partial u}{\partial z} \right) = \frac{\partial p}{\partial x} \quad (2.4)$$

and

$$\frac{\partial}{\partial z} \left(\mu \frac{\partial v}{\partial z} \right) = \frac{\partial p}{\partial y} \quad (2.5)$$

Equations (2.4) and (2.5) are integrated with respect to z twice to obtain:

$$u = \left(\frac{1}{\mu} \right) \frac{\partial p}{\partial x} \frac{z^2}{2} + \frac{cz}{\mu} + d \quad (2.6)$$

$$v = \left(\frac{1}{\mu} \right) \frac{\partial p}{\partial y} \frac{z^2}{2} + \frac{c_1 z}{\mu} + d_1 \quad (2.7)$$

In order to determine the integration constants in equations (2.6) and (2.7), the boundary conditions are required to be defined. The boundary conditions for u at the plate and cylindrical surface are $u = u_1$ at $z = h$ and $u = u_2$ at $z = 0$, from which the stream wise velocity distribution of the fluid is obtained:

$$u = \left(\frac{1}{2\mu} \right) \frac{\partial p}{\partial x} (z^2 - zh) + \frac{z}{h} (u_1 - u_2) + u_2 \quad (2.8)$$

The boundary conditions for v at the plate and cylindrical surface are $v = v_1$ at $z = h$ and $v = v_2$ at $z = 0$, respectively from which the flow-normal velocity distribution of the fluid is obtained:

$$v = \left(\frac{1}{2\mu} \right) \frac{\partial p}{\partial y} (z^2 - zh) + \frac{z}{h} (v_1 - v_2) + v_2 \quad (2.9)$$

The continuity equation or conservation of mass in two dimensions can be written as:

$$\frac{\partial}{\partial x}(\dot{m}_x) + \frac{\partial}{\partial y}(\dot{m}_y) + \frac{\partial}{\partial t}(\rho h) = 0 \quad (2.10)$$

where $\dot{m}_x = \rho q_x = \rho \int_0^h u dz$, $\dot{m}_y = \rho q_y = \rho \int_0^h v dz$

By substituting equations (2.8) and (2.9) into (2.10) gives:

$$\frac{\partial}{\partial x} \left(\rho \int_0^h u dz \right) + \frac{\partial}{\partial y} \left(\rho \int_0^h v dz \right) + \frac{\partial}{\partial t} (\rho h) = 0 \quad (2.11)$$

where:

$$\rho \int_0^h u dz = - \left(\frac{\rho h^3}{12\mu} \right) \left(\frac{\partial p}{\partial x} \right) + (u_1 + u_2) \left(\frac{\rho h}{2} \right) \quad (2.12)$$

$$\rho \int_0^h v dz = - \left(\frac{\rho h^3}{12\mu} \right) \left(\frac{\partial p}{\partial y} \right) + (v_1 + v_2) \left(\frac{\rho h}{2} \right) \quad (2.13)$$

Thus, substituting equations (2.12) and (2.13) into (2.11), the Reynolds equation for the Newtonian fluid can be derived as [36]:

$$\begin{aligned} \frac{\partial}{\partial x} \left[\frac{\rho h^3}{12\mu} \frac{\partial p}{\partial x} \right] + \frac{\partial}{\partial y} \left[\frac{\rho h^3}{12\mu} \frac{\partial p}{\partial y} \right] = \\ \frac{\partial}{\partial x} \left[\rho h \left(\frac{u_1 + u_2}{2} \right) \right] + \frac{\partial}{\partial y} \left[\rho h \left(\frac{v_1 + v_2}{2} \right) \right] + \frac{\partial}{\partial t} (\rho h) \end{aligned} \quad (2.14)$$

The first and second terms describe the net flow rate and are known as the 'Poiseuille terms'. The Poiseuille terms are a result of pressure gradients in the thin fluid film. The third and fourth terms, which are the 'Couette terms', represent the net entrainment flow rates due to the wall motion. The last term, which is the local expansion, describes the density change of the fluid over time. The physical changes in a thin fluid film can be explained by these terms [37]. It can be observed that the flow speed, density, and viscosity are all part of the mechanism of pressure generation in a viscous thin fluid film.

The Reynolds equation for a line contact problem stated in terms of dimensionless values can be derived by introducing the following non-dimensional parameters [38]:

$$\begin{aligned}
X &= \frac{x}{b} & P &= \frac{p}{p_h} & \bar{\rho} &= \frac{\rho}{\rho_0} & H &= \frac{hR'}{b^2} \\
W &= \frac{w}{E'R'} & \bar{\mu} &= \frac{\mu}{\mu_0} & t^* &= \frac{u_m t}{b} & b &= R' \left(\frac{8W}{\pi} \right)^{0.5} \\
U &= \frac{u_m \mu_0}{E'R'} & u_m &= \frac{u_1 + u_2}{2} & \frac{1}{R'} &= \frac{1}{R_1} + \frac{1}{R_2} & p_h &= E' \left(\frac{W}{2\pi} \right)^{0.5}
\end{aligned}$$

Thus, the applied Reynolds equation in dimensionless form for an EHL line contact problem is:

$$\frac{\partial}{\partial X} \left(\varepsilon \frac{\partial P}{\partial X} \right) = \frac{\partial}{\partial X} (\bar{\rho} H) + \frac{\partial}{\partial t^*} (\bar{\rho} H) \quad (2.15)$$

where

$$\varepsilon = \frac{\bar{\rho} H^3}{\bar{\mu}} \left(\frac{b^3 p_H}{12 \mu_0 u_m R'^2} \right)$$

It can be noticed that the above Reynolds equation is a partial differential equation (PDE). Usually, a mathematical model for a non-linear problem is commonly solved by using a numerical method, where it is necessary to change the form of the Reynolds equation from the differential equation into the discretized equation by applying the finite difference method [39, 40]. The discretized equation can then be solved by using algebraic methods, such as the Newton-Raphson method and the multigrid method. The numerical method used in this problem and the flow chart of calculations are explained further in the appendix three and appendix four, respectively.

2.3 The film thickness equation

The contact between the cylinder and the plate is considered to be a non-conforming contact and referred to as a Hertzian contact. Hertz made the following assumptions [9, 35, 41].

- The strains are small.

- Each solid can be considered as an elastic half-space in the proximity of the contact region.
- The surfaces are frictionless.
- The surfaces are continuous, smooth and non-conforming.
- The geometry of the initially undistorted surfaces touching at a point or along a line is described by quadratic terms only, as the region of interest is very close to a point or line.

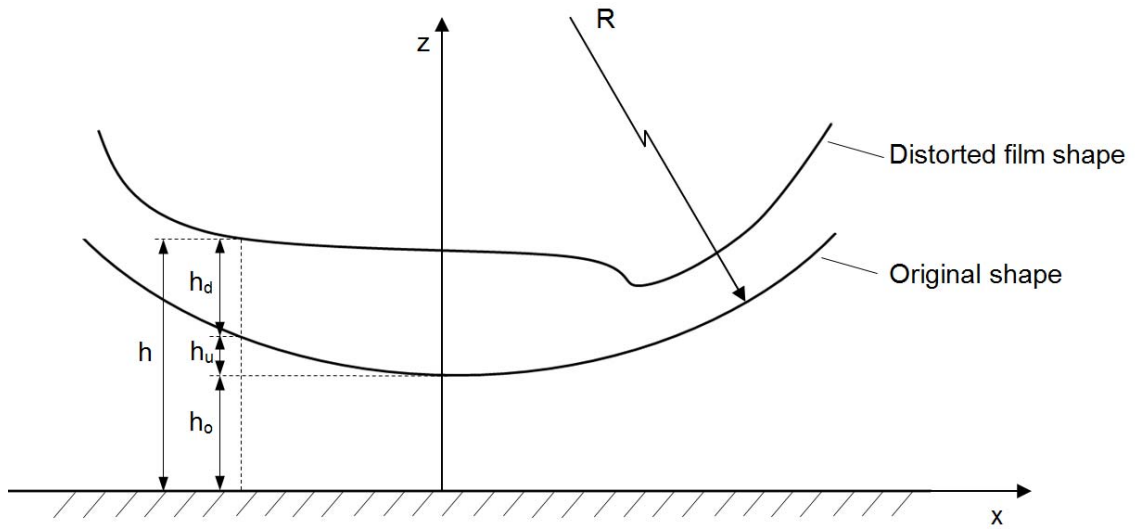


Figure 2-2: EHL film shape [35, 42].

Consider a cylinder rolling over a lubricated plate. The oil film thickness, separating the surface of solids, can be represented by the film thickness equation for the EHL problems, which consists of three parts as described in Figure 2-2. The first component (h_o) is the undeformed gap between the cylinder and the plate or known as the ‘minimum film thickness’. The second component (h_u) is the parabolic approximation for the undeformed geometry which is assumed to be a parabola following Hertz’s theory. The last term (h_d) is the elastic deformation of a surface due to a pressure field, $p(x)$. It is obtained by integrating the pressure distribution over the x coordinate, as suggested by Timoshenko and Goodier [10, 43, 44]. At any point, the film shape can be expressed as:

$$h(x) = h_o + h_u(x) + h_d(x) \quad (2.16)$$

Therefore, the film thickness equation can be computed by the following:

$$h = h_o + \frac{x^2}{2R'} - \frac{2}{\pi E'} \int_{-\infty}^{\infty} p(\xi) \ln(|x - \xi|^2) d\xi \quad (2.17)$$

where E' is an effective elastic modulus, and x_o is the distance at which the elastic deformation is zero. E' can be calculated from the Young's modulus and the Poisson ratios of the contacting bodies as:

$$\frac{2}{E'} = \frac{1 - \nu_1^2}{E_1} + \frac{1 - \nu_2^2}{E_2} \quad (2.18)$$

where subscript 1 refers to the cylinder and subscript 2 refers to the plate.

2.4 The force balance equation

After the Reynolds equation is solved, it is necessary to ensure that the applied load on a cylinder is balanced by integrating the pressure generated over the contact region. The moving direction of the top cylinder can be moved up or down depending on the balance of the generated pressure and the applied load. The proportion of the unbalanced force (defect) is used to calculate the vertical displacement of the cylinder. This can be done by integrating the pressure distribution over the contact area so that:

$$w = \int_{-\infty}^{\infty} p dx \quad (2.19)$$

where w is an applied load (N/m). Thus, correcting the undeformed gap term in equation (2.17) is given by:

$$h_o^{new} = h_o^{old} + c \cdot defect \quad (2.20)$$

and

$$defect = \left(w - \int_{-\infty}^{\infty} p dx \right) \quad (2.21)$$

where c is a constant affecting the stability of the solution. The solution will generally converge faster with larger c , but may not be stable or converge in some cases. The c parameter can be considered an under-relaxation factor that is determined in the numerical implementation, c by using trial and error which typically takes a number of attempts.

2.5 Rheology

Rheology is the study of fluid properties such as viscosity, velocity, and shear stress [45]. The main variables that influence viscosity in a flow are the shear stress and the strain rate. The viscosity index can be measured by a rotational viscometer as shown in Figure 2-3. Additionally, Figure 2-4 shows the bob that is rotated while the cup is a stationary part [43, 46, 47].



Figure 2-3: The rotational viscometer [48].

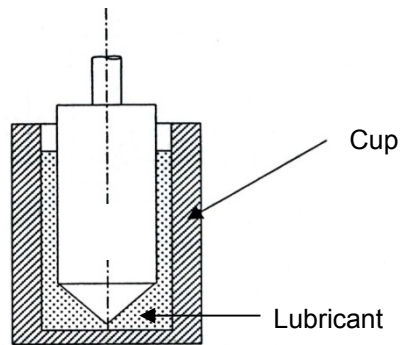


Figure 2-4: The standard cup to measure the viscosity of fluids using a rotational viscometer [48].

In order to specify the type of fluid according to its traction behaviour, it is necessary to consider the relationship between shear stress and strain rate. From this, a fluid can be classed either as a Newtonian fluid or non-Newtonian fluid [46].

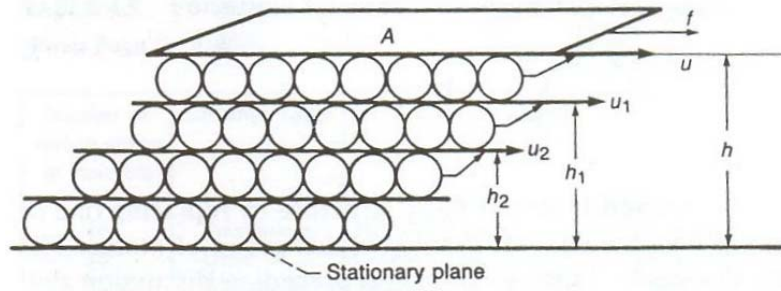


Figure 2-5: Schematic of Newton's postulate [49].

2.5.1 Newtonian fluid

If the relationship between the shear stress and the shear strain rate in each layer of fluid is constant, the fluid behaviour is considered to be Newtonian. The relationship between dynamic viscosity and shear stress was found by Newton [35] and it can be written as:

$$\mu = \frac{(F / A)}{(u / h)} = \frac{\tau}{\dot{\gamma}} \quad (2.22)$$

where $\dot{\gamma}$ is the shear strain rate and τ is the shear stress.

By the Newton's law of viscosity, a laminar flow assumes a layer of fluid which consists of oil molecules as shown in Figure 2-5. Each cylinder represents a small molecule of oil that rotates on the oil layer beneath it. The translational velocity of each layer has a different magnitude and each layer has a friction coefficient called dynamic viscosity. This principle can be written as:

$$\tau = \mu \frac{du}{dy} \quad (2.23)$$

Therefore, the relationship between shear stress and shear strain rate of the Newtonian fluid has to be linear, as shown in Figure 2-6. It is well understood that the dynamic viscosity (absolute viscosity) μ of a lubricant increases with pressure, especially in the case of a thin film. Models for the relation between pressure and viscosity in lubricants are proposed by Barus [50], Chu and Cameron [51] and Roelands [6]. The Roelands model is a popular model for the EHL problem. The model relates the pressure and the dynamic viscosity as:

$$\mu_{Roeland} = \mu_0 \exp \left\{ \left[\ln(\mu_0) + 9.61 \right] \left[-1 + \left(1 + 5.1 \times 10^{-9} p \right)^n \right] \right\} \quad (2.24)$$

where μ_0 is the viscosity at atmospheric pressure, p is the pressure and n is the pressure viscosity index that can be calculated from:

$$n = \frac{\alpha}{5.1 \times 10^{-9} [\ln(\mu_0) + 9.67]} \quad (2.25)$$

However, the viscosity equation as shown in equation (2.24) can only be used in the case of an isothermal analysis. The influence of thermal gradients is significant on the viscosity of a fluid, in particular for the case of a high rolling speed and heavy load [52]. Then, the Roeland model was further developed to obtain accurately the viscosity as a function of pressure and temperature by Houpert [53]. Therefore, the complete viscosity relationship is given by:

$$\mu_{Houpert} = \mu_0 \exp \left\{ [\ln(\mu_0) + 9.61] \left[-1 + (1 + 5.1 \times 10^{-9} p)^n \right] \left(\frac{T - 138}{T_0 - 138} \right) - c(T - T_0) \right\} \quad (2.26)$$

where $c = (\ln(\mu_0) + 9.61) (1 + 5.1 \times 10^{-9} p)^n \left(\frac{S_0}{T_0 - 138} \right)$

$$S_0 = \beta \left(\frac{T_0 - 138}{\ln(\mu_0) + 9.61} \right)$$

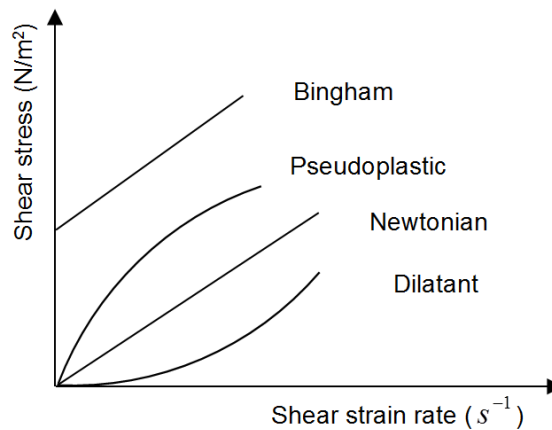


Figure 2-6: The relation of shear stress and shear strain rate for different types of fluids [54].

2.5.2 Non-Newtonian fluids

Referring to Figure 2-6, it can be observed that the relationship between shear stress and shear strain rate is non-linear for pseudoplastic fluids (shear thinning

fluids), viscoplastic fluids (yield stress fluids), or dilatant fluids (shear-thickening fluids). In general, the viscosity of non-Newtonian fluids is dependent on the shear strain rate. Several models have been proposed to explain the behaviour of non-Newtonian fluid flow, for example, the Power law model [36], the Carreau model [55] and the Ree-Eyring model [56]. The viscosity of a non-Newtonian fluid can be described in term of the strain rate (rate of deformation) tensor, which is given by:

$$\dot{\gamma} = \nabla \mathbf{u} + (\nabla \mathbf{u})^T \quad (2.27)$$

where \mathbf{u} is the velocity vector, ∇ is the gradient operator, and T indicates the matrix transpose. The equivalent shear strain rate, which is related to the second invariant of the rate of deformation tensor ($\dot{\gamma}$), can be defined as:

$$\dot{\gamma}_{eq} = \left(\frac{1}{2} \dot{\gamma} : \dot{\gamma} \right)^{1/2} \quad (2.28)$$

where the $:$ is the double scalar product. Substituting equation (2.27) into equation (2.28) gives:

$$\dot{\gamma}_{eq} = \frac{1}{\sqrt{2}} \left[\left(\nabla \mathbf{u} + (\nabla \mathbf{u})^T \right) : \left(\nabla \mathbf{u} + (\nabla \mathbf{u})^T \right) \right]^{1/2} \quad (2.29)$$

$$\dot{\gamma}_{eq} = \frac{1}{\sqrt{2}} \left\| \nabla \mathbf{u} + (\nabla \mathbf{u})^T \right\| \quad (2.30)$$

In tensor form, the equivalent shear strain rate is written as:

$$\dot{\gamma}_{eq} = \left[\frac{1}{2} \left(\frac{\partial u_i}{\partial x_j} + \frac{\partial u_j}{\partial x_i} \right)^2 \right]^{1/2} \quad (2.31)$$

i) The Power law model

The Power law model [36] is often used to represent the behaviour of fluid flow because it is a simple model and can represent both non-Newtonian and Newtonian fluids, especially pseudoplastic fluids. This model was developed by using curve fitting experimental data and the type of fluid flow can be defined by a viscosity index (n). The viscosity of fluid which follows the power law model can be expressed as [46]:

$$\mu_{power} = m [\dot{\gamma}_{eq}]^{n-1} \quad (2.32)$$

where $n=1$ for a Newtonian fluid,

$n > 1$ for a non-Newtonian fluid of the dilatant type,

$n < 1$ for a non-Newtonian fluid of the pseudoplastic type, and

$\dot{\gamma}_{eq}$ is the equivalent shear strain rate.

The m and n are the consistency coefficient of the fluid and the Power law index, respectively. It should be noted that the Power law model has a weak point as both parameters are dependent on a shear strain rate. Therefore, using the power law model may not be accurate in the case of high and low shear strain rates.

ii) The Carreau model

The Carreau viscosity model [55] can be used to predict the flow behaviour of the fluid flow for the same type as the Power law model. For the pseudoplastic fluid, finite values of shear stress occur as the shear strain rate is zero or tends to infinity and these conditions cannot be calculated by the Power law model. On the contrary, the Carreau viscosity model, which includes zero shear strain rate and the infinite shear strain rate terms, is given by:

$$\mu_{carreau} = \mu_{\infty} + (\mu_c - \mu_{\infty}) \left[1 + (\lambda \cdot \dot{\gamma}_{eq})^2 \right]^{(n-1)/2} \quad (2.33)$$

where

μ_c is the zero-shear strain rate viscosity,

μ_{∞} is the infinite-shear strain rate viscosity,

λ is a time constant, which can be expressed as $\lambda = \mu_0 / G$,

G is a shear modulus,

n is the power index, and

$\dot{\gamma}_{eq}$ is the equivalent shear strain rate.

iii) The Ree-Eyring model

The Ree-Eyring model is widely used for modelling non-Newtonian fluids in the EHL problem. This model was proposed by Eyring [57] in 1936 to explain the increase of viscosity with the shear stress. Johnson and Tevaarwerk [56] later experimentally curve fitted the model with five different fluids and found that the

sinh law can be used to predict the shear thinning behaviour very well. In order to produce the non-linear viscous function, the zero shear strain rate viscosity, a reference shear stress and a reference shear rate modulus are used to define $\dot{\gamma}_{eq}$ in the Ree-Eyring model:

$$\dot{\gamma}_{eq} = \frac{\dot{\tau}}{G} + \frac{\tau_0}{\mu_0} \sinh\left(\frac{\tau}{\tau_0}\right) \quad (2.34)$$

Bair et al. [58, 59] suggested that the elastic term $\dot{\tau}G^{-1}$ in equation (2.34) can be ignored as the time-dependency of viscosity is not significant when this model is applied to the EHL problem. Thus, the shear strain rate can be approximated by:

$$\dot{\gamma}_{eq} = \frac{\tau_0}{\mu_0} \sinh\left(\frac{\tau}{\tau_0}\right) \quad (2.35)$$

According to the Newton's law of viscosity, the relation among shear stress, equivalent shear strain rate and the Ree-Eyring viscosity can be defined as:

$$\tau = \mu_{Ree-Eyring} \dot{\gamma}_{eq} \quad (2.36)$$

Therefore, the shear-thinning of EHL lubricants can be calculated from the following formula:

$$\mu_{Ree-Eyring} = \frac{\tau_0}{\dot{\gamma}_{eq}} \sinh^{-1}\left(\frac{\mu_0 \dot{\gamma}_{eq}}{\tau_0}\right) \quad (2.37)$$

where $\dot{\gamma}_{eq}$ is the equivalent shear strain rate,

μ_0 is the viscosity at atmospheric pressure, and

τ_0 is the reference shear stress.

The viscosity of fluid in the EHL problem is a function of pressure and the temperature, thus the μ_0 term in equations (2.37) is estimated by $\mu_{Houpert}$ as presented in equation (2.26).

2.6 The density equation

In the EHL problem, the density of lubricants is affected when the pressure or temperature of the lubricant changes. The relationship between pressure and density in the thin film problems developed by Dawson and Higginson in 1962

[38, 60] is widely used in EHL problems. In addition, the experimental study by Hirano et al. [61] presented a relationship for the density of mineral oil and pressure which can be written as:

$$\rho = \rho_0 \left(1 + \frac{0.59 \times 10^{-9} p}{1 + 1.7 \times 10^{-9} p} \right) \quad (2.38)$$

where ρ_0 is the density at atmospheric pressure. However, a realistic rheological model for the compressibility of the film thickness in the EHL problem should also account for thermal effect. The pressure-density and temperature relationship for a lubricant is given by [62, 63]:

$$\rho = \rho_0 \left(1 + \frac{0.59 \times 10^{-9} p}{1 + 1.7 \times 10^{-9} p} \right) [1 - \varepsilon (T - T_0)] \quad (2.39)$$

where T_0 is the ambient temperature and ε is the thermal expansivity of the lubricant (1/K).

2.7 Energy equation

Among a number of factors, the main influence of heat on the film thickness in the EHL problem is due to viscous shear [64]. In addition, compression in the fluid film is also important for the heat generated [35] in an oil film. An increase in temperature can affect lubricant properties, such as viscosity and density. Particularly for the heavy load and high sliding rate case, the temperature within the lubricant film will rise significantly, thereby reducing the viscosity and the density of the lubricant. As a result, the thermal effect should be accounted for in a well formulated EHL model. Therefore, both the Reynolds equation and an energy equation will be simultaneously solved for predicting the characteristics of the TEHL problem.

In order to determine the energy equation governed by the law of conservation of energy, some assumptions are made. The variation of pressure across the fluid thickness is negligibly small because the film thickness in the TEHL problem is very thin and thus thermal gradients across the film thickness are not taken into consideration. In addition, the heat convection across the fluid film and the heat conduction along the film thickness are also very small and, thus,

equally ignored. The appropriate boundary conditions, including the pressure and temperature at the inlet, are kept at ambient conditions, while the outlet temperature is extrapolated from the interior domain. The energy equation, which is a compound of convection, conduction and heat source terms for the EHL line contact problem, can be expressed as follows [7, 65-67]:

$$\frac{\partial}{\partial z} \left(k \frac{\partial T}{\partial z} \right) = \rho C_p \left(u \frac{\partial T}{\partial x} + \frac{\partial T}{\partial t} \right) + \varepsilon T \left(u \frac{\partial p}{\partial x} + \frac{\partial p}{\partial t} \right) - \mu \left(\frac{\partial u}{\partial z} \right)^2 \quad (2.40)$$

where k is thermal conductivity and ε the thermal expansivity of the lubricant.

In the Reynolds equation model of section (2.2), the calculation of the temperature increase over a moving surface is obtained by Carslaw and Jaeger [68, 69]. They derived the conductive heat transfer from fluid film to solid surfaces (temperatures at the top cylinder: T_c and the bottom plate: T_p) as expressed by the following equations:

$$T_p(x, 0) = T_0 + \frac{k_f}{\sqrt{\pi \rho_1 C_{p1} k_1 u_1}} \int_{-\infty}^x \frac{\partial T}{\partial z} \Big|_{z=0} \frac{1}{\sqrt{x-x'}} dx' \quad (2.41)$$

$$T_c(x, h) = T_0 - \frac{k_f}{\sqrt{\pi \rho_2 C_{p2} k_2 u_2}} \int_{-\infty}^x \frac{\partial T}{\partial z} \Big|_{z=h} \frac{1}{\sqrt{x-x'}} dx' \quad (2.42)$$

According to the work of Cheng and Sternlicht [70], the singularity at $x = x'$ can be removed by assuming a linear function for a heat flux term. In order to predict the characteristic of the TEHL problem, the Reynolds equation and the energy equation will be simultaneously solved. Then, the pressure and the temperature obtained will be used to update the lubricant properties in each iteration, until convergence is achieved.

In the CFD models of section (5.5), the Cheng and Sternlicht [70] model is not used and the temperature is imposed as constant and equal to the ambient temperature.

Chapter 3

Surface Roughness

3.1 Introduction

It is important to understand the surface roughness of a workpiece as it plays an important role in the contact with other components. This chapter briefly describes the definition and characteristics of surface roughness, including the measurement of surface roughness. The parameters used to characterise a surface roughness profile, which are the average surface roughness (R_a), the root mean square (R_q), the skewness value (R_{sk}) and the kurtosis (R_{ku}), are explained. Then, the Abbott-Firestone curve that is commonly used to illustrate the properties of bearing surfaces is presented. Furthermore, examples of the surface roughness of a cylindrical roller bearing measured using the Surtronic 3+ are presented and analysed. Finally, a number of techniques used to filter the wave form of the profile of the measured surface roughness are explained, in addition to the theory of probability distribution used to generate a synthetic surface roughness, such as the Gaussian distribution and the Pearson distribution.

3.2 Surface texture characterization

3.2.1 The nature of surfaces

The surface roughness plays an important role in a number of applications, for example, vehicular brake systems require a high roughness to increase the friction coefficient on the lining surface. In contrast, the aim of lubrication is to

alleviate the negative effect of rough surfaces on workpieces, or control and minimize them as much as possible. Infact, it is difficult and expensive to control the surface roughness in the manufacturing process and the effect of rough surface finishes is often managed through lubrication. This field has gained more attention from researchers including, but not limited to, the effects of rough surfaces on friction, lubrication and wear [3].

Generally speaking, all surfaces of solids are rough. The shape and the magnitude of the roughness depends upon the production process [71] and the material type. Figure 3-1 illustrates how an actual surface profile of a workpiece can be separated into three components as follows:

- An error of form or a slope of long wavelength that can occur in the manufacturing process, depending on the condition of the machine used.
- A profile of waviness in the transverse direction is similar to a roughness profile, but a magnitude of the waviness is higher than the rough profile. Waves on a surface profile can be caused by vibration of the fabrication machine.
- A roughness describing fluctuations of short wavelength on the surface. It is typically a random deviation from the centreline as magnitude and direction are varied.

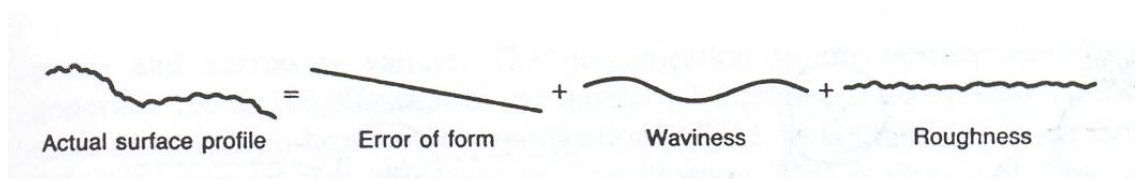


Figure 3-1: The actual surface profile of a solid component [47].

3.2.2 Surface texture parameters

Several parameters in statistical analysis are proposed to explain the characteristics of surface roughness. However, there are two commonly used forms to represent the amplitude of a rough surface:

1. Arithmetical average roughness (R_a) [72] is the average distance of the peaks and valleys of a material surface profile from the centreline average (CLA) as sketched in Figure 3-2. The R_a parameter is defined as:

$$R_a = \frac{1}{L} \int_{x=0}^{x=L} |y(x)| dx \quad (3.1)$$

or

$$R_a = \frac{1}{n} \sum_{i=1}^n |y_i| \quad (3.2)$$

where L is the sampling length and y is the distance of the surface from the mean line.

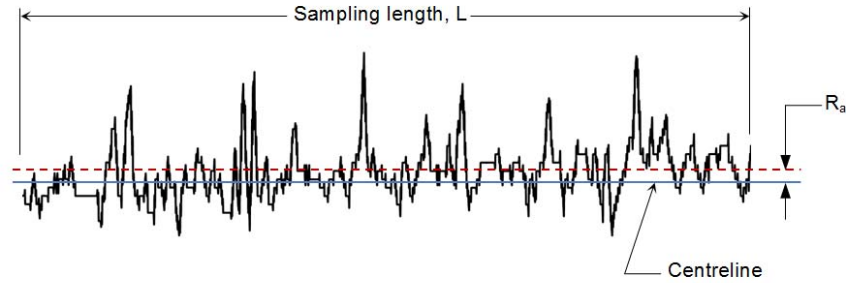


Figure 3-2: A schematic of the roughness parameter, R_a .

2. R_q is the root mean square (RMS) roughness. In general, the value of R_q is higher than R_a by around 11% for the same surface roughness [73]. The R_q value is expressed in terms of the sample standard deviation and it can be written as [72]:

$$R_q = \sqrt{\frac{1}{n} \sum_{i=1}^n y_i^2} \quad (3.3)$$

The values of R_a and R_q represent similar quantities in that they both describe the magnitude of the roughness but do not give any indication of the sharpness of the surface geometry.

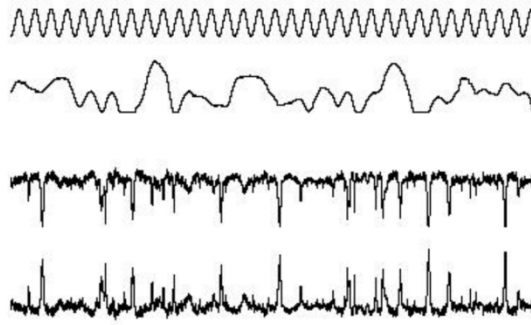


Figure 3-3: Different profiles of surface roughness with the same R_a value [74].

Figure 3-3 presents four different roughness profiles, sharing the value of R_a . It can be inferred that the R_a parameter alone is inadequate for representing the physicality of the surface roughness profile because it cannot describe the shape or the character of these surfaces. In order to represent a profile of a rough surface, the probability distribution of the asperities should be considered, as it gives a statistical representation of the roughness over the entire surface. Figure 3-4 shows the relationship between the Probability Density Function (PDF) of height on a rough surface and the cumulative PDF. The cumulative PDF of surface roughness has been widely used for describing the percentage of material within the surface roughness profile, and is also known as the ‘Abbott- Firestone curve’.

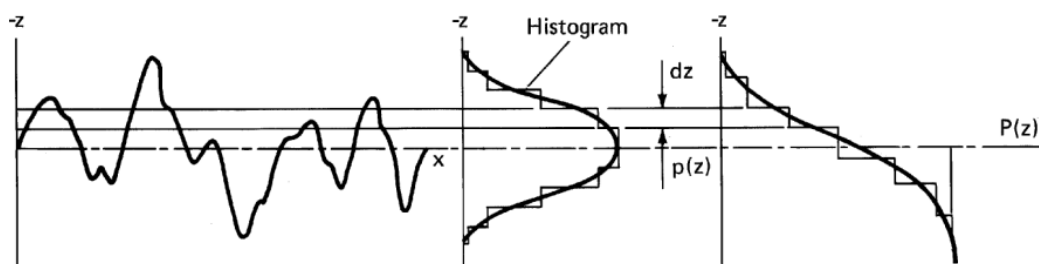


Figure 3-4: Relationship between the height profile and the cumulative PDF of surface roughness [75].

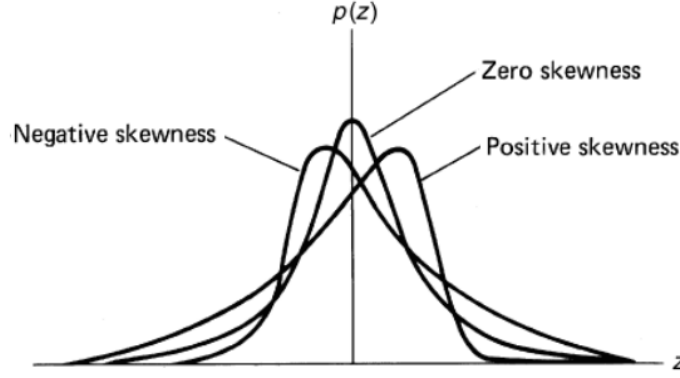


Figure 3-5: Schematic of variance skewness [75].

It can be seen that the asymmetry of the probability density function with respect to $z = 0$ can be explained by the skewness value (R_{sk}) as shown in Figure 3-5. The different surface textures displayed in Figure 3-3 affect the sign of the skewness value. If the skewness value is negative, the surface roughness profile will have lots of peaks. In contrast, if the skewness value is positive, many valleys will occur in the profile as shown in the third and fourth profiles of Figure 3-3, respectively. The R_{sk} value is expressed in the terms of the R_q value and the standard deviation as:

$$R_{sk} = \frac{1}{nR_q^3} \sum_{i=1}^n (y_i)^3 \quad (3.4)$$

In addition, the sharpness of each asperity peak can be described by the Kurtosis (R_{ku}) value:

$$R_{ku} = \frac{1}{nR_q^4} \sum_{i=1}^n (y_i)^4 \quad (3.5)$$

If R_{ku} is higher than 3.0, the distribution curve is less likely to produce a large roughness peak when compared to a normal distribution. In contrast, the distribution curve of a uniformly rough profile, with no large peaks has $R_{ku} < 3$, as depicted in Figure 3-6. It can be observed that for $R_{ku} > 3$, there is more diversity of peaks and valleys in a roughness profile than that of $R_{ku} < 3$. If $R_{sk} = 0$ and $R_{ku} = 3.0$, the PDF is a normal distribution, also known as the 'Gaussian distribution'. The nature of surfaces is random and surface height distributions

do not fall into an ideal Gaussian distribution [76]. However, it is nevertheless a good approximation and it is commonly used to characterize surface roughness or to generate a synthetic, computer generated, surface roughness [77].

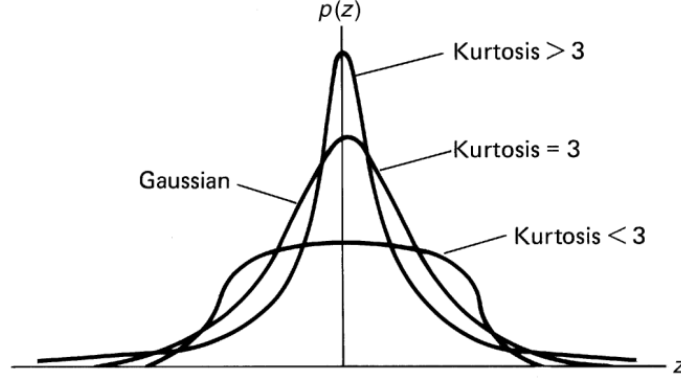


Figure 3-6: Representing distribution curve with variance kurtosis [75].

3.2.3 Abbott-Firestone curve

The evaluation of the surface texture can help better understand the property of surface roughness. The most popular method used is known as the 'Abbott-Firestone curve' or the 'Bearing Area Curve'. The Abbott-Firestone curve is an important tool for representing the percentage ratio of material within the surface roughness profile and was introduced by Abbott and Firestone in 1993 [78]. It is often used to evaluate the surface of workpieces in the automotive part industry.

Figure 3-7 presents the relationship between the cumulative probability density function of surface roughness height and the percentage material ratio within the evaluation length. By the DIN 4776 standard [79], the Abbott-Firestone curve is obtained by integrating the PDF obtained from the rough surface trace along the evaluation length [80]. With this standard, the Abbott-Firestone curve is divided into three zones. The first zone (R_{pk}), from 0% to M_{r1} , is where the slope dramatically changes, and represents the peaks in the roughness profile. Usually this zone of the surface texture will disappear in the running-in operation [81]. The second zone (R_k) is between M_{r1} to M_{r2} where the slope

is constant. This represents the average roughness of the surface, and is the 'core' of the roughness profile. The last zone (R_{vk}) is from M_{r2} to 100%, and represents the valleys of surface roughness. This zone is useful in lubrication as it serves to retain the lubricating film.

The properties of surfaces can be evaluated by observing these zones. For example, if the R_{pk} zone is wider than others, there may be many peaks in the surface roughness. This shape is similar to the case of a positive skewness. In contrast, if the R_{vk} zone is wider than other zones, there may be many valleys in the surface roughness [82].

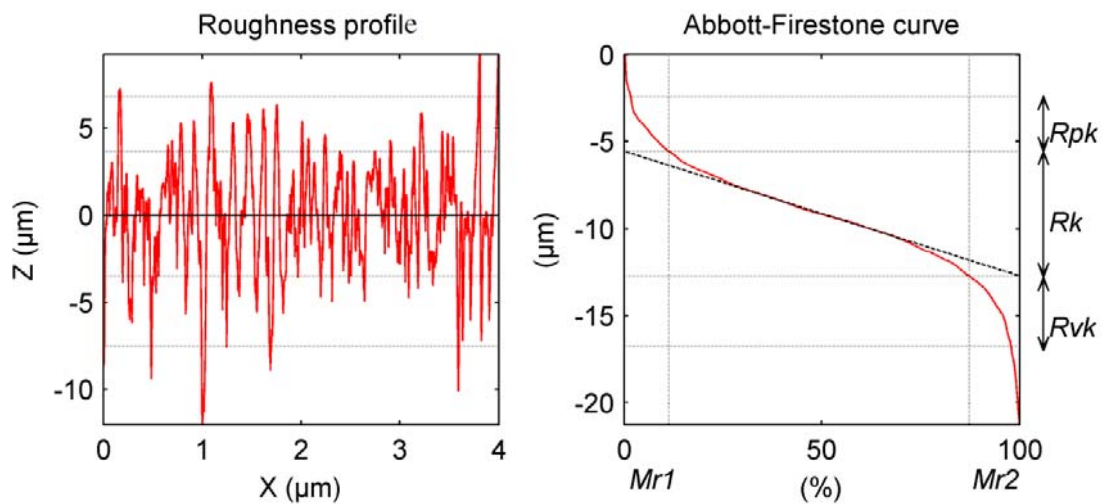


Figure 3-7: Abbott-Firestone curve [83].

Figure 3-8 demonstrates an example of the histogram and Abbott-Firestone curve of a surface roughness. The histogram represents the depth distribution of the roughness profile from 0 to 340 nm. Meanwhile the red line indicates the percentage material ratio, which is calculated from the accumulation of the histogram, for each depth level in the evaluation length. For example, the histogram shows that 14.5% of the points along the surface have a depth that lies between 34 and 51 nm. 92 % of the points along the surface have a depth that lies between 0 and 170 nm.

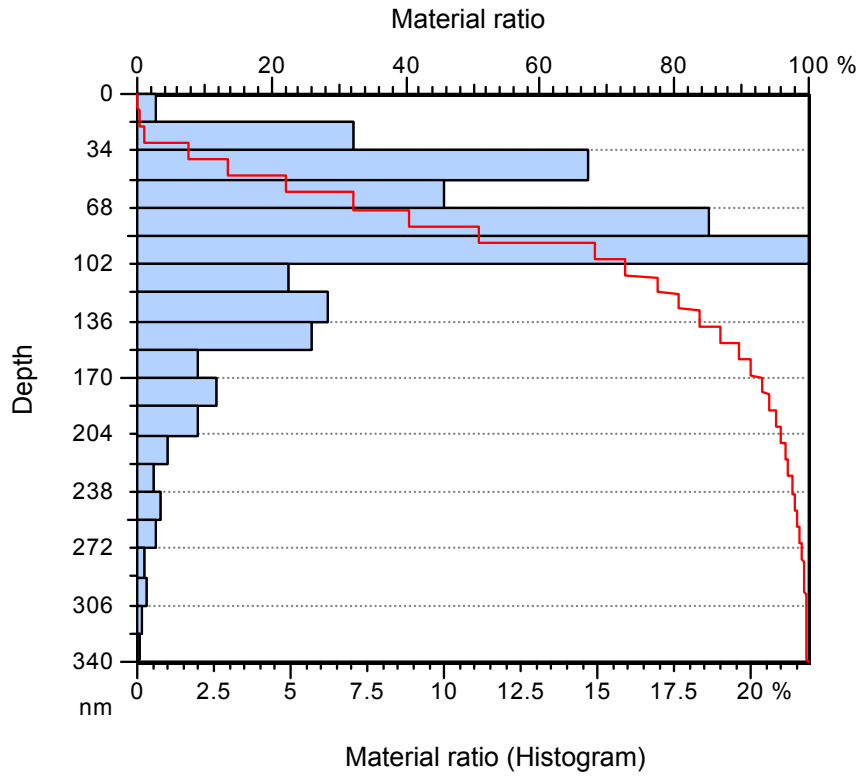


Figure 3-8: Representing the depth distribution histogram and the Abbott-Firestone curve.

3.3 Filters

Traditionally, there have been many ways to separate a waviness profile from the primary profile such as fitting, filtering, and skidded measurement. The filtering technique is most often used to separate the components of a surface profile, which numerically is based on a weighting function. This technique is also preferred in the electronic engineering field to separate noise from the signal. Currently, there are a number of weighting functions that can be used to filter out the waviness profile such as 2RC filter [84], Gaussian filter [85], Spline filter [86, 87], and Robust spline filter [88].

The 2RC filter is a high pass filter where the mean of the primary roughness profile is calculated by convolving the primary roughness profile with the weighting function of the 2RC as given by [84]:

$$g(x) = \frac{C}{\lambda_c} \left(2 - C \frac{|x|}{\lambda_c} \right) \exp \left(-C \frac{|x|}{\lambda_c} \right) \quad (3.6)$$

where $C=3.64$ (75 % of transmission) and λ_c is the cut-off wavelength of the filter. The filtered roughness profile is obtained by subtracting the primary roughness profile from the calculated mean. Generally speaking, the transmission ratio of the 2RC filter at the cut-off is defined as 75%. The 2RC filter is included in the ASME B46.1 standard [89]. However, the 2RC filter is not as widely used as the Gaussian filter because of distortion in the obtained roughness profile, especially in the case of a high cut-off value [90].

The Gaussian filter [85] has been widely used to separate short and long waves from the primary surface. This filtering method is also accepted by the ASME B46.1 [89] and the ISO 11562 standard [91]. The transmission ratio of the Gaussian filter at the cut-off is defined as 50%. The weighting function of the Gaussian filter for a roughness profile in one dimension can be written as [85]:

$$g(x) = \frac{1}{\alpha \lambda_c} \exp \left[-\pi \left(\frac{x}{\alpha \lambda_c} \right)^2 \right] \quad (3.7)$$

where λ_c is cut-off wavelength of the filter and $\alpha=0.4697$. In order to exclude a long wavelength waviness profile, $w(x)$, from a primary surface roughness profile, $s(x)$, by the Gaussian filter, the weighting function in equation (3.7) and the primary surface roughness profile are convolved:

$$w(x) = s(x) * g(x) \quad (3.8)$$

The filtered roughness profile, $r(x)$, can be obtained by subtracting the primary surface from the waviness profile as follows:

$$r(x) = s(x) - w(x) \quad (3.9)$$

Figure 3-9 shows the application of the Gaussian filter on the primary surface with three different cut-off values. It is evident that the cut-off value plays an important role in the evaluation of roughness and waviness profiles. The recommended cut-off values by Taylor [92] are 0.25 mm, 0.80 mm, and 2.5 mm.

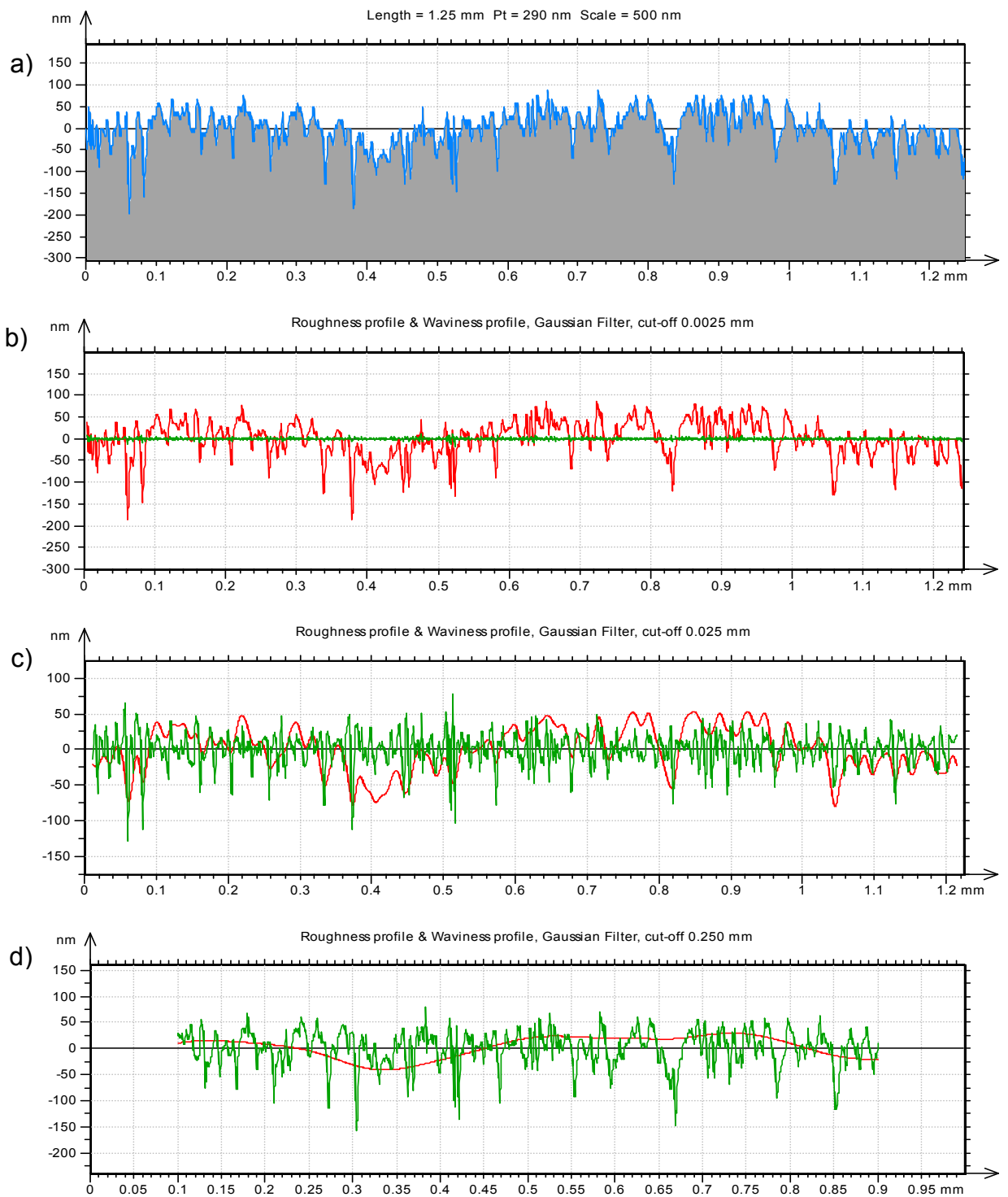


Figure 3-9: The influence of the cut-off values on waviness and roughness profiles using the Gaussian filter. Measured primary surface roughness (blue line), long wavelength waviness profile (red line), filtered roughness profile (green line)

If the selected cut-off value is shorter than the wavelength of the roughness, the amplitudes of the roughness profile will be significantly changed as shown in Figure 3-9b. Thus the appropriate cut-off value must be between the wavelengths of roughness and waviness, because shorter wavelengths will be filtered out by the high pass filter.

Figure 3-9d depicts the obtained roughness and waviness profiles when the cut-off value is 0.25 mm. It can be clearly seen that the roughness profile is adequately filtered out from the waviness profile. Thus, the cut-off value at 0.25 mm is appropriate for separating the waviness from the original roughness profile in this study. Not only the cut-off value is significant to the filter profile, but the evaluation length also significantly affects the waviness and roughness profiles. In fact, the evaluation length should be at least 5 times that of the selected cut-off value.

Using the Gaussian filter gives an error of the separated waviness at the edge of the roughness profile. This can be ignored by excluding the edge of the obtained result. The roughness and waviness profiles span the length from 0.1 mm to 0.9 mm. It can be observed that the length of the errors at both edges is directly proportional to the chosen cut-off wavelength value. Krystek [85] suggested to use a fast convolution algorithm to calculate a waviness profile of a surface profile by using the Gaussian filter. Krystek reduced the edge error problem by starting the calculation after the n_c point as shown below:

$$n_c = \sqrt{\frac{\log\left(\frac{c_o}{dx \cdot c_1}\right)}{\pi}} \cdot c_o^{-1} + 1 \quad (3.10)$$

where $c_o = dx/(\lambda_c \cdot \alpha)$, $\alpha=0.4697186$, $c_1 = 0.001$ and λ_c is the cut-off value. The waviness profile is chosen to start after the n_c point and finish at the $N - n_c$ point, where N is the total number of data points on the primary roughness profile.

3.4 Measurement of Surface Roughness

It is essential to consistently measure the surface roughness of work pieces as broad definitions of 'smooth surface' or 'rough surface' are inadequate. The ideal method by which to characterise surface roughness is through direct measurement with an appropriate tool. In this context surface roughness is usually quantified by the vertical deviations of a surface from its mean profile.

Historically, the stylus instrument was the most widely accepted method to measure surface roughness as it gave more accurate results compared to other methods. Presently, many surface measuring instruments are used in manufacturing. For example, stylus instruments are widely used in the automotive industry, while optical instruments are often used in manufacturing where a non-contact method is required. Optical instruments do not make contact with surfaces and thus do not leave any trace or damage. Surface measuring instruments currently used in manufacturing can be sorted into two groups as follows:

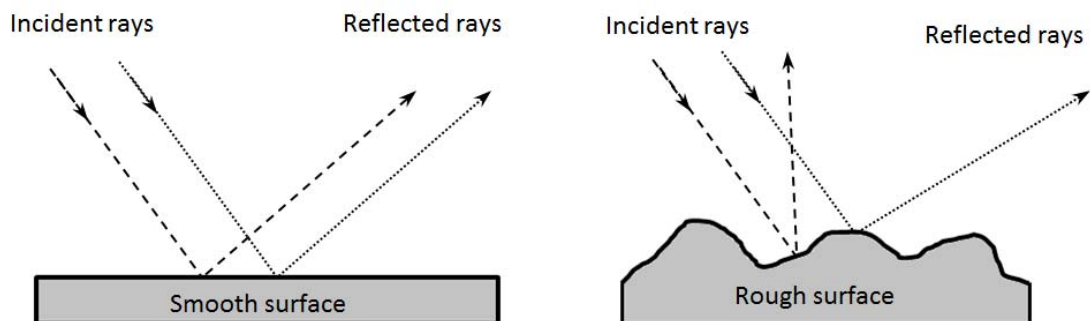


Figure 3-10: Representative scheme for reflecting of light with smooth and rough surfaces [93].

A. Non-Contact approach

Optical profilometry measures surface roughness by using the laws of reflection as shown in Figure 3-10. Instruments that use this technique make use of focus detection, interferometry, and projected light. The optical interference method is suitable for measuring roughness of soft materials which are easily damaged. It is widely used in manufacturing of lenses and hard disk equipment. Figure 3-11

shows the schematic of the optical surface profile. The main idea of the optical interference instrument is to identify the wavelengths of the light beams that are reflected from the test material and the reference mirror. Both wavelengths of the light beam will be used to calculate the height differences over a surface profile [94]. The performance of the optical interference instrument is continually improving and is currently able to measure surfaces with roughness amplitude from 50 nm to 1.5 μm [94].

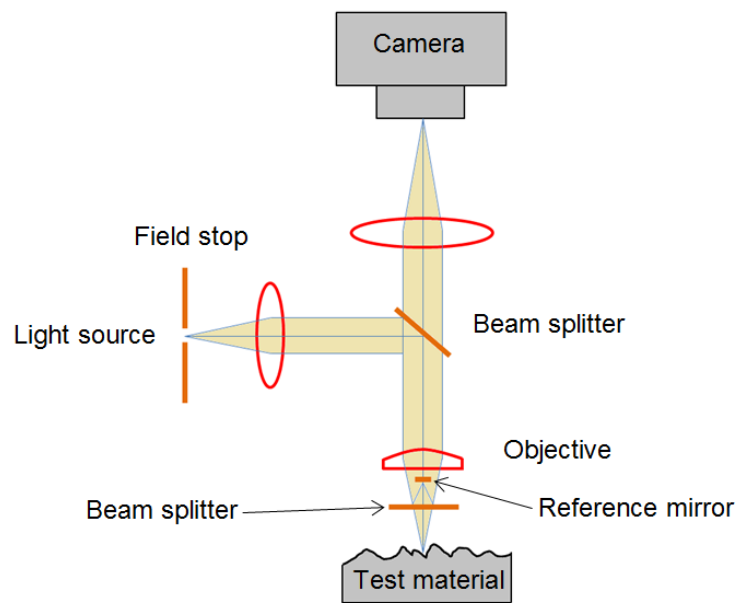


Figure 3-11: Schematic of the optical surface profile [94].

B. Contact approach

Surface profilometry, also known as the 'Stylus method', is operated by moving a stylus along a surface. The stylus moves up and down following the peaks or valleys in the surface, and records this in terms of Cartesian coordinates as shown in Figure 3-13. At the same time, a waviness profile can be measured and filtered from the primary surface roughness profile by the motion of the skid. In general, the radius of the skid is larger than the spacing between roughness elements. However, these coordinates are not an exact replica of the measured surface texture, as they represent the movement of the centre of the stylus. Figure 3-14 shows the effect of using different sizes of stylus, resulting in different profiles of the measured surface. The instrument will produce a distortion of the real profile if the stylus is bigger than the minimum curvature of

the peaks or valleys [95]. Figure 3-15 shows the relationship between the ratio of stylus tip radius to actual R_a of surface roughness and the percent of the reduction of R_a . It can be noticed that the error on the R_a increases, when the ratio the ratio of stylus tip radius to actual R_a of surface roughness is increased. However, with the improvement of manufacturing techniques, the head of the stylus can now be produced to a size of $0.001\text{ }\mu\text{m}$ [96]. As a result, they can capture surface roughness profiles in extremely fine detail and are thus widely accepted in industry.

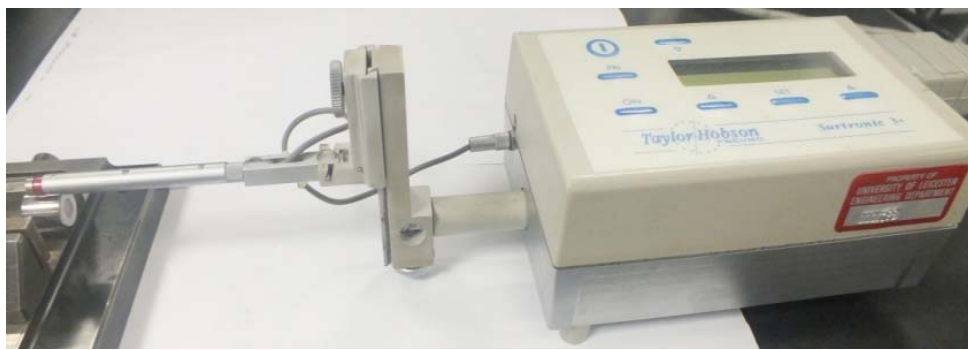


Figure 3-12: Surtronic 3+ [92].

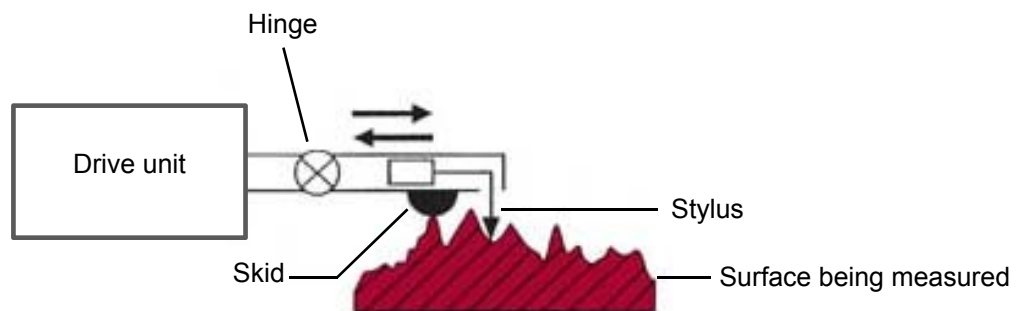


Figure 3-13: Schematic of the working principle of a stylus profilometer [97]

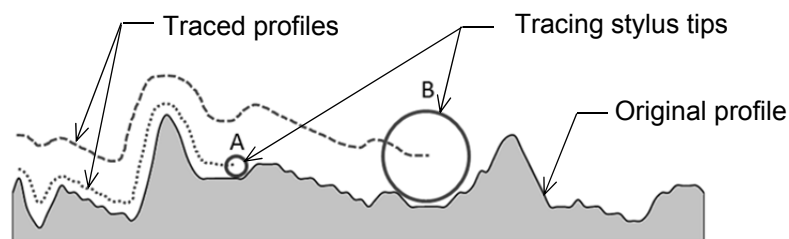


Figure 3-14: Comparison of the surface measurements between stylus A and B.

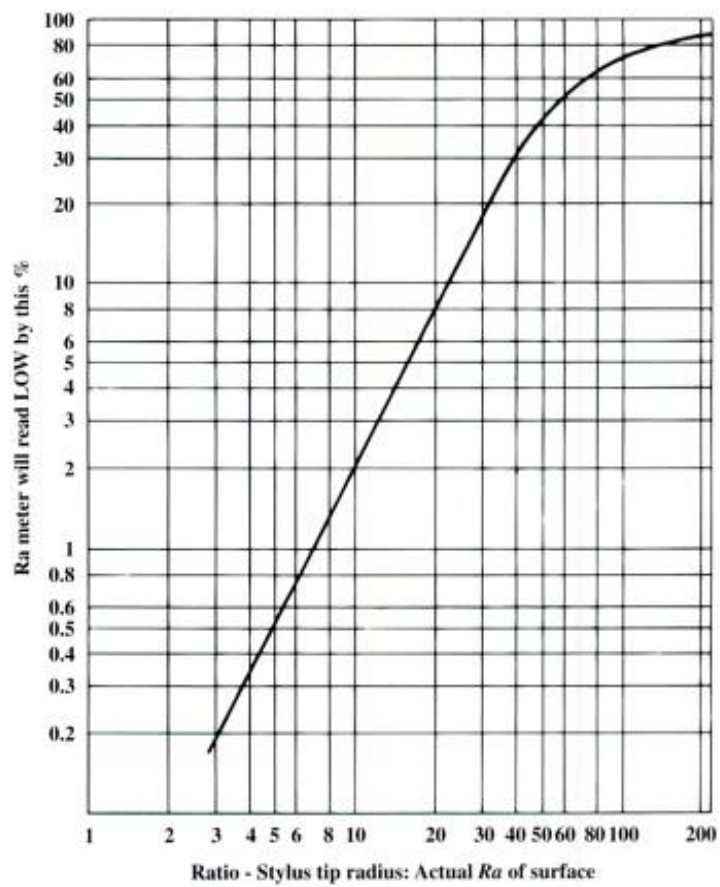


Figure 3-15: Error due to stylus tip radius [98]



Figure 3-16: The sample of a cylindrical roller bearing for measuring the surface texture.

To understand the characteristics of real surface roughness on bearings, a new 'as-manufactured' sample of a cylindrical roller bearing (NJ 306E), illustrated in Figure 3-16, was employed to measure the surface of the roller cylinder and the surface of the bearing case by using the Surtronic 3+ stylus profilometer [92] as shown in Figure 3-12. The radius of the stylus tip in SUR 3+ is 5 μm . The bearing dimensions are $d30 \times D72 \times B19$ mm, where d is the inside diameter of the bearing, D is the outside diameter of the bearing, and B is the thickness of the bearing. The rollers and bearing case are made of chrome steel (GCr15), surface-finished by grinding and buffing after heat-treatment [99].

3.4.1 Surface roughness of the bearing case in the azimuthal direction

The objective of this measurement is to study the real surface roughness of the bearing case. The measured surface roughness of this component will be used to study the effect of surface roughness on the EHL problem by applying it to the surface of the bottom plate in the CFD model.

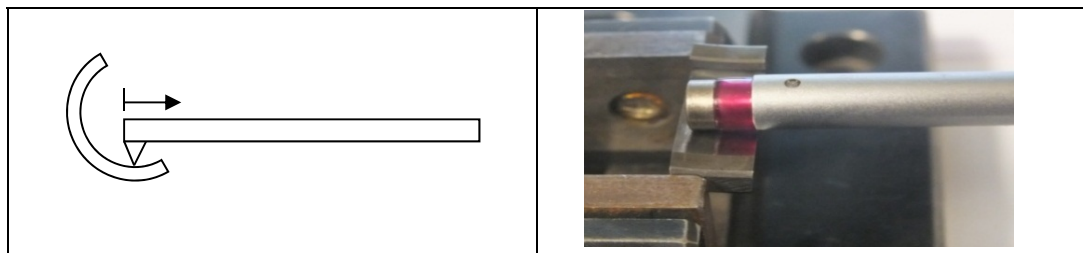


Figure 3-17: The stylus is moved tangentially over the surface of the bearing case.

Figure 3-17 shows the stylus moving on the surface of the bearing case. Figure 3-18a shows the surface roughness profile obtained. In this project, only the roughness profile is of interest, thus it is necessary to separate the waviness from the primary surface roughness profile. Figure 3-18a reports by the blue line the measured primary surface roughness profile which is comprised of two components that can be separated by the Gaussian filter. The first part of the primary surface roughness is the roughness profile presented by the green fluctuating line in Figure 3-18b, while the red line in Figure 3-18b shows the waviness profile.

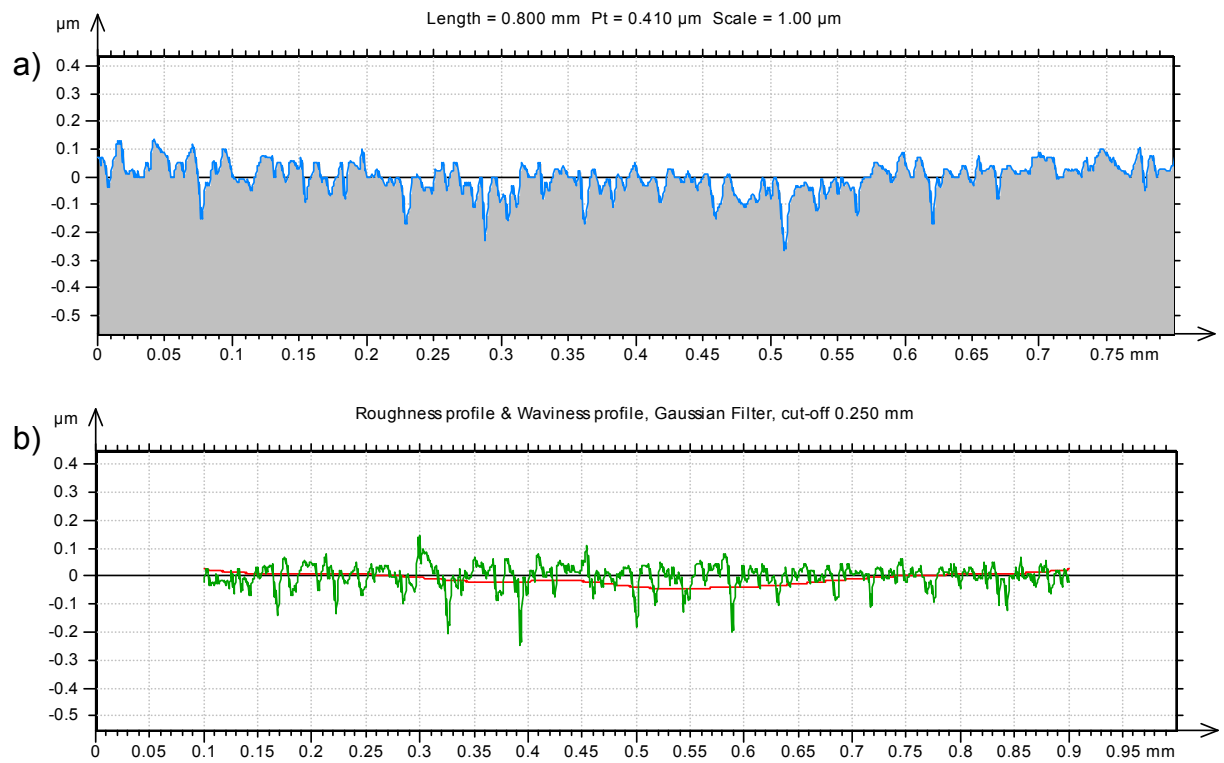


Figure 3-18: The surface texture of the bearing case in the azimuthal direction.

3.4.2 Surface roughness of the bearing case in the axial direction

The surface roughness of the bearing case is also measured in the axial direction as shown in Figure 3-19.

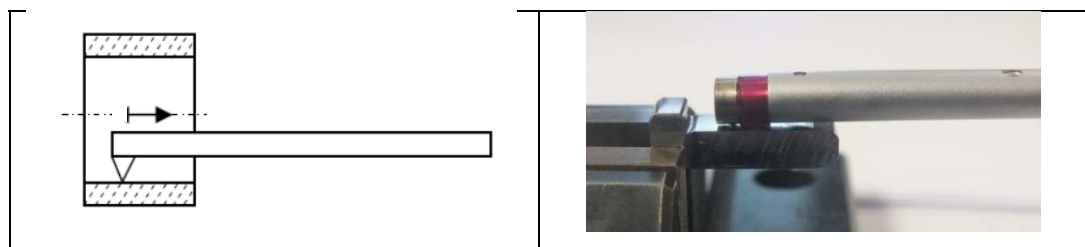


Figure 3-19: The stylus is moved axially along the surface of the bearing case.

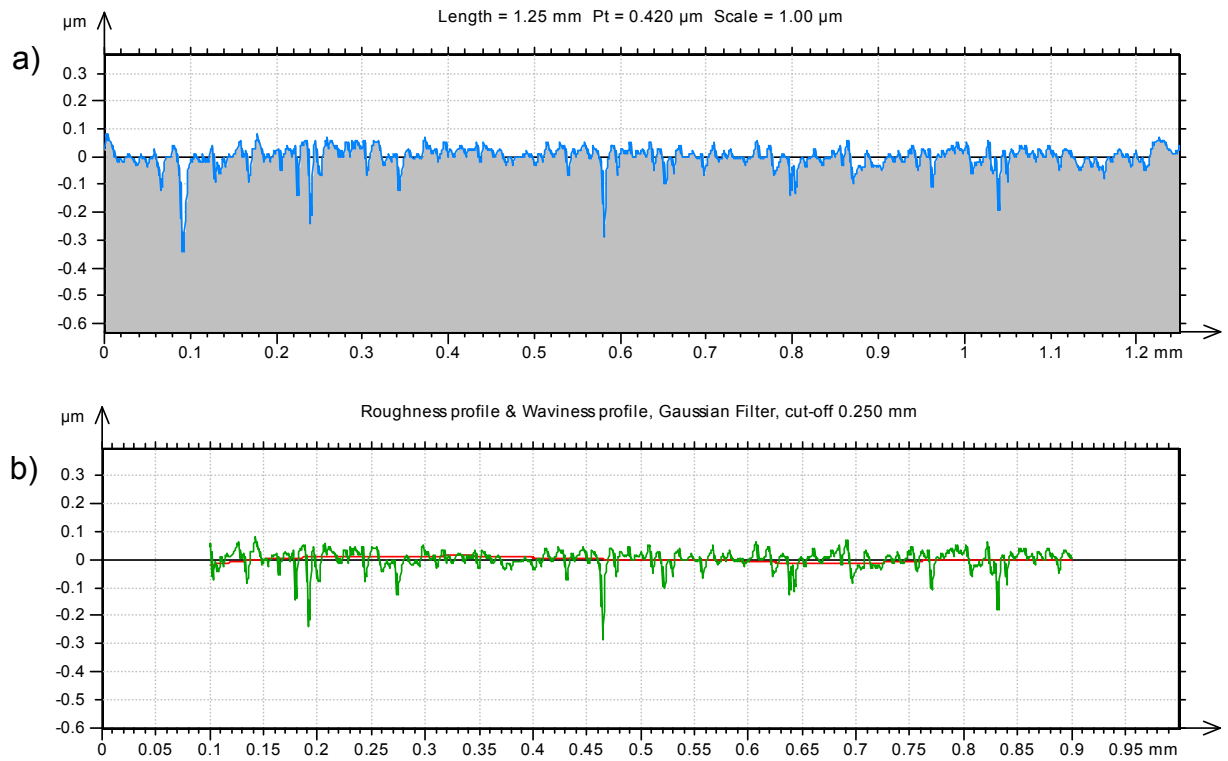


Figure 3-20: The surface texture of the bearing case in the axial direction.

The EHL in this project is considered to be a line contact problem. The azimuthal surface roughness is only applied to the CFD model for studying the effect of surface roughness. However, the surface roughness in the axial direction should be studied as it will give more detail about the characteristics of the surface roughness of the bearing case. In addition, it will be useful to further develop the CFD scheme to model an EHL point contact. Figure 3-19 shows the stylus measuring the surface roughness of the bearing case in the axial direction. The primary surface roughness profile obtained by this measurement, and the filtered roughness profile (green line) and the waviness profile (red line), are presented in Figure 3-20a and Figure 3-20b respectively.

3.4.3 Surface roughness of the roller in the azimuthal direction

This section studies the surface roughness of the roller in the azimuthal direction. This will be applied to the surface of the top cylinder of the CFD model. Figure 3-21 shows the stylus moving on the bearing roller in the tangential direction. As before, Figure 3-22a shows the measured primary surface roughness profile and Figure 3-22b shows the profiles of azimuthal

roughness (green line) and waviness (red line), respectively. The azimuthal roughness profile coincided with the tangential roughness profile by the subtraction of the waviness from the measured primary surface roughness profile.

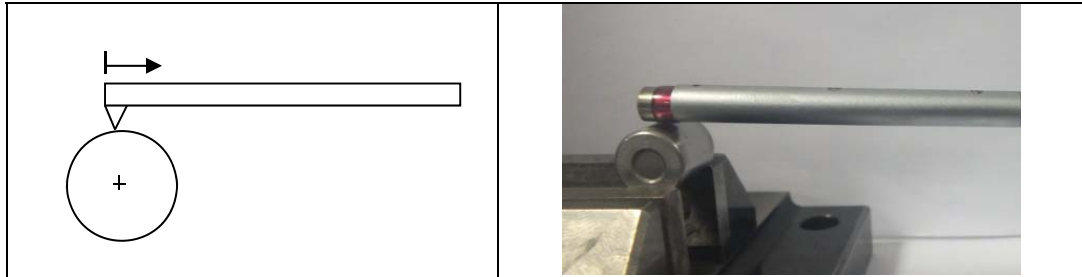


Figure 3-21: The stylus is moved across the surface of the cylindrical roller.

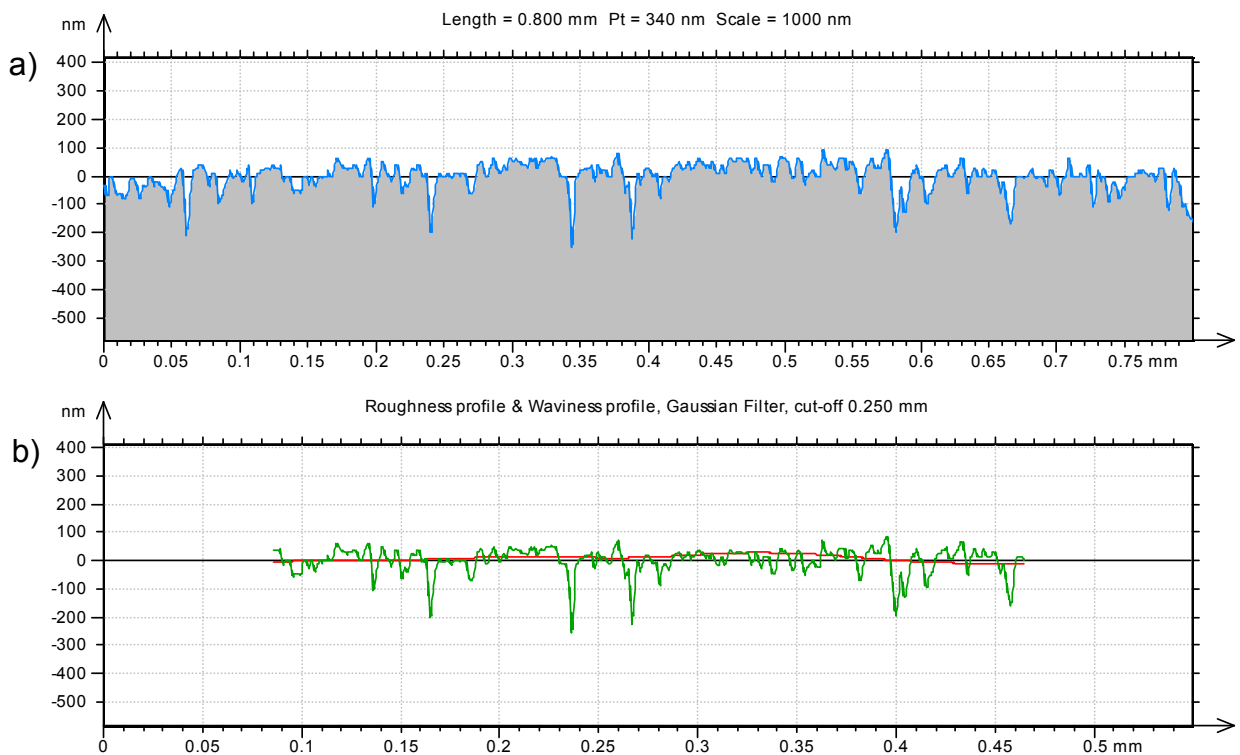


Figure 3-22: The surface texture of the cylindrical roller in the tangential direction.

3.4.4 Surface roughness of the roller in the axial direction

This section also studies the surface roughness of the roller measured in the axial direction, as shown in Figure 3-23. The original surface roughness profile

obtained (blue line) is presented in Figure 3-24a. The roughness profile (green line) and waviness profile (red line), are presented in Figure 3-24b.

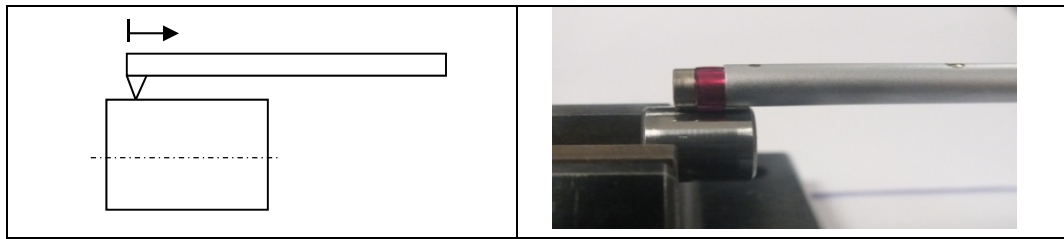


Figure 3-23: The stylus is moved axially on the surface of the cylindrical roller.

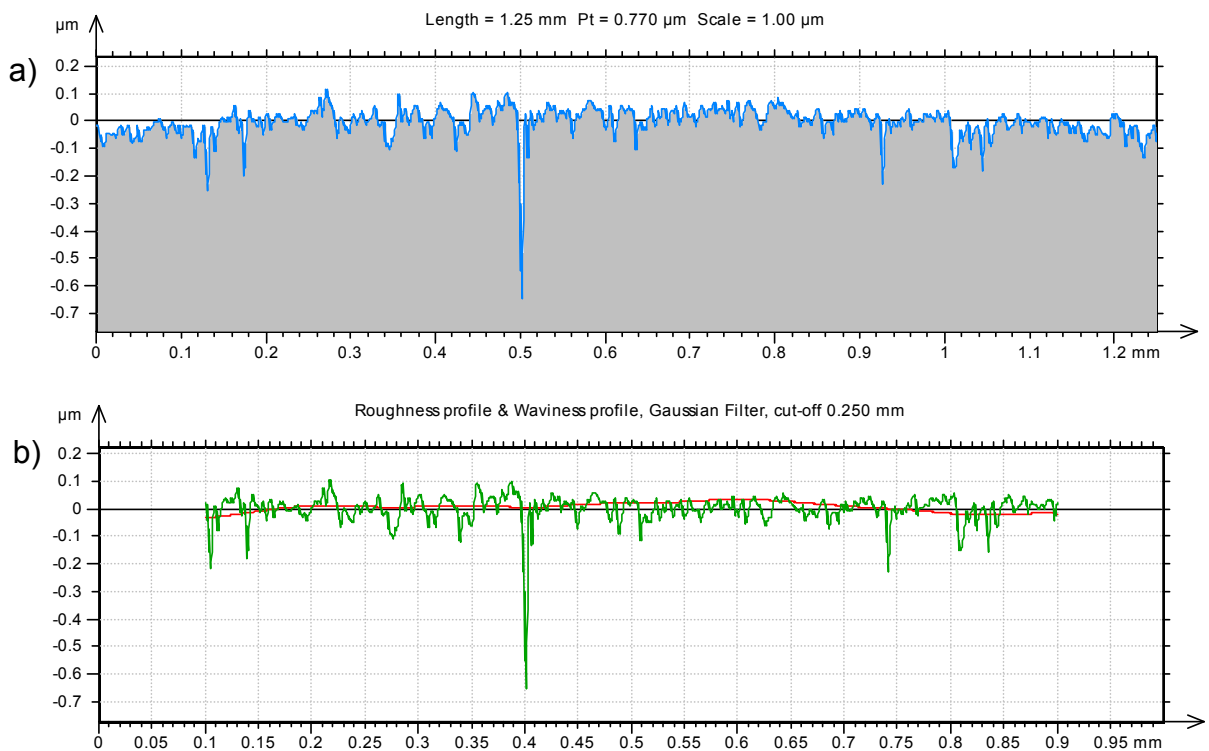


Figure 3-24: The surface texture of the cylindrical roller in the axial direction.

The surface roughness profiles of sections 3.4.1 and 3.4.3 are measured over a short horizontal length of 0.8 mm, due to the limitations of the stylus profilometer used. A low vertical range was chosen as the average roughness of bearings is very small - if the instrument is set up to use a high vertical range, it cannot capture the finer details of small scale roughness. However, the limited vertical range of the profilometer does not affect the measurement in cases 2 and 4, as the design shape of these components in the axial direction is a

straight line horizontal. Therefore, the trace of the profilometer was constrained by the vertical displacement of the stylus due to the shape curvature of the bearing case and of the roller in the azimuthal direction.

Table 3-1 presents the surface roughness parameters calculated from the measurements in sections 3.4.1 to 3.4.4. It can be noticed that the average surface roughness of the cylindrical roller bearing (R_a) is very small, ranging from 0.01 μm to 0.03 μm . The surface profiles of all cases have kurtosis values higher than 3 and negative skewness values, because there are many deep valleys on the surface roughness profile. From these measurements, it can be inferred that the depth density distribution of the real surface roughness on used bearings is a non-Gaussian distribution.

Table 3-1: Calculated surface roughness parameters

Measured case	R_a (μm)	R_q (μm)	R_{sk}	R_{ku}
3.4.1 Bearing case (azimuthal direction)	0.0320	0.0455	-1.46	6.30
3.4.2 Bearing case (axial direction)	0.0198	0.0333	-2.94	19.1
3.4.3 Roller (azimuthal direction)	0.0175	0.0280	-2.52	17.3
3.4.4 Roller (axial direction)	0.0287	0.0493	-7.26	78.6

According to the Abbott-Firestone curve of the roller and the bearing casing as shown in Figure 3-25, it was found that the highest peak of the roller surface is lower than that of the bearing case. The peak zone of the surface roughness of the roller is narrower than that of the bearing case as presented in Figure 3-25 c and d. Furthermore, the middle zone of the Abbott-Firestone curve of the roller is wider than that of the bearing case. It can be evaluated that the material ratio of the roller at the depth level 0.15 μm is almost 85%, while the material ratio of the bearing case is only 70% at the same level.

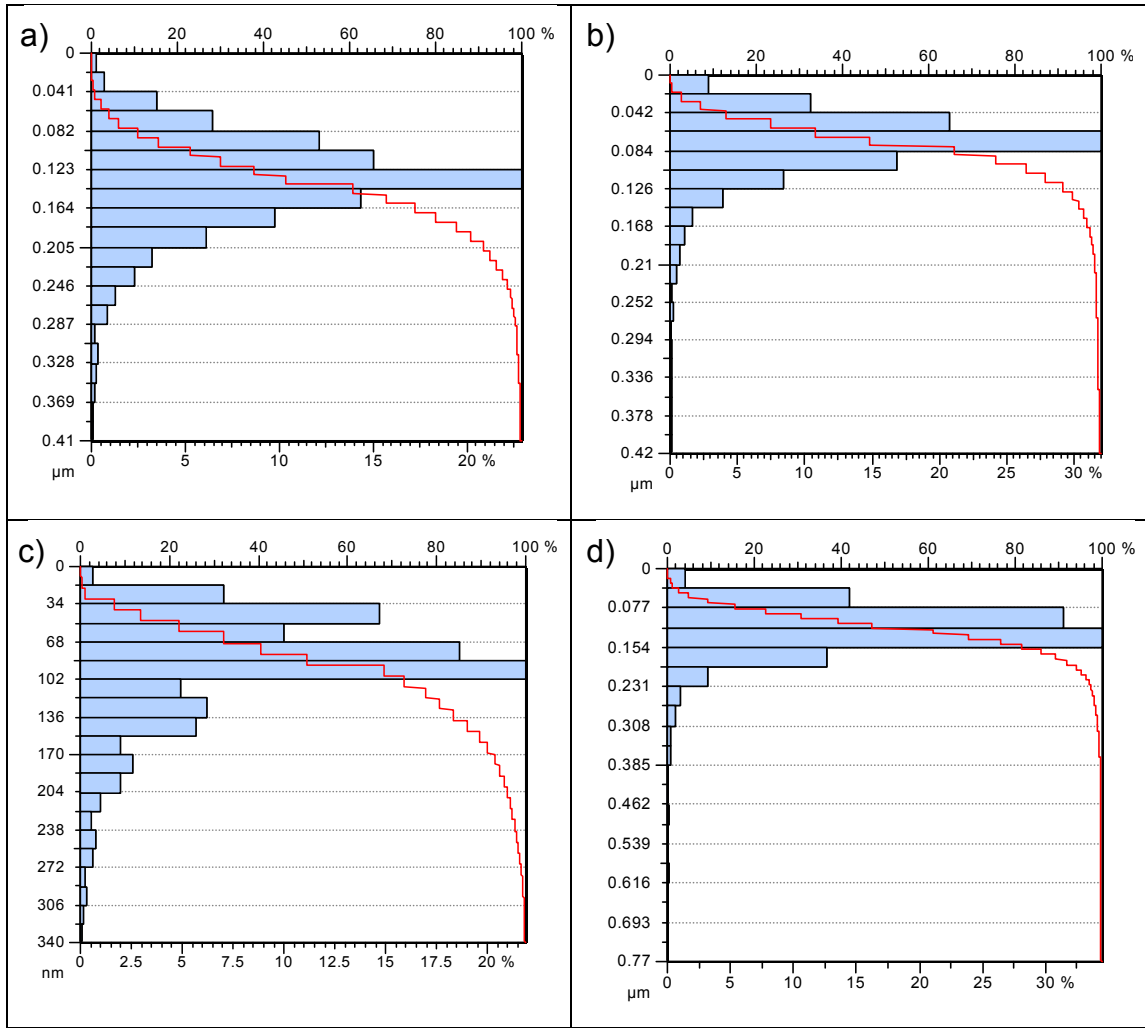


Figure 3-25: The depth distribution histogram and Abbott-Firestone curve measured in sections 3.4.1(a), 3.4.2 (b), 3.4.3(c) and 3.4.4 (d), respectively.

3.5 Generation of surface roughness

Previous investigations of real surface roughness found that the roughness profile does not have a normal distribution [100]. The roughness parameters of the studied cases are also different, even when the instrument used to measure the surface roughness is identical. In order to study the effects of surface roughness shapes, it is thus necessary to generate the surface roughness with the influence of parameters such as the average roughness (R_a), root mean square roughness (R_q), skewness (R_{sk}) and kurtosis (R_{ku}).

Many mathematical models for sample distribution generators have been proposed to model a general surface roughness, such as the Gaussian or normal distribution [100, 101], the binomial distribution [102], the Poisson distribution [103], the exponential distribution [104], and the Pearson distribution [77], etc. The Pearson distribution can be used to predict the surface roughness using skewness and kurtosis parameter, and thus is the most appropriate distribution among the above listed ones to model the surface roughness profiles in this study.

A computer number generator implement in Matlab, also known as the ‘pseudo-random number generator’, is used to create random numbers which are uniformly distributed in the interval [0, 1]. For example, a linear congruential method is a simple algorithm, and widely used to generate random numbers. It can be defined as follows [105]:

$$x_{n+1} = (ax_i + c) \bmod m \quad (3.11)$$

where x is the sequence of pseudorandom values, a is the multiplier (constant value), c is the increment, and m is the modulus. The obtained random numbers depend on the input seed value and the applied algorithm. Presently, the computer generator utilizes more complex seeds and fewer predictable sequences, whereby date and time are used as the seed.

In order to generate a surface roughness with the influence of the chosen distribution, it is necessary to modify the result of the computer generator by a transformation of probabilities [106]. There are many transform methods available such as the inverse transform method, the acceptant and rejection method, the convolution method, and the composition method [105, 107-109].

The Pearson model, which can be used to represent many continuous probability distributions characterized by four quantities (R_a , R_q , R_{sk} and R_{sku}), was proposed in 1895 [106]. It was developed from a generalisation of a differential equation with respect to x as given below:

$$\frac{dy}{dx} = \frac{y(m-x)}{a+bx+cx^2} \quad (3.12)$$

Thus, the solution of equation (3.12) is:

$$y = C(a+bx+cx^2)^{-1/(2c)} \exp \left[\frac{(b+2cm) \tan^{-1} \left(\frac{b+2cx}{\sqrt{4ac-b^2}} \right)}{c\sqrt{4ac-b^2}} \right] \quad (3.13)$$

The possible distribution of the Pearson model depends on the value of the parameters: a , b and c in equation (3.13) which can be sorted into 8 types [106, 110] :

1. Pearson type 0 (Normal) distribution when $b=c=0$ and $a>0$.
2. Pearson type I (Beta) distribution when the $b^2/4ac < 0$ and $0 \leq x \leq 1$.
3. Pearson type II (Symmetric Beta) distribution when $b^2/4ac=0$ and $c < 0, c_1 \leq x \leq \infty$ where $c_1 \equiv \sqrt{-c/a}$.
4. Pearson type III (Gamma) distribution when $b^2/4ac = \infty$ and $c=0$, $c_1 \leq x \leq \infty$ where $c_1 \equiv -a/b$.
5. Pearson type IV distribution when $0 < b^2/4ac < 1$ and $-\infty < x < \infty$.
6. Pearson type V (Inverse Gamma) distribution when $b^2/4ac = 1$ and $c_1 \leq x \leq \infty$, where $c_1 \equiv -b/2a$.
7. Pearson type VI (F distribution) distribution when $b^2/4ac > 1$ and $c_1 \leq x \leq \infty$, where c_1 is the larger root.
8. Pearson type VII (Student's T) distribution when $b^2/4ac = 0$ and $-\infty < x < \infty$, where $c > 0$.

The Pearson model has been used for generating the topography of a rough surface where the distribution is non-Gaussian [111-113]. Therefore, this model will be used to generate the depth distribution of a rough surface with the influence of R_a , R_q , R_{sk} and R_{ku} in this study. The constant values in equation (3.13) are calculated from the roughness parameters as given by:

$$\begin{aligned} a &= (4\beta_2 - 3\beta_1)/(10\beta_2 - 12\beta_1 - 18) \\ b &= (R_{sk} \times (\beta_2 + 3))/(10\beta_2 - 12\beta_1 - 18) \\ c &= (2\beta_2 - 3\beta_1 - 6)/(10\beta_2 - 12\beta_1 - 18) \end{aligned} \quad (3.14)$$

where

$$\begin{aligned}\beta_1 &= R_{sk}^2 \\ \beta_2 &= R_{ku}\end{aligned}\tag{3.15}$$

The parameters R_a and R_q will be used to normalize the input data X . This relation can be expressed as below:

$$x = \frac{(X - \mu)}{\sigma}\tag{3.16}$$

where μ and σ are equal to R_a and R_q , respectively.

In order to control the extremities of the generated surface roughness, it is necessary to limit the maximum and the minimum values of the profile within realistic bounds. Thus, the random number is bounded between the minimum valley depth (R_v) and the maximum peak height (R_p) by imposing $R_v < \text{radius of roller}$ and $R_p < \text{the minimum film thickness}$.

3.6 Roughness and the EHL problem

The influence of surface roughness on the EHL line contact problem can be simulated by including the surface roughness profile in the film thickness equation, thus equation (2.17) becomes the following [114-116]:

$$h = h_o + \frac{x^2}{2R'} + R_1(x, t) + R_2(x, t) - \frac{2}{\pi E'} \int_{-\infty}^{\infty} p(\xi) \ln(x - \xi)^2 d\xi\tag{3.17}$$

where $R_1(x_i, t)$ and $R_2(x_i, t)$ denote the roughness profiles of the surfaces 1 (top cylinder) and 2 (bottom plate) respectively. Since the top cylinder and the bottom plate are moving, the surfaces 1 and 2 are moved with the same velocity of the respective surface where u_1 is the velocity of the top cylinder and u_2 is the velocity of the moving bottom plate in x direction. Thus, the displacements of both surfaces are time dependent and can be computed as follows [117]:

$$\begin{aligned}R_1(x, t) &= s_1(x + u_1 t) \\ R_2(x, t) &= s_2(x + u_2 t)\end{aligned}\tag{3.18}$$

Chapter 4

The Computation Fluid Dynamics platform

4.1 Introduction

Numerical methods have become important tools for researchers and engineers. In particular, the CFD approach, which is mainly based on the finite volume method, has been widely used for predicting the behaviour of fluid flows. In this research, the CFD approach will be used to solve and analyse the EHL line contact problem.

The first part of this chapter deals with the Navier-Stokes equations. The mathematical models based on conservation laws for the governing equations of computational fluid dynamics, such as the mass equation, the momentum equation and the energy equation, are presented. Then, the finite volume method and the discretized equations are briefly described. Following that, the appropriate boundary conditions defined in the CFD model for the EHL problem are explained. Then, the mixture model applied to the CFD model is illustrated and the full cavitation model used in this study is discussed in this chapter. Finally, the numerical schemes employed to solve the discretized governing equations, for example the SIMPLE and PISO schemes, are described.

4.2 The governing equations

In general, the characteristics of a fluid flow can be described by applying the conservation form of the flow governing equations. The modelling of fluid flow was developed by Claude-Louis Navier (1785-1836) and George Gabriel Stokes (1819-1903) by applying Newton's second law to fluid motion. The conservation of momentum has been widely used and is known as the 'Navier-

Stokes equation' [118, 119]. Although it is based on the momentum equation, both continuity and momentum equations are generally referred to as 'Navier-Stokes equations' [120].

4.2.1 The continuity equation

The continuity equation, also known as the conservation of mass, is used to analyse mass flow in a control volume. The continuity equation is composed of two terms: the first represents the accumulation of mass in the control volume, while the second describes the mass balance between the mass flows in and out of the control volume.

Let the velocity vector be $\mathbf{u} = u_1\mathbf{e}_1 + u_2\mathbf{e}_2 + u_3\mathbf{e}_3$

and gradient operator be $\nabla = \frac{\partial}{\partial x_1}\mathbf{e}_1 + \frac{\partial}{\partial x_2}\mathbf{e}_2 + \frac{\partial}{\partial x_3}\mathbf{e}_3$, defined in a fixed orthogonal Cartesian reference system (x_1, x_2, x_3) with coordinate unit vectors $\mathbf{e}_1, \mathbf{e}_2, \mathbf{e}_3$.

The continuity equation for compressible flows can be expressed as:

$$\frac{\partial \rho}{\partial t} + \nabla \cdot (\rho \mathbf{u}) = 0 \quad (4.1)$$

Since the density of fluid is time invariant t in incompressible flows, the continuity equation for incompressible flows becomes:

$$\nabla \cdot (\rho \mathbf{u}) = 0 \quad (4.2)$$

The density of the lubricant in the EHL problem is a function of pressure and temperature, as presented in equation (2.39). Therefore, the continuity equation, as presented in equation (4.1), is chosen to describe the mass flow in the CFD model for the EHL problem.

In this research, the mixture model is employed to model the liquid and vapour phases in the EHL flow. The liquid phase is assumed to be a continuous flow and a secondary phase is applied as a dispersion that comprises bubbles.

Therefore, continuity equation (4.1) needs to be rewritten for the mixture of the continuous and dispersed phases as [121]:

$$\frac{\partial}{\partial t} \sum_{i=1}^n (\alpha_i \rho_i) + \nabla \cdot \sum_{i=1}^n (\alpha_i \rho_i \mathbf{u}_i) = 0 \quad (4.3)$$

where α_i is the volume fraction of phase i and n is the number of phases. The velocity and density of the mixture are defined as:

$$\rho_m = \sum_{i=1}^n (\alpha_i \rho_i) \quad (4.4)$$

$$\mathbf{u}_m = \frac{1}{\rho_m} \sum_{i=1}^n (\alpha_i \rho_i \mathbf{u}_i) \quad (4.5)$$

where \mathbf{u}_m is the mass-averaged velocity.

4.2.2 The momentum equation

Neglecting gravitational effects, the momentum equation, which is used to conserve the momentum of fluid flow in a control volume, is composed of four terms. These terms are: unsteady acceleration, convection (motion of fluid), pressure gradient (the force due to pressure), and diffusivity of momentum (viscous force). The gravitational effects are negligible in this study due to the motion of the oil film being predominantly horizontal. The momentum equation of fluid motion can be expressed as follows [122]:

$$\frac{\partial(\rho \mathbf{u})}{\partial t} + \nabla \cdot (\rho \mathbf{u} \mathbf{u}) = -\nabla p + \nabla \cdot \tau \quad (4.6)$$

where τ is a function representing the shear stress tensor, which is given by [121]:

$$\tau = \mu \left[\left(\nabla \mathbf{u} + (\nabla \mathbf{u})^T \right) - \frac{2}{3} \mathbf{I} \nabla \cdot \mathbf{u} \right] \quad (4.7)$$

where T denotes the transpose of matrix $\nabla \mathbf{u}$ and \mathbf{I} is the unit tensor.

The momentum equation (4.6) as modified for the mixture phase [121] can be written as:

$$\frac{\partial}{\partial t} \sum_{i=1}^n (\alpha_i \rho_i \mathbf{u}_i) + \nabla \cdot \sum_{i=1}^n (\alpha_i \rho_i \mathbf{u}_i \mathbf{u}_i) = - \sum_{i=1}^n \alpha_i \nabla p_i + \nabla \cdot \sum_{i=1}^n (\alpha_i \tau_i) + \nabla \cdot \sum_{i=1}^n (\alpha_i \rho_i \mathbf{u}_{dr,i} \mathbf{u}_{dr,i}) \quad (4.8)$$

where $\mathbf{u}_{dr,i}$ is the drift velocity for the second phase ($\mathbf{u}_{dr,i} = \mathbf{u}_i - \mathbf{u}_m$). The mixture density (ρ_m), mixture velocity vector (\mathbf{u}_m) and mixture diffusivity equations (4.4) and (4.5) are substituted into equation (4.8), giving:

$$\frac{\partial}{\partial t} (\rho_m \mathbf{u}_m) + \nabla \cdot \rho_m \mathbf{u}_m \mathbf{u}_m = - \nabla p_m + \nabla \cdot \tau_m + \nabla \cdot \sum_{i=1}^n (\alpha_i \rho_i \mathbf{u}_{dr,i} \mathbf{u}_{dr,i}) \quad (4.9)$$

$$\text{where } \tau_m = \sum_{i=1}^n (\alpha_i \mu_i) \left[(\nabla \mathbf{u}_m + (\nabla \mathbf{u}_m)^T) - \frac{2}{3} \mathbf{I} \nabla \cdot \mathbf{u}_m \right]$$

4.2.3 The energy equation

According to the concept of energy conservation, the rate of change of energy is equal to the amount of heat supplied and work done to a control volume. The energy equation that is governed by the first law of thermodynamics, consisting of the rate of change of energy, convection, diffusion, and heat source terms, as given overleaf:

$$\frac{\partial (\rho \bar{E})}{\partial t} + \nabla \cdot (\mathbf{u} (\rho \bar{E} + p)) = \nabla \cdot (k \nabla T) + S_T \quad (4.10)$$

$$\text{where } \bar{E} = h - \frac{p}{\rho} + \frac{u^2}{2} \text{ and } h = \int_{T_{ref}}^T c_p dT$$

Not only do the mass and momentum equations have to be modified, but the energy equation (4.10) is also adapted for the mixture model by summing specific energy equations for all phases. Thus, the conservation of energy equation can be rewritten for the mixture phase as:

$$\frac{\partial}{\partial t} \sum_{i=1}^n (\alpha_i \rho_i \bar{E}_i) + \nabla \cdot \sum_{i=1}^n (\alpha_i \mathbf{u}_i (\rho_i \bar{E}_i + p)) = \nabla \cdot (k \nabla T) + \sum_{i=1}^n S_{T,i} \quad (4.11)$$

where

$$\bar{E}_i = h_i - \frac{p}{\rho_i} + \frac{u_i^2}{2} \text{ and } h_i = \int_{T_{ref}}^T c_{p,i} dT,$$

k is defined as the effective conductivity,

$S_{T,i}$ is the total heat source term for each phase.

In order to apply the energy equation of the CFD model to simulate the thermal effect on the EHL problem in a manner similar to the Reynolds equation, it is necessary to add heat source terms. According to equation (2.40), which is employed to predict the temperature rise in the EHL problem with the Reynolds equation, there are two heat source terms. The first is the heat generated in the fluid film due to the viscous effect (Q_{shear}), also known as the ‘dissipation of energy’, and the second is the heat generated by the compression work ($-W$). Both heat source terms are included in equation (4.10) in the total heat source term ($S_T = Q_{shear} - W$).

Expanding the heat source terms:

$$Q_{shear} = \mu \left(\nabla \mathbf{u} : \nabla \mathbf{u} + \nabla \mathbf{u} : (\nabla \mathbf{u})^T - \frac{2}{3} (\nabla \cdot \mathbf{u})^2 \right) \quad (4.12)$$

From $\mathbf{a} \cdot \mathbf{b} = \mathbf{a}^T \cdot \mathbf{b}$, then:

$$\begin{aligned} \nabla \mathbf{u} : \nabla \mathbf{u} + \nabla \mathbf{u} : (\nabla \mathbf{u})^T &= \frac{1}{2} \left[\nabla \mathbf{u} : (\nabla \mathbf{u})^T \right] : \left[\nabla \mathbf{u} : (\nabla \mathbf{u})^T \right] \\ &= \frac{1}{2} \left| \nabla \mathbf{u} + (\nabla \mathbf{u})^T \right|^2 \\ &= \dot{\gamma}_{eq}^2 \end{aligned} \quad (4.13)$$

In tensor form:

$$\begin{aligned} \dot{\gamma}_{eq}^2 &= 2 \left[\left(\frac{\partial u_1}{\partial x_1} \right)^2 + \left(\frac{\partial u_2}{\partial x_2} \right)^2 + \left(\frac{\partial u_3}{\partial x_3} \right)^2 \right] + \left(\frac{\partial u_1}{\partial x_2} + \frac{\partial u_2}{\partial x_1} \right)^2 \\ &\quad + \left(\frac{\partial u_1}{\partial x_3} + \frac{\partial u_3}{\partial x_1} \right)^2 + \left(\frac{\partial u_2}{\partial x_3} + \frac{\partial u_3}{\partial x_2} \right)^2 \end{aligned} \quad (4.14)$$

and

$$\frac{2}{3} (\nabla \cdot \mathbf{u})^2 = \frac{2}{3} \left(\frac{\partial u_1}{\partial x_1} + \frac{\partial u_2}{\partial x_2} + \frac{\partial u_3}{\partial x_3} \right)^2 \quad (4.15)$$

Equations (4.14) and (4.15) are inserted into equation (4.12), which gives:

$$Q_{shear} = \mu \left(2 \left[\left(\frac{\partial u_1}{\partial x_1} \right)^2 + \left(\frac{\partial u_2}{\partial x_2} \right)^2 + \left(\frac{\partial u_3}{\partial x_3} \right)^2 \right] + \left(\frac{\partial u_1}{\partial x_2} + \frac{\partial u_2}{\partial x_1} \right)^2 + \left(\frac{\partial u_1}{\partial x_3} + \frac{\partial u_3}{\partial x_1} \right)^2 + \left(\frac{\partial u_2}{\partial x_3} + \frac{\partial u_3}{\partial x_2} \right)^2 - \frac{2}{3} \left(\frac{\partial u_1}{\partial x_1} + \frac{\partial u_2}{\partial x_2} + \frac{\partial u_3}{\partial x_3} \right)^2 \right) \quad (4.16)$$

$$\begin{aligned}
W &= -\frac{T}{\rho} \left(\frac{\partial \rho}{\partial T} \right) (\mathbf{u} \cdot \nabla p) \\
&= -\frac{T}{\rho} \left(\frac{\partial \rho}{\partial T} \right) \left(u_1 \frac{\partial p}{\partial x_1} + u_2 \frac{\partial p}{\partial x_2} + u_3 \frac{\partial p}{\partial x_3} \right)
\end{aligned} \tag{4.17}$$

The heat generated by the shear and compression forces in the fluid film will be transferred toward the adjacent walls (top cylinder and bottom plate). Thus, the thermal boundary condition at the walls can be expressed as:

$$\begin{aligned}
q_f &= q_s \\
k_f \left(\frac{\partial T}{\partial n} \right)_f &= k_s \left(\frac{\partial T}{\partial n} \right)_s
\end{aligned} \tag{4.18}$$

where k_f and k_s are the thermal conductivity of fluid and solid respectively.

The governing equations can be written in a general transport form, where each equation consists of rate of change, convection, diffusion, and other effects. The rate of change term represents the net rate of change of an intensive property ϕ in the fluid element. The second term represents the net rate of flow of ϕ across the fluid element boundaries due to the flow velocity, \mathbf{u} . The diffusive term, which is the third term in equation (4.10), represents the diffusion of ϕ through the fluid element. The general transport equation of all fluid flow equations for the variable ϕ can be written in the general form as [123]:

$$\frac{\partial(\rho\phi)}{\partial t} + \nabla \cdot (\rho\mathbf{u}\phi) = \nabla \cdot (\Gamma \nabla \phi) + S_\phi \tag{4.19}$$

It can be noted that the Navier-Stokes equations are non-linear partial differential equations that must be solved simultaneously. There are many numerical methods that can be used to solve discretized equations, for example, the finite difference method (FDM) [124], the finite element method (FEM) [125] and the finite volume method (FVM) [126]. The FVM, FDM and FEM are similar but the FDM is widely used to solve simpler elastic problems. The FEM was developed for complex stress problems and is a common approach used in solid mechanic problems. Conversely, the FVM is more commonly used to evaluate and analyse fluid flow problems. The FVM, that is based on the conservation of physical properties at a local element, such as energy, mass and momentum, is evaluated by integrating the transport

equations over an arbitrary control volume [127, 128]. Furthermore, the FVM is also easily adapted when the grids used are non-uniform. For those reasons, the FVM was chosen to solve the Navier-Stokes equations in this study. The FVM uses the integral form of the generalized transport equations over a control volume, CV as its starting point [129]. Thus, equation (4.19) becomes:

$$\int_{CV} \frac{\partial(\rho\phi)}{\partial t} dV + \int_{CV} \nabla \cdot (\rho\phi\mathbf{u}) dV = \int_{CV} \nabla \cdot (\Gamma\nabla\phi) dV + \int_{CV} S_\phi dV \quad (4.20)$$

where Γ is a diffusion coefficient, S a general source term and ϕ an intensive property of the flow. The first term in equation (4.20) is equal to zero in a steady state problem. This simplifies equation (4.20) in:

$$\int_{CV} \nabla \cdot (\rho\phi\mathbf{u}) dV = \int_{CV} \nabla \cdot (\Gamma\nabla\phi) dV + \int_{CV} S_\phi dV \quad (4.21)$$

In an unsteady flow problem, it is also necessary to integrate equation (4.20) with respect to time t over a small interval Δt from t until $t + \Delta t$. Thus, the general form of the transport equations becomes:

$$\int_{\Delta t} \frac{\partial}{\partial t} \left(\int_{CV} \rho\phi dV \right) dt + \int_{\Delta t} \int_{CV} \nabla \cdot (\rho\phi\mathbf{u}) dV dt = \int_{\Delta t} \int_{CV} \nabla \cdot (\Gamma\nabla\phi) dV dt + \int_{\Delta t} \int_{CV} S_\phi dV dt \quad (4.22)$$

4.3 Cavitation model

Cavitation phenomena can occur when the pressure of the liquid flow suddenly drops below the saturated vapour pressure of the liquid. In the EHL problem, the pressure of the lubricant at the contact centre is very high and rapidly drops below the operating pressure at the outlet region. Gasani [130] studied the film thickness at the contact centre of a nitride rubber sphere and a flat Perspex disk by using ultrasonic reflection techniques. The study shows that film thickness varies according to the slide to roll ratio (SRR) between the sphere and the disk. Furthermore, Gasani also observed the cavitation phenomenon at high speeds, as shown in Figure 4-1. The experiment indicated that fluid velocity and the amount of vapour phase are directly correlated.

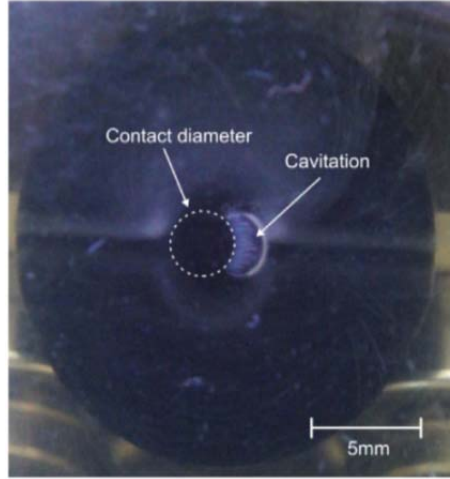


Figure 4-1: The cavitation phenomenon at the outlet region of point contact [130].

Typically, all negative pressures calculated in a solving an EHL problem are set to zero, as the Reynolds equation does not model the cavitation effect [23]. However, using a cavitation model in conjunction with the CFD model for the EHL problem can prevent the occurrence of negative pressure. Some of the liquid phase is changed to the vapour phase when the calculated pressure is lower than vapour pressure, and some of the vapour phase will be collapsed back to the liquid phase when the pressure is higher than the saturated vapour pressure. The full cavitation model, which is based on Rayleigh-Plesset equation, used in this research is given by [131, 132]:

$$\frac{\partial}{\partial t}(\rho_m f) + \nabla \cdot (\rho_m \mathbf{u}_v f) = \nabla \cdot (\zeta \nabla f) + R_v - R_c \quad (4.23)$$

where R_v and R_c are the vapour generation and collapse rates terms respectively, as given by:

$$\text{if } p_{sat} > p, \quad R_v = C_v \frac{V_{ch}}{\sigma} \rho_l \rho_v \sqrt{\frac{2(p_{sat} - p)}{3\rho_l}} (1 - f) \quad (4.24)$$

$$\text{if } p_{sat} < p, \quad R_c = C_c \frac{V_{ch}}{\sigma} \rho_l \rho_v \sqrt{\frac{2(p - p_{sat})}{3\rho_l}} (f) \quad (4.25)$$

where p_{sat} is the liquid saturation vapour pressure at the given temperature,

f is the mass fraction,

σ is the surface tension of the liquid,

V_{ch} is the characteristic velocity that is defined the same as the velocity of mixture phase ,
 ζ is effective exchange coefficient,
and C_v, C_c are empirical constants, usually defined as 0.2 and 0.1 respectively [121].

The fluid density, ρ_m can be calculated from the relationship between the liquid phase and the vapour phase of the fluid, as stated in equation (4.18). For a two phase flow, equation (4.18) becomes:

$$\frac{1}{\rho_m} \equiv \frac{f}{\rho_v} + \frac{1-f}{\rho_l} \quad (4.26)$$

and the volume fraction is given by:

$$\alpha_i = f_i \frac{\rho_m}{\rho_i}, \quad (4.27)$$

where subscript i represents the vapour (v) and liquid (l) phases. The density of the lubricant for the liquid phase is a function of pressure as shown in equation (2.38). The density of the vapour phase is considered to be a constant. Therefore, the density of the mixture can be written as:

$$\rho_m = \alpha_v \rho_v + (1 - \alpha_v) \rho_l \quad (4.28)$$

The viscosity of the mixture can be expressed in a similar way as equation (4.28):

$$\mu_m = \alpha_v \mu_v + (1 - \alpha_v) \mu_l \quad (4.29)$$

4.4 The discretized equations

A partial differential equation can be solved by two methods, an analytical and a numerical solution. The analytical method gives the exact solution but cannot be used with complex problems, while the numerical method is widely used but the solution it yields is an approximation. It should be noted that the residual of the numerical methods is very small when a solution converges. In order to

approach an exact solution, it is necessary to choose the right scheme to solve the discretized equations.

In order to solve the transport equations with a high degree of accuracy, it is necessary to divide the continuous domain into a finite number of sub-domains, which are known as 'cells' or 'control volumes'. The node points are located at the centre of each cell. Then the integral form of the transport equation (4.22) is discretized. There are many numerical schemes to reconstruct the distribution of the transported quantity ϕ at the boundaries of each control volume from the value average of the control volume and of its neighbouring control volumes. These numerical schemes are recommended for use in different situations and are defined according to ANSYS FLUENT [121] as follows:

- "The first-order upwind scheme is the simplest numerical scheme providing the most accurate spatially stable calculations. It is also, however, very diffusive. On the whole, it forms the starting point of the calculation procedure.
- The central differencing scheme yields more accurate results than the first-order upwind scheme, but also leads to oscillations in the solution, where the Peclet number (Pe) is higher than 2.
- The power-law scheme stems from the analytical solution of the one-dimensional convection-diffusion equation. The face value is the result of an exponential profile through the cell-averaged values. Overall, this scheme is more accurate than the first-order upwind scheme when the local Reynolds number is lower than 5.
- The second-order upwind scheme is more accurate and stable than the first order-upwind scheme. The downside is that, in regions with strong gradients, the resulting face values can fall outside the cell-averaged values. In this case, it is necessary to apply limiters to the predicted face values.
- The quadratic upwind interpolation for convective kinetics (QUICK) scheme is accurate but not in regions with high gradients, where it can result in unstable calculations".

By applying the gauss divergence theorem to the advection and diffusion terms, equation (4.22) becomes:

$$\int_{\Delta t} \int_{\Delta V} \frac{\partial(\rho\phi)}{\partial t} dV dt + \int_{\Delta t} \oint_{\Delta S} \rho\phi \mathbf{u} \cdot \mathbf{n} dS dt = \int_{\Delta t} \oint_{\Delta S} \Gamma \phi \cdot \mathbf{n} dS dt + \int_{\Delta t} \int_{\Delta V} S_\phi dV dt \quad (4.30)$$

Let $\phi = \frac{1}{\Delta V} \int_{\Delta V} \phi dV$ then

$$\frac{\partial(\rho\phi)}{\partial t} \Delta V + \sum_f^{N_{faces}} \rho_f \phi_f \mathbf{u}_f \cdot \mathbf{A}_f = \sum_f^{N_{faces}} \Gamma_f (\nabla \phi)_n \cdot \mathbf{A}_f + S_\phi \Delta V \quad (4.31)$$

There are three methods to compute the gradient of the scalar field available in Fluent: the Green-Gauss cell-based method, the Green-Gauss node-based method, and the Least squares cell-based method [121]. Green-Gauss node-based is chosen in this study because the calculated gradient from this method is more accurate than the ones from the other two schemes. The computation of the gradient of the scalar ϕ at the cell centre P using the Green-Gauss method can be expressed as:

$$(\nabla \phi)_P = \frac{1}{V} \sum_f \bar{\phi}_f \mathbf{A}_f \quad (4.32)$$

where the face value, $\bar{\phi}_f$ can be calculated by the arithmetic average between the cell centre and the neighbouring cells. In order to compute the convection and diffusion terms in the equation (4.31), the data at the finite-volume faces can be provided by using the interpolation schemes in Ansys Fluent [121]. In addition, the first order implicit method is employed to predict the value of variable ϕ for the next time step. Based on Figure 4-2, the discretized equation for the generalized transport equation (4.22) is:

$$\left[\frac{(\rho\phi) - (\rho\phi)^{old}}{\Delta t} \right] \Delta V + [(\rho u \Delta A) \phi]_e - [(\rho u \Delta A) \phi]_w + [(\rho v \Delta A) \phi]_n - [(\rho v \Delta A) \phi]_s = \left[\left(\Gamma \frac{\partial \phi}{\partial y} \right) \Delta A \right]_n - \left[\left(\Gamma \frac{\partial \phi}{\partial y} \right) \Delta A \right]_s + \left[\left(\Gamma \frac{\partial \phi}{\partial x} \right) \Delta A \right]_e - \left[\left(\Gamma \frac{\partial \phi}{\partial x} \right) \Delta A \right]_w + [S_\phi \Delta V] \quad (4.33)$$

The discretized form of the general transport equation (4.33) can be rearranged into a simple form as:

$$a_P c_P = a_W c_W + a_N c_N + a_E c_E + a_S c_S + b \quad (4.34)$$

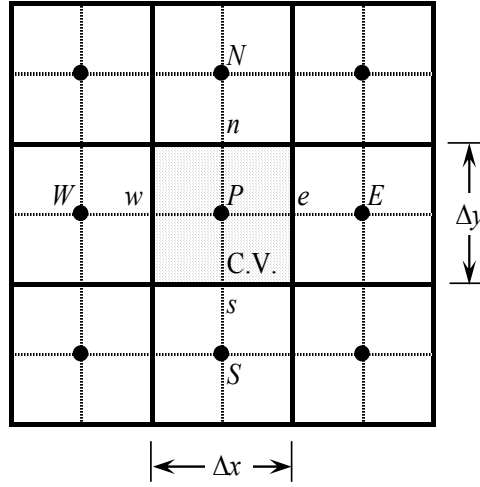


Figure 4-2: Schematic of a discretized computational domain.

The discretized equation (4.33) contains the unknown variable ϕ at the cell centre, as well as in the surrounding neighbour cells. Therefore, the general form for the linearized transport equation can be written as:

$$a_P \phi_P = \sum_{nb} a_{nb} \phi_{nb} + b \quad (4.35)$$

where subscript nb in the notation denotes the neighbour cells of cell P , the a parameter is the coefficient of variable ϕ and b is the net flow rate into cell P . In order to compute the unknown variables in the domain by using approximate methods, the initial state and the appropriate boundary conditions are required. Then, the transport equation (4.35) can be solved iteratively for all the cells in the domain by the Gauss-Seidel iterative method [108] and the algebraic multigrid scheme (AMG) [133].

4.5 Shear stress at wall

A wall is a boundary in a confined fluid flow problem. In general, fluid flow near the wall can be considered as laminar. In the EHL line contact problem, the surfaces of the cylinder and the bottom plate are defined as solid walls. The

cylinder is rotated around the z axis while the bottom plate is travelling in the x – direction. Typically, the shear condition between the fluid and the wall is considered to be no-slip in the EHL problem. This is due to the fact that the viscosity of the fluid is very high (viscous flow). For the wall moving at the maximum speed of 2.5 m/s, the calculated Reynolds number of the viscous fluid flow in the narrow gap between the top cylinder and the bottom plate is between 0.01 and 20. It can be seen that the Reynolds number is very low as viscous forces dominate the flow. Therefore, the flow pattern of the thin fluid film is considered as laminar in this study. Accordingly, wall shear stress is expressed by a normal velocity gradient at the wall [127, 129, 134]:

$$\tau_w = \mu \left(\frac{\partial u}{\partial n} \right) \quad (4.36)$$

Thus, the shear force F_s per unit length of roller is given by:

$$F_s = - \int_{x_{inlet}}^{x_{outlet}} \tau_w dx \quad (4.37)$$

and the friction coefficient can be calculated from the formula:

$$\mu_f = \frac{F_s}{w} \quad (4.38)$$

where w is the applied load.

4.6 Numerical scheme

There are two solvers available in ANSYS FLUENT (pressure-based and density-based solvers). Traditionally, the pressure-based solution is employed to solve the Navier-Stokes equations for incompressible flows, while the density-based solver is commonly used in compressible flows. However, the pressure-based solver has been continually developed and has been extended to solve compressible flow problems. In the CFD model for the EHL problem, the flow is treated as compressible as the density of the lubricant is a function of pressure. The mixture model, which is applied to the CFD model, is only available in the pressure-based solver. Therefore, the pressure-based solver has been chosen to calculate the transport equations in this study.

In order to initiate the iteration solution process, the velocity and the pressure fields are approximated for the first iteration. These variables are subsequently used to solve the momentum equation and the pressure correction equation. These values will be corrected in each iteration until an acceptable convergence of pressure and velocity is achieved. In order to avoid the divergence of the solution, it is common to apply a relaxation factor to reduce numerical changes from one iteration to the next one in the iterative solution procedure when updating the unknown variables. A relaxed update is obtained by:

$$\phi_{new,relaxed} = (1 - \mathcal{G})\phi_{old} + \mathcal{G}\phi_{new} \quad (4.39)$$

where \mathcal{G} is the relaxation factor, $\mathcal{G} < 1$ is under-relaxation, $\mathcal{G} = 1$ corresponds to no relaxation and $\mathcal{G} > 1$ is over-relaxation. Relaxation will help improve the stability of the calculation but may slow down convergence in the case of under-relaxation. There is no general rule for choosing the best value of \mathcal{G} ; a suitable \mathcal{G} can be found by trial and error. The optimum value depends upon a number of factors, such as the nature of the problem, the number of grid points, grid spacing and the iterative procedure used.

There are two pressure-based algorithms available for solving the system of algebraic equations; first, is the segregated algorithm and second the coupled algorithm. The segregated pressure-based algorithm is suitable for compressible and incompressible flows at a low Mach number, whereas the coupled pressure-based algorithm is appropriate at a high Mach number [121]. If the segregated method is applied, the momentum, continuity and energy equations are separately solved for all cells in each iteration. By contrast, in the case of the coupled method, all conservation equations are solved simultaneously. The Mach number of the lubricant flows in the CFD model is only 2.06×10^{-3} . Thus, so the segregated method is employed in this study. In order to provide more detail about the numerical schemes that are based on the segregated method (such as SIMPLE and PISO), the algorithms will be discussed in the next section.

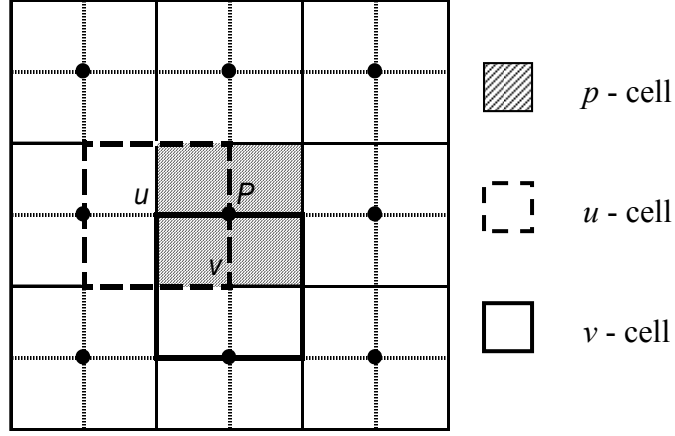


Figure 4-3: Schematic of a staggered grid arrangement.

4.6.1 SIMPLE algorithm

The semi-implicit method for pressure-linked equations (SIMPLE) algorithm of Patankar and Spalding [135] is essentially a guess and correction procedure for the calculation of pressure on the staggered grid arrangement shown in Figure 4-3. Typically, density is considered to be a constant in incompressible flows and is not linked to pressure. The SIMPLE algorithm is employed to account for fixing the lack of results obtained from the continuity and momentum equations. The scalar variables (for example pressure, density and viscosity) are located at the centre of cells (P) whereas the vector variables such as velocity in the x and y directions are stored at the centres of the cell faces of each control volume. The pressure and velocity fields are approximated and the discretized momentum equations (4.35) are solved so that:

$$a_{i,j} u_{i,j}^* = \sum_{nb} a_{nb} u_{nb}^* + (p_{i-1,j}^* - p_{i,j}^*) A_{i,j} + b_{i,j} \quad (4.40)$$

$$a_{i,j} v_{i,j}^* = \sum_{nb} a_{nb} v_{nb}^* + (p_{i,j-1}^* - p_{i,j}^*) A_{i,j} + b_{i,j} \quad (4.41)$$

The values of $u_{i,j}^*$ and $v_{i,j}^*$ are calculated, then the pressure correction equation is solved to obtain the new value of pressure:

$$a_{i,j} p'_{i,j} = a_{i-1,j} p'_{i-1,j} + a_{i+1,j} p'_{i+1,j} + a_{i,j-1} p'_{i,j-1} + a_{i,j+1} p'_{i,j+1} + b_{i,j} \quad (4.42)$$

The pressure needs to be updated and can be obtained from:

$$p_{i,j} = p_{i,j}^* + p'_{i,j} \quad (4.43)$$

Similarly, the approximated velocity $u_{i,j}^*$ and $v_{i,j}^*$ are corrected:

$$u_{i,j} = u_{i,j}^* + u'_{i,j}, \quad u'_{i,j} = \frac{A_{i,j}}{a_{i,j}} (p'_{I-1,j} - p'_{I,j}) \quad (4.44)$$

$$v_{I,j} = v_{I,j}^* + v'_{I,j}, \quad v'_{I,j} = \frac{A_{I,j}}{a_{I,j}} (p'_{I-1,j} - p'_{I,j}) \quad (4.45)$$

Subsequently, all other discretized transport equations are solved as:

$$a_{I,j} \phi_{I,j} = a_{I-1,j} \phi_{I-1,j} + a_{I+1,j} \phi_{I+1,j} + a_{I,j-1} \phi_{I,j-1} + a_{I,j+1} \phi_{I,j+1} + b_{\phi_{I,j}} \quad (4.46)$$

The new value of each unknown variable is compared to the old one to evaluate the residual in each iteration. If the residual is greater than the pre-defined value, pressure and velocity have to be corrected by calculating the momentum equation again and the whole procedure is repeated until a converged solution is obtained.

4.6.2 PISO algorithm

While the SIMPLE algorithm is only used in a steady flow, this research models time-dependent flow. As such, the pressure-implicit with splitting operators (PISO) algorithm, proposed by Issa [136], is more suitable for this study. The PISO algorithm is a pressure-velocity calculation procedure developed originally for non-iterative computations in unsteady compressible flows. This method is similar to the SIMPLE algorithm, but computes flow using an additional corrector step work respect to the SIMPLE method. In general, PISO is employed to solve time-dependent flows as it can improve convergence speeds faster than the SIMPLE scheme.

The PISO algorithm has the same starting calculation process as SIMPLE whereby the pressure and velocity fields are approximated by equations (4.40) and (4.41). Following that, the pressure correction equation (4.42) is calculated to obtain the pressure and velocity corrections. The pressure correction equation is resolved to obtain $p''_{i,j}$ that can be written as:

$$a_{I,j} p''_{I,j} = a_{I-1,j} p''_{I-1,j} + a_{I+1,j} p''_{I+1,j} + a_{I,j-1} p''_{I,j-1} + a_{I,j+1} p''_{I,j+1} + b_{I,j} \quad (4.47)$$

The second corrected pressure and velocity are obtained from:

$$p_{I,j}^{***} = p_{I,j}^* + p'_{I,j} + p''_{I,j}, \quad u_{i,j}^{***} = u_{i,j}^* + u'_{i,j} + u''_{i,j}, \quad v_{I,j}^{***} = v_{I,j}^* + v'_{I,j} + v''_{I,j} \quad (4.48)$$

$$u_{i,J}^{***} = u_{i,J}^* + d_{i,J} (p'_{I-1,J} - p'_{I,J}) + \frac{\sum a_{nb} (u_{nb}^{**} - u_{nb}^*)}{a_{i,J}} + d_{i,J} (p''_{I-1,J} - p''_{I,J}) \quad (4.49)$$

$$v_{I,j}^{***} = v_{I,j}^* + d_{I,j} (p'_{I,J-1} - p'_{I,J}) + \frac{\sum a_{nb} (v_{nb}^{**} - v_{nb}^*)}{a_{I,j}} + d_{I,j} (p''_{I,J-1} - p''_{I,J}) \quad (4.50)$$

$$d_{i,J} = \frac{A_{i,J}}{a_{i,J} - \sum a_{nb}}; \quad d_{I,j} = \frac{A_{I,j}}{a_{I,j} - \sum a_{nb}}$$

where $A_{i,J}$ and $A_{I,j}$ denote the cell face area of the u and v control volumes.

Chapter 5

The CFD Models for the EHL Problem

5.1 Introduction

On the basis of the CFD theory, the EHL theory, and the surface roughness measurements presented in the previous chapters, the basic method for designing the CFD model to predict the characteristics of the EHL line contact problem will be briefly described in first part of this chapter. The appropriate boundary conditions and the initial conditions employed in the CFD model will also be presented along with some assumptions for the model. The mesh dependence test of the resolution for the CFD model will then be discussed and comparison between the results of the CFD model and the Reynolds equation will also be presented. Finally, the CFD models designed for predicting the behaviour of EHL in the cylinder–plate contact and the cylinder–cylinder contact will be discussed.

5.2 The application of the CFD to the EHL problem

5.2.1 The modelling geometry

The aim of this study is to design and develop the CFD model for predicting the characteristics of the EHL problem in the cylindrical roller bearing as presented in Figure 3-16. The focus is only on the contact area between the roller and the bearing case where the ratio of the contact length to the radius of the cylindrical roller bearing is small.

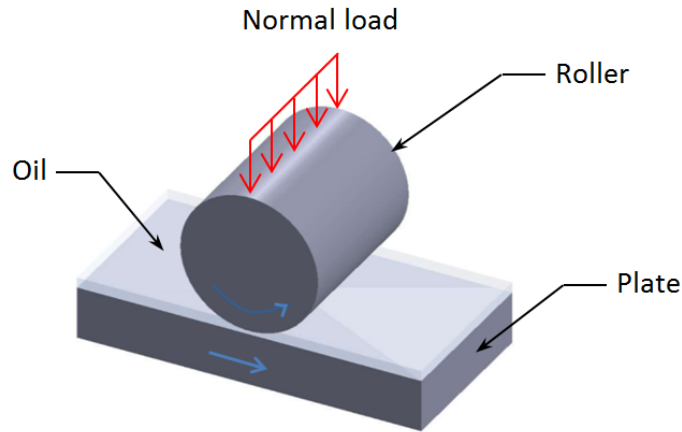


Figure 5-1: The analytical model for EHL line contact problem.

To simplify the EHL problem, the bearing case is assumed to be a line (plate), as presented in Figure 5-1. Although there is the curve on the casing of bearing, the effect of the curvature of the casing is considered via the effective curvature in the film thickness equation. A normal load is applied to the roller which is rotated on the plate – the plate is assumed to be a rigid body while the roller is a solid; however, the material properties of the plate are accounted for by the effective elastic modulus in the film thickness equation (2.17). The roller and the plate are modelled as infinitely long in the transverse direction, thus there is no oil leak at the side of the roller. The pressure distribution in the axial direction of the roller is thus uniform. As such, the CFD model for the fluid film lubricant of the cylindrical roller bearing can be considered to be a 2D problem.

5.2.2 Boundary conditions and initial condition

In order to solve the discretized transport equations, it is essential to identify the appropriate boundary conditions for the CFD model. Poorly defined boundaries may lead to an error in the results or divergence where the solution is not stable [129]. In order to solve the EHL line contact problem using the CFD model as shown in Figure 5-2, the boundary conditions are defined as follows:

- The gauge pressures at the inlet and outlet regions are 0 Pa, and the operating pressure is 1.01325×10^5 Pa.
- The initial temperatures of roller and the plate are 298.15 K.

- The inlet temperature of fluid is constant at 298.15 K, while the outlet temperature is extrapolated from the interior domain.
- The average velocity of plate and roller are presented in Table 5-1.
- The no-slip condition is enforced on the CFD model at all walls.

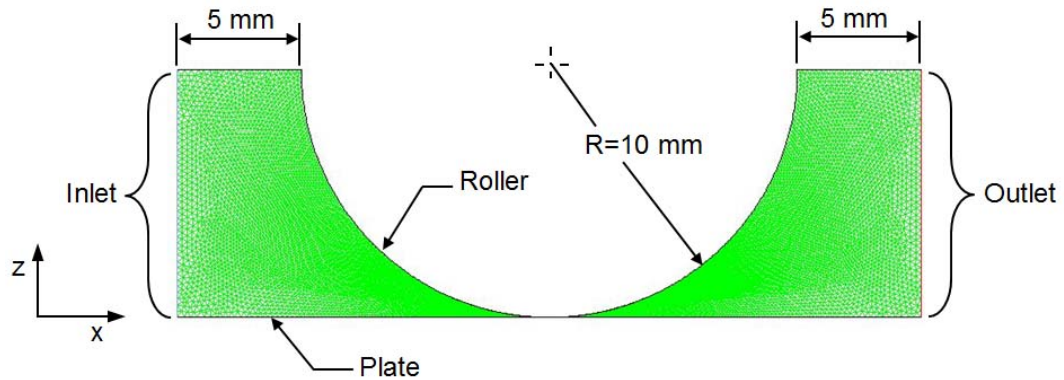


Figure 5-2: Creating geometry and meshing.

The properties of the fluid and solid used in the CFD model are listed in Table 5-1. According to the ANSYS FLUENT manual, the gauge total pressure (static pressure + dynamic pressure, Pa) is required for the inflow boundary. In addition, the ANSYS FLUENT also requires the operating pressure (reference pressure) that is defined as equal to the atmospheric pressure [121]. The absolute pressure is calculated by adding the gauge pressure and the operating pressure together.

5.2.3 Model meshing and solver

In order to solve the discretized equations, the CFD geometry has to be divided into a number of small elements; a process known as 'meshing'. To achieve an accurate solution using the numerical method, a quantity termed the 'mesh quality' is a very important factor. The mesh quality also plays an important role in the stability of the numerical calculation. The mesh quality relates to the skewness, smoothness and node point distribution. It can be evaluated by many criteria such as aspect ratio, cell skewness and orthogonal quality, and depends on the type of mesh employed.

Table 5-1: The common parameters [137].

Parameters	Value	Unit
Input data		
An applied load, w	50,000.0	N/m
Average velocity, u_m	2.5	m/s
Roller radius, R_c	10	mm
Surface roughness, R_a	0.0216	μm
Solid properties (roller and plate)		
Elastic modulus, E	210	GPa
Poisson's ratio, ν	0.3	-
Specific heat, C_p	460	J/(kg·K)
Density, ρ	7,850	kg/m ³
Lubricant properties		
Inlet viscosity of lubricant, μ_0	0.01	Pa·s
Vapour dynamic viscosity, μ_v	8.97×10^{-6}	Pa·s
Liquid density, ρ_l	850.0	kg/m ³
Vapour density, ρ_v	0.0288	kg/m ³
Pressure-viscosity index, z	0.689	-

In this study, the geometry of the CFD model for predicting the behaviour of an EHL problem is created by using the ICEM CFD version 13.0 [138]. Figure 5-2 shows the geometry and the grid of the CFD model. The surfaces of roller and plate are assumed to be smooth. The minimum gap between the roller and the plate is 0.1 mm. The triangular-mesh type is applied to generate meshes for the CFD model. There are 208,759 nodes in total. The minimum and maximum face areas are $6.4825 \times 10^{-9} \text{ m}^2$ and $3.3022 \times 10^{-4} \text{ m}^2$ respectively.

In order to ensure that the CFD geometry, as shown in Figure 5-2, can be used to investigate the fluid flow of the EHL problem, it is essential to check the mesh quality first for fixing the worst cells. It found that the minimum orthogonal quality is 0.9061 – this value is acceptable, as the mesh quality is defined between 0 and 1, where 0 is a worst mesh and 1 is the best quality mesh. The maximum aspect ratio is 3.0064. According to the FLUENT recommendation [121], the accepted maximum aspect ratio should not over 5. Therefore, the mesh quality of the CFD model depicted in Figure 5-2 is good and is appropriate for the calculation.

In this research, the ANSYS FLUENT 13.0 is implemented to solve the discretized momentum equation and the continuity equation [121], where the fluid flow is considered to be laminar. The surface roughness effect on EHL problems is simulated an unsteady flow condition. It is necessary to ensure that the computation results are physically realistic. The residuals of the conservation equations are monitored as [121]:

$$R^\phi = \frac{\sum_{\text{cells } P} \left| \sum_{\text{nb}} a_{\text{nb}} \phi_{\text{nb}} + b - a_P \phi_P \right|}{\sum_{\text{cells } P} a_P \phi_P} \quad (5.1)$$

The converged solution is verified by ensuring the residuals of all parameters monitored are less than 0.001.

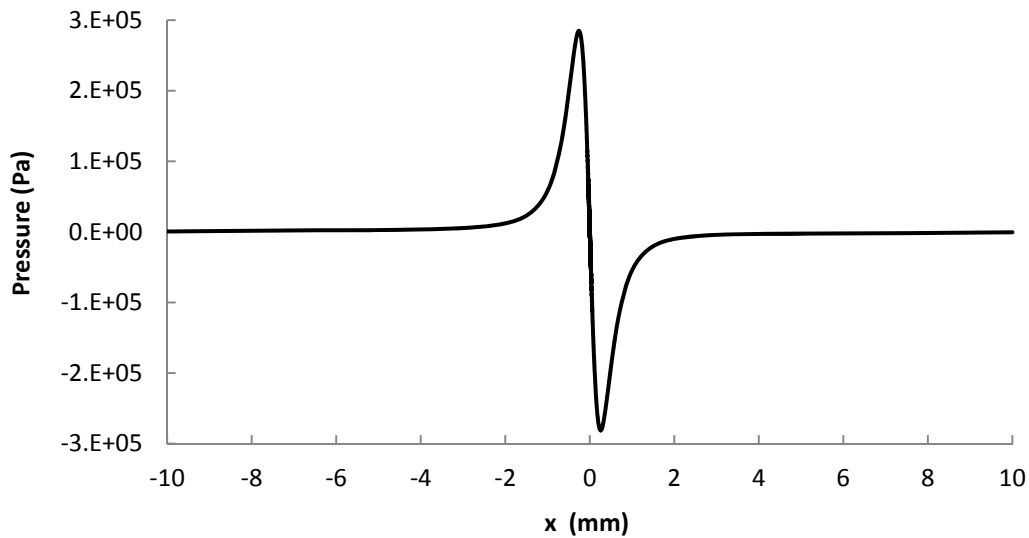


Figure 5-3: The static pressure in the fluid film at the contact zone.

Figure 5-3 shows the pressure distribution in the fluid film between the roller and the plate. It can be seen that the pressure is rapidly increased from 0 Pa at $x \approx -3$ mm to around 28 MPa at $x \approx -0.3$ mm, then it is reduced to the lowest pressure at -28 MPa within a short distance, and then returned to 0 Pa. The pressure distribution fluctuates by a large amplitude of 56 MPa in the contact zone between -3 mm and 3 mm, reaching the highest value in a very short length. This implies that the total length of the CFD model geometry can be reduced from 30 mm to 20 mm to save simulation time as the inlet and outlet are still located far from the pressure distribution zone. In addition, the pressure drop is lower than the operating pressure when the fluid flows through the narrow conduit; this is known as the ‘cavitation phenomenon’. This negative absolute pressure is unphysical and it can be corrected by applying the cavitation model as presented in the previous chapter.

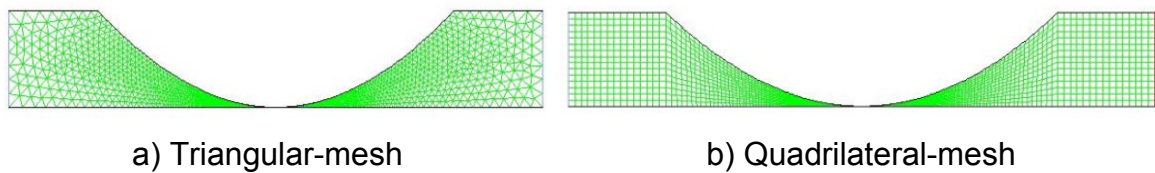


Figure 5-4: Two types of CFD model meshes for the EHL problem.

Typically, triangular (tri) and quadrilateral (quad) cell shapes are available for discretising the computational domain of a 2D problem. The tri-mesh (Unstructured mesh) is often used in a complex geometry while the quad-mesh (Structured mesh) is commonly used with a simple geometry. Both types of meshing are applied to the CFD models in this study. Figure 5-4 shows the improved CFD models by using the tri-mesh and the quad-mesh respectively to discretise the 20 mm long computational domain. After the reduction in total length from 30 to 20 mm, the new mesh has half the number of cells of the original mesh.

The quality of the spatial discretization in the CFD model must be verified to check whether the CFD mesh is sufficiently fine to calculate the pressure and velocity at the contact region within an acceptable engineering accuracy. The predicted pressure distribution from the CFD model, Figure 5-3, shows that the

fluid pressure is expected to change significantly along the contact zone. The mesh resolution in the contact zone must be sufficiently fine to resolve this localised pressure change, while a coarse mesh can be applied outside of the contact zone to reduce the simulation time.

The triangular-mesh is found to be unsuitable for modelling the flow in the EHL problem of table 5-1, due to issues with the mesh quality. The geometry of the meshes in the CFD model must alter as the roller moves. This can be achieved by implementing dynamic meshing that accounts for the elastic deformation of the roller. The elastic deformation is estimated by a user-defined function (UDF) is applied to the CFD model. It is found that the quality of the triangular-mesh reduced after the roller is moved up or down. Some cells that are smaller than the specific minimum size of the re-meshing will be combined when the roller surface deforms downwards. In contrast, some cells are split if the cell size is distorted or extended over the specific maximum size when the roller surface deforms upwards. In ANSYS FLUENT, the maximum cell skewness parameter is employed to drive the re-meshing process. The maximum cell skewness limit is required when the triangular type mesh is applied to the CFD model to avoid the violation of skewness or size criteria. However, it is difficult to control the size and quality of the cells after they are re-meshed as the cells at the contact area and outside are of different size. For those reasons, the approach using a triangular type mesh for generating meshes in the CFD model is not considered further.

Fortunately, such an issue does not arise with the quadrilateral-mesh, where the smoothing mesh method is employed instead of the re-meshing method. The layers of the quadrilateral-mesh are increased or decreased in thickness similarly to the displacement of a spring when the roller is moved down or up, respectively. Thus, only the quadrilateral type mesh is used in the CFD model for the current EHL line contact problem, as presented in Figure 5-4b

5.2.4 Dynamic mesh

According to the film thickness equation, the surface of the cylinder is deformed due to high pressure. The mesh motion in the deforming zone is controlled by the dynamic mesh function. There are three dynamic mesh methods in ANSYS FLUENT that are available to control the position of mesh nodes in the interior of the computational domain when the compute on domain boundary is moving or deforming; these are smoothing, dynamic layering, and local re-meshing. The spring-based smoothing method is the only method that can be employed in this study, because the deformation at the surface of the cylinder is small compared with the cell size at the contact area. In addition, the mesh size applied to the CFD model is totally different between the contact area and the outside of the contact area, so that the dynamic layering and the local remeshing techniques are not suitable for generating a dynamic mesh in this case.

According to the concept of the spring-based smoothing method, the links between the cell vertices are modelled as a network of interconnected springs. The net force of all springs in the interior nodes tends to equilibrium. Thus, the displacement of nodes after the boundary has moved can be calculated as [121]:

$$\Delta \mathbf{x}_i^{m+1} = \frac{\sum_j^{n_i} k_{ij} \Delta \mathbf{x}_j^m}{\sum_j^{n_i} k_{ij}} \quad (5.2)$$

where $\Delta \mathbf{x}_i$ and $\Delta \mathbf{x}_j$ are the displacements of the node i and of its neighbour node j , respectively. n_i is a number of neighbouring nodes that are linked to node i . The superscript m refers to a number of iterations. The stiffness, k_{ij} is defined as:

$$k_{ij} = \frac{1}{\sqrt{|\mathbf{x}_i - \mathbf{x}_j|}} \quad (5.3)$$

The displacement of the node i as depicted in equation (5.2) is calculated by solving the $n \times n$ sparse matrix for all interior nodes at time m to obtain the nodal displacements $\Delta \mathbf{x}^{m+1}$. Then the new position of node i is updated for the next time step $(t+1)$ by:

$$x_i^{t+1} = x_i^t + \Delta x_i^{m-\text{convergence}} \quad (5.4)$$

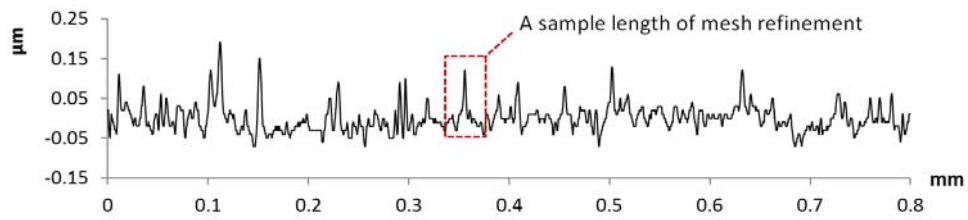
5.2.5 User-Defined Functions

In general, the pressure distribution in the EHL problems is higher than 0.4 GPa, but the maximum pressure in Figure 5-3 is only 30 MPa. To improve the prediction, User-Defined Functions (UDFs) are developed for modelling the viscosity and the density as presented in equations (2.24) and (2.38). Furthermore, a UDF code for estimating the elastic deformation of the walls due to the pressure is also required by the CFD model [139]. The UDF code language accepted by the FLUENT software is C [140, 141]. Therefore, UDFs were written in C to estimate the density and viscosity of lubricant. These UDFs were implemented so that these properties are updated at every iteration after the continuity and the momentum equations are solved. The UDF for elastic deformation of the solids are implemented so that the position of the solid walls is updated at every time step [142]. Moreover, the UDF for the heat source in the fluid film as explained by equation (4.10) was used where the thermal effect is expected to be significant [143]. More detailed information about the UDFs operation are explained in appendixes 2 (UDF codes) and 4 (the flow chart for simulating the EHL problem using the CFD model).

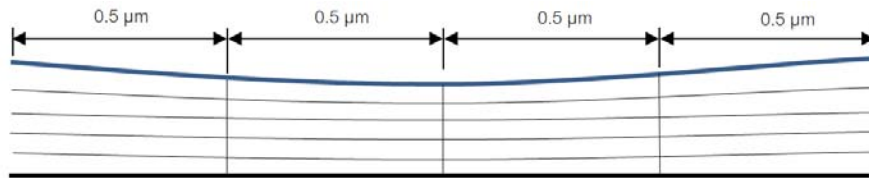
5.3 Mesh dependence test

The previous section presented the computational meshes to be used by the CFD model of an EHL line contact problem. It is necessary to test the sensitivity of the CFD model on the spatial discretization by testing the mesh dependence of the predictions. The quality and the resolution of the mesh play an important role in the simulation results as different spatial discretizations will lead to different solutions. If a mesh resolution is not sufficiently fine, the results are expected to display a greater difference from the real physical phenomena. Thus, it is important to ensure that the generated mesh size of the CFD model is fine enough to capture all the relevant flow features that the accuracy of the results.

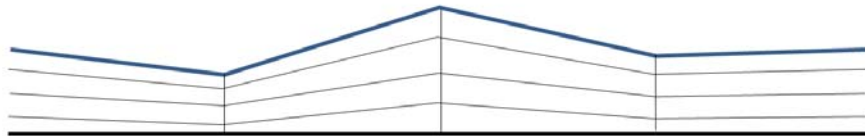
A) Measured surface roughness profile



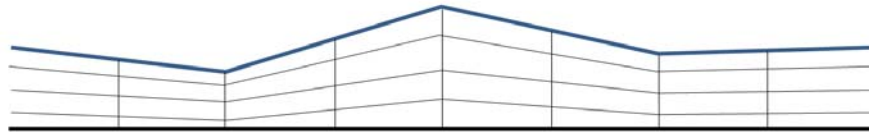
B) Meshing a smooth surface, $\Delta x = 0.5 \mu\text{m}$



C) Meshing a surface with roughness (Original profile), $\Delta x = 0.5 \mu\text{m}$



D) Meshing a surface with roughness (Interpolated profile), $\Delta x = 0.25 \mu\text{m}$



E) Meshing the surface roughness (Interpolated profile), $\Delta x = 0.167 \mu\text{m}$

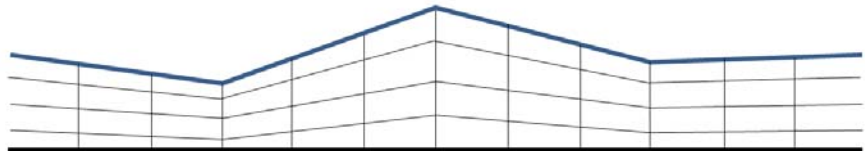


Figure 5-5: Schematic representation of the mesh refinement process.

Figure 5-5 shows the basic concept for defining the characteristic length scale of the unit cells and for refining mesh. Figure 5-5A shows the surface roughness profile measured on bearing surfaces by the Surtronic 3+. This shows in (x, y) coordinates the bearing surface texture. The vertical position of the stylus is recorded over the surface of roller every $0.5 \mu\text{m}$ as shown in Figure 5-5A. Thus the minimum size of the mesh in x is set as $0.5 \mu\text{m}$, to match the sampling length of the surface roughness profile, as shown in Figure 5-5B. Although the

x - spacing of the mesh at $0.5\ \mu\text{m}$ is very small, it still may not be sufficiently fine to get an accurate result. Thus, the spacing of the mesh is reduced from $0.5\ \mu\text{m}$ to $0.25\ \mu\text{m}$ and $0.167\ \mu\text{m}$ as presented in Figure 5-5C and Figure 5-5D, respectively. Even though the spacing of the mesh is refined, the roughness profile applied to the finer mesh still maintains the same profile as the original mesh by using a linear interpolation technique. It can be seen that the mesh is only refined in x - direction because the spacing (layer) of mesh in y - direction ($\Delta y = 0.0186\ \mu\text{m}$) is very small when compared with spacing of the mesh in x - direction.

It can be clearly seen that the pressure outside of the Hertzian contact zone is very low and only changes slightly as presented in Figure 5-3. The grid spacing at the Hertzian contact zone is uniform, while the grid spacing outside of the Hertzian contact zone is increased by a constant ratio. The CFD model for different EHL problems will be accommodated for by different Hertzian contact zone sizes to retain the same length for all CFD models. Thus, the size of the fine mesh is kept constant for the investigated length from $-0.3\ \text{mm}$ to $0.3\ \text{mm}$, while the mesh size outside this length is increased by a 1.01 ratio between the neighbour meshes to reduce the simulation time. In addition, the spacing of the mesh in the centre of the contact area is also used to calculate the displacement of the surface roughness (time dependent) where the movement of the surface depends upon time and on the velocity of the solid.

All simulations use the same material properties of the solid and of the lubricant listed in Table 5-1. The real rough surface, shown in Figure 3-22, will be applied to the CFD model. Figure 5-6 shows the geometry and the mesh of this CFD model for the EHL line contact problem. The rotating roller can be moved up or down to balance between the generated pressure and the normal load, while the plate is assumed to be a rigid body and fixed at $z=0$. Although the plate is undeformed, the material properties of the plate are included in the elastic deformation term of the film thickness equation.

The calculation of the elastic deformation in this study is the same as the film thickness equation in the Reynolds equation. The speed of the plate is maintained as the same as that of the roller surface at 2.5 m/s (pure rolling condition). The lubricant viscosity is modelled as a Newtonian fluid. The density and viscosity depend only on the pressure, as the flow is assumed as isothermal in this simulation. The time step is calculated from the relationship between the mesh size and the fluid velocity. The maximum Courant number ($C = u\Delta t / \Delta x$) for each CFD model is defined as equal to 1. The corresponding time steps for the CFD models, $\Delta x = 0.5 \mu\text{m}$, $0.25 \mu\text{m}$, and $0.167 \mu\text{m}$, are 0.2×10^{-6} , 0.1×10^{-6} and 0.6×10^{-7} seconds, respectively. Thus, the time step of 0.6×10^{-7} second is chosen for simulating all CFD models in this task.

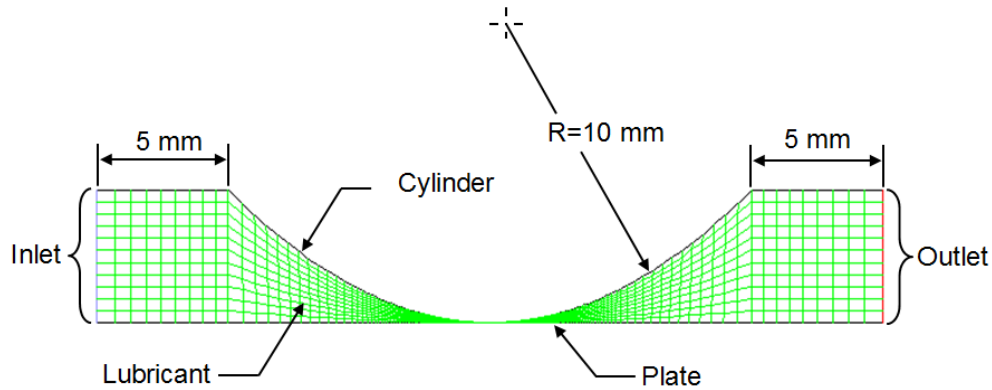


Figure 5-6: A CFD model for an EHL problem.

Table 5-2: The mesh independence test

Parameters	Minimum mesh size (μm)		
	0.500	0.250	0.167
Total number of cells	13,874	23,474	33,074
Maximum pressure - Smooth (GPa)	0.4740	0.4729	0.4724
Minimum film thickness - Smooth (μm)	0.1869	0.1870	0.1870
Maximum pressure - Rough (GPa)	0.9015	1.4483	1.4864
Minimum film thickness - Rough (μm)	0.1662	0.1619	0.1610
Simulation time - Smooth (hr.)	8.14	20.21	38.34

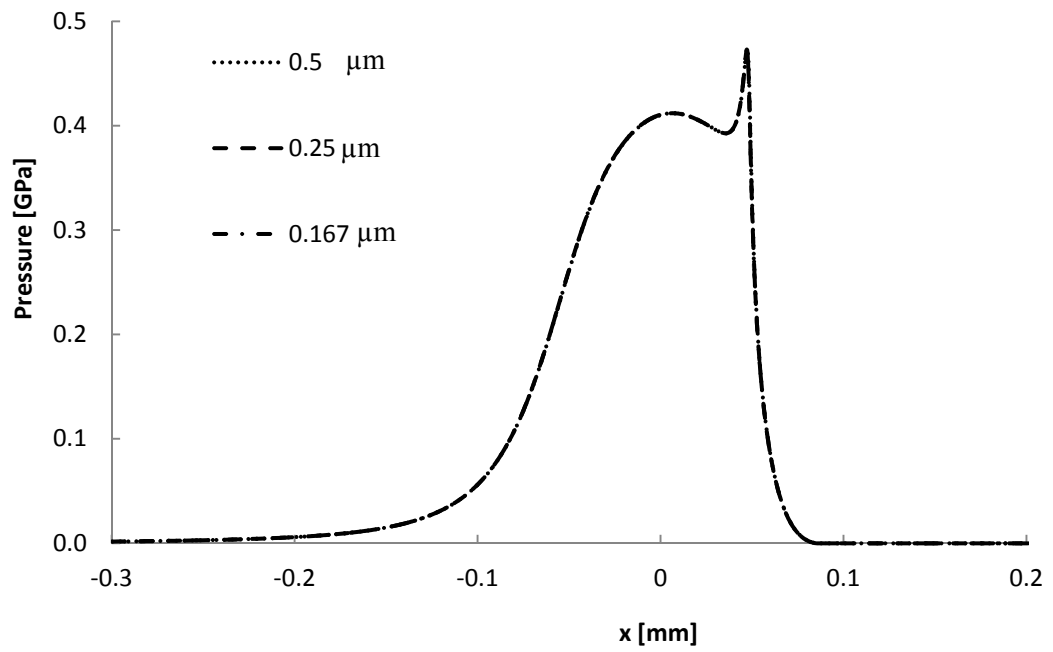


Figure 5-7: Pressure distribution using different mesh sizes (smooth surface).

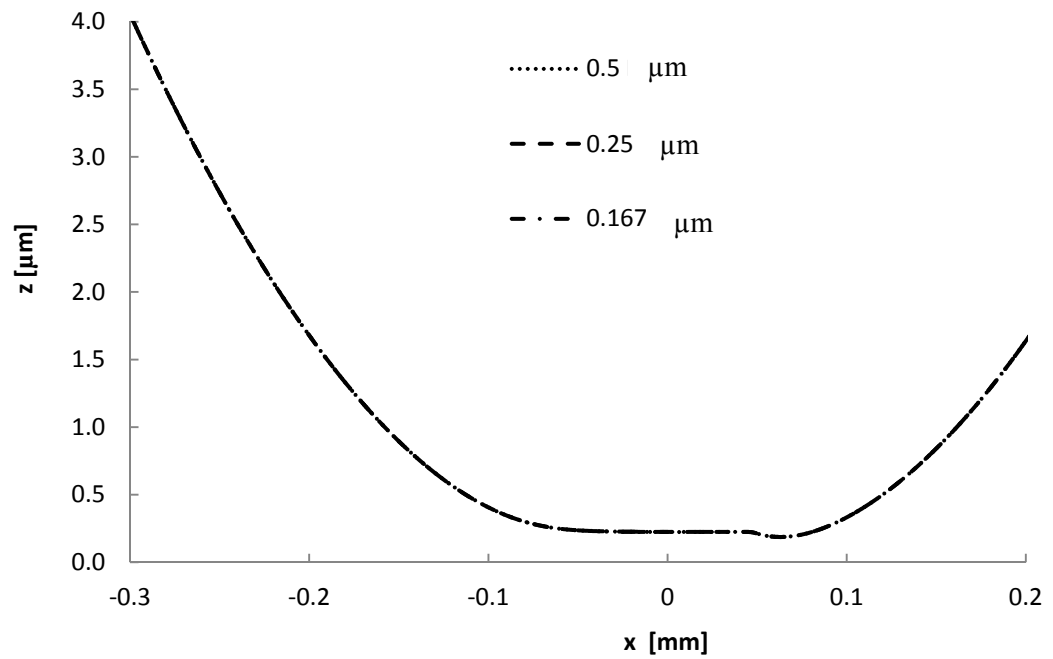


Figure 5-8: Film thickness using different mesh sizes (smooth surface).

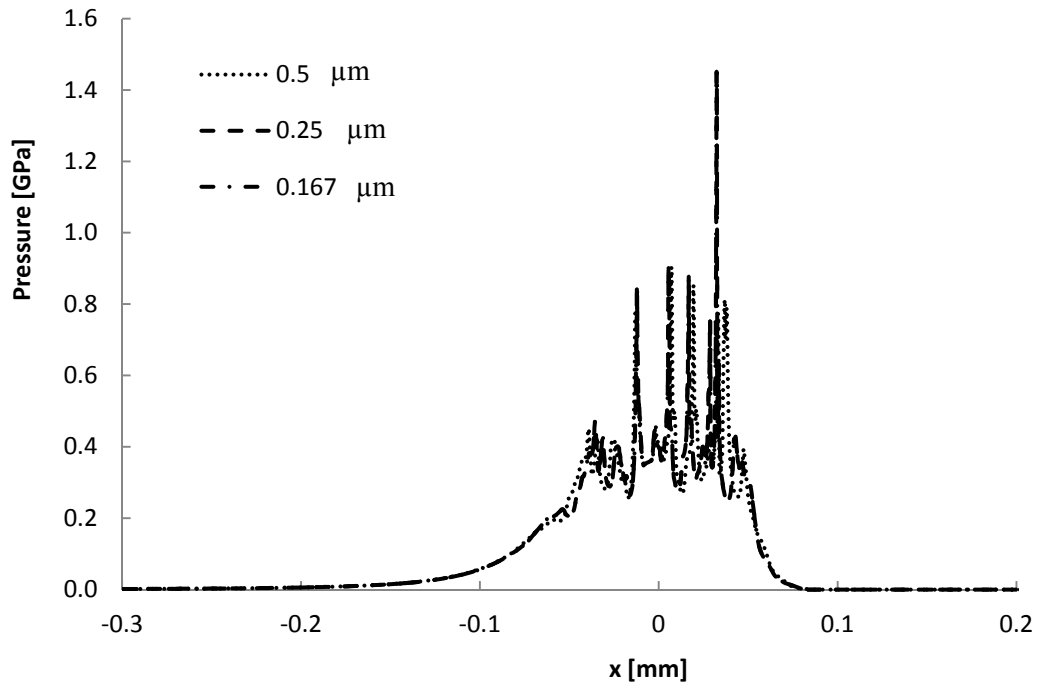


Figure 5-9: Pressure distribution using different mesh sizes (rough surface).

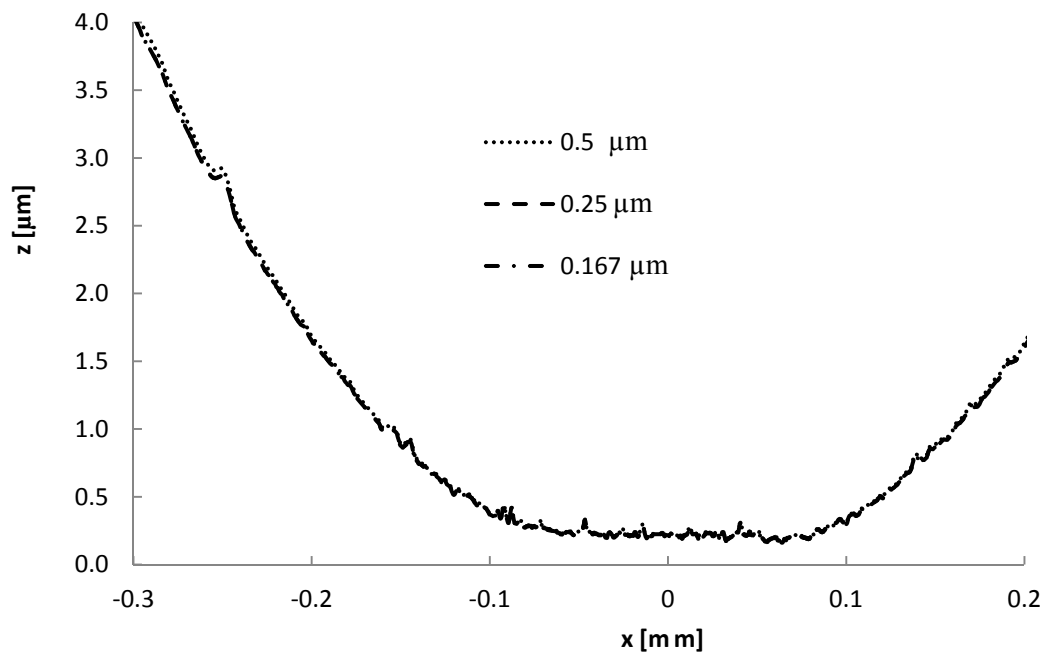


Figure 5-10: Film thickness using different mesh sizes (rough surface).

Figure 5-7 to Figure 5-10 show the pressure distributions and the film thicknesses for grid spacings of $0.50\ \mu\text{m}$, $0.25\ \mu\text{m}$, and $0.167\ \mu\text{m}$, in the cases of smooth surface and rough surface, respectively. It can be seen that the pressure distributions and the film thicknesses for grid spacings of $0.50\ \mu\text{m}$, $0.25\ \mu\text{m}$, and $0.167\ \mu\text{m}$ are the same for the smooth surface case. However, it is found that the grid spacing is a significant parameter that influences the pressure distribution and the film thickness when the surface roughness is applied to the CFD model. The maximum difference in the predicted pressure distributions with the grid spacing of $0.50\ \mu\text{m}$ and $0.25\ \mu\text{m}$ in the rough surface case are 15.3% and 2.3% respectively, in comparison to the result obtained with the finest mesh size at $0.167\ \mu\text{m}$.

The difference of 0.7% is regarded as acceptable, therefore, the minimum mesh size of $0.25\ \mu\text{m}$ will be used to generate the meshes at the contact area of the CFD model for the EHL line contact problem. Although the obtained results with the minimum mesh size between $0.25\ \mu\text{m}$ and $0.167\ \mu\text{m}$ are very close, the minimum mesh size with $0.25\ \mu\text{m}$ reduces the simulation time by 47% in comparison to the finest mesh size of $0.167\ \mu\text{m}$.

5.4 Validation of the CFD approach

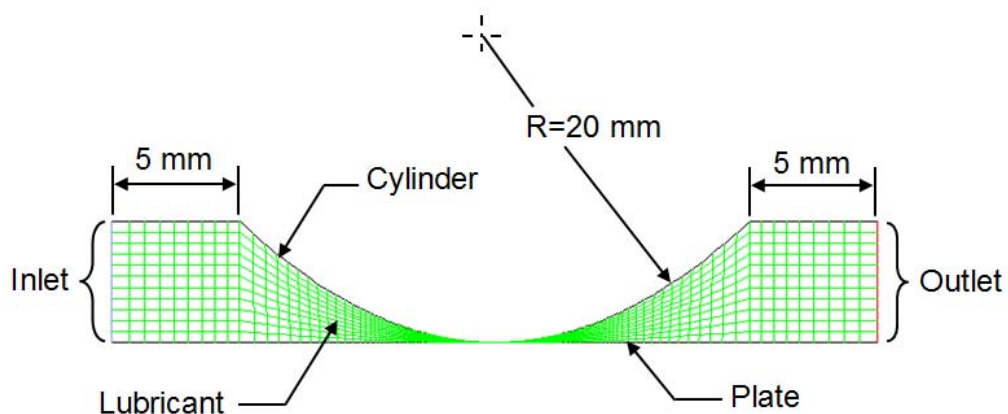


Figure 5-11: The CFD model used to compare with the Reynolds equation.

Table 5-3: Common parameters [144]

Parameters	Value	Unit
Input data		
An applied load, w	79,920.88	N/m
Average velocity, u_m	2.5	m/s
Roller radius, R_c	20	mm
Surface roughness, R_a	0.0275	μm
Ambient temperature, T_0	313.0	K
Solid properties (roller and plate)		
Elastic modulus, E	200	GPa
Poisson's ratio, ν	0.3	-
Specific heat, C_p	460	J/kg·K
Density, ρ	7,850	kg/m ³
Thermal conductivity, k	47	W/m·K
Lubricant properties		
Inlet viscosity, μ_o	0.01	Pa·s
Vapour dynamic viscosity, μ_v	8.97×10^{-6}	Pa·s
Liquid density, ρ_l	846.0	kg/m ³
Vapour density, ρ_v	0.0288	kg/m ³
Inlet temperature, T	313.0	K
Thermal conductivity, k	0.14	W/m·K
Temperature-viscosity, β	6.4×10^{-4}	1/K
Specific heat, C_p	2,000	J/ kg·K
Thermal expansivity, \mathcal{E}	4.5×10^{-4}	1/K
Pressure -viscosity index, Z	0.689	-

The comparison between the simulated results from the CFD model and the Reynolds equation will be presented in this section. In order to establish a fair comparison, the same geometry and flow parameters are used in the CFD

model and the Reynolds equation wherever possible. The parameters and some assumptions defined in the CFD model are listed as follow:

- The lubricant in this case is modelled as a Newtonian fluid.
- There is no slip between the walls and the fluid.
- The thermal effect is taken into consideration in the calculation of viscosity and density.
- The input data, the lubricant properties and the properties of the solids in Table 5-3 are used in this comparative analysis.
- The geometry of the CFD model as shown in Figure 5-11 is employed to simulate the EHL problem in this section.

The CFD model result is compared with that from the Reynolds equation presented by Chu et al. [144] as reported in Figure 5-12. The pressure distribution and the film thickness of the CFD model and the Reynolds equation are in good agreement. The maximum difference between the pressure distributions $P(X)$ from the Reynolds equation and from the CFD model is 0.78%, while the maximum difference of the film thickness $H(X)$ is 1.73%.

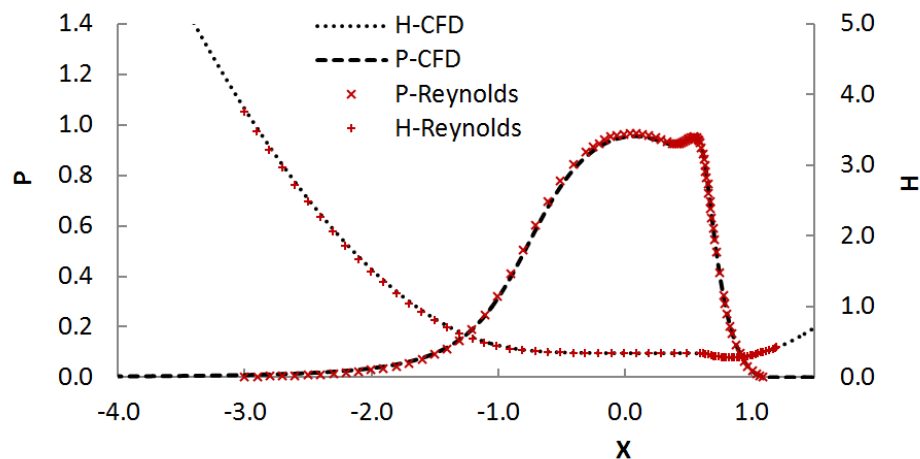


Figure 5-12: Comparison of dimensionless pressure (P) and film thickness (H) distributions between the CFD model and the Reynolds equation. ($W=1.8182 \times 10^{-5}$, $U=7.2727 \times 10^{-12}$ and $G=3500$).

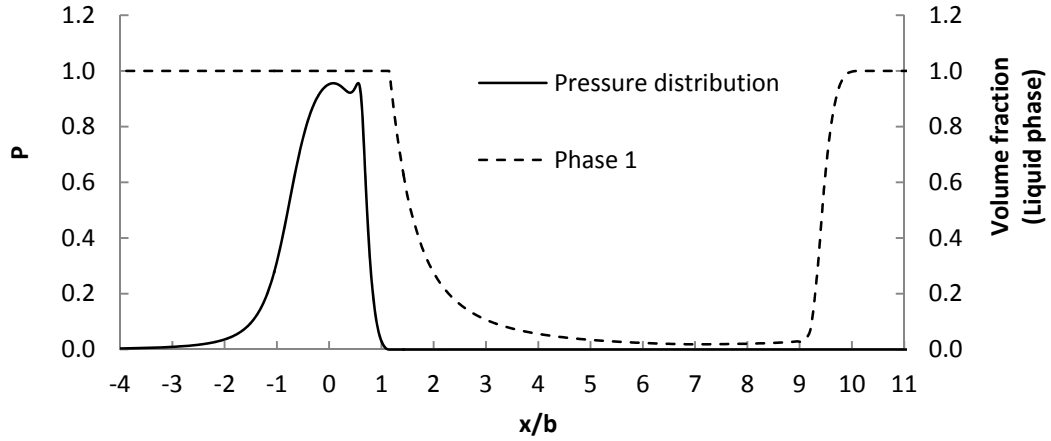


Figure 5-13: The relationship between dimensionless pressure distribution (P) and the volume fraction along the non-dimensional Hertzian contact zone length x/b , where b is the half-width of Hertzian contact (0.14263 mm).

The results of both methods are in good agreement, even though the CFD model includes the cavitation effect. It is found that cavitation occurs at the outlet region as shown in Figure 5-13 and, as such, it is remote from the contact area. Figure 5-13 shows that part of the lubricant is changed from the liquid phase to the vapour phase over the range $X=1.2$ to 9.2 , while the gauge pressure distribution drops to zero at $X=1$. This is due to the fact that the generated pressure within the oil film at the Hertzian contact zone that is very high ($p_{\max}=0.36$ GPa), suddenly drops to the atmospheric pressure at the outlet region. This may explain why the pressure distributions of both models are similar even when cavitation is applied to the CFD model.


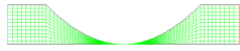




Although the cavitation phenomenon in the EHL problem does not have any effect on the pressure distribution at the contact region, it has a significant effect on the density of the lubricant at the outlet region.

5.5 The simulation models

The CFD models developed in this study are divided into three models. The first model was used in section 5.4 to represent the calculation of the EHL problem in comparison with the Reynolds equation. The second model will be used to

predict the behaviour of the EHL problem in the case of two cylinders. The third model is similar to the second, but the radius of the two cylinders are different. The effective radius and the effective elastic modulus for all models are kept the same. The details of these models are described in Table 5-4. The models are designed to be compatible with the CFD approach which will be used to study the effects of surface roughness on the EHL line contact problem.

Table 5-4: The CFD models for each contact

Model	Radius of roller (mm)		Geometry	CFD model
	Top (R_1)	Bottom (R_2)		
1	10	-		
2	20	20		
3	15	30		

5.5.1 Roller and plate contact

The first CFD model is designed to study the effects of surface roughness on the fluid film in the case of the roller and the plate EHL line contact. This model, presented previously in Figure 5-6, will be used to predict the fluid film properties fluid film in the Hertzian contact zone. The roughness profile will be applied to the surface of the roller, while the plate is assumed to be a smooth surface. The case study of the roughness effect on this model can be divided into 6 cases as follows:

- Influence of non-Newtonian fluid.
- Influence of the viscosity parameter.

- Influence of the normal load parameter.
- Influence of the velocity parameter.
- Influence of the thermal field.
- Influence of the material parameter.

The details of these cases and the simulation results will be presented in chapter 6.

5.5.2 Two rollers contact

The second case for the CFD model studies the EHL problem for two cylinders in contact. Figure 5-14 presents a schematic for the evaluation of the fluid film problem for this configuration. Within the figure, model 1 represents the equivalent model based on the calculation of the Reynolds equation. On the other hand, the geometries of the models 2 and 3 are used to create the CFD models as shown in Figure 5-15 and Figure 5-16, respectively. The solid cylinders in the CFD model 2 and 3 are assumed to be infinitely long.

The effective elastic modulus (E') and the effective curvature (R') are used to calculate the elastic deformation term in the film thickness equation for CFD model 1. The Young's modulus (E_1) and radius (R_1) of the top cylinder are directly used to compute the elastic deformation of the top roller in model 2. In the same way, E_2 and R_2 parameters are employed to evaluate the elastic deformation of the bottom roller. Furthermore, the surface roughness profiles will be applied to the top and bottom cylinders directly. This is the advantage of the CFD model for assessing pressure build up and deformation in the fluid film at the contact area.

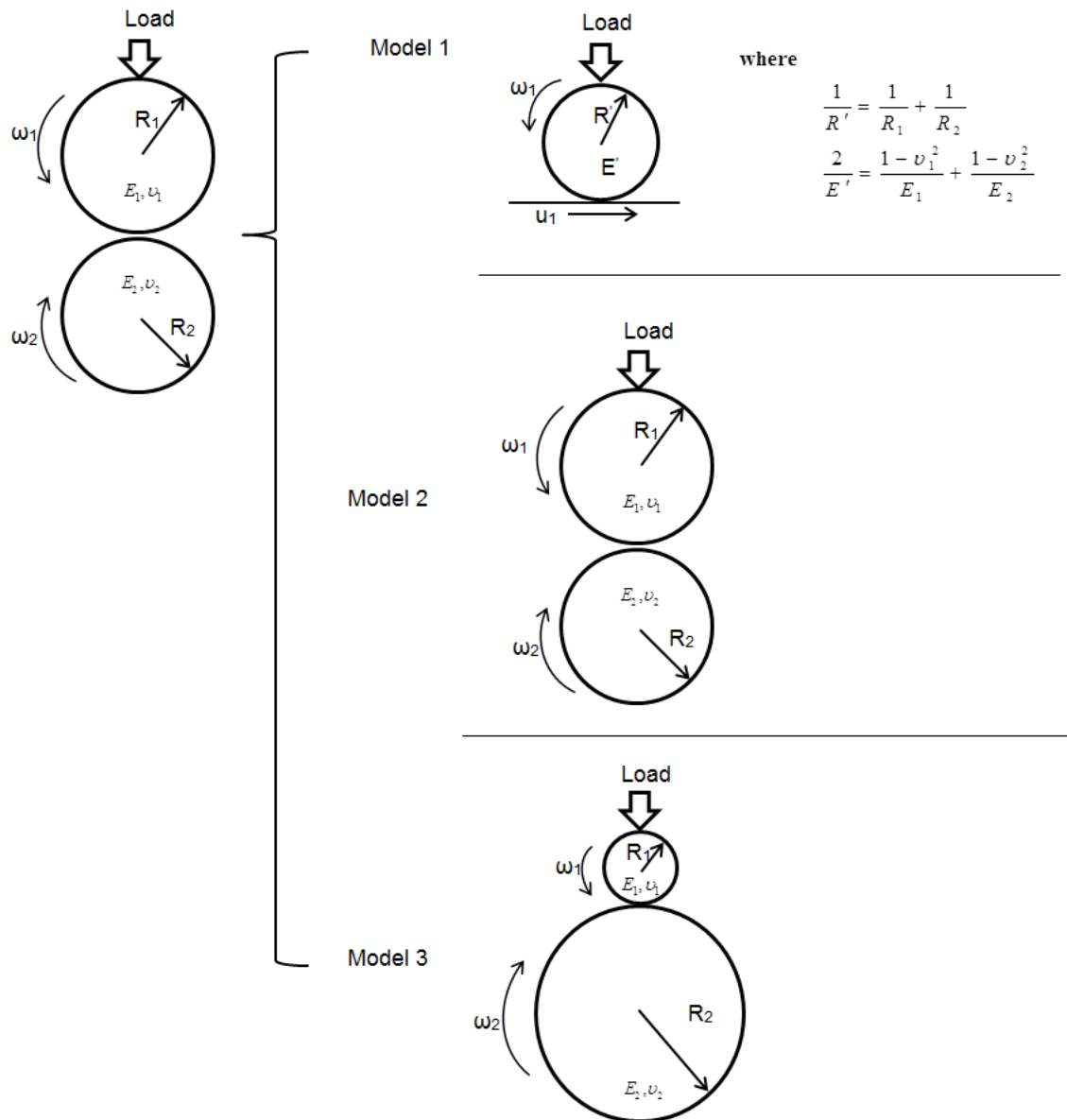


Figure 5-14: The comparison schematic of the EHL problem for cylinders contact between the Reynolds equation (Model 1) and the CFD models (Models 2 and 3).

Subsequently, the CFD model 3 for predicting the contact between two different radius cylinders, as shown in Figure 5-16, will be used to simulate and analyse the EHL line contact problem. In this case, the radius of the top roller is smaller than that of the bottom roller. The CFD model for the EHL problem will be used first to investigate the contact with a smooth surface, and then the effects of the profiles of surface roughness for the top and bottom rollers will be studied. The surface roughness profiles for the top and bottom rollers are the same as in the

previous study of section 5.3. The investigation of the influence of different solid material properties on the EHL problem is divided into three cases. The first case is the contact between iron rollers; the second, contact between brass roller of radius (R_1) and ceramic roller of radius (R_2); and the third, contact between a ceramic roller (R_1) and a brass roller (R_2). All simulation results obtained will be reported in chapter 7.

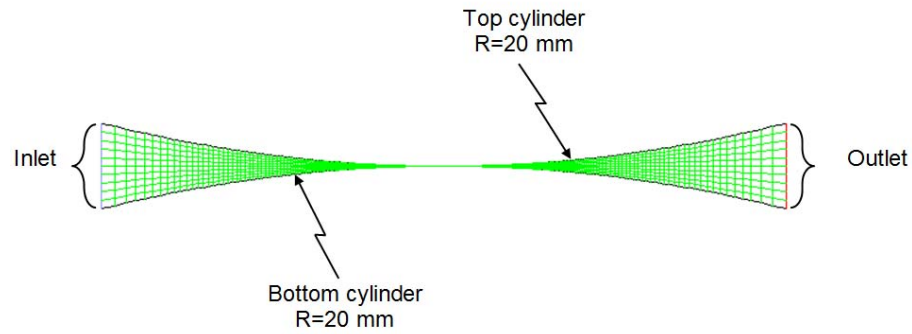


Figure 5-15: The CFD model 2 for predicting two cylinders contact ($R_1 = R_2$).

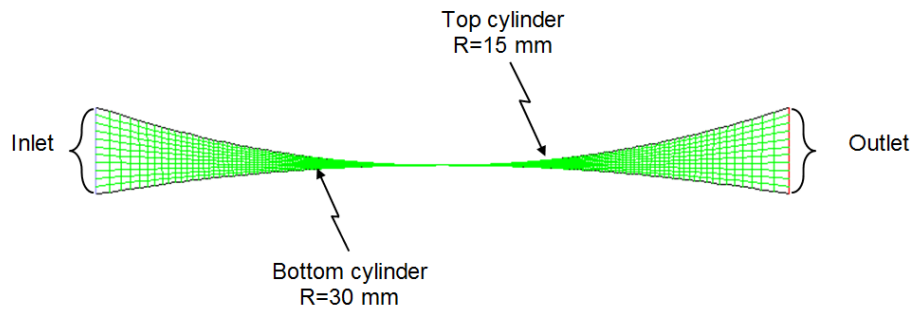


Figure 5-16: The CFD model 3 for predicting two cylinders contact ($R_1 \neq R_2$).

Chapter 6

CFD Model for Roller and Plate Contact

6.1 Introduction

In this chapter, the simulated results of the CFD model for the EHL problem in the case of the roller and plate contact are presented. The boundary conditions and the geometry of the CFD model are kept the same for all cases. For the purpose of simplification, the EHL problem with the Newtonian fluid and isothermal conditions will be studied first. Then, the rheological effects (non-Newtonian fluid) will be investigated. The Roelands and the Ree-Eyring models are used to study the behaviour of Newtonian and non-Newtonian fluids respectively. The common parameters and the geometry model are identical to those previously used. Additionally, the effects of various parameters on the behaviour of the EHL line contact problem are studied, including the applied load, the velocity, the slide to roll ratio (SRR), the viscosity of the lubricant and the material properties. All cases are assumed to be in isothermal conditions with the same boundary conditions as previously discussed. Finally, the thermal condition is applied to non-Newtonian fluids in the CFD model. This will affect the viscosity and the density of the lubricant. The effect of temperature on the elastic properties of the solid walls of the CFD model will also be investigated.

6.2 Influence of non-Newtonian fluid

The aim of this section is to investigate the influence of non-Newtonian fluid behaviour on the EHL problem with surface roughness using the CFD model. The geometry of the CFD model, as shown in Figure 5-6, and the common data, as listed in Table 5-1, are used in this task. Additionally, the Ree-Eyring and Roelands models are used to study the behaviour of the non-Newtonian and Newtonian fluids, respectively. The velocity of the roller and plate are varied to explore the non-Newtonian effects in the sliding condition. It should be noted that thermal effects are not considered in this section.

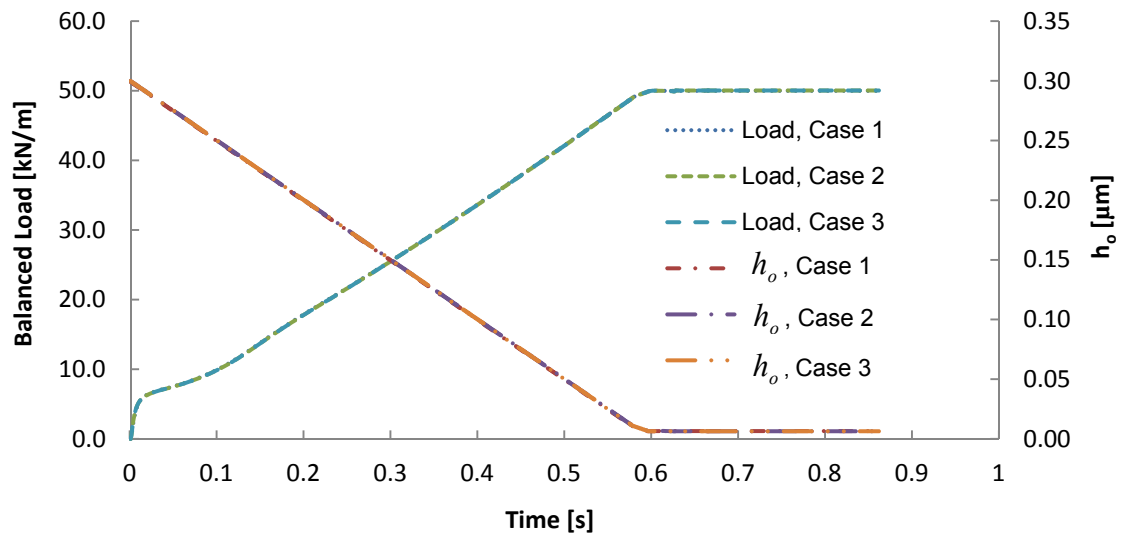


Figure 6-1: The relationship between the undeformed gap (h_o) and the pressure generated (time dependent).

The undeformed gap (h_o) between roller and plate in the film thickness equation plays an important role in balancing an applied load on the roller and the generated pressure in the lubricant film. The aim of this section is to investigate the time required for balancing the load for different test cases. Three different cases are used to simulate the point of balance as follows:

- The first case is the simulation with a Newtonian fluid under pure rolling conditions.

- The second case is the simulation with a non-Newtonian fluid and a slide to roll ratio (SRR) of 1.
- The third case is the simulation with a non-Newtonian fluid under a pure rolling condition.

It was observed that generated pressure increased when the value of h_o decreased as illustrated in Figure 6-1. The relationship between the undeformed gap and the generated pressure shows that the balanced point in all cases is very similar at about 0.6 seconds. The roller is slightly moved in the vertical direction after it reaches the balanced point. It is very difficult to observe and analyse the trend of the surface roughness effect, if the results obtained are presented at different times. Thus, all study cases are presented at 0.8 seconds to align the positions of surface roughness.

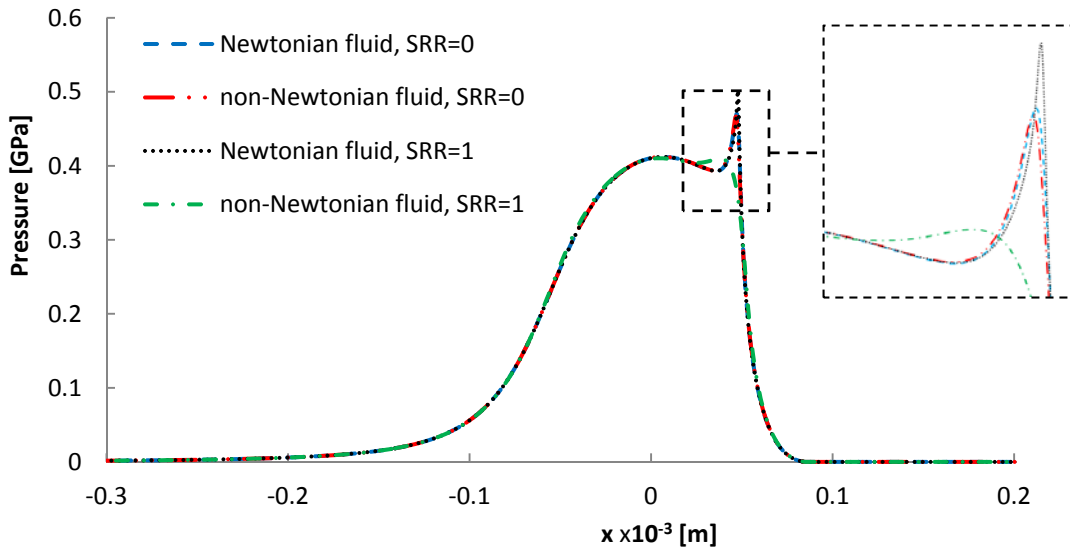


Figure 6-2: Comparison of pressure distributions between Newtonian and non-Newtonian fluids when $SRR = 0$ and 1.

The pressure and film thickness distributions obtained using the CFD model are presented in Figure 6-2, where Newtonian and non-Newtonian fluids over smooth surfaces are compared. There are slight differences in the pressure distributions between the Newtonian and non-Newtonian fluids at $SRR = 0$. This is due to the fact that the shear rate effect is very low under pure rolling

conditions. As a result, the shear strain rate term in the Ree-Eyring model does not change the value of the viscosity of the lubricant to a significant extent.

Furthermore, the friction coefficients of the Newtonian fluid simulations are higher than that of the non-Newtonian fluid simulations, specifically the friction coefficients of Newtonian and non-Newtonian fluid simulations at $SRR = 0$ and 1 are (0.0028, 0.0027) and (0.0766, 0.0275), respectively. At $SRR = 1$, the friction coefficient increases with respect to the $SRR = 0$ case due to the increase velocity gradient.

The results show that the shear strain rate in the lubricant film is increased when the SRR ratio increases. It can be observed that the pressure spike at the outlet of the Hertzian contact zone with the non-Newtonian fluid reduces as the SRR value increases. The pressure spike is therefore inversely correlated to the SRR value. It can be noticed that the influence of the viscosity model in the oil film thickness takes place on molecular scale as shown in Figure 6-3. What is more, the deformation at the minimum film thickness only slightly changes in the case of the non-Newtonian fluid while it changed rapidly in the case of the Newtonian fluid. This may explain why the pressure spike of the non-Newtonian fluid simulation is lower than that of the Newtonian fluid simulation. In addition, it is found that the non-Newtonian fluid model can be used to predict the EHL problem at high SRR values, where it gives a more numerically stable simulation than the Newtonian fluid.

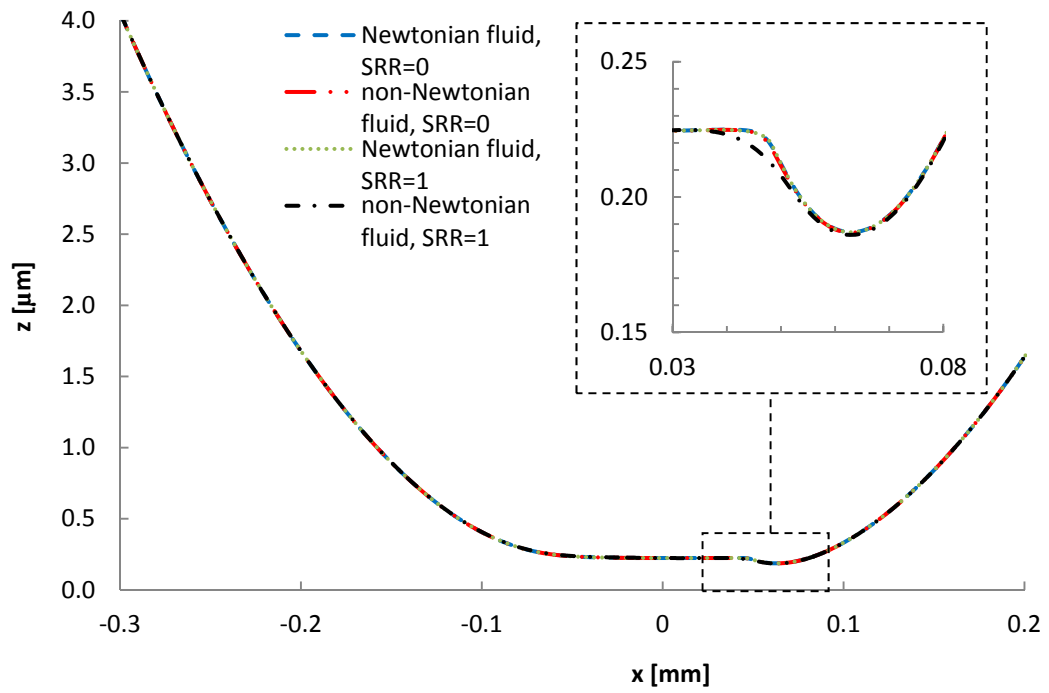


Figure 6-3: Comparison of film thicknesses between Newtonian and non-Newtonian fluids when $SRR = 0$ and 1 .

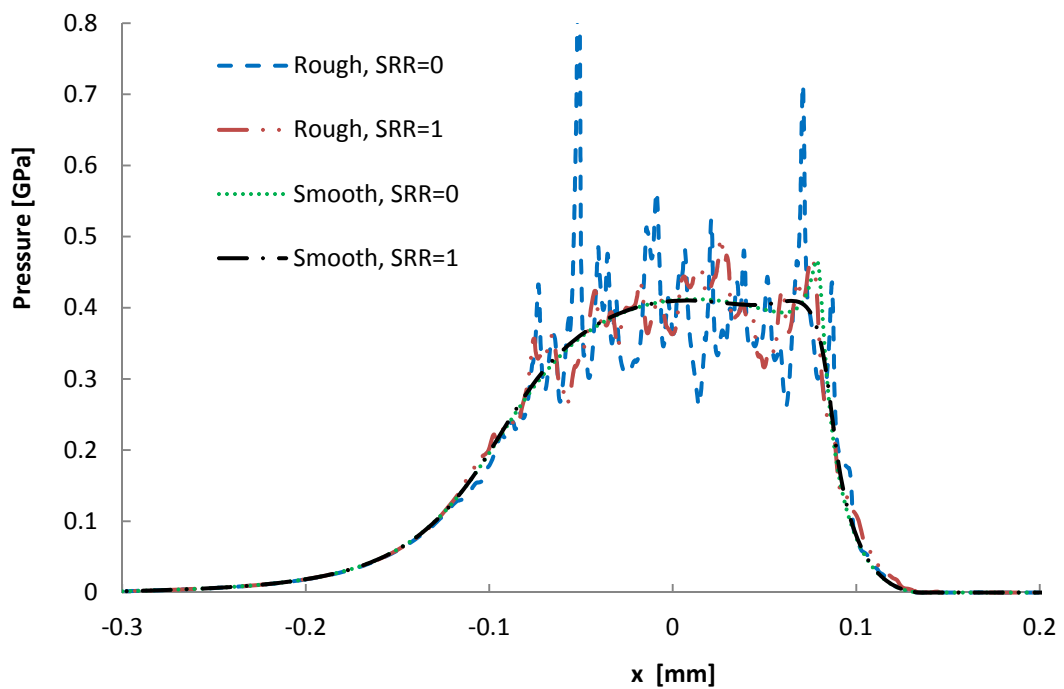


Figure 6-4: Effect of surface roughness on pressure distribution at $SRR = 0$ and 1 for non-Newtonian fluid.

Figure 6-4 shows the influence of using a non-Newtonian fluid on the pressure distribution with surface roughness when SRR is varied from 0 to 1. It can be clearly seen that surface roughness is a significant factor affecting the pressure distribution. The shape of the pressure distribution tends to fluctuate according to the profile of the surface roughness with an amplitude that decreases when the SRR is increased from 0 to 1. This is due to the roller surface velocity reduction from 2.50 m/s to 1.25 m/s, as the influence of the rough surface, with respect to the lubricant flow pattern, is increased at high velocity.

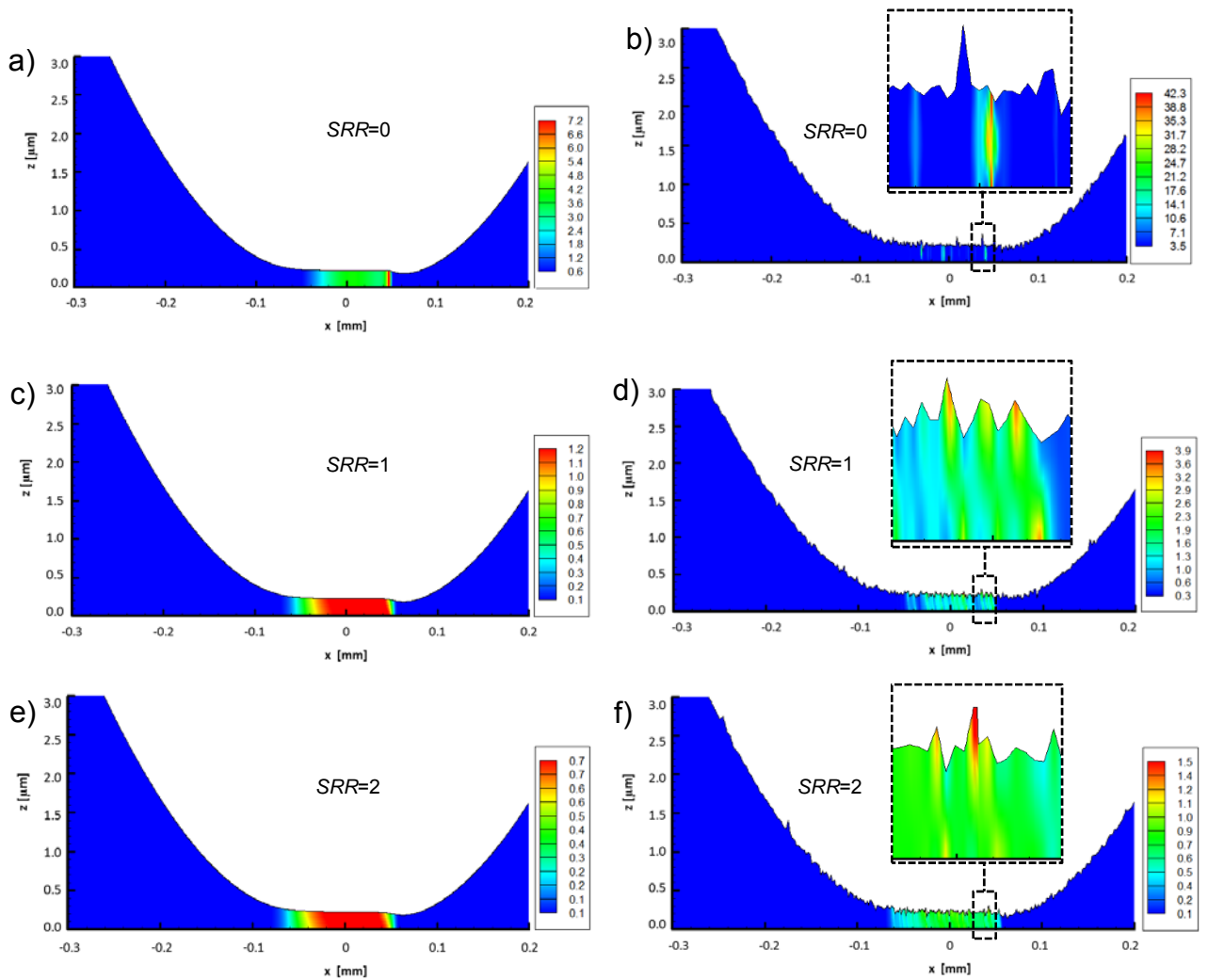


Figure 6-5: Effect of non-Newtonian fluid on viscosity (Pa·s) at $SRR = 0, 1$ and 2 for smooth (a, c and e) and rough (b, d and f) surfaces.

Figure 6-5a, Figure 6-5c, and Figure 6-5e show by colour iso-levels the viscosity of the lubricant at $SRR = 0$, 1 and 2 respectively. The Ree-Eyring model is used to estimate the value of the lubricant viscosity. The shear strain rate in the lubricant film is very significant in determining the viscosity value of the lubricant as the viscosity is decreased from 7.2 to 0.7 Pa·s when the SRR value is increased from 0 to 2. In addition to the SRR value, the surface roughness is also a significant factor affecting the value of viscosity. The viscosity of the lubricant under a rough surface, as shown in Figure 6-5b, is higher than that in Figure 6-5a by approximately 6 times. This is due to the pressure distribution that is more affected by the surface roughness under pure rolling conditions. In addition, the viscosity of the lubricant under a rough and smooth surfaces are decreased when the SRR value increases, as indicated in Figure 6-5e and Figure 6-5f. This is due to the effect of a surface roughness decreased when the angular velocity of the roller is reduced as shown in Figure 6-4.

The results of the simulation of the EHL line contact problem using the CFD model with the non-Newtonian fluid show that surface roughness significantly affects the pressure distribution and the lubricant viscosity. The results also show the effect of surface roughness is highest in the case of pure rolling conditions and that this effect decreases when the SRR value is increased. Therefore, it can be concluded that surface roughness and the shear strain rate in the lubricant film have a significant influence over the characteristics of the EHL problem.

However, it is not clear why the influence of the surface roughness will reduce when the SRR value is increased, as there are two transformed parameters when the SRR value is changed. These parameters are viscosity and velocity. Thus, the viscosity and velocity effects on the EHL line contact problem will be studied separately in the next sections. Additionally, the thermal effect caused by the shear strain rate term should be considered in the EHL problem as well.

6.3 Influence of lubricant viscosity

The behaviour of the EHL problem depends on the viscosity–pressure correlation, as the previous section showed that the non-Newtonian fluid viscosity is affected by the pressure distribution and by the film thickness. In addition, viscosity also influences the friction coefficient, as stated in equations (4.36) and (4.38). Therefore, the effect of different lubricant viscosities on the film thickness and pressure distribution in smooth and rough surface cases will be studied using the CFD model.

The roughness profile and the CFD model used in this section are the ones shown in Figure 3-22 and Figure 5-6 respectively, while the fluid and solid properties are listed in Table 5-1. The boundary conditions and the initial condition are identical to those in section 6.2 (Influence of non-Newtonian fluid). Three different lubricants are considered that differ only their values of viscosity at ambient condition (μ_0). Specifically, the viscosity of the lubricants at atmospheric conditions are 0.01 Pa·s, 0.05 Pa·s and 0.1 Pa·s. The pure rolling and isothermal conditions are applied to the CFD model.

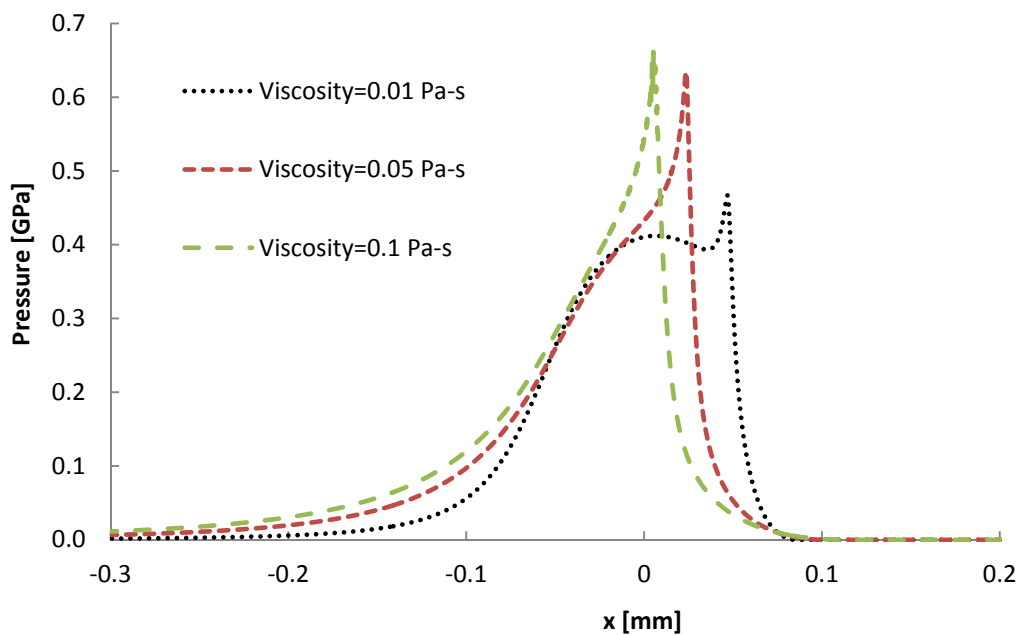


Figure 6-6: Effect of viscosity on pressure distribution (smooth surface).

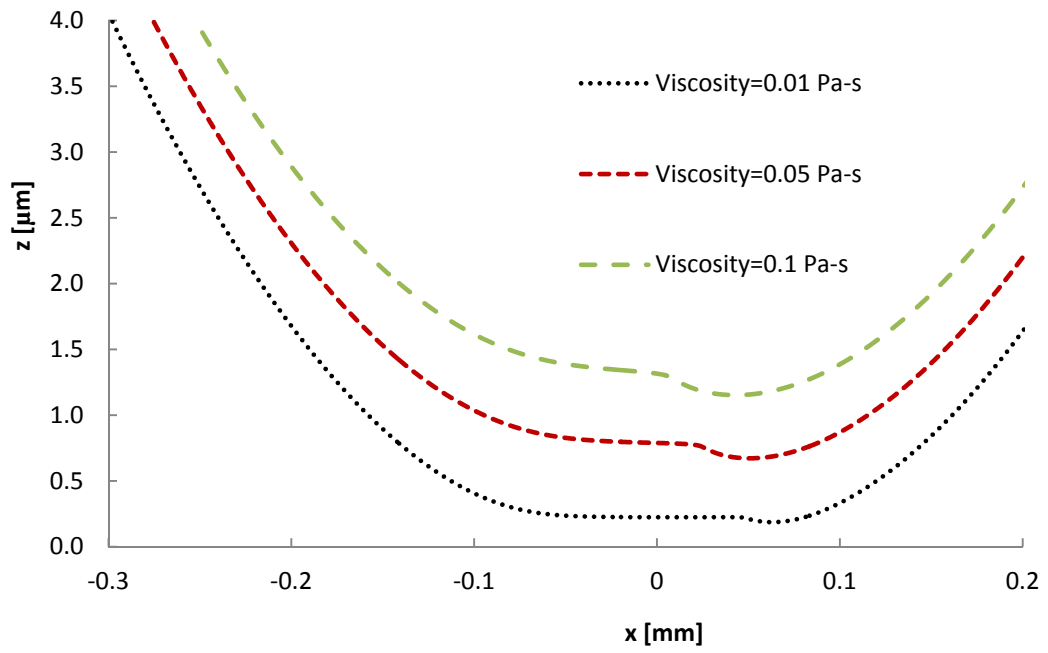


Figure 6-7: Effect of viscosity on film thickness (smooth surface).

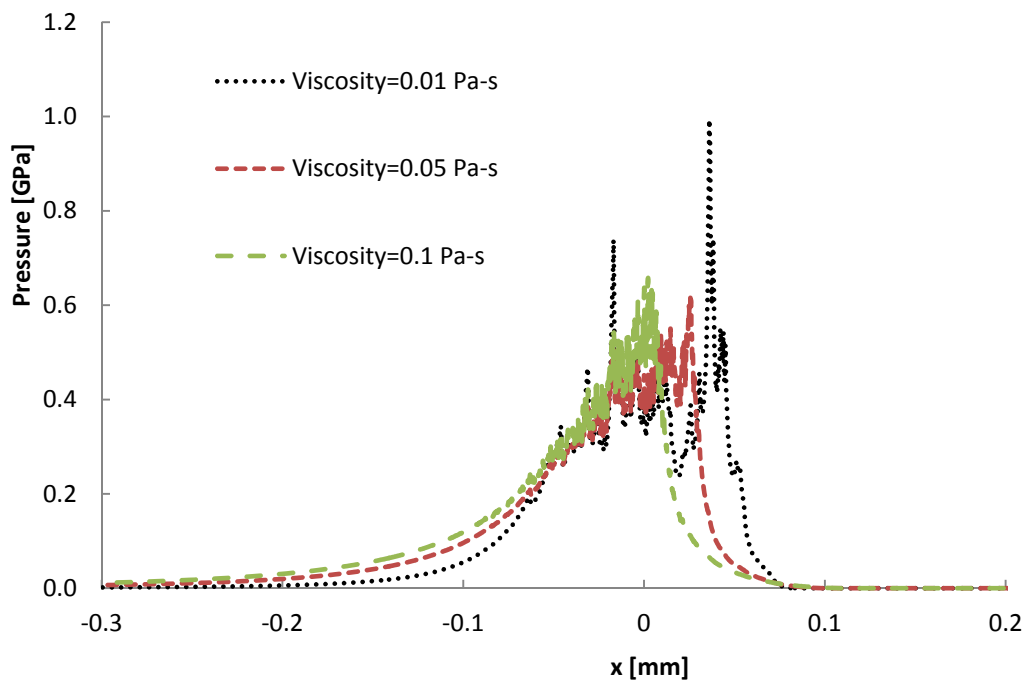


Figure 6-8: Effect of viscosity on pressure distribution (rough surface).

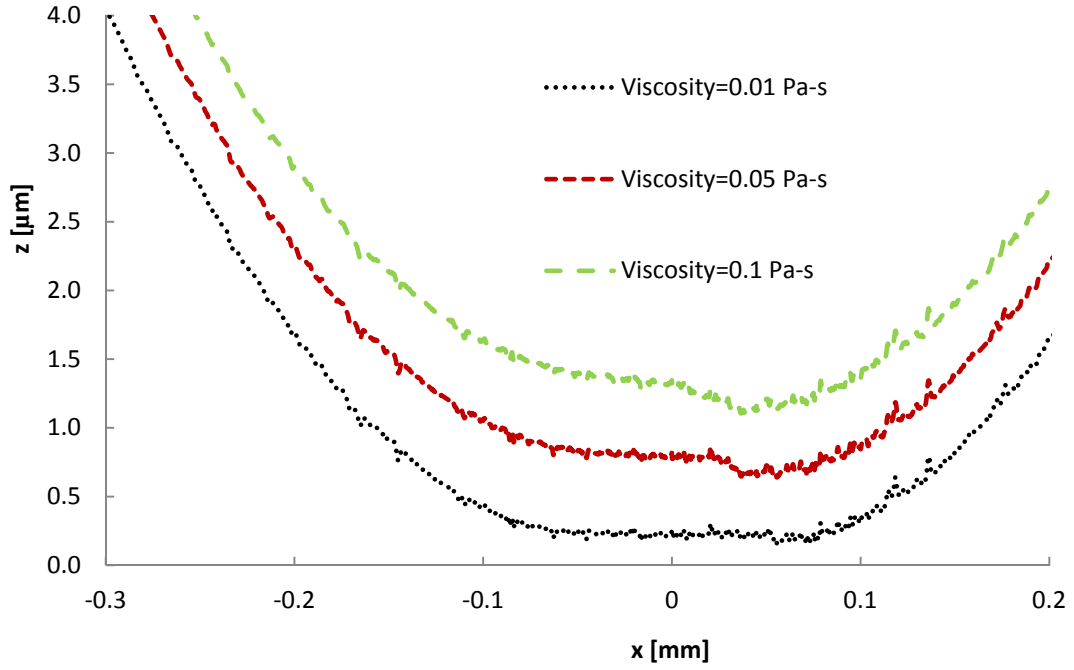


Figure 6-9: Effect of viscosity on pressure distribution (rough surface).

Figure 6-6 shows the pressure distributions when the viscosity values at atmospheric pressure (μ_0) are 0.01 Pa·s, 0.05 Pa·s and 0.1 Pa·s under a pure rolling condition and for a smooth surface EHL contact problem. It can be seen that the lubricant viscosity significantly affects the pressure distribution.

The shapes of the pressure distribution at $\mu_0 = 0.01$ Pa·s and 0.1 Pa·s are also different because the oil film is thinner at the lower viscosity. This phenomenon can be confirmed by the predicted film thickness of the lubricant as reported in Figure 6-7. The average oil film thickness is increased at 3.58% and 6.93% when the viscosity of lubricant is increased from $\mu_0 = 0.01$ Pa·s to 0.05 Pa·s and 0.1 Pa·s, respectively. In addition, the variation of the average oil film thickness is directly proportional to the viscosity at atmospheric pressure.

Furthermore, the viscosity also affects the friction coefficient: for $\mu_0 = 0.01$ Pa·s, 0.05 Pa·s and 0.1 Pa·s the corresponding friction coefficients are 0.0027, 0.0119, and 0.0211, respectively. It can be seen clearly that the friction coefficient is also directly proportional to the viscosity.

Figure 6-8 presents the influence of viscosity on the pressure distribution for the rough roller surface test case. The pressure fluctuation in the low viscosity case is higher than in the high viscosity case. This is due to the influence of the rough surface being reduced as the film thickness increases by using a more viscosity lubricant. In addition, it is found that the friction coefficient of the rough surface in the fluid film is higher than the one of a smooth surface, specially $\mu_f = 0.0152$, 0.0278 and 0.0373 for $\mu_0 = 0.01$, 0.05 and 0.1 Pa·s respectively. The influence of the surface roughness on the film thickness is similar to that of the smooth surface when viscosity is increased, as shown in Figure 6-9. It is found that the average oil film thickness of the surface roughness is slightly higher than that of smooth surfaces.

It can be concluded that the lubricant viscosity has a significant effect on the film thickness and pressure distribution. Film thickness will be increased when a more viscous lubricant is used at the same speed and applied load. The surface roughness effect on the pressure distribution is reduced when a more viscous lubricant is used.

6.4 Influence of surface speed

The prediction of the EHL problem in section 6.2 for a non-Newtonian fluid shows the effect of the *SRR* in combination with surface roughness. The influence of the surface roughness on the lubricant viscosity under pure rolling conditions (*SRR* = 0) is higher than in pure sliding conditions (*SRR* = 2). Therefore, the influence of the velocity of the moving surfaces on the EHL problem will be investigated using the CFD model. All parameters and boundary conditions are kept identical to the one used in section 6.2, except for the angular velocity of the roller and the plate velocities. The roller rotation velocity is set at 200 rad/s, 300 rad/s, and 400 rad/s, while the plate is stationary.

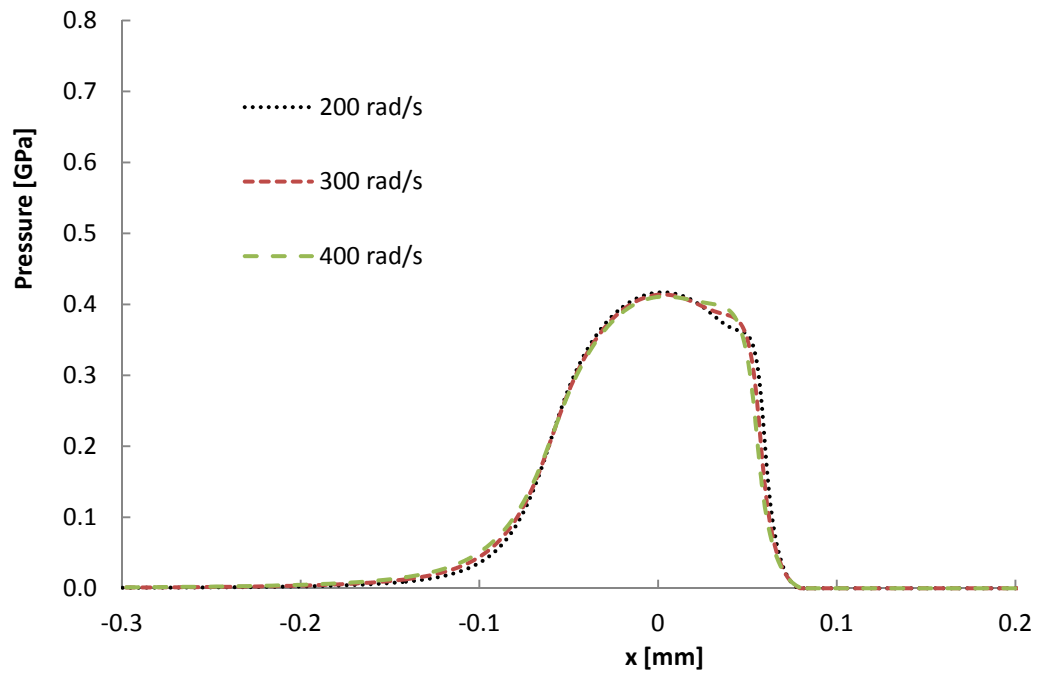


Figure 6-10: Effect of velocity on pressure distribution (smooth surface).

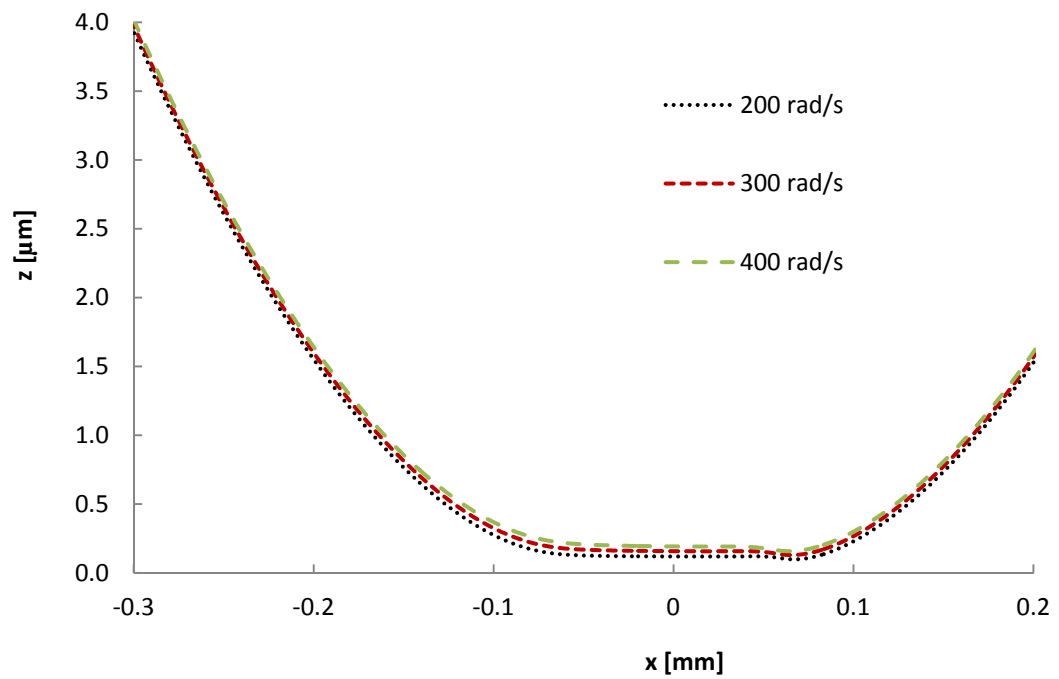


Figure 6-11: Effect of velocity on film thickness (smooth surface).

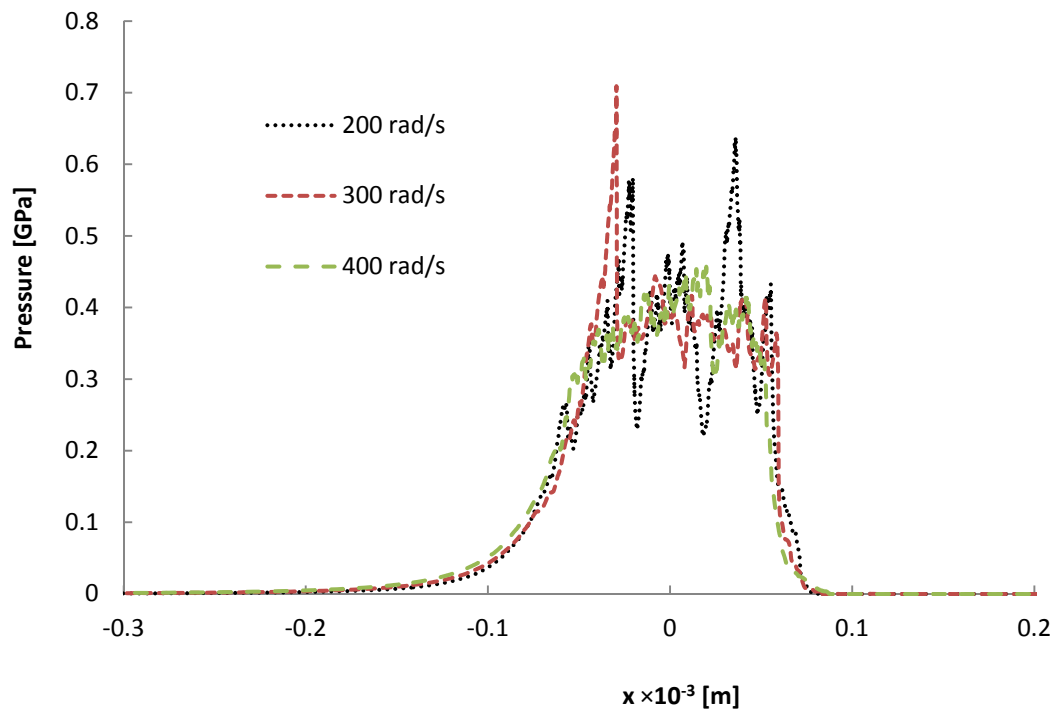


Figure 6-12: Effect of velocity on pressure distribution (rough surface).

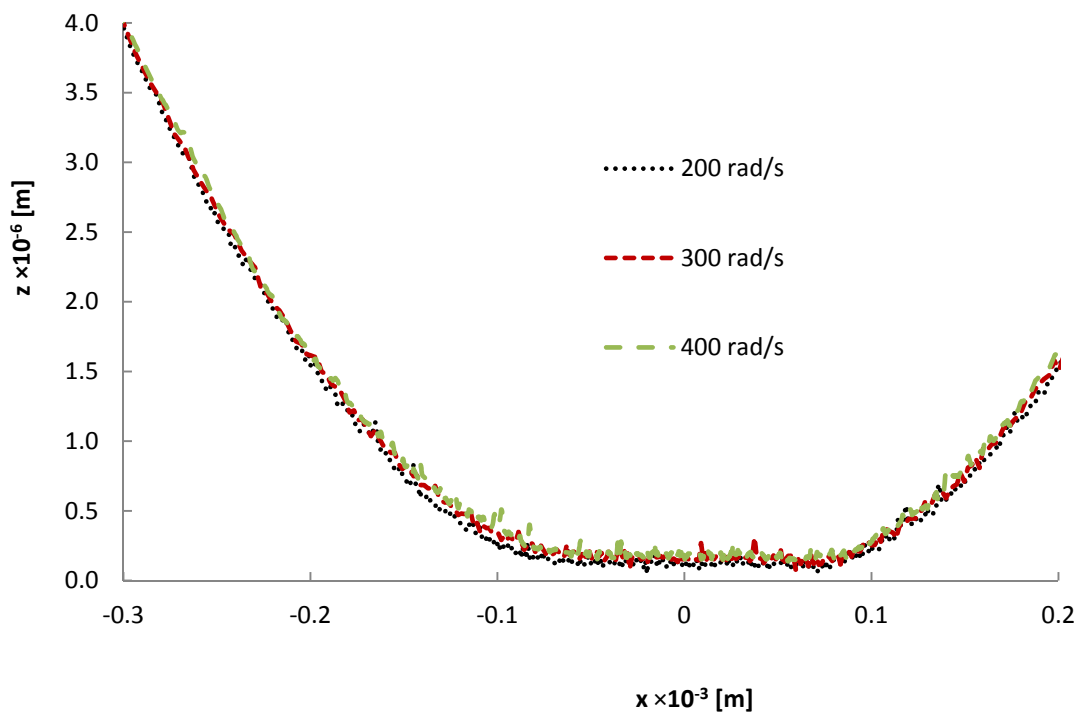


Figure 6-13: Effect of velocity on film thickness (rough surface).

Figure 6-10 and Figure 6-11 illustrate the effect of velocity on the pressure distribution and on the oil film thickness respectively, using the CFD model with smooth roller and plate surfaces. Figure 6-11 shows that the oil film thickness is increased as the velocity increases. The increment of the minimum oil film thickness is about 21.04% and 91.11% when the angular velocity of the roller is increased from 200 rpm to 300 rpm and 400 rpm respectively. This increasing trend was also present in the experimental results of Krupka et al. [145].

Once surface roughness is applied to the surface of the roller, the trends of the pressure distribution and oil film thickness, when the angular velocity of the roller increases, are predicted to be similar to the ones for a smooth surface. Figure 6-13 shows that the average oil film thickness is increased by 0.28% and 0.47% when the angular velocity of the roller is increased from 200 rpm to 300 rpm and 400 rpm, respectively. Figure 6-12 shows the surface roughness effect on pressure distribution. The influence of the surface roughness on the pressure fluctuation is reduced when the angular velocity of the roller is increased. This effect relates to the increment in the oil film thickness with increased angular velocity, which is shown in Figure 6-13. Furthermore, it is found that the oil film thickness of the surface roughness case is slightly higher than that of the smooth surface case.

The results from this study clearly show that the velocity of the solid parts plays an important role in determining the oil film thickness, and that increasing the velocity of the solid parts reduces roughness effect. The latter is explained by the change in the oil film thickness. Thus, it can be confirmed that the influence of surface roughness on the EHL problem depends primarily on the oil film thickness.

6.5 Influence of the normal load

Typically, bearing damage can be due to several factors. One of them is overload, which will be investigated using the CFD model in this section. A CFD model geometry and lubricant parameters identical to the ones in section 4 will be used in this section. However, the applied load per unit span will be changed from 50 kN/m to 200 kN/m. In addition, the lubricant is considered to be a non-Newtonian fluid. The properties of the lubricant (viscosity and density) depend on pressure only by equation (2.37) and (2.38). In order to avoid the effect of the shear forces that occur in a sliding contact configuration, the pure rolling contact condition only is implemented in this section.

Figure 6-14 and Figure 6-15 present the influence of applied loads on the pressure distribution and the oil film thickness build-up for the smooth surface contact configuration. From the simulation, the average pressure in the Hertzian zone is predicted to increase by 93.50%, 181.35% and 264.60% as the applied load per unit span is increased from 50 kN/m to 100 kN/m, 150 kN/m and 200 kN/m, respectively. At the same time, the average oil film thickness is reduced by 1.86%, 3.30%, and 4.47%, respectively. The trends of the applied load effect on the behaviour of the EHL line contact using the CFD model are in good agreement with the experimental results of Fu and Guo [146] and Ivan [147]. The influence of the applied load on the oil film thickness is very low, but the effect on the deformation of the roller in the range $-0.1 \mu\text{m} \leq x \leq 0.1 \mu\text{m}$ is greater, as indicated in Figure 6-15 that shows a noticeable growth of the roller flattened area in x with increasing load.

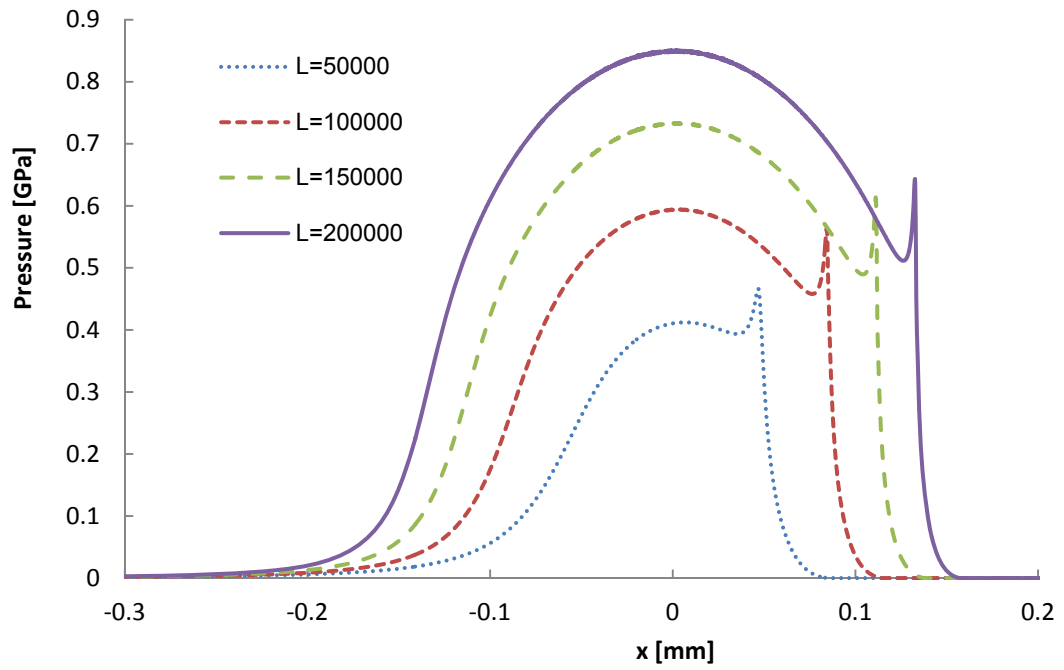


Figure 6-14: Effect of loads (N/m) on pressure distribution (smooth surface).

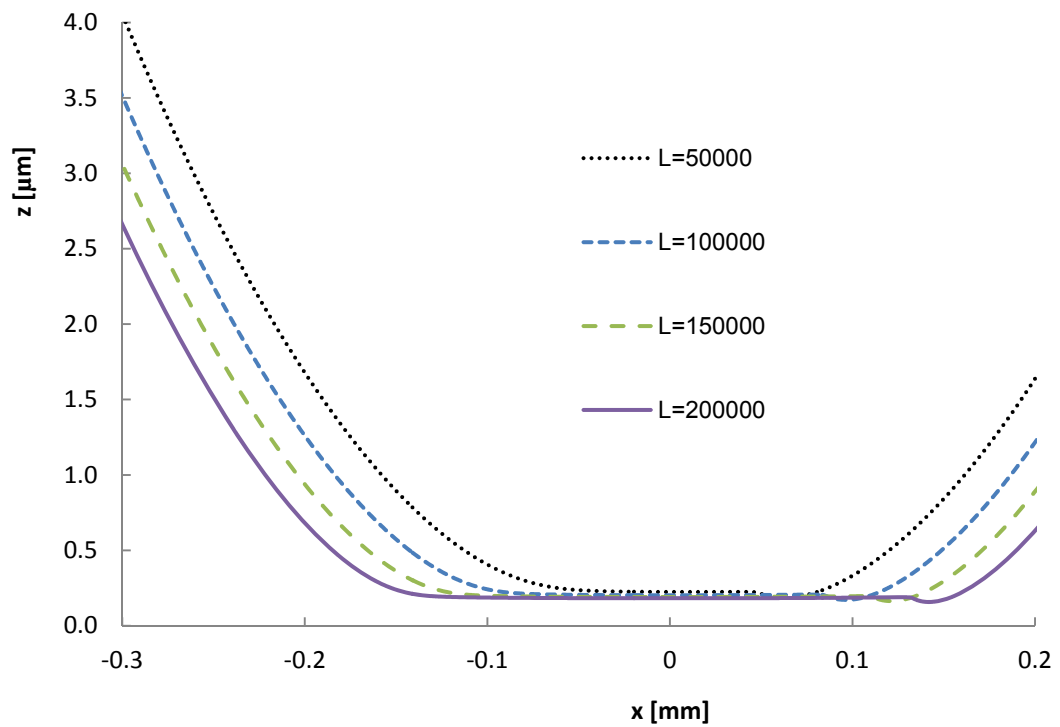


Figure 6-15: Effect of loads (N/m) on oil film thickness (smooth surface).

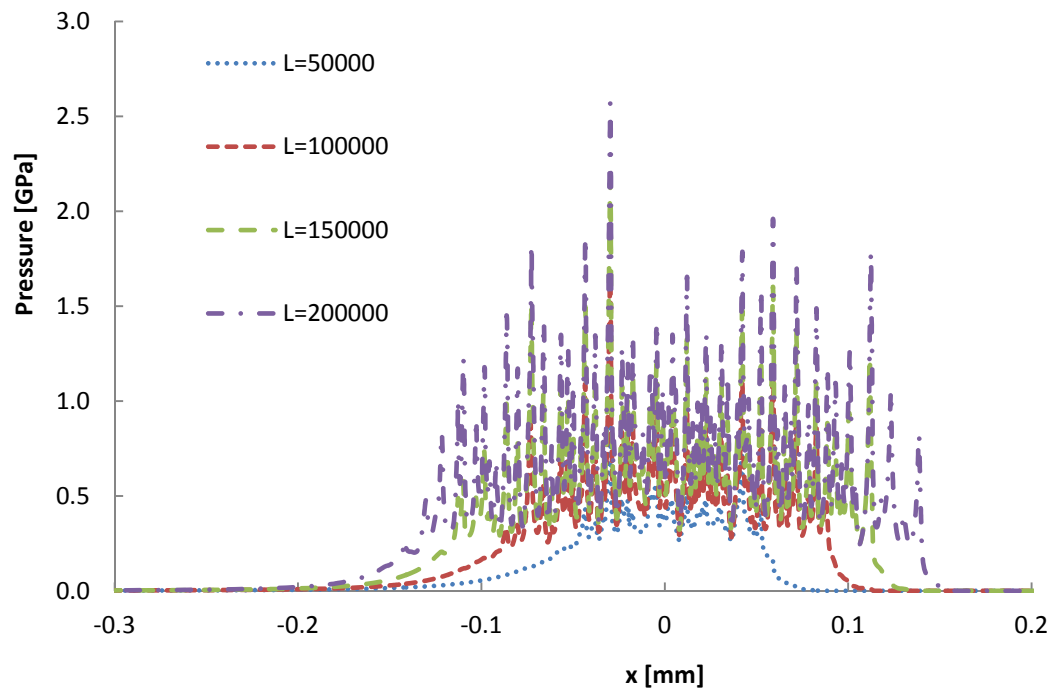


Figure 6-16: Effect of loads (N/m) on pressure distribution (rough surface).

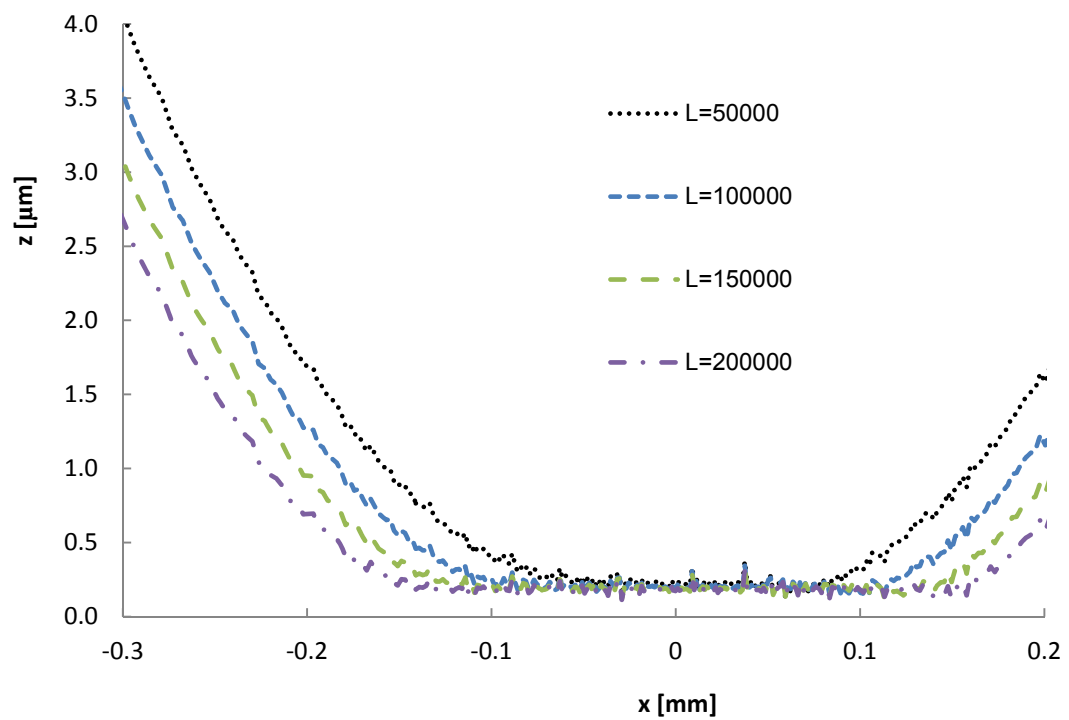


Figure 6-17: Effect of loads (N/m) on oil film thickness (rough surface).

Figure 6-16 and Figure 6-17 show the influence of the surface roughness on the EHL line contact problem when the applied load is increased. The pressure distribution fluctuation amplitude increases as the applied load increases. The average oil film thickness is reduced by 1.88%, 3.29% and 4.47% when the applied load is increased from 50 kN/m to 100 kN/m, 150 kN/m and 200 kN/m respectively. In addition, it is found that the film thickness of the surface roughness cases is slightly higher than those of the smooth surface cases.

It can be concluded that the applied load per unite span significantly affects the pressure distribution and the deformation of the roller. The influence of the surface roughness on the pressure distribution at a high applied load is higher than in the corresponding low load cases.

6.6 Influence of material properties

Thin film bearings can be produced from many material types. The bearings are designed to work in various conditions; for example, a ceramic bearing can be used at both high speeds and high operating temperatures [148]. As such, the effect of the materials type on the characteristics of the EHL line contact problem with respect to surface roughness will be examined in this section using the CFD model.

Traditionally, the effective elastic modulus parameter has been used to represent the modulus of elasticity of the roller and the plate when the EHL problem is solved by the Reynolds equation. The aim of this section is to investigate the characteristics of the EHL line contact problem using the effective elastic modulus to calculate the deformation in the solid parts from the film thickness equation. Model 1 in Table 5-4 will be used in this section. The deformations of the cylinder and the plate are considered in the deformation term of the film thickness equation. In addition, the surface roughness profiles from Figure 3-22b and from Figure 3-18b, which are imposed on the surface of the cylinder and the plate respectively, are also included in the film thickness

equation. The material properties of the cylinder and the plate used in this study are listed in Table 6-1.

Table 6-1: Properties of materials [149, 150]

Material	E (GPa)	ν	C_p (J/ (kg·K))	ρ (kg/m ³)	k (W/(m·K))
Steel	210	0.30	460	7850	47
Brass	130	0.33	380	8450	125
Ceramic	450	0.15	1050	3800	29

In this study, the isothermal condition is applied to the CFD model. The lubricant viscosity is considered to be a non-Newtonian fluid behaviour according to the Ree-Eyring model. The contact between the roller and the plate is defined as a pure rolling ($SRR = 0$). Four different material combinations for the roller and the plate are investigated, as described in Table 6-2.

Table 6-2: The materials of the top and bottom rollers

Cases	Materials	
	Top roller	Bottom plate
1	Brass	Iron
2	Iron	Iron
3	Iron	Ceramic
4	Brass	Ceramic

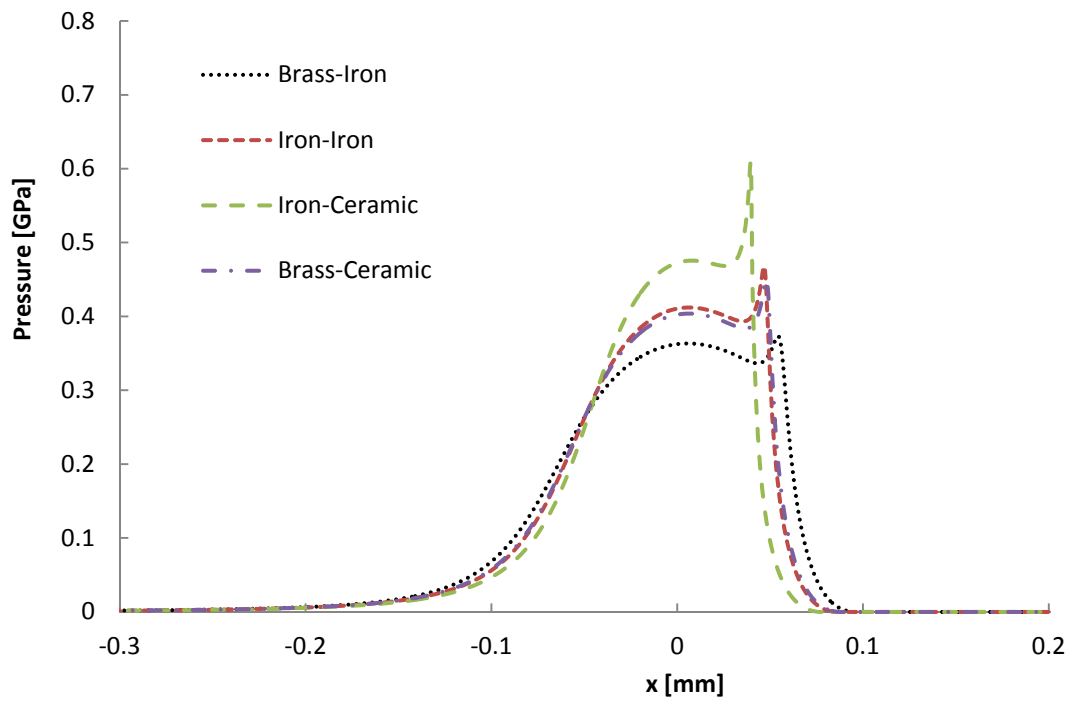


Figure 6-18: Effect of material properties on the pressure distribution (smooth surfaces).

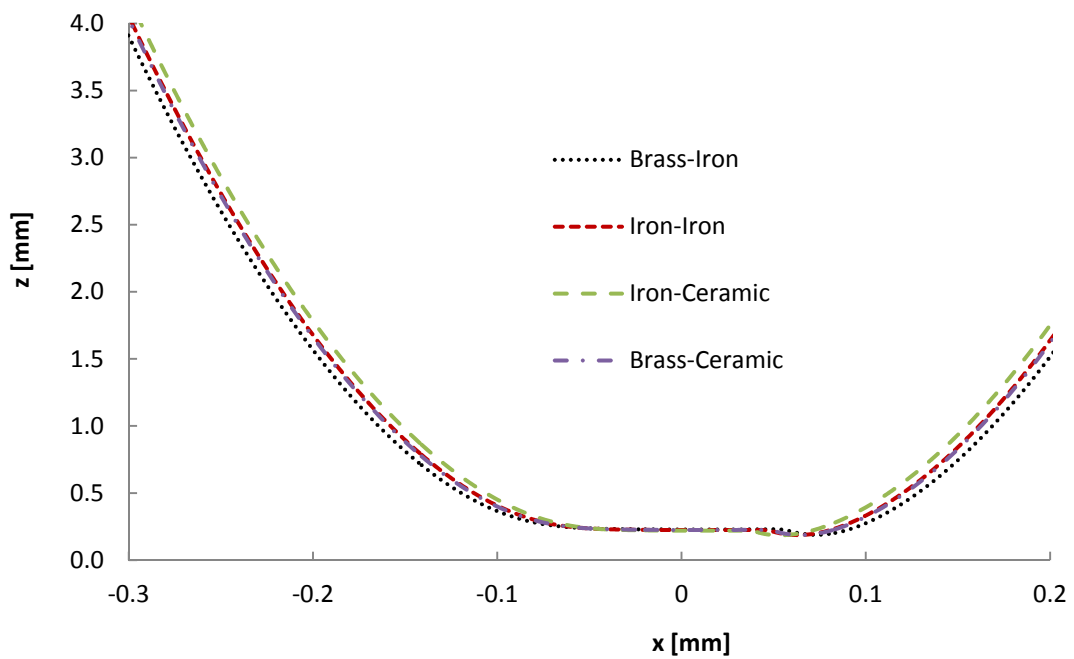


Figure 6-19: Effect of material properties on the film thickness (smooth surfaces).

Figure 6-18 shows the effect of different materials on the EHL line contact problem for smooth surfaces according to model 1. It is found that the influence of different materials on the pressure distribution trend from the CFD model is similar to the one in the experimental results of Sperrfechter and Haller [151]. It can be noticed that the pressure values from the contact between materials of low hardness (brass-iron) in Figure 6-18 are lower than the corresponding values from the contact of materials of high hardness (iron-ceramic), but the width of the pressure distribution in the case of the brass-iron contact is larger as shown in Figure 6-19. This can be confirmed by the film shapes of the contact between brass and iron and the contact between iron and ceramic, as shown in Figure 6-19. The average oil film thicknesses for brass–iron, iron–iron, iron–ceramic, and brass–ceramic contacts are $16.00\text{ }\mu\text{m}$, $16.09\text{ }\mu\text{m}$, $16.16\text{ }\mu\text{m}$ and $16.07\text{ }\mu\text{m}$, respectively.

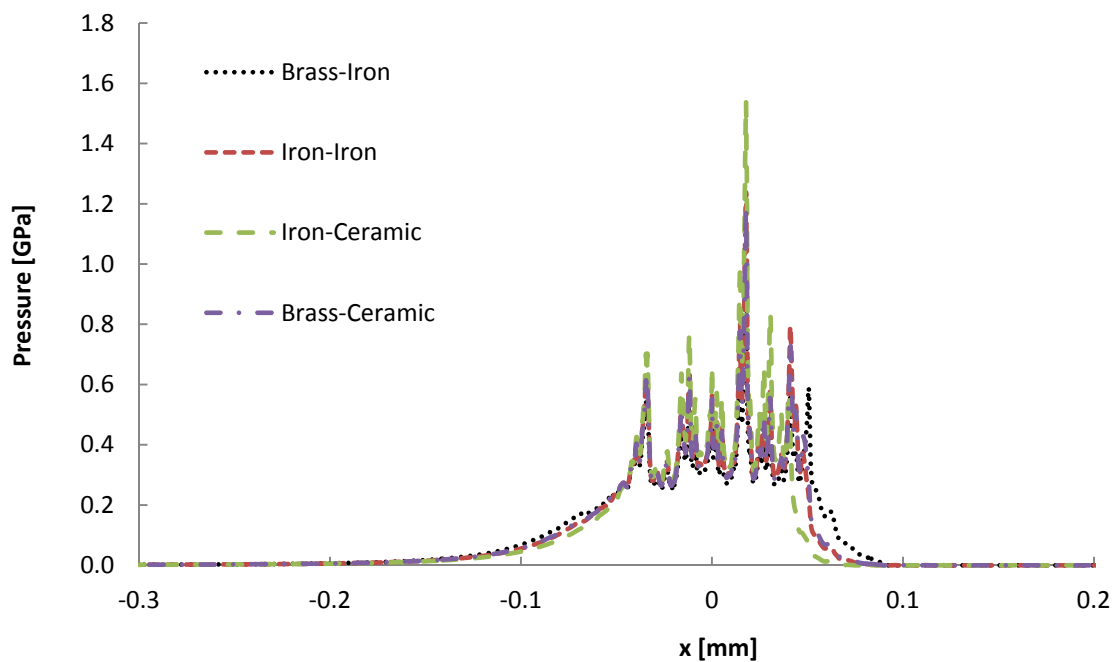


Figure 6-20: Effect of material properties on the pressure distribution (rough surfaces).

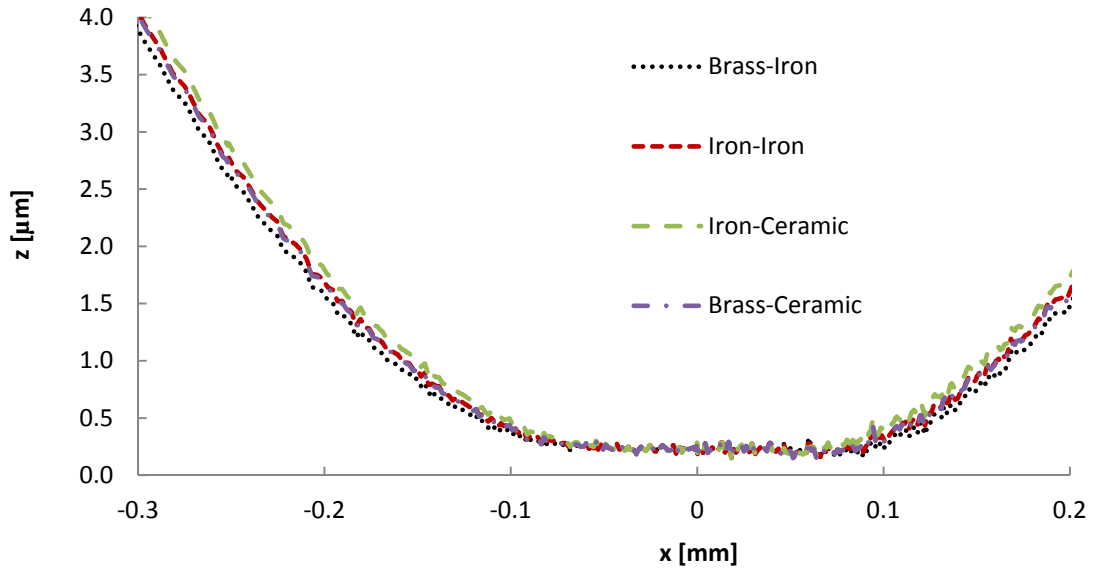


Figure 6-21: Effect of material properties on the film thickness (rough surfaces).

Figure 6-20 shows the surface roughness effect on the pressure distribution in the oil film for different combinations of roller and plate materials. Pressure is fluctuates. The highest pressure is observed in the contact case between iron and ceramic around 1.6 GPa, which is higher than their smooth surface contact pressure peak, which is at around 0.9 GPa. According to the oil film thickness presented in Figure 6-21, the contact between materials of low hardness materials is more deformed than the contact surface profile between materials of high hardness, similar to the smooth contact case presented in Figure 6-19. The average oil film thickness for the contact between iron and ceramic (minimum deformation) is at around $16.17 \mu\text{m}$, while it is only $16.01 \mu\text{m}$ in the contact between brass and iron (maximum deformation).

6.7 Thermal effects

The aim of this section is to investigate the influence of temperature on the characteristics of the EHL problem by using the CFD model with surface roughness. The Ree-Eyring model, which is the viscosity model for the non-Newtonian fluid, is used to represent the effect of pressure and temperature rise on the lubricant viscosity. The temperature rise effect is also included in the density equation as presented in equation (2.39). The conservation equations

(momentum, continuity and energy equations) are implemented to compute the velocity field, pressure, density, and temperature rise in the fluid film in this study.

The CFD model of Figure 5-6 will be employed to investigate the influence of surface roughness on the TEHL problem. The input data and the properties of the lubricant and the solids used are listed in Table 6-3. In order to study the thermal effect on the TEHL problem, the slide to roll ratio will be varied, as the velocity gradient affects the heat generated in the fluid film. In the sliding contact case, the velocity difference between roller and plate will produce a shear force in the lubricant film and generate heat via the viscous shear stress. In addition, the heat generated by the compression force in the lubricant is also considered in the CFD model. From the previous section, it can be seen that film thickness at the contact region is very thin ($<0.5 \mu\text{m}$). Therefore, the heat convection across the film thickness and the heat conduction alongside the film thickness can be neglected in this study.

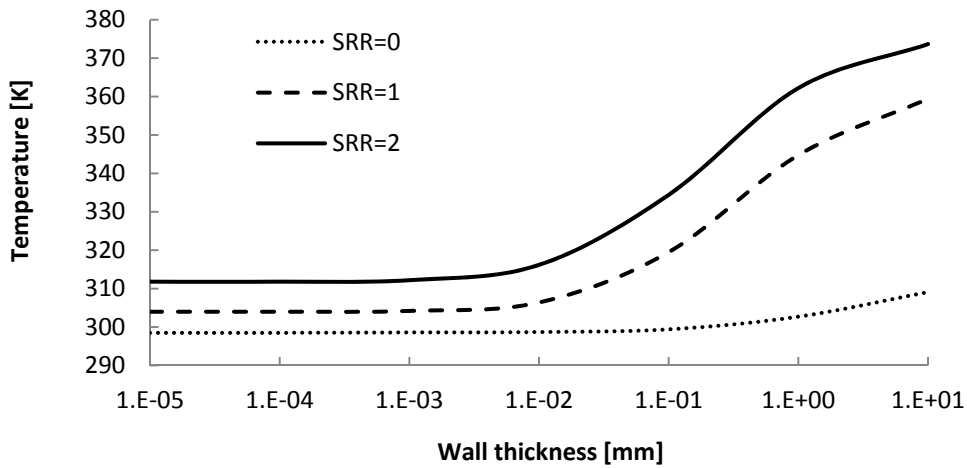


Figure 6-22: Maximum temperature when wall thickness is increased.

In continuum mechanics, heat transfers from a high temperature region to a low temperature region by a combination of conduction, convection and radiation. In the present study, the heat generated by the compression force and shear force in the lubricant is transferred from the lubricant to the roller and plate mainly by conduction. The top roller and bottom plate surfaces are considered to be solid

walls. The temperatures at the wall boundaries are imposed as equal to an ambient temperature of 298.15 K. Thus, the thermal capacitance of the walls is assumed to be sufficiently high to absorb the heat transferred from the fluid without significantly changing the wall surface temperature. This assumption is appropriate for modelling the flow during the start-up of a cold-started bearing.

Table 6-3: Common parameters

Parameters	Value	Unit
Input data		
An applied load, w	50,000	N/m
Average velocity, u_m	2.50	m/s
Roller's radius, R_c	10	mm
Surface roughness, R_a	0.0275	μm
Ambient temperature, T_0	298.15	K
Solid properties (roller and plate)		
Elastic modulus, E	210	GPa
Poisson's ratio, ν	0.30	-
Specific heat, C_p	460	J/kg·K
Density, ρ	7,850	kg/m ³
Thermal conductivity, k	47	W/(m·K)
Lubricant properties		
Inlet viscosity, μ_0	0.01	Pa·s
Vapour dynamic viscosity, μ_v	8.97×10^{-6}	Pa·s
Liquid density, ρ_l	850.0	kg/m ³
Vapour density, ρ_v	0.0288	kg/m ³
Inlet temperature, T_0	313.0	K
Thermal conductivity, k_f	0.15	W/(m·K)
Temperature-viscosity coefficient, β	6.45×10^{-4}	1/K
Specific heat capacity, C_p	2,300	J/(kg·K)
Thermal expansivity, ε	4.50×10^{-4}	1/K
Pressure-viscosity index, z	0.689	-

Figure 6-22 shows the correlation between wall thickness and maximum temperature rise at the lubricant. It can be seen that the temperature rises rapidly when the wall thickness is over 0.01 mm for $SRR = 1$ and 2. The temperature of the lubricant rises because the shear strain rate increases with higher SRR . Therefore, a wall thickness of 0.001 mm is chosen as the default value in order to study the effect of surface roughness on the thermo-elastohydrodynamic lubrication (TEHL) line contact problem in the present study.

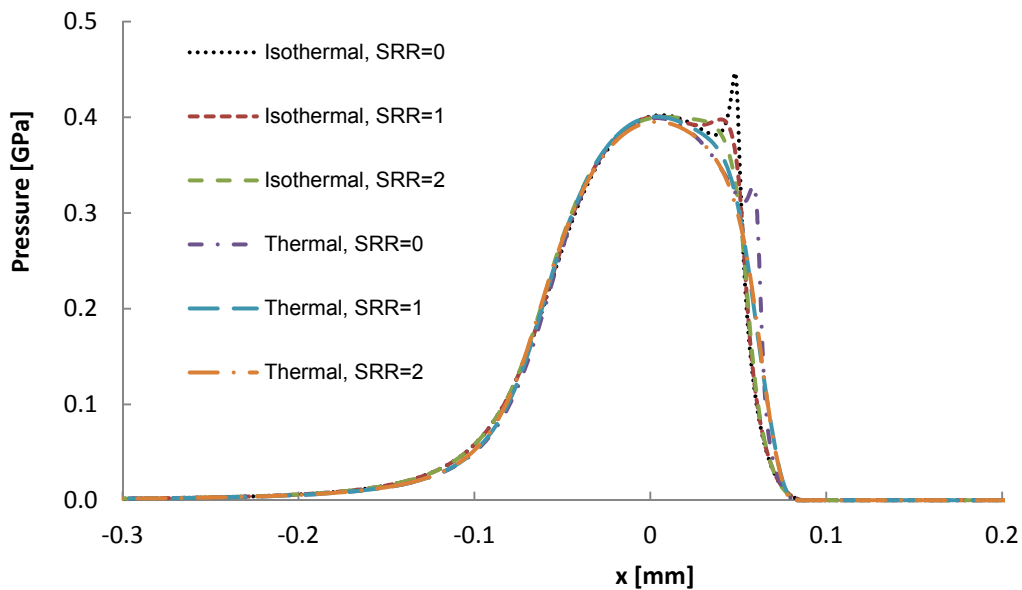


Figure 6-23: Comparison of pressure distributions at $SRR = 0, 1$ and 2 between the isothermal and thermal cases (smooth surfaces).

Figure 6-23 and Figure 6-24 show the results of the TEHL line contact problem with the smooth contact. The thermal effect plays an important role in the characteristics of the EHL problem. The pressure spike of the isothermal case is higher than its thermal equivalent, as shown in Figure 6-23, especially at the condition of pure rolling contact ($SRR = 0$). Figure 6-24 presents the oil film thickness of the thermal and isothermal cases with $SRR = 0, 1$, and 2 . The average oil film thickness with $SRR = 0, 1$, and 2 for the isothermal and the thermal cases are (16.0870 μm , 16.0874 μm , 16.0873 μm) and (16.0258 μm , 15.9254 μm , 15.3525 μm). It can be seen that the average oil film thickness of

the thermal cases is thinner than that of the isothermal ones. This is due to the fact that the lubricant viscosity of the thermal case is lower than in the isothermal case, especially under pure sliding contact conditions.

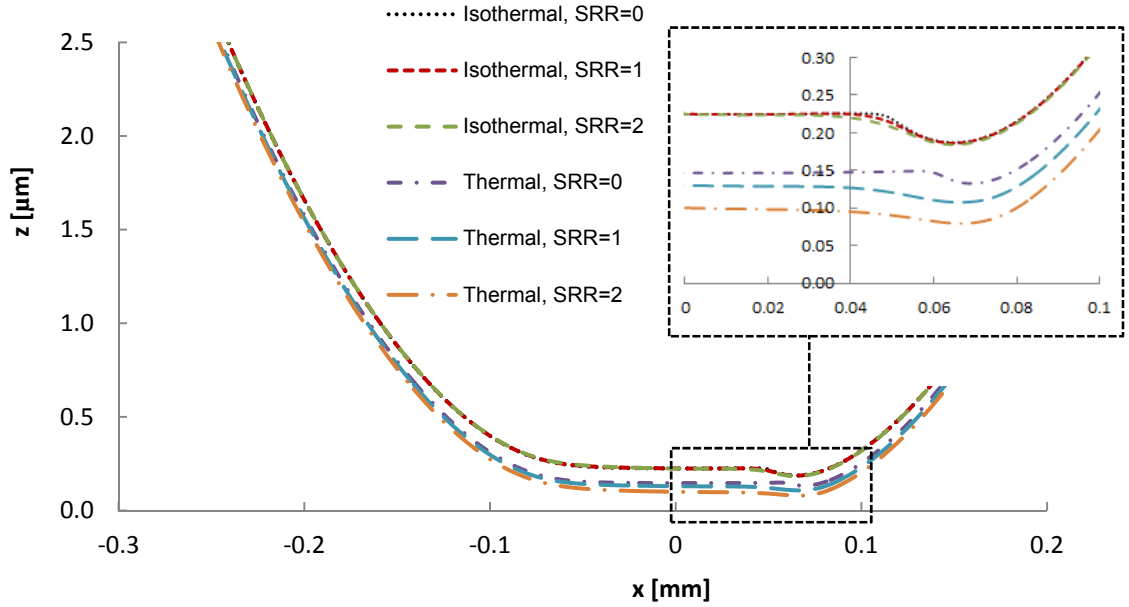


Figure 6-24: Comparison of film thicknesses at $SRR = 0, 1$ and 2 between the isothermal and thermal cases (smooth surfaces).

In the previous section, it was shown that the pressure distribution generated in the lubricant film is inversely proportional to viscosity. Figure 6-25a, Figure 6-25c, and Figure 6-25d show the iso-levels of the temperature rises in the EHL line contact problem at $SRR = 0, 1$ and 2 for smooth surfaces. The temperature rise with the SRR value as a result of the increasing shear force, which is directly proportional to the SRR . The maximum temperatures for $SRR = 0, 1$ and 2 are 298.3 K, 303.9 K and 311.6 K respectively. This means that the influence of the compression force on the heat generated is lower than the shear force as the temperature rise in pure rolling contact conditions is only 298.3 K.

In addition, surface roughness also affects the rise in temperature. Figure 6-25b, Figure 6-25d and Figure 6-25f show the temperature rise from modelling a rough roller surface at $SRR = 0, 1$ and 2 , respectively. The temperature increase in the rough surface case is predicted to be higher than in the smooth

surface case. The effects of surface roughness on the pressure distribution and the oil film thickness are shown in Figure 6-26 and Figure 6-27 to be similar to the results shown in section 5.4. However, the influence of the surface roughness on the pressure distribution in the thermal case is higher than in the isothermal case, as the maximum pressure in Figure 6-26 is higher than that in Figure 6-4 by about 0.1 GPa.

Figure 6-27 shows the thermal effect on the oil film thickness predicted by the CFD model with the rough surface roller. It is found that the average film thickness slightly decreases when SRR is increased. This is due to the effect of temperature on the decreasing of the viscosity and density of lubricant.

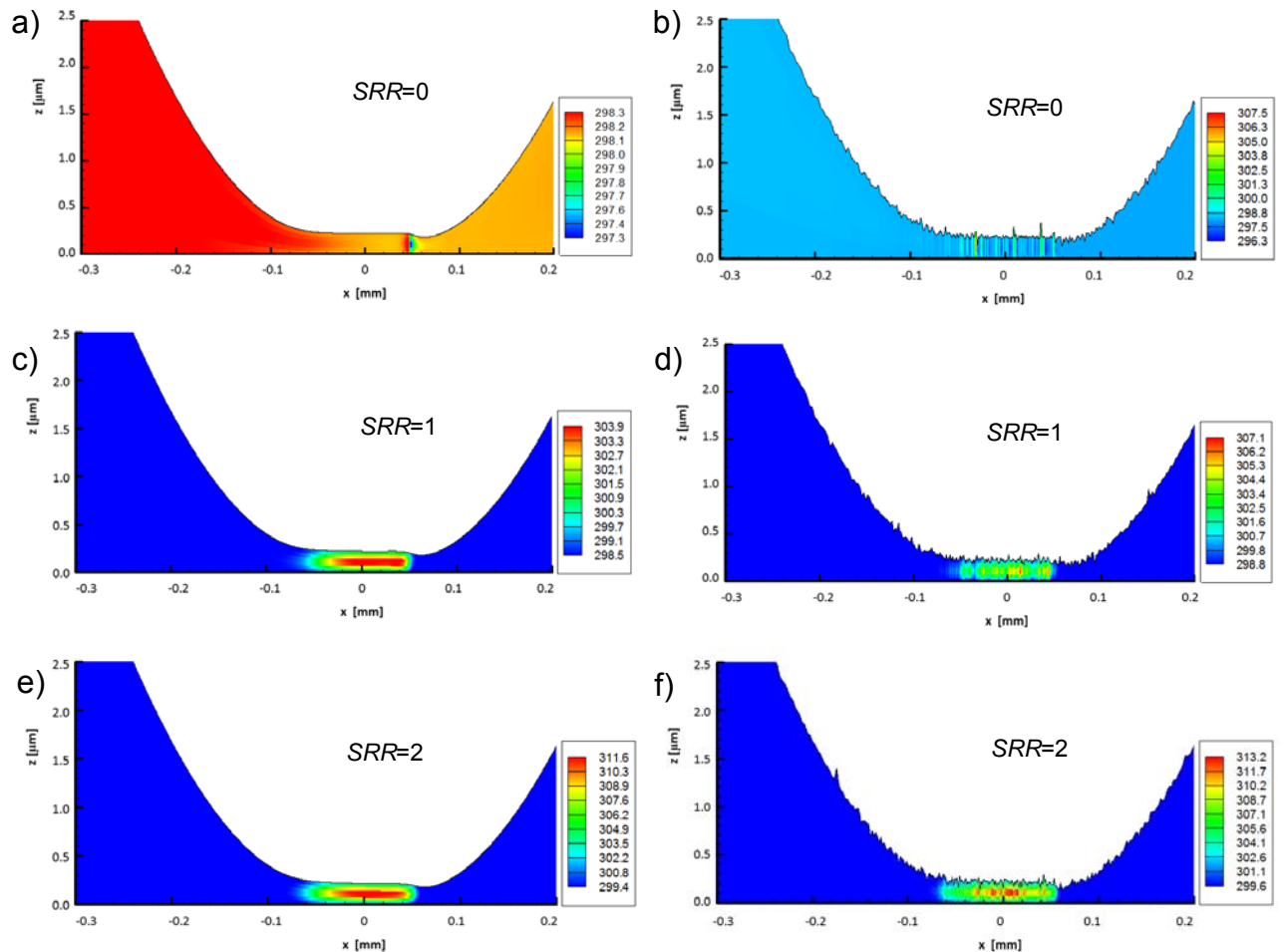


Figure 6-25: Effect of surface roughness on iso-levels of temperature (K) at $SRR = 0, 1$ and 2 (Left: smooth surface; Right: rough surface).

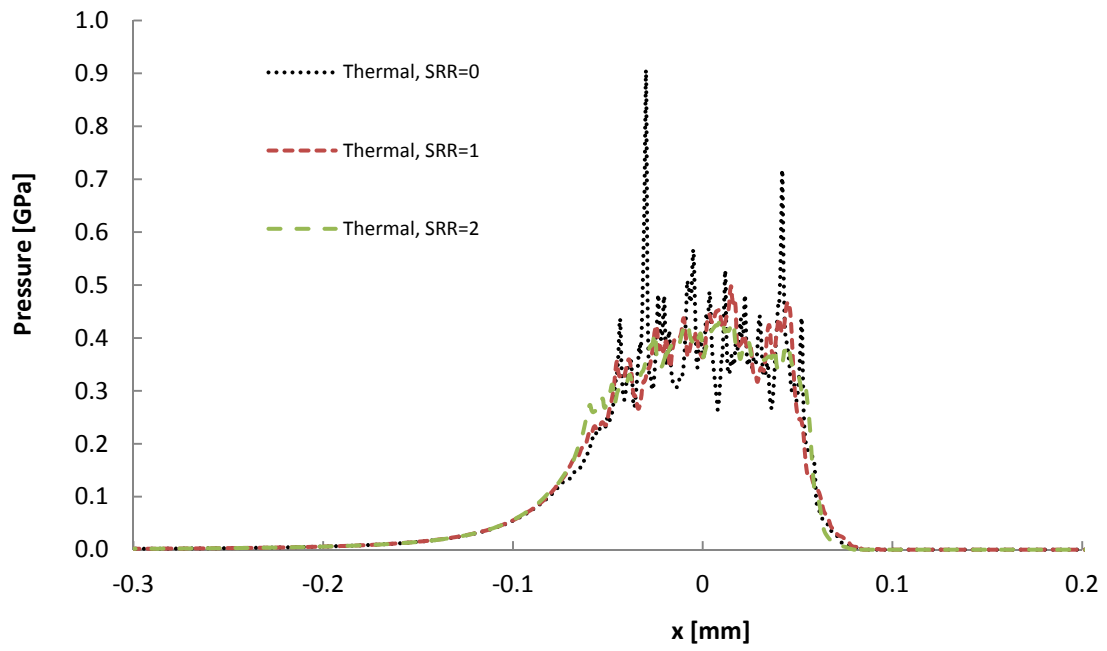


Figure 6-26: Effect of surface roughness on pressure distribution at $SRR = 0, 1$ and 2.

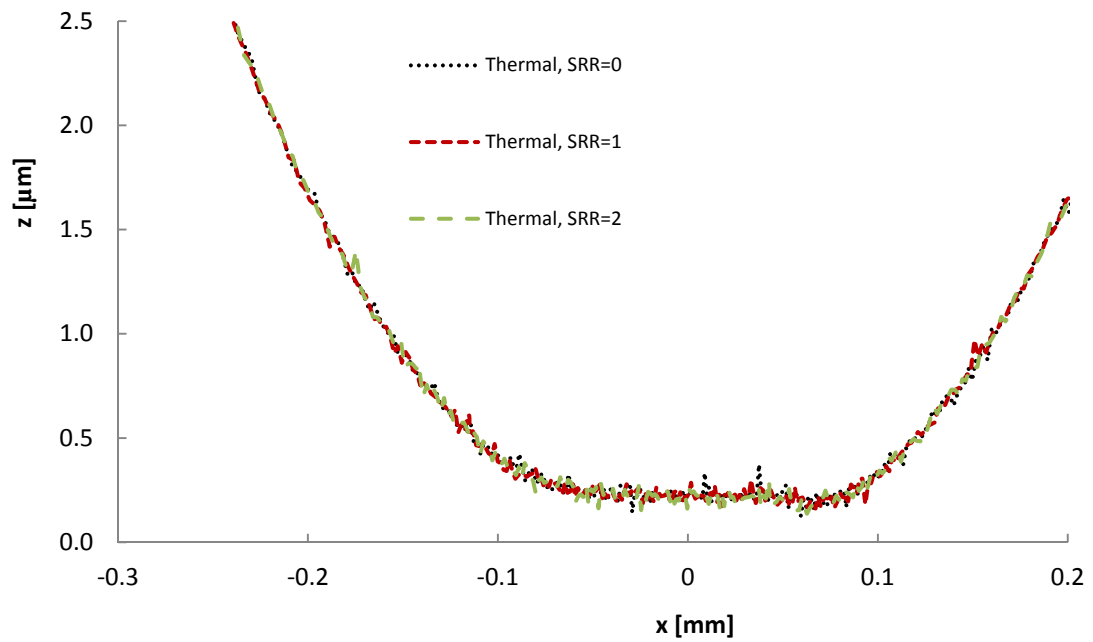


Figure 6-27: Effect of surface roughness on film thickness at $SRR = 0, 1$ and 2.

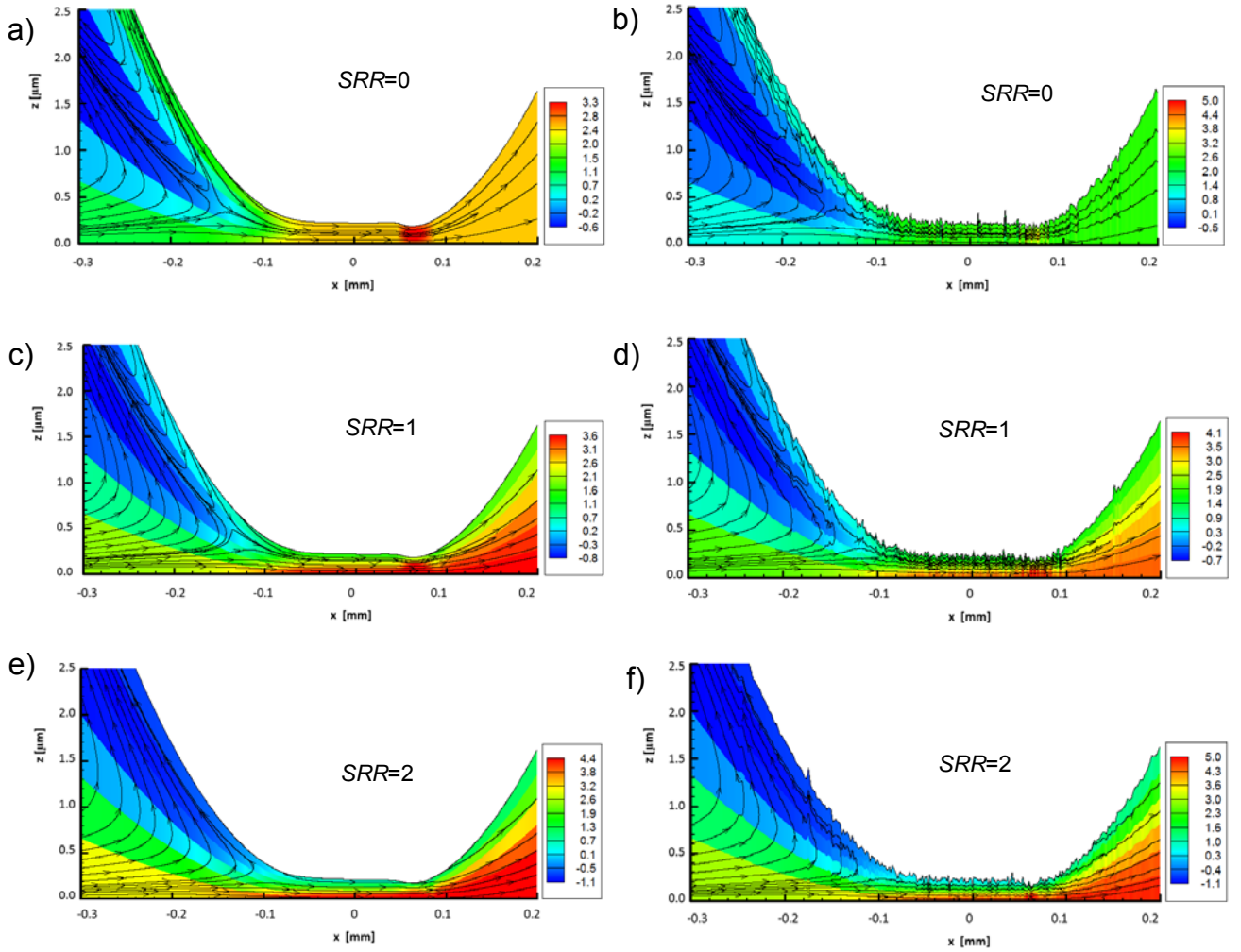


Figure 6-28: Effect of surface roughness on velocity magnitude iso-levels (m/s) at $SRR = 0, 1$ and 2 (Left: smooth surface; Right: rough surface).

Figure 6-28 presents the iso-levels of the velocity magnitude of the lubricant flow with smooth and rough surfaces at $SRR = 0, 1$ and 2 . These results explain why the pressure distribution fluctuates as shown in Figure 6-26. It can be seen that the velocity magnitude in the pure rolling case (Figure 6-28b) is higher along the roller surface as the rough profile on the roller surface is moving at 2.5 m/s faster than under pure sliding contact conditions (Figure 6-28f) where the roller is stationary. The transported flow mass in the crevices of the roller rough surface is therefore expected to be higher in the pure rolling case than when the roller is stationary. This creates an effect similar to a general pump by which the addition of fluid mass by the rotating teeth generates pressure pulses at the tooth passing frequency. In this case, the positive displacement of lubricant fluid

by the surface roughness crevices causes localised pressure fluctuations. This phenomenon is easily explained with reference to the conservation of momentum in the frame of reference of the roller surface. Ignoring viscous effects $\frac{D}{Dt}\mathbf{U} + \nabla p = 0$. Therefore, the combination of surface motion in the material operator and of the non-uniform velocity \mathbf{U} cause the observed fluctuations in pressure. In the model where the roller is stationary Figure 6-28f shows that the predicted velocity magnitude is higher than in the model with a pure rolling contact. The velocity peaks close to the smooth surface flat plate. This reduces the occurrence of pressure fluctuations due to the smooth of the surface over which the lubricant flows faster.

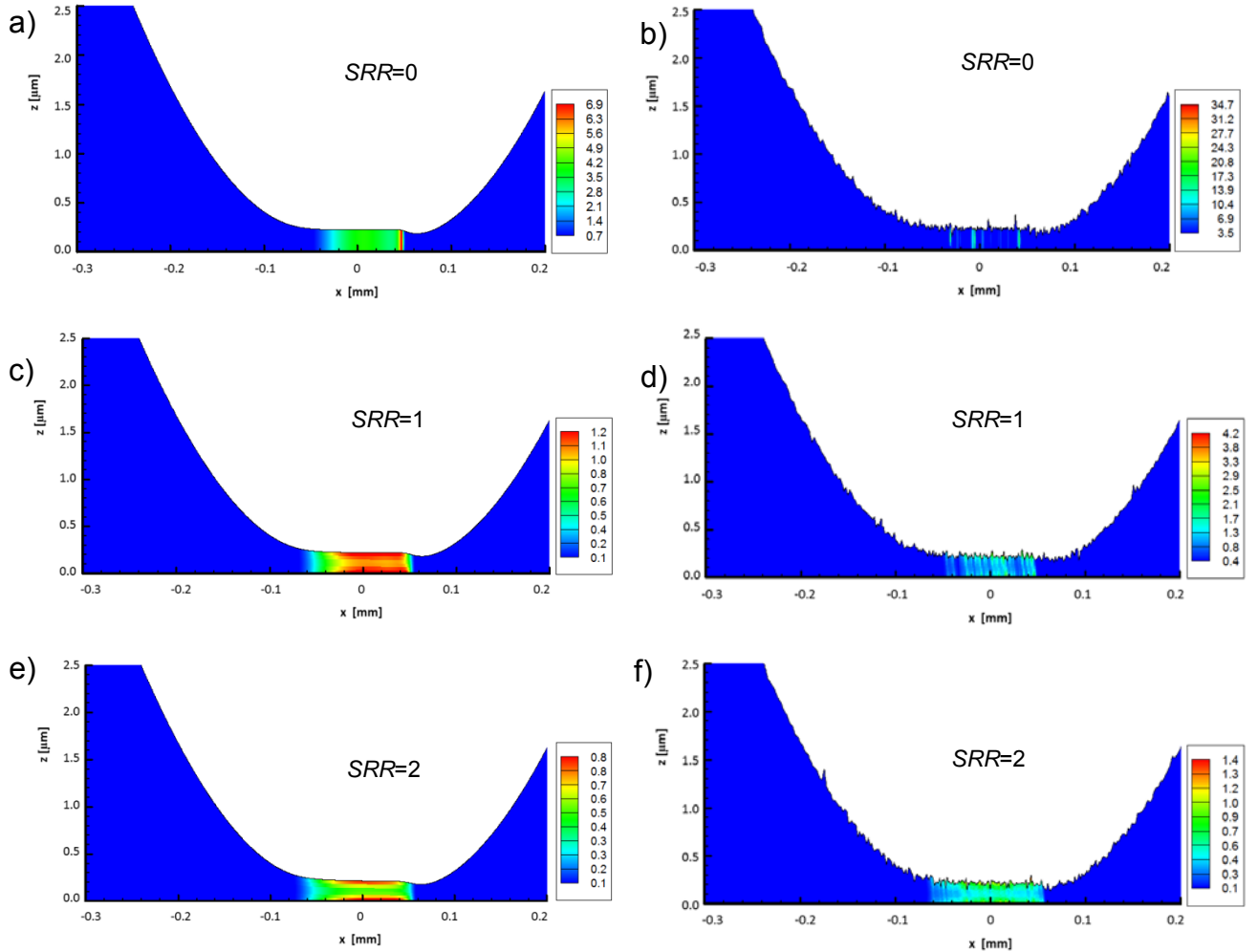


Figure 6-29: Effect of surface roughness on the iso-levels of viscosity (Pa·s) at $SRR = 0, 1$ and 2 (Left: smooth surface; Right: rough surface).

In the TEHL model, the viscosity of the lubricant is affected by the lubricant temperature. Figure 6-29 shows the effect of surface roughness on the lubricant viscosity under thermal conditions. It can be noticed that the viscosity at the surface of solids is higher than at the centre of the oil film thickness because it is there that the fluid temperature reaches its peak. This is due to the highest amount of frictional heat being retained at the centre of oil film in the sliding contact case.

According to the Reynolds approach, the pressure across the oil film thickness is considered to be a constant. This assumption can be accepted when the surfaces of solids are smooth, but it is inapplicable when the surface roughness effect is considered. Figure 6-30 shows the significance of the surface roughness on the velocity gradients close to the surface roughness at $SRR = 0$. It can be seen that the velocity gradients parallel and perpendicular to the lubricant flows vary when the surface is rough. The peaks of surface roughness affect the velocity gradient along the fluid flow direction, as shown in Figure 6-30b. These velocity gradients have an effect on the pressure gradient. According to the momentum equation, the pressure gradients streamwise and normal can be obtained from:

$$\begin{aligned} \frac{\partial(\rho u)}{\partial t} + \rho u \frac{\partial u}{\partial x} + \rho v \frac{\partial u}{\partial z} = -\frac{\partial p}{\partial x} + \frac{\partial}{\partial x} \left(2\mu \frac{\partial u}{\partial x} \right) + \frac{\partial}{\partial z} \left(\mu \frac{\partial u}{\partial z} \right) \\ + \frac{\partial}{\partial z} \left(\mu \frac{\partial v}{\partial x} \right) - \frac{\partial}{\partial x} \left(\frac{2}{3} \mu \left[\frac{\partial u}{\partial x} + \frac{\partial v}{\partial z} \right] \right) \end{aligned} \quad (6.1)$$

and

$$\begin{aligned} \frac{\partial(\rho v)}{\partial t} + \rho u \frac{\partial v}{\partial x} + \rho v \frac{\partial v}{\partial z} = -\frac{\partial p}{\partial z} + \frac{\partial}{\partial z} \left(2\mu \frac{\partial v}{\partial z} \right) + \frac{\partial}{\partial x} \left(\mu \frac{\partial v}{\partial x} \right) \\ + \frac{\partial}{\partial x} \left(\mu \frac{\partial v}{\partial x} \right) - \frac{\partial}{\partial z} \left(\frac{2}{3} \mu \left[\frac{\partial u}{\partial x} + \frac{\partial v}{\partial z} \right] \right) \end{aligned} \quad (6.2)$$

where x and z represent the spatial coordinates along (parallel to) and across (perpendicular to) the flow directions respectively.

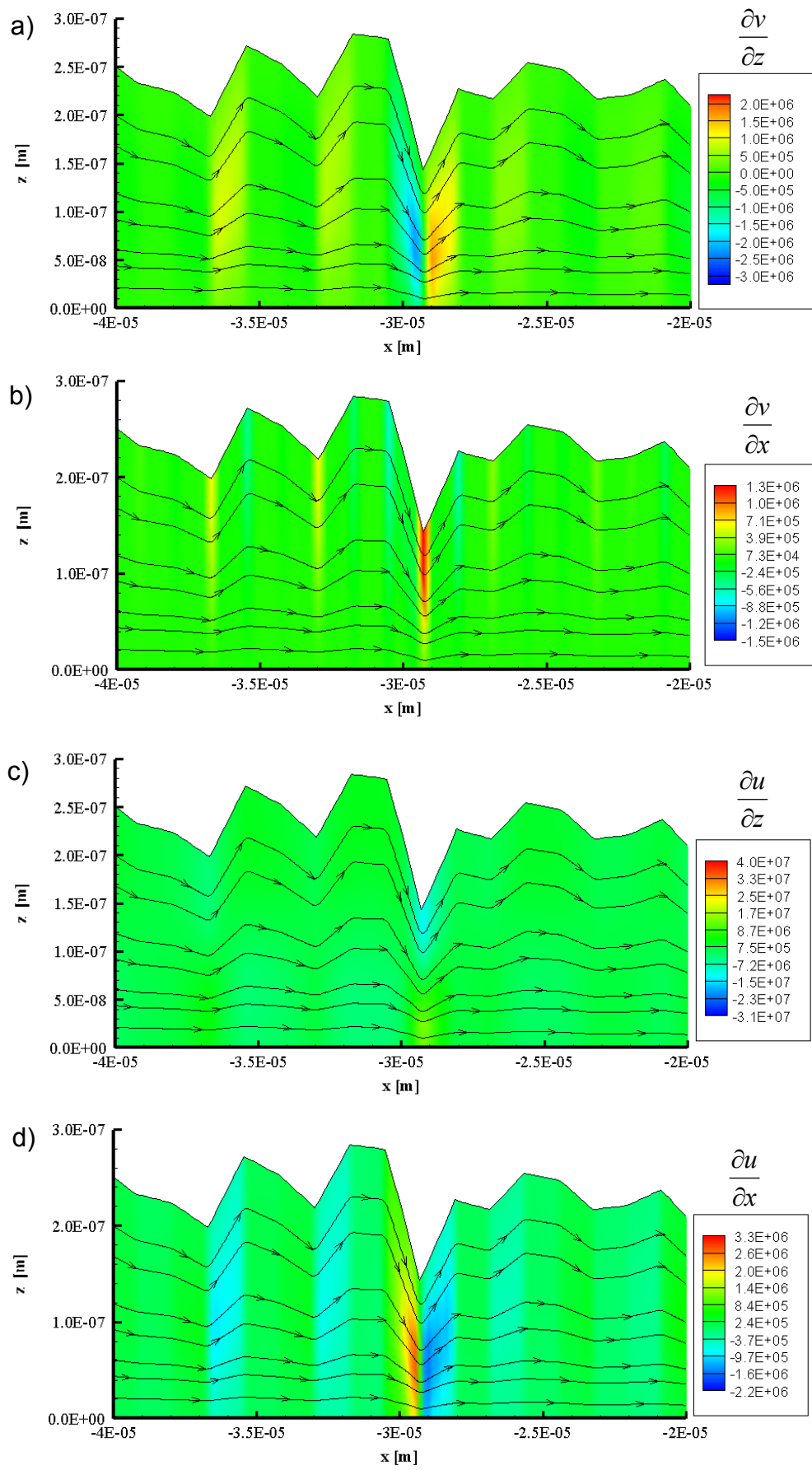


Figure 6-30: Effect of surface roughness on velocity gradients (s^{-1}).

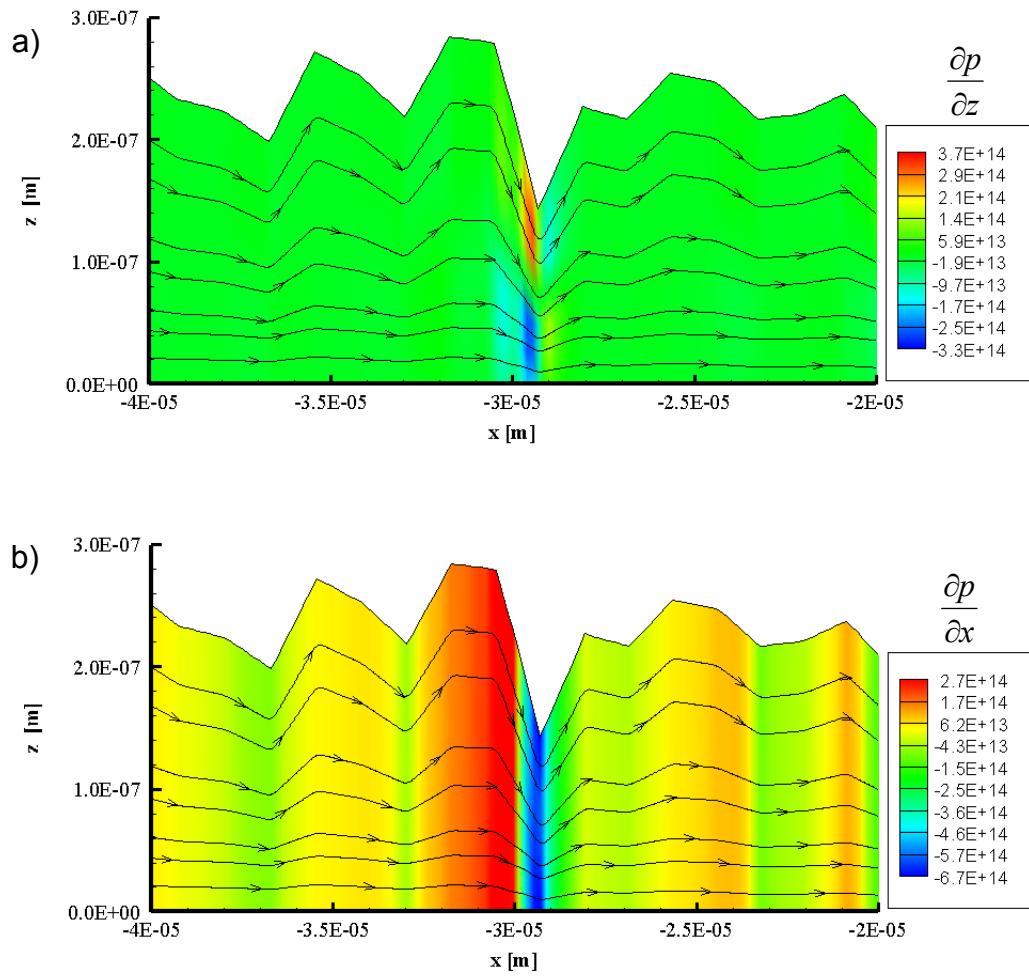


Figure 6-31: Effect of surface roughness on pressure gradients ($\text{Pa} \cdot \text{m}^{-1}$).

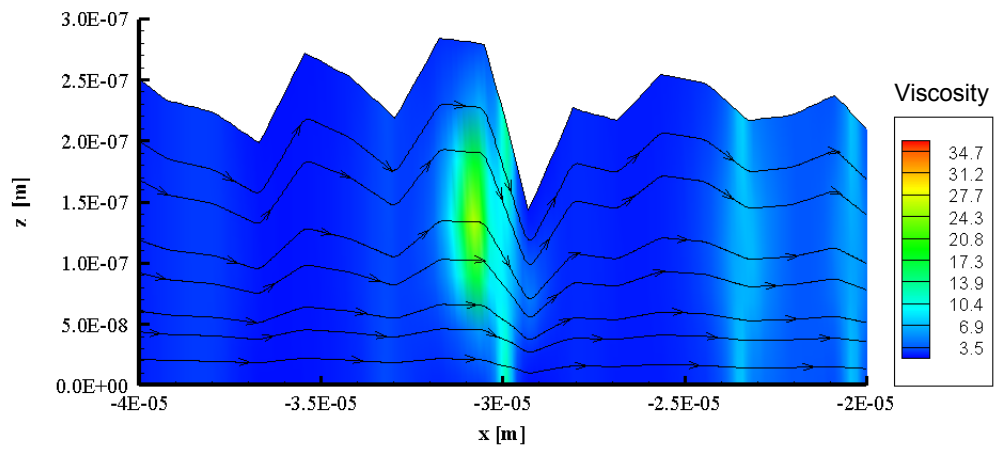


Figure 6-32: Effect of surface roughness on viscosity of lubricant ($\text{Pa} \cdot \text{s}$).

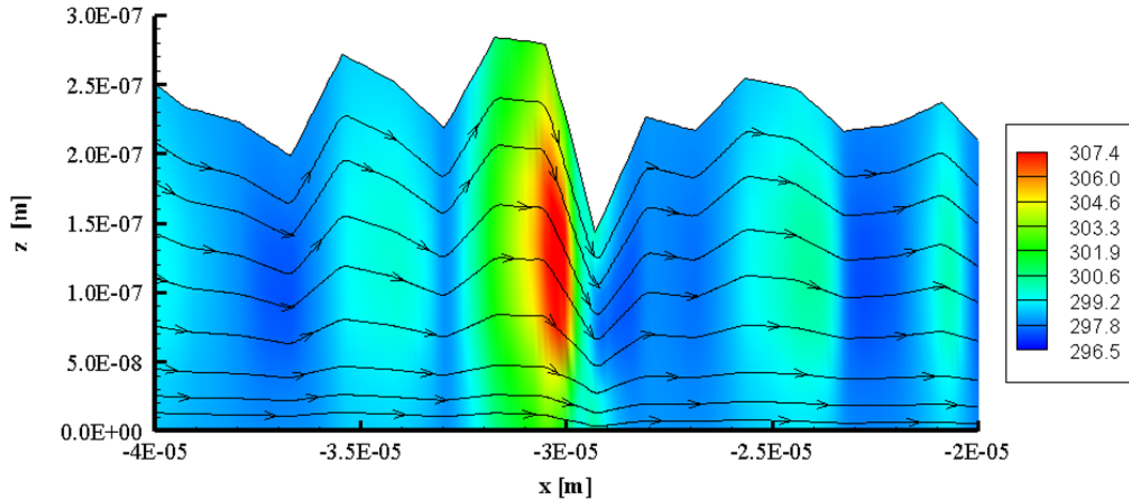


Figure 6-33: Effect of surface roughness on temperature field (K).

The velocity gradient term is very high because the Δx and Δz at the contact zone are very small ($\Delta x = 0.25 \mu\text{m}$ and $\Delta z \cong 0.01 \mu\text{m}$). Thus, the diffusion term, which is the function of viscosity and the second order of velocity gradient, is higher than the other terms. For example the maximum values of the acceleration and convection terms are only about $3.54 \times 10^9 \text{ N/m}^3$ and $7.01 \times 10^9 \text{ N/m}^3$ respectively while the maximum diffusivity of momentum term is around $9.16 \times 10^{15} \text{ N/m}^3$. The analysis has shown that the term which includes the viscosity variation (Figure 6-32) along the fluid flow direction has the dominant effect on the pressure gradient, as presented in Figure 6-31b, when compared with the others, such as the convection and rate of change terms.

In addition, the velocity gradient across the film thickness also influences the pressure gradient as shown in Figure 6-31a. The pressure gradient in both flow directions shows the significance of surface roughness on the behaviour of the EHL problem. Specifically, the pressure obtained by the CFD model varies across the entire film thickness.

Figure 6-33 shows the surface roughness effect on the temperature close to the roller wall as predicted by the TEHL model at a $SRR = 0$. It can be clearly seen that the surface roughness has a significant effect on the temperature field. The temperature is increased when the lubricant flows through the narrow gap

between the peaks of surface roughness as the pressure gradient (Figure 6-31) and the viscosity of lubricant (Figure 6-32) are both high in that region.

From the results of the CFD simulation of the TEHL line contact problem with modelled surface roughness, the following conclusions are drawn:

- Frictional heating is a greater cause of temperature rise than compression forces in the oil film.
- Viscosity is inversely proportional to temperature.
- The influence of surface roughness on pressure distribution can be greater in the case of thinner films.
- The pressure spike in the TEHL case is lower than in the EHL case.
- The oil film thickness of the TEHL case is slightly thinner than that in the EHL problem with isothermal case.

Chapter 7

The CFD Model for Two Rollers Contact

7.1 Introduction

The results of the CFD model for the contact between the two rollers under full film lubrication are reported in this chapter. The effects of surface roughness in the two rollers contact case will be presented and compared with the previous chapter. In the first part of this chapter, the material effect on the contact between two rollers of equal radius will be presented. Then, the contact between different radius rollers will be investigated to predict the influence of the surface roughness and of material on the EHL line contact problem. The influence of surface roughness parameters on the EHL line contact problem will be explored by generating different shapes of surface texture and applying these shapes to the CFD model for the two rollers contact. The study of the generated rough surfaces will be sorted into three groups. The first group will be studied to determine the influence of the average roughness parameter. The second group will be focused on the influence of the kurtosis parameter (R_{ku}) for $R_{ku} < 3$, $R_{ku} = 3$, and $R_{ku} > 3$. The last group will examine the influence of the skewness parameter (R_{sk}) for negative, positive, and zero R_{sk} . The thermal effects on the fluid flow between the contact of two different radius rollers will also be discussed.

7.2 Influence of material properties

The aim of this section is to investigate the material effect on the EHL problem using the CFD model. The first case has cylinders of identical radius and the other case has cylinders of different radii. Both CFD models are used to predict

the elastic deformation of the rollers that are modelled as made of different materials. The combinations brass - iron, iron - iron, iron - ceramic and brass - ceramic are considered for the top and bottom rollers, respectively.

7.2.1 Two rollers contact ($R_1=R_2$)

The CFD model for the two same sized rollers TEHL line contact problem, as sketched in Figure 5-14 (Model 2), is used to solve the EHL problem in this section. The quadrilateral mesh generated by the CFD model 2 is shown in Figure 5-15. The mesh size used in this model is identical to the previous model in chapter 5 but the bottom side has a cylindrical curve. The boundary conditions and the initial condition used in this section are identical to the ones in section 6.6. The surface roughness models 1 and 2 from Figure 3-22b and Figure 3-18b are applied to the surfaces of the top and bottom cylinder respectively. The pressure distribution and the deformed cylinder surfaces of the top and bottom cylinders will be compared with the ones from previous model.

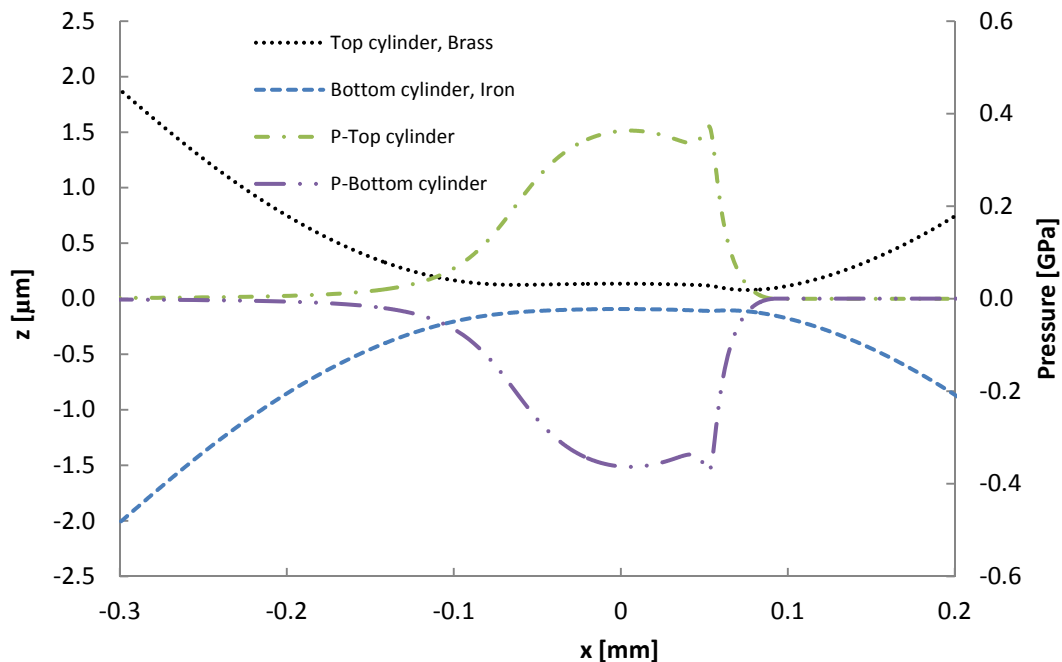


Figure 7-1: Material effects on the pressure distributions and the deformed cylinder surfaces (smooth surface).

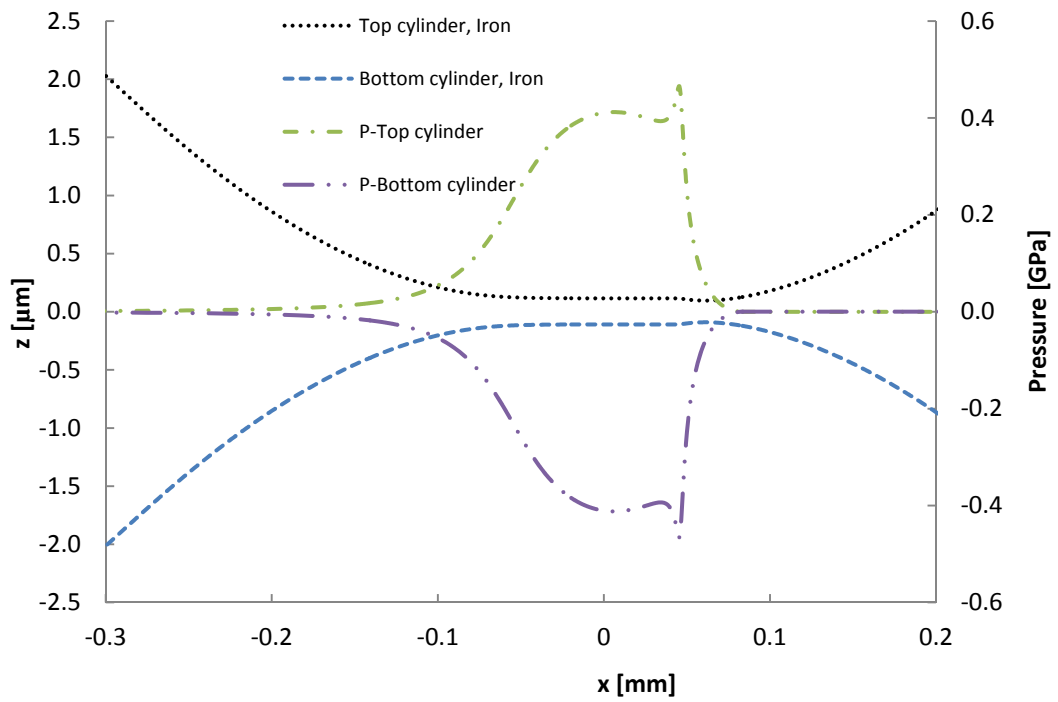


Figure 7-2: Material effects on the pressure distributions and the deformed cylinder surfaces (smooth surface).

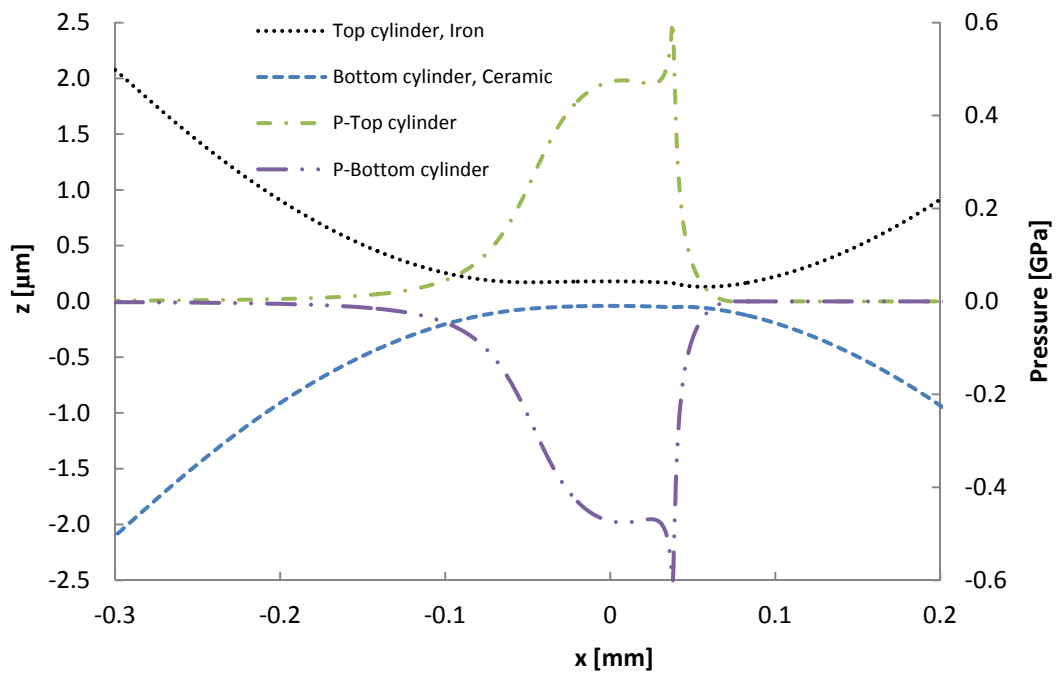


Figure 7-3: Material effects on the pressure distributions and the deformed cylinder surfaces (smooth surface).

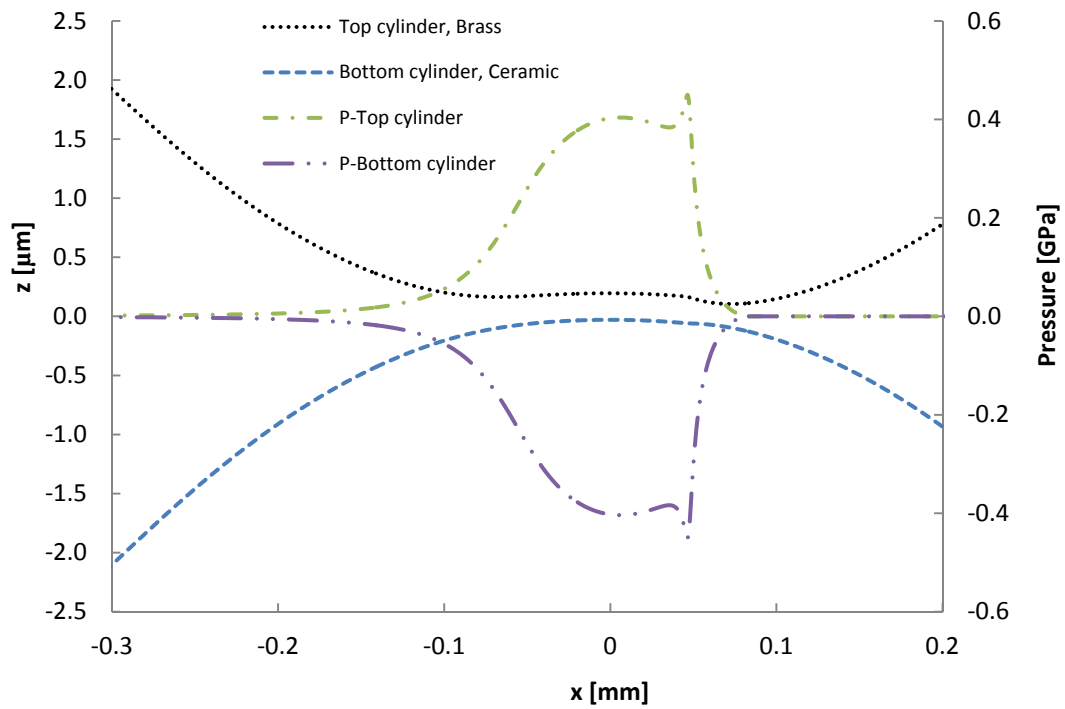


Figure 7-4: Material effects on the pressure distributions and the deformed cylinder surfaces (smooth surface).

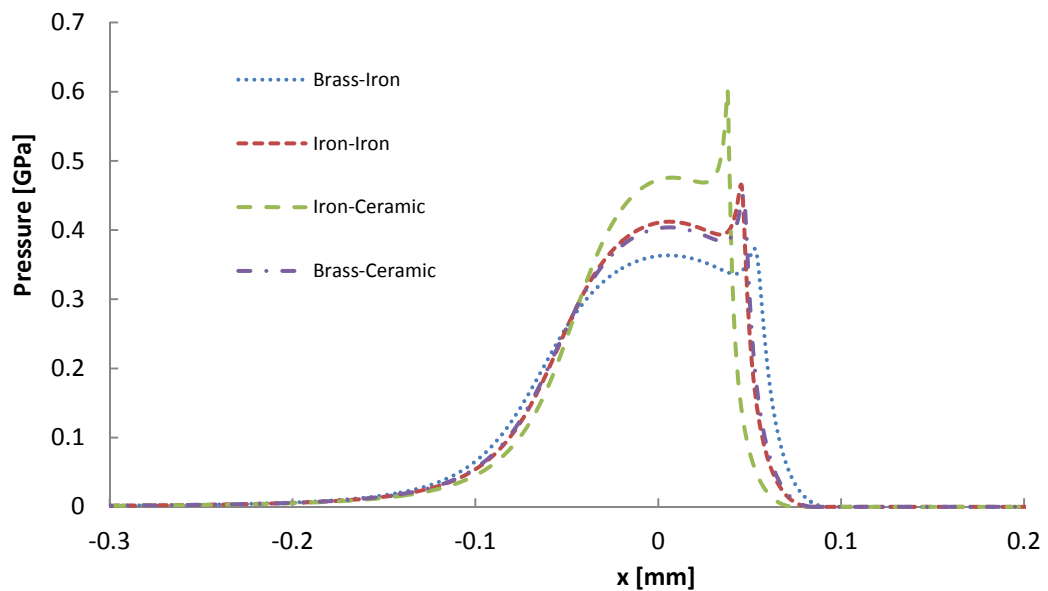


Figure 7-5: Comparison of the pressure distribution (top cylinder) among different material contacts.

Figure 7-1 to 7-4 show the elastic deformation of the top and bottom cylinders caused by the high pressure along the central line of the contact zone. It can be noticed that the pressure distributions on the top and bottom cylindrical surfaces are the same, while the elastic deformations on both surfaces are different, especially for the brass–ceramic roller combination and their contact, as shown in Figure 7-4. This is due to the Young's modulus (elastic modulus) of the top cylinder being lower than that of the bottom cylinder. The elastic deformations of the solid surfaces are symmetry when the same material are applied on the top and bottom cylinders as shown in Figure 7-2. Figure 7-3 shows the contact between iron cylinder and ceramic cylinder. It can be clearly seen that the pressure distribution at the Hertzian contact zone is very high and the surfaces of both cylinders are smaller deformed than other cases.

In Figure 7-5, the pressure distribution between the surfaces of the top and bottom cylinders with the brass–iron, iron–iron, iron–ceramic, and brass–ceramic contacts are compared. It is found that the highest pressure occurs for the iron and ceramic contact, while the minimum pressure occurs for the brass and iron contact. The pressure distribution from the iron and the ceramic EHL line contact is higher than for all other combinations at material considered here, but it has also the narrowest Hertzian contact area. This is due to the iron–ceramic contact having the highest effective elastic modulus ($E' = 307.43$ GPa) whereas the brass–ceramic contact has the lowest effective elastic modulus ($E' = 221.56$ GPa).

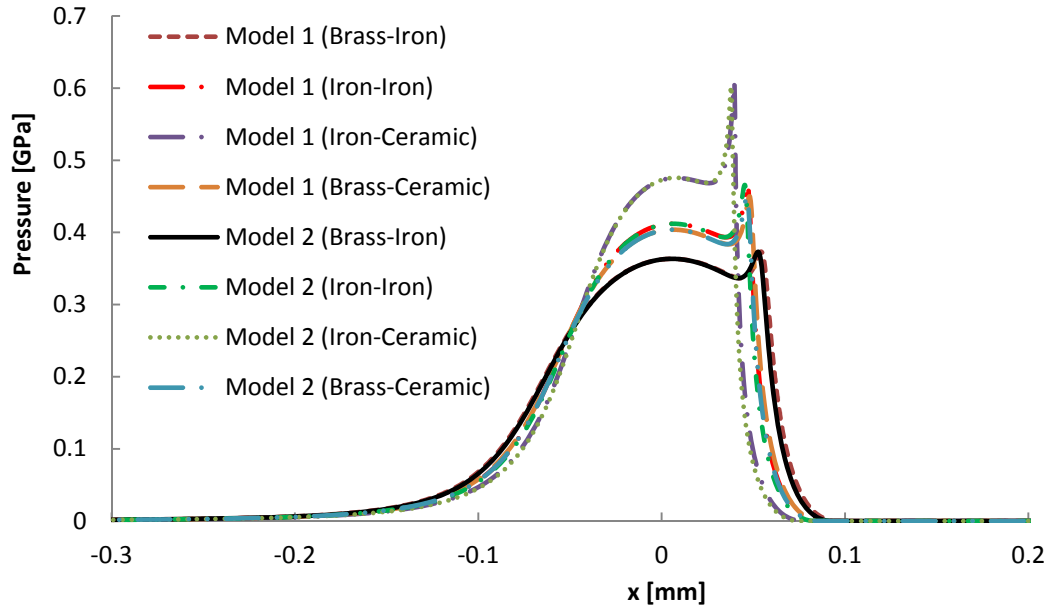


Figure 7-6: Comparison of the material effects on the pressure distributions between CFD model 1 and CFD model 2 from Table 5-4.

The pressure distributions of different types of material from CFD model 1 (roller and plate geometry) and CFD model 2 (roller of equal radii) are compared in Figure 7-16. It is found that, although both models are very similar, their pressure profiles are slightly different at the outlet region. The maximum error of pressure between model 1 and model 2 by about 0.0555 GPa, 0.0889 GPa, 0.2042 GPa, 0.0823 GPa for the brass–iron, iron–iron, iron–ceramic, and brass–ceramic contacts, respectively. Furthermore, the pressure spike in model 1 is shifted further to the outlet region in comparison to model 2, which is due to the fact that the elastic deformation terms of models 1 and 2 are different. In the CFD model 1, the elastic deformation is computed from the effective elastic modulus, while elastic deformation in CFD model 2 is directly calculated from the modulus of elasticity of each cylinder.

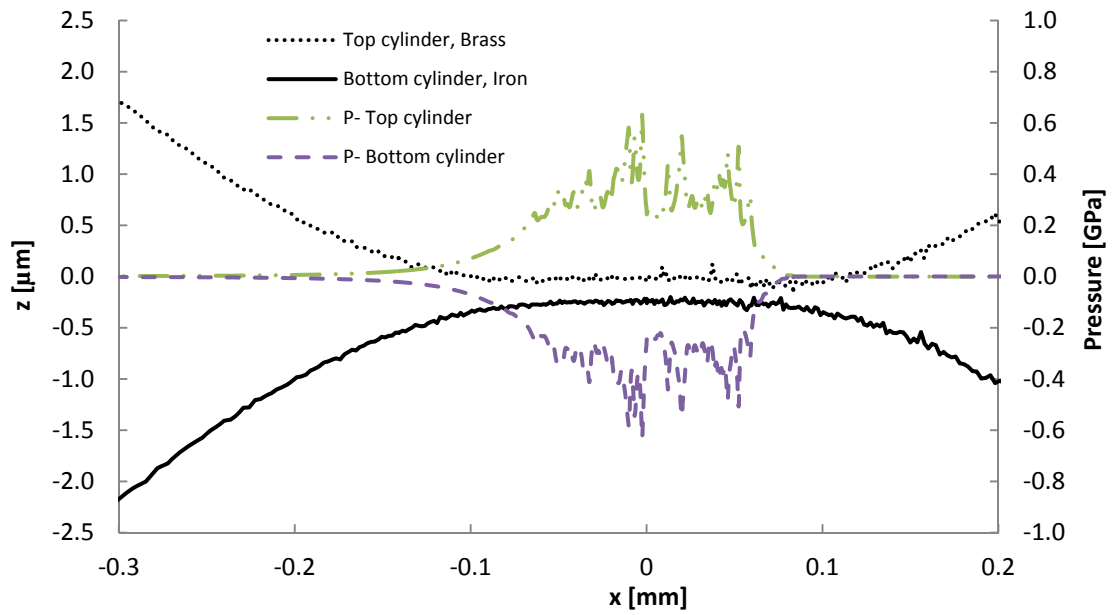


Figure 7-7: Material effects on the pressure distributions and on the deformed cylinder surface (rough surface).

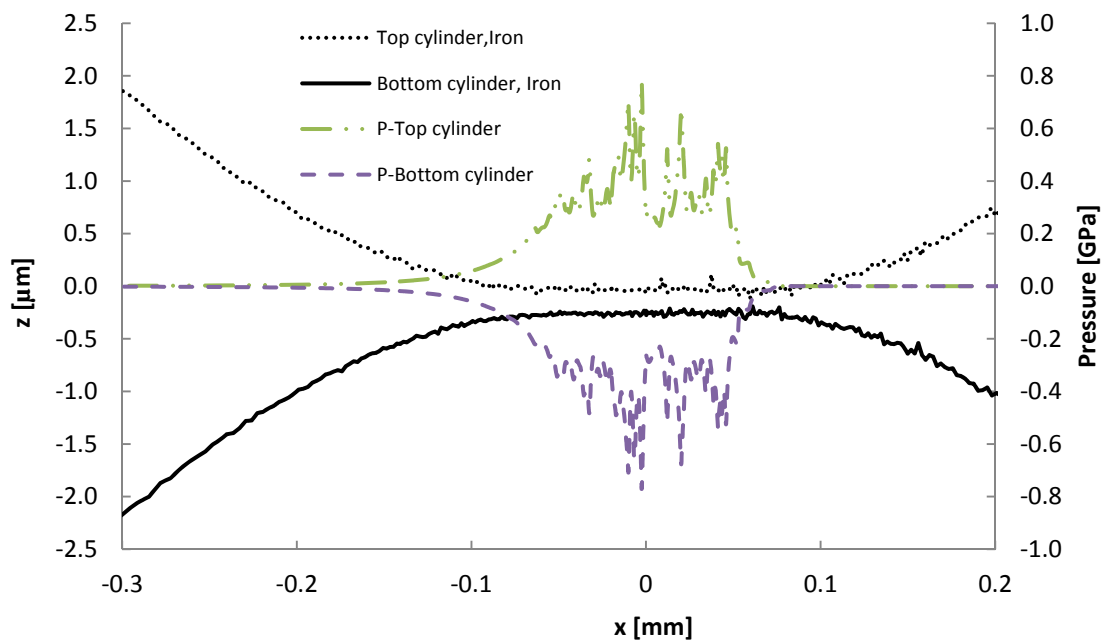


Figure 7-8: Material effects on the pressure distributions and on the deformed cylinder surface (rough surface).

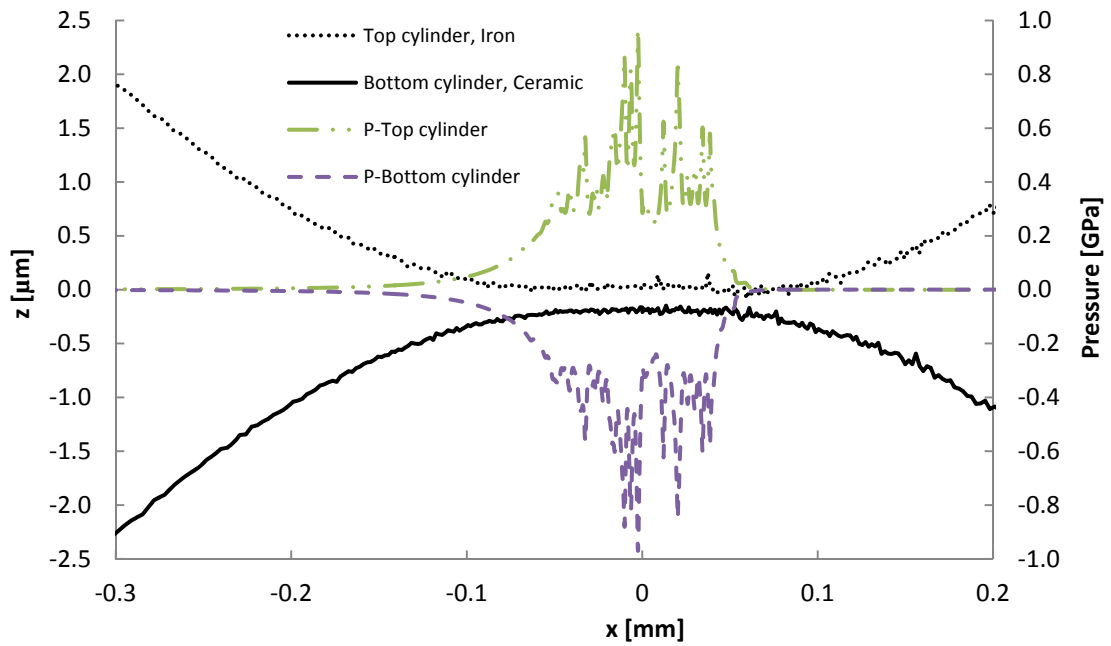


Figure 7-9: Material effects on the pressure distributions and on the deformed cylinder surface (rough surface).

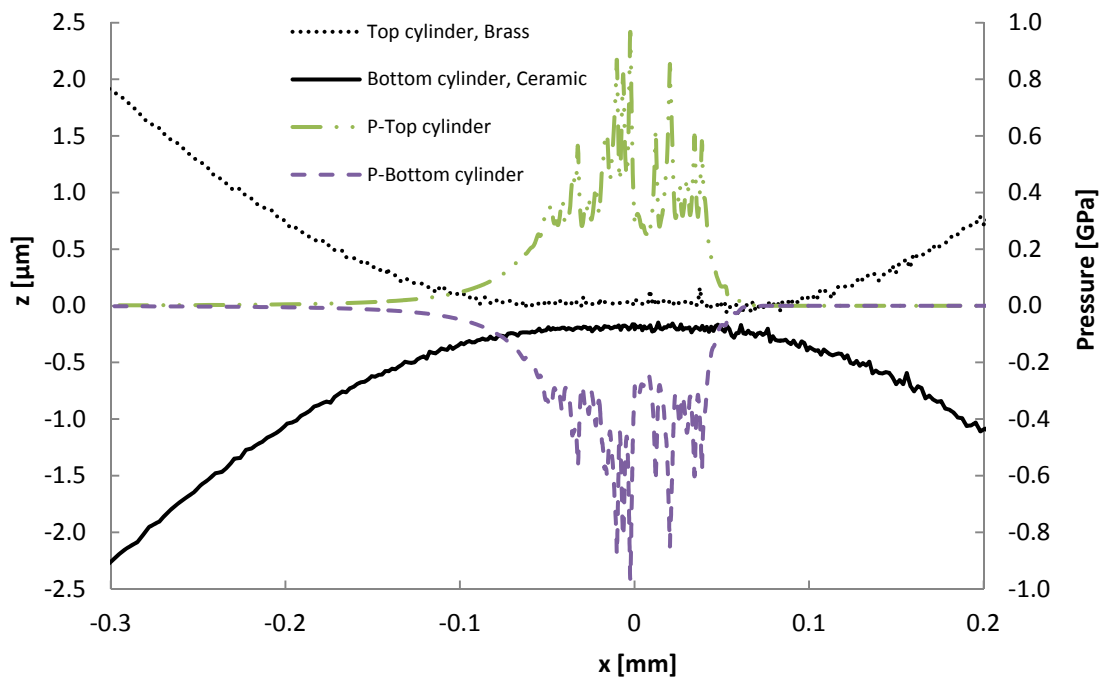


Figure 7-10: Material effects on the pressure distributions and on the deformed cylinder surface (rough surface).

Table 7-1: Comparison of the maximum pressure and film thickness of the CFD models 1 and 2

Match of contacts			Brass-Iron	Iron-Iron	Iron-Ceramic	Brass-Ceramic
Smooth surface	Cylinder & Plate	p(GPa)	0.3733	0.4675	0.6088	0.4500
		h(μm)	16.0053	16.087	16.1644	16.0749
	2 cylinders	p(GPa)	0.3731	0.4657	0.6027	0.4498
		h(μm)	15.7825	15.8652	15.9762	15.9761
Rough surface	Cylinder & Plate	p(GPa)	1.00212	1.23844	1.53837	1.19477
		h(μm)	16.0076	16.0911	16.1725	16.0786
	2 cylinders	p(GPa)	0.6315	0.7750	0.9700	0.9673
		h(μm)	15.8143	15.8984	15.9768	15.9765

Figure 7-7 to Figure 7-10 show the effects of surface roughness on the EHL problem through the CFD model when using different material contacts. The results show the effect of surface roughness on the pressure distribution. It can be seen that pressure fluctuation is highest in the case of the iron–ceramic contact and lowest in the case of the brass–iron contact. This is due to the material effect as presented in the previous section. Therefore smooth and rough roller surfaces exhibit the same of dependence on the material properties.

Table 7-1 shows the maximum pressure and the average oil film thickness of model 1 and model 2 for contacts in both smooth and rough surfaces. It is found that the maximum pressures from model 1 (cylinder–plate) is the Hertzian contact zone are higher than the corresponding ones from model 2 (two cylinders contact, $R_1 = R_2$) for both surface types by around 0.43% and 32.77% for the smooth and rough surface cases, respectively. The average oil film thickness of rough surface cases (Model 1) is about 0.03% higher than that of the smooth surface cases. According to the results obtained, the effect of surface roughness on the EHL problem by model 2 is similar to model 1, but the average film thickness is higher than that of the smooth surface case by about 0.10%.

7.2.2 Two cylinders contact ($R_1 \neq R_2$)

The CFD model 3 for the two rollers contact, as depicted in Figure 5-14, is used to solve the EHL problem in this section. The quadrilateral-mesh generated for this model is depicted in Figure 5-16. The mesh size used here is identical to the model in the previous section, but the top and bottom sides have a different cylindrical curve ($R_1=15$ mm and $R_2=30$ mm). The boundary conditions and the initial condition used are identical to the ones reported in section 6.6. The surface roughness profiles 1 and 2 from Figure 3-22b and Figure 3-18b are applied to the surfaces of the top and bottom cylinder, respectively. The predicted pressure distribution and the oil film thickness between the top and bottom cylinders will be compared with the corresponding predictions from the previous model.

Table 7-2: Effect of material on two cylinders contact ($R_1 \neq R_2$)

Materials	At the contact centre, $x=0$ mm			
	Δz_1 (μm)	Δz_2 (μm)	Average pressure (GPa)	Film thickness (μm)
Iron – iron ($E_1=E_2$)	0.0890	0.1369	0.41063	0.2238
Brass – ceramic ($E_1<E_2$)	0.1867	0.0435	0.40254	0.2245
Ceramic – brass ($E_1>E_2$)	0.0194	0.2625	0.40258	0.2243

Note: Δz_1 and Δz_2 refer to the elastic deformation at the top and bottom cylinders, respectively.

Figure 7-11, Figure 7-12 and Figure 7-13 present the film thicknesses and the pressure distributions when the materials used for the top and bottom cylinders are iron – iron, brass – ceramic and ceramic – brass, respectively. It is found that the elastic deformation of the bottom cylinder is higher than that of the top cylinder, as depicted in Figure 7-11. Although the materials of both cylinders are the same, the indentation of the bottom cylinder is deeper than that of the top cylinder around $0.0479 \mu\text{m}$ as described in Table 7-2. It is interesting to notice that the results deviate from those in the previous section in that the deformations are no longer equal between the two cylinders.

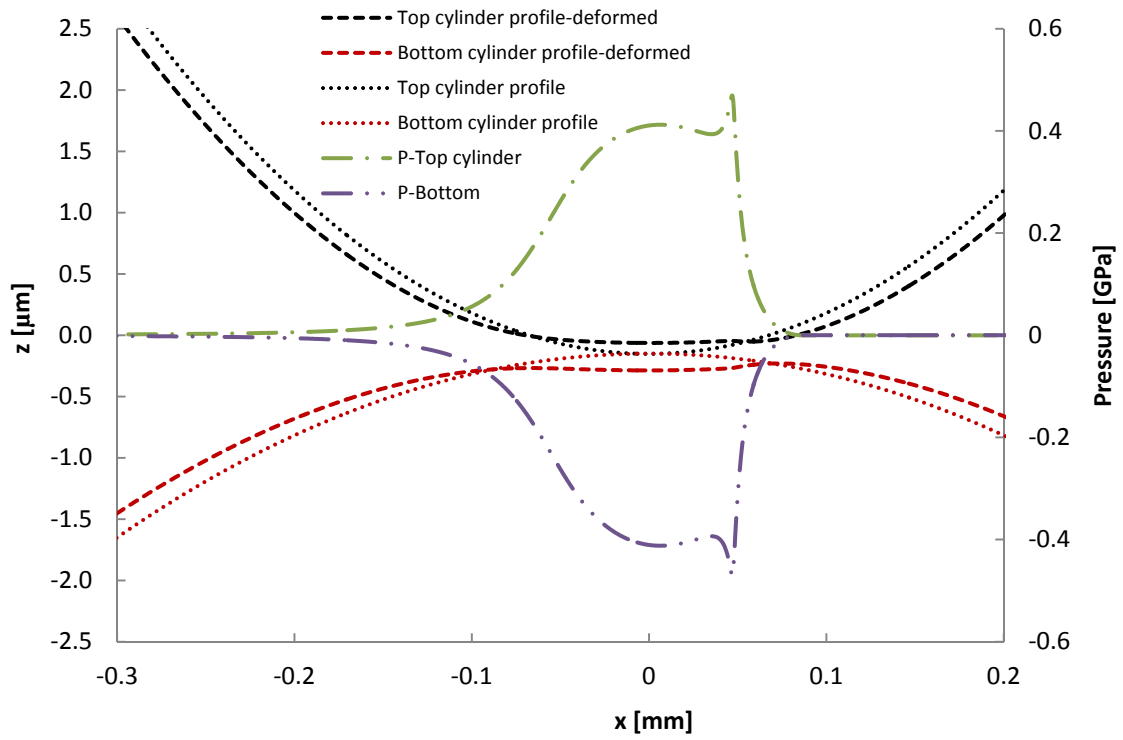


Figure 7-11: The pressure distributions and profiles of cylinders ($E_1 = E_2$).

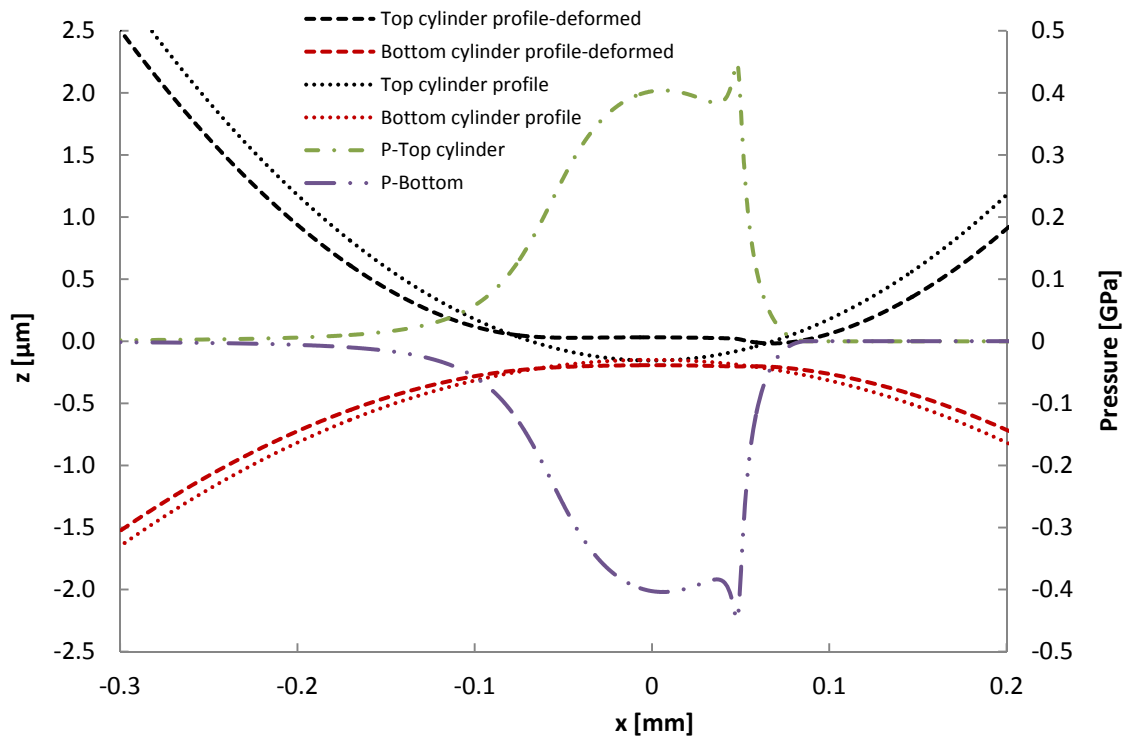


Figure 7-12: The pressure distributions and profiles of cylinders ($E_1 < E_2$).

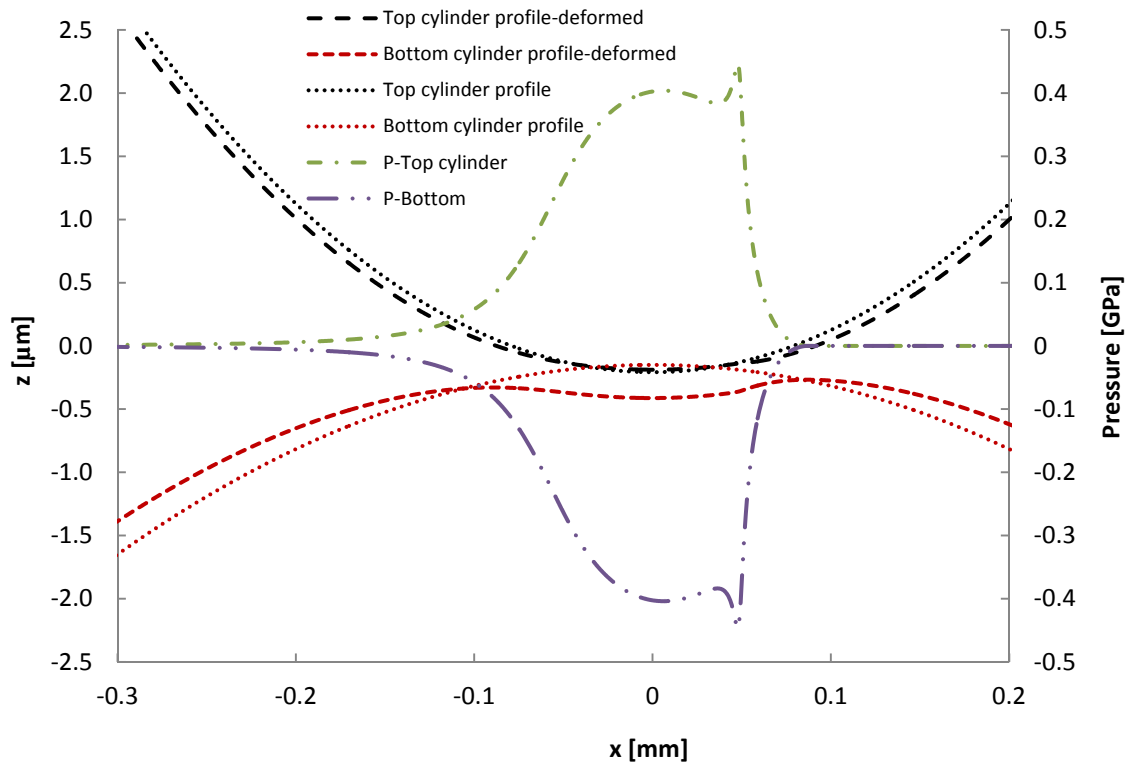


Figure 7-13: The pressure distributions and profiles of cylinders ($E_1 > E_2$).

The previous results show that the elastic deformations of the top and bottom cylinders are symmetric when the radius and the material of both cylinders are the same, as presented in Figure 7-2. This means that the elastic deformation of each cylinder depend on both the material and radius of the cylinder, broadly following Hook's law $\sigma = E\varepsilon$.

Figure 7-12 and Figure 7-13 show the effects of materials on the elastic deformations of the top and bottom cylinders when the materials used are different. The radius and material of cylinders play an important role for the elastic deformations in the CFD model 3, especially in the case of the small cylinder, which is harder than the big one, as depicted in Figure 7-13. Specifically, Figure 7-13 shows that most of the deformation takes place in the bottom cylinder. The Reynolds equation cannot be used to represent the elastic deformation for each cylinder since this equation gives the equivalent combined deformation of the two solid boundaries through the film thickness and not the individual values of the deformations of each solid boundary.

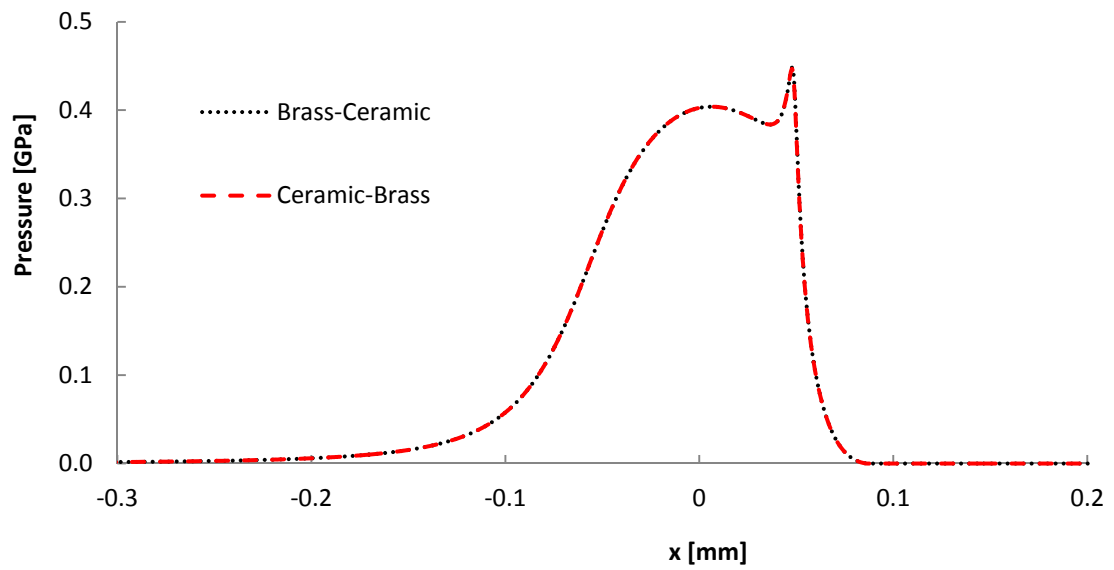


Figure 7-14: The pressure distributions when $E_1 < E_2$ and $E_1 > E_2$ with the CFD model 3.

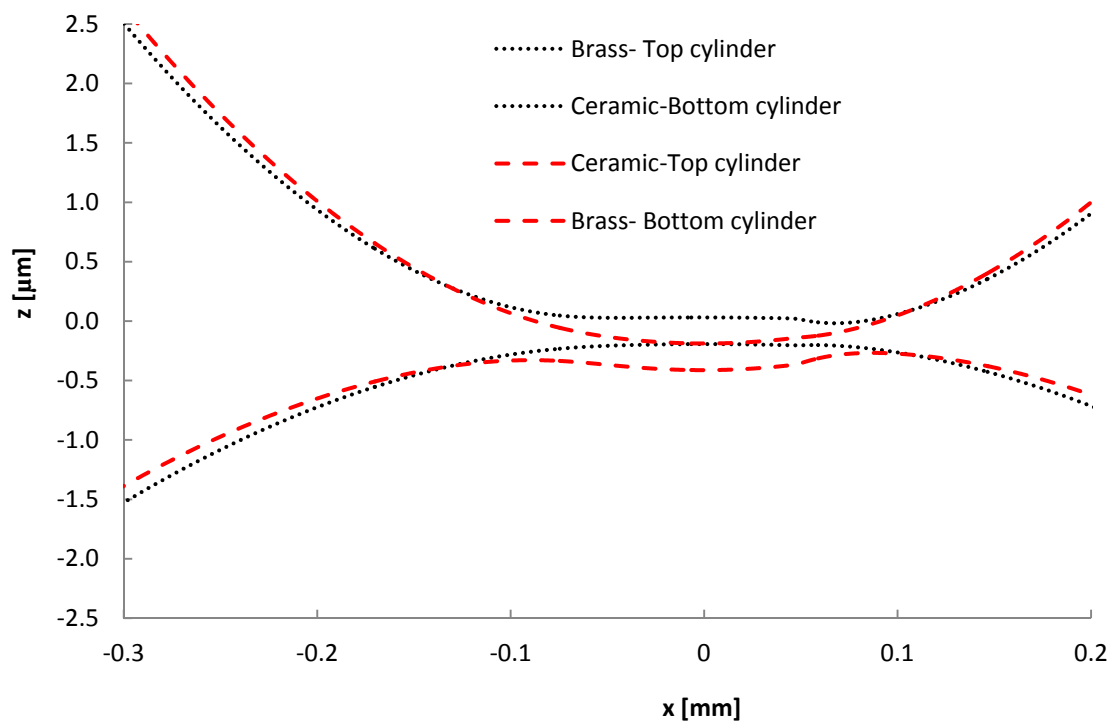


Figure 7-15: Comparison of the deformations when top and bottom cylinders are brass–ceramic and ceramic–brass.

Figure 7-14 reports the predicted pressure distributions generated in the lubricant film in the case of different materials and radii of the cylinders. The pressure profiles of brass–ceramic and ceramic–brass contact are the same, while the elastic deformations of both cases are entirely different, as presented in Figure 7-15. It can be inferred that the film thickness in the Hertzian contact region of both cases are similar although the elastic deformations of the top and bottom cylinder surface are different.

Figure 7-16 presents the pressure distributions of the CFD models 1, 2, and 3, respectively. The pressure profiles of all CFD models are the same when the materials defined on the top and bottom cylinders of three models are the same - i.e. the top cylinder is defined to be ceramic and the bottom is defined to be brass. The elastic deformations of the top and bottom cylinders for each CFD model are significantly different, but the film thickness at the contact area remains the same for all cases.

According to the results, radii and material parameters significantly affect the elastic deformations of both cylinders. As shown in Figure 7-17, the gaps between the top and the bottom cylinders at the contact areas of models 1 (black colour), 2 (green colour) and 3 (red colour) are similar. Thus, it can be concluded that the elastic deformation of each contact depends on the radius and the material properties while the pressure building up in the fluid film depends only on the film thickness at the contact zone.

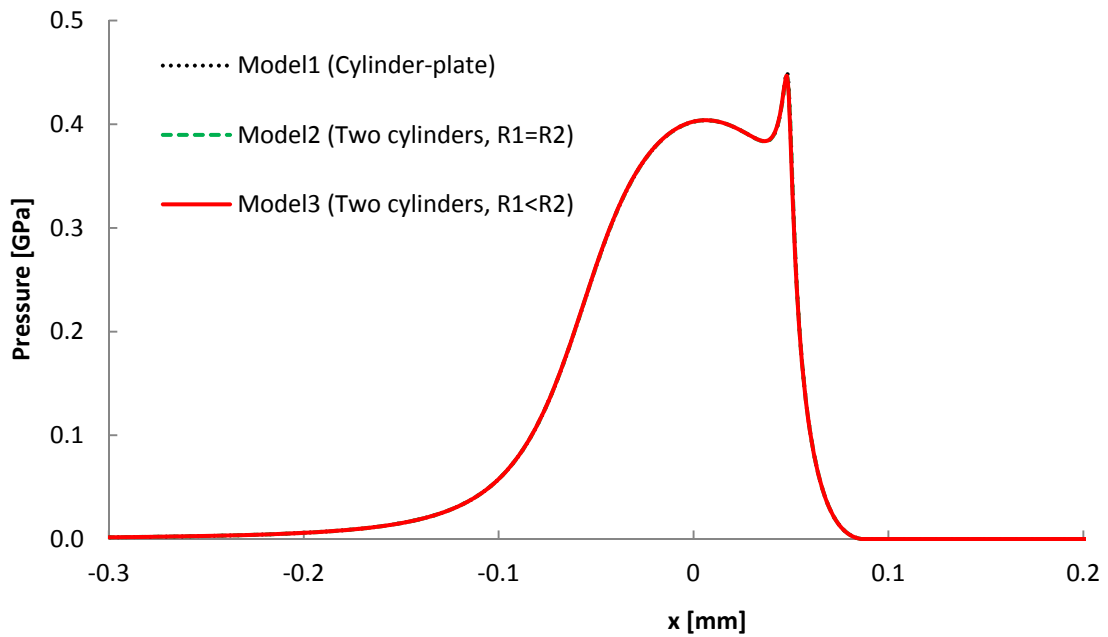


Figure 7-16: Comparison of the pressure profiles among models 1, 2 and 3.

Evaluating the elastic deformation of the EHL problem by using the Reynolds equation will lead to an error in cases where the radius and the material of the cylinders are different. Specially, the apportioning of the elastic deformation between the top and bottom solid boundaries is not given in the solution of the equation. Conversely, the CFD models can produce predictions of the individual deformations of the top and bottom boundaries. This is another advantage of the CFD approach over the Reynolds equation.

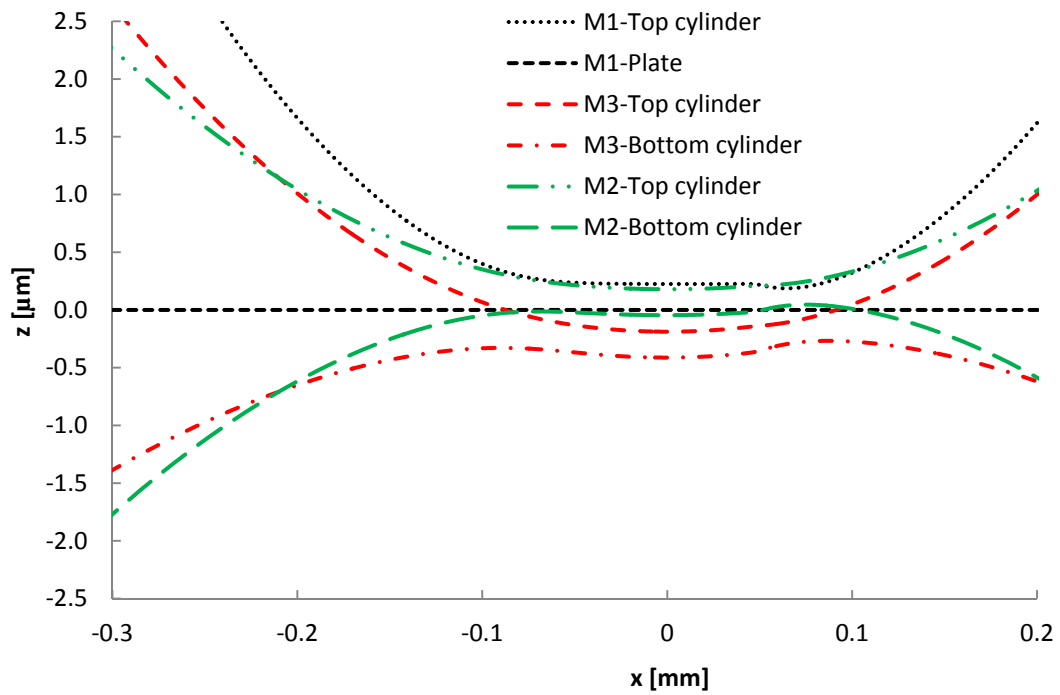


Figure 7-17: Comparison of the film thickness among models 1, 2 and 3.

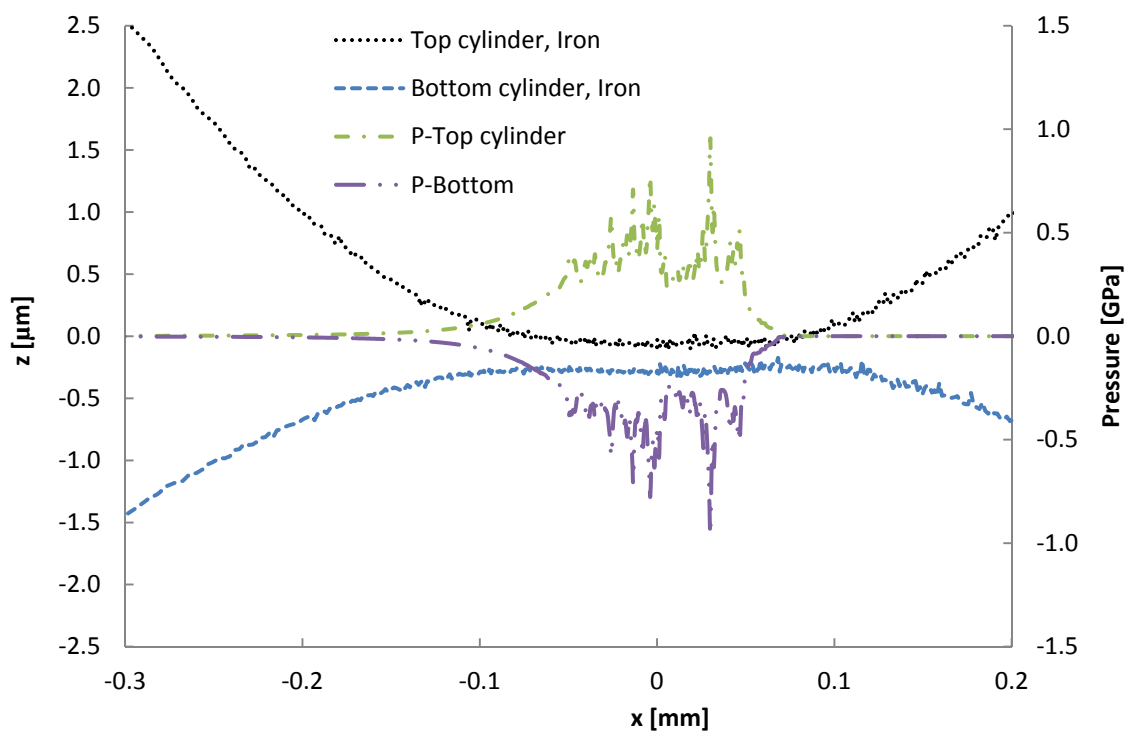


Figure 7-18: Pressure distribution and film thickness (iron – iron).

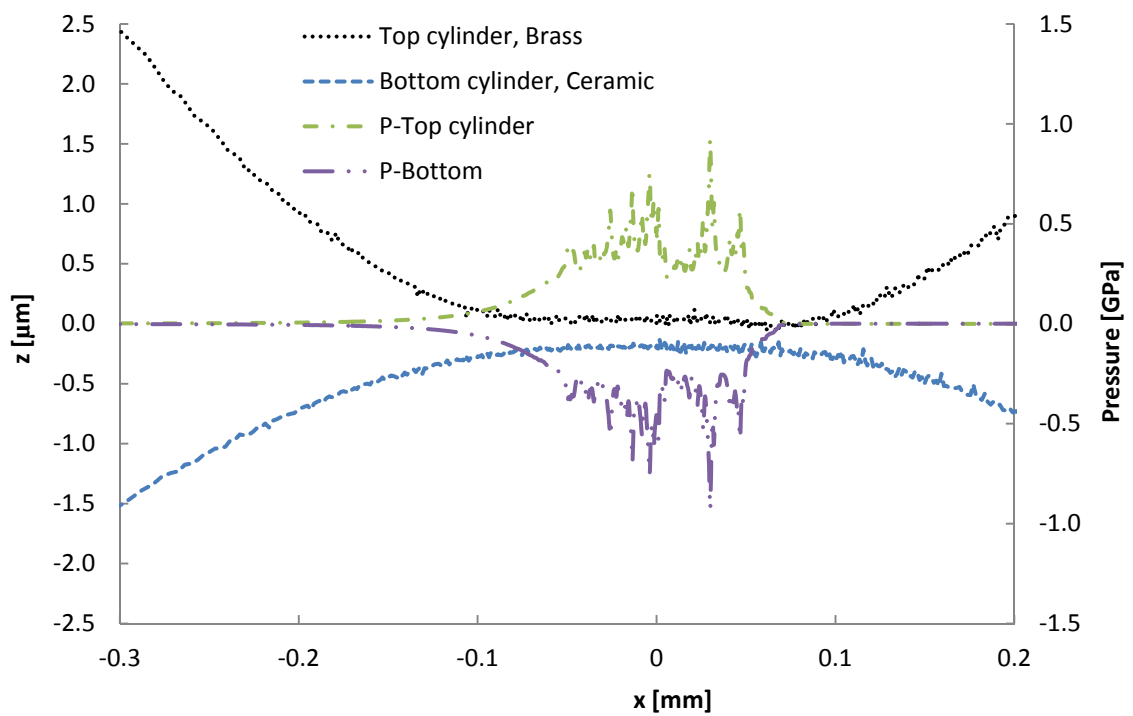


Figure 7-19: Pressure distribution and film thickness (brass – ceramic).

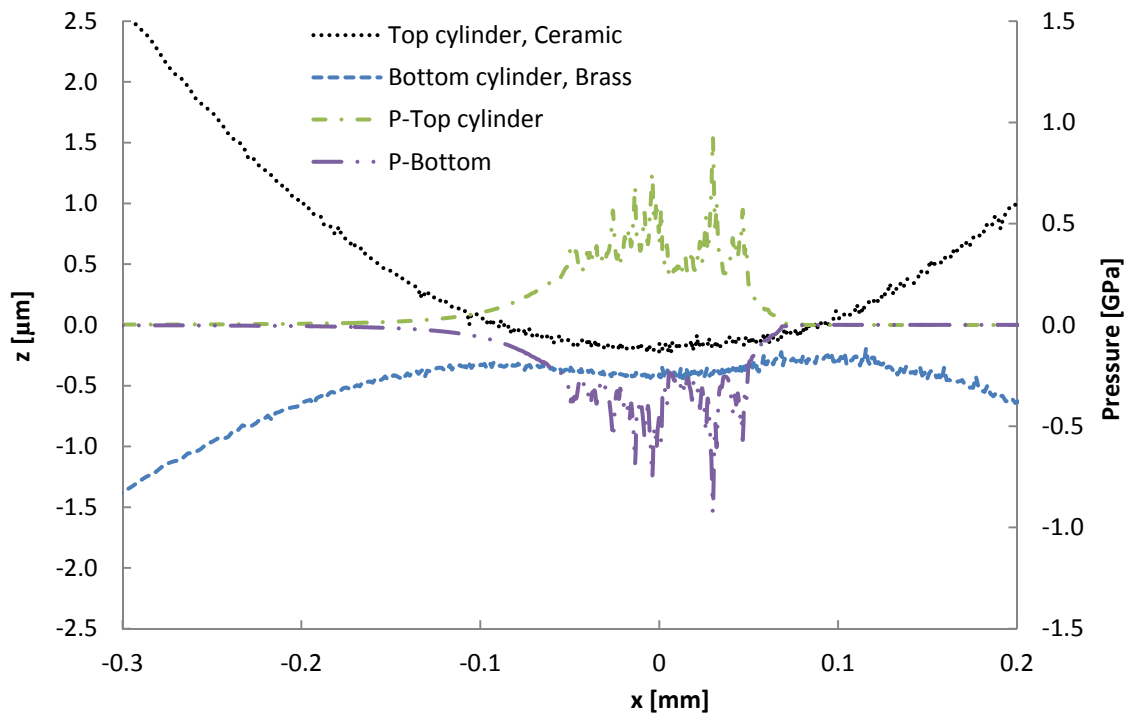


Figure 7-20: Pressure distribution and film thickness (ceramic-brass).

The surface roughness effect on the EHL line contact problem for two cylinders with different radii ($R_1 \neq R_2$) is predicted by using the CFD model geometry shown in Figure 5-16. The CFD results of Figure 7-18, Figure 7-19 and Figure 7-20 present the effects of different combination of cylinder materials on the pressure distribution and the film thickness, taking into account surface roughness. Figure 7-18 shows the influence of the surface roughness on the axial pressure distribution in the fluid when the top and bottom cylinders are of the same material (iron–iron). The second and third cases present the effects of using different materials. It can be seen that the elastic deformations of the surface of the cylinders with roughness display a similar trend towards top and bottom cylinder deformation in rough surfaces is similar in smooth surfaces, shown in Figure 7-15. The highest deformation of the bottom cylinder occurs in the case where the small cylinder (top cylinder) is of a hard material (ceramic) and the big cylinder is of a soft metal (brass). Figures 7-18 to 7-20 show that the pressure distributions over the top and bottom cylinder surfaces are the same, because the film thickness is very thin.

7.3 Influence of the roughness parameters

The CFD models in the previous sections showed that surface roughness has significant effects on the EHL line contact problem. It must be pointed out that all simulations used the same surface roughness profile ($R_a = 0.0216 \mu\text{m}$). Thus, it is important to study the effects of surface roughness on the EHL problem when R_a , R_{sk} and R_{ku} are varied. Such line contact problems will be investigated in this section as follows:

- Surface roughness profiles (1, 2 and 3), as shown in Figure 7-21, will be used to study the influence of the average roughness value (R_a).
- Surface roughness profiles (1, 4 and 5), as depicted in Figure 7-22, will be used to study the influence of the peaks of the surface texture for $R_{ku} < 3$, $R_{ku} = 3$, and $R_{ku} > 3$.
- Surface roughness profiles (1, 6 and 7), as presented in Figure 7-23 where the skewness values (R_{sk}) are negative ($R_{sk} = -0.70$), zero (R_{sk}

=0), and positive ($R_{sk}=0.72$), will be used to study the influence of the distribution shape of surface roughness.

All surface roughness profiles are generated using the Pearson function provided by MATLAB (R2013b) [152, 153]. The surface roughness parameters of the surface roughness profiles 1 to 7 are listed in Table 7-3. This table reports the input parameter in brackets and the computed parameter of the generated surface roughness profile in plain text. It can be seen that there are some differences between the input and output data. It is very difficult to keep the output of the generated profile the same as the input parameters but it can be accepted, but it can be accepted. This is due to a computer number generator can produce a different data in each time, as explained in section 3.5. Whereas the output roughness parameters and different the input values, the variation in output parameter in Table 7-2 enables to study the effects of R_a , R_{sk} and R_{ku} as intended.

Table 7-3: The roughness parameters for profiles 1 to 7 ($\Delta x = 0.5 \mu\text{m}$)

Roughness profile	R_a (μm)	R_q (μm)	R_{sk}	R_{ku}
1	0.0234 (0.0200)	0.0299 (0.0300)	0.0038 (0.0000)	3.01 (3.00)
2	0.0363 (0.0300)	0.0454 (0.0450)	0.0051 (0.0000)	3.01 (3.00)
3	0.0484 (0.0400)	0.0604 (0.0600)	0.0085 (0.0000)	2.99 (3.00)
4	0.0254 (0.0200)	0.0300 (0.0300)	0.0052 (0.0000)	2.00 (2.00)
5	0.0223 (0.0200)	0.0302 (0.0300)	0.0068 (0.0000)	5.60 (6.00)
6	0.0247 (0.0200)	0.0302 (0.0300)	-0.7024 (-0.7000)	3.01 (3.00)
7	0.0249 (0.0200)	0.0301 (0.0300)	0.7031 (0.7000)	3.00 (3.00)

The aim of this simulation is only the study the trend of the effect of the skewness parameter (R_{sk}) on the behaviour of the EHL line contact problem. It should be noted that the generated surface roughness from Pearson distribution with the effects of skewness is limited between -1.2 and 1.2 when the kurtosis (R_{ku}) is equal to be 3.0. In order to investigate the effect of a high skewness parameter, it is necessary to increase the kurtosis parameter.

The surface of the top cylinder is defined as a rough surface with a roughness profile from Figure 7-21 to 7-23 while the bottom cylinder is assumed to be a smooth surface. In this section the CFD model geometry, shown in Figure 5-15 is used to simulate the characteristics of the EHL problem with different roughness profiles. Viscosity is considered to be a non-Newtonian fluid. The isothermal condition is considered for the viscosity and density of the fluid.

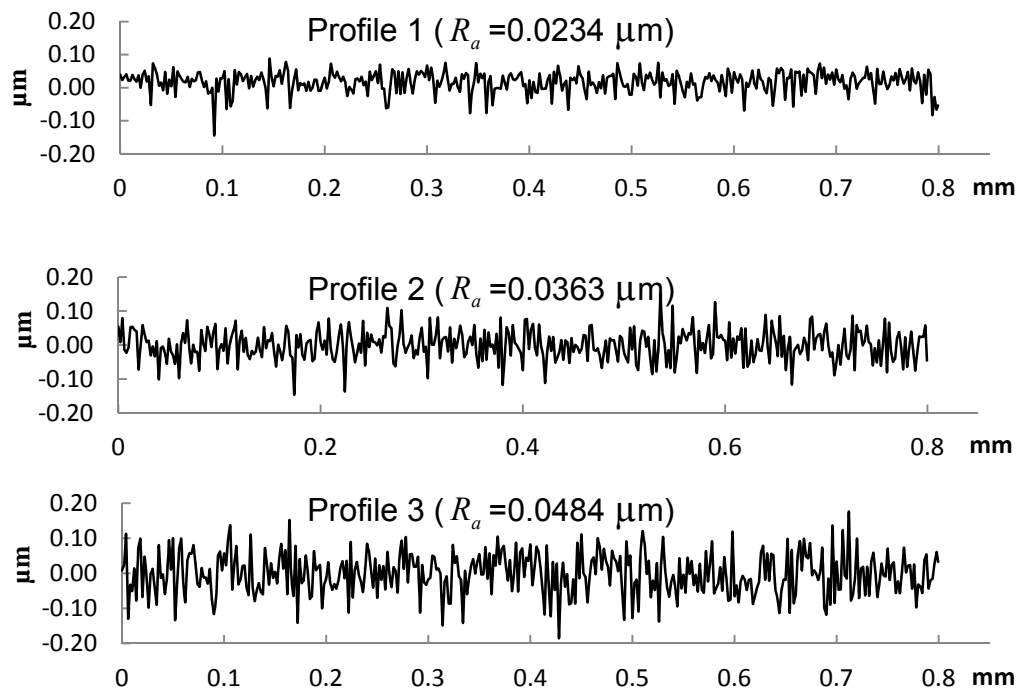


Figure 7-21: Surface roughness profiles when R_a is increased.

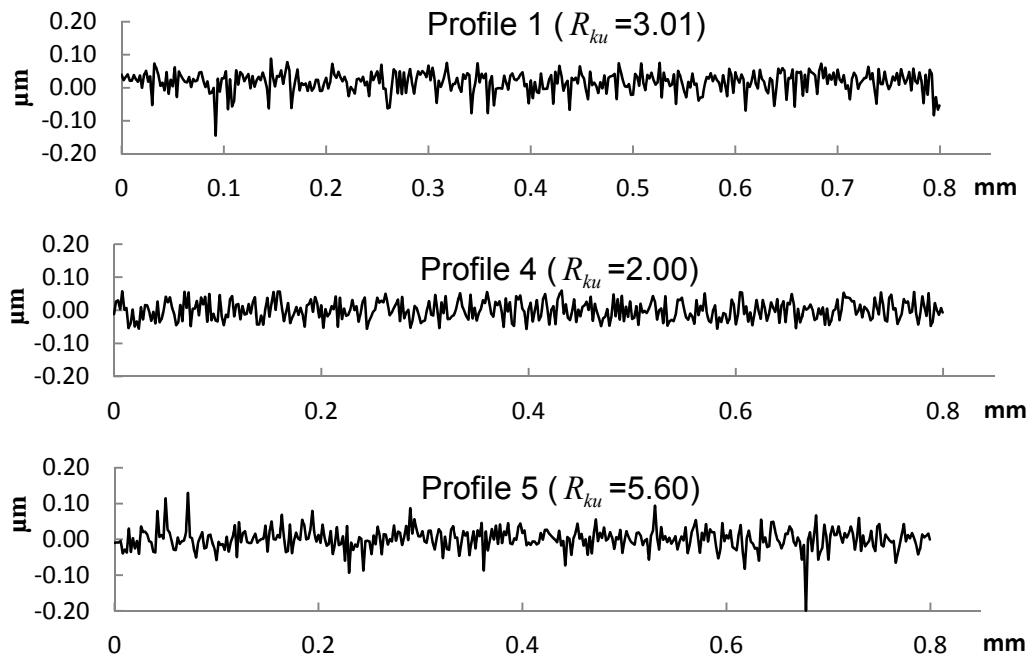


Figure 7-22: Influence of kurtosis on the surface roughness profiles.

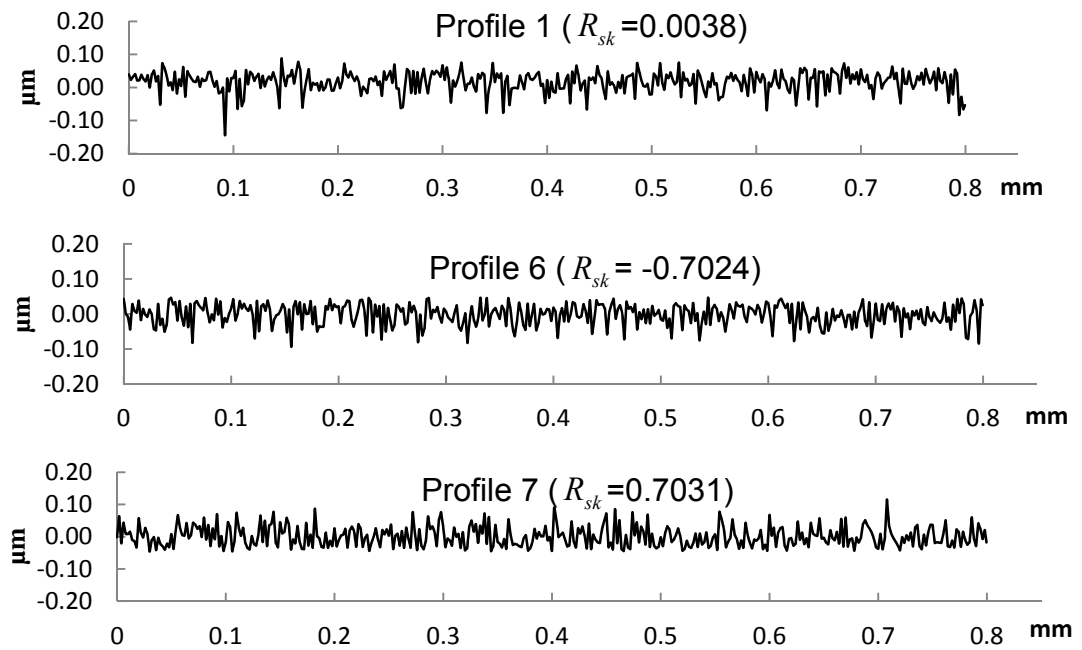


Figure 7-23: Influence of skewness on the surface roughness profiles.

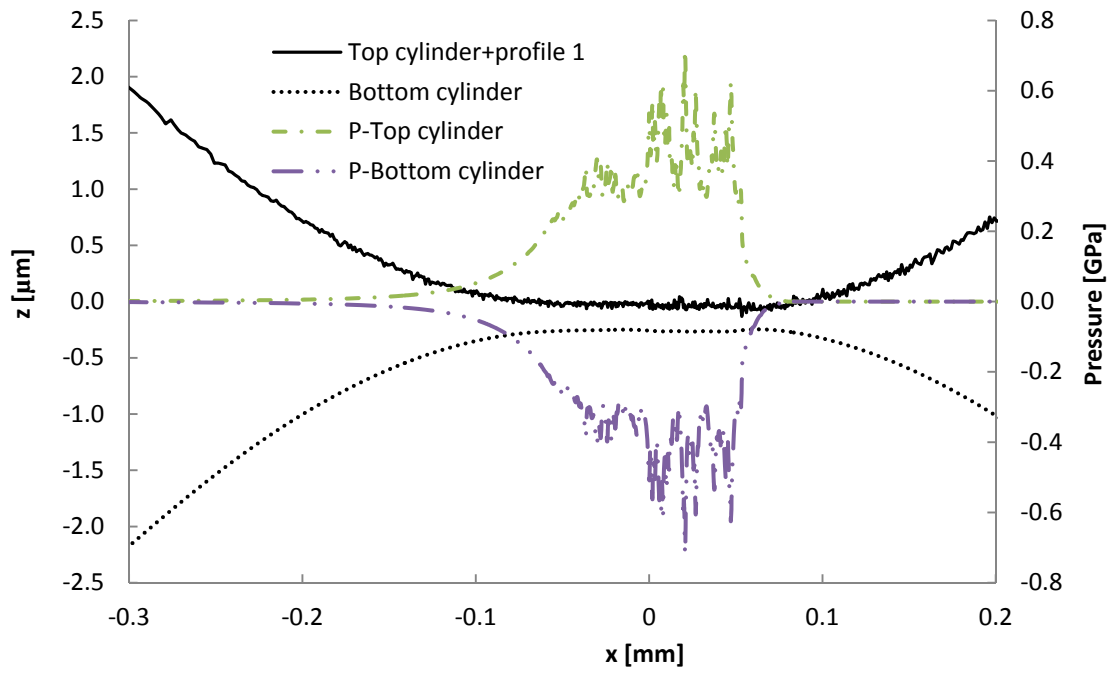


Figure 7-24: Effect of surface roughness when the top cylinder is rough (Profile 1).

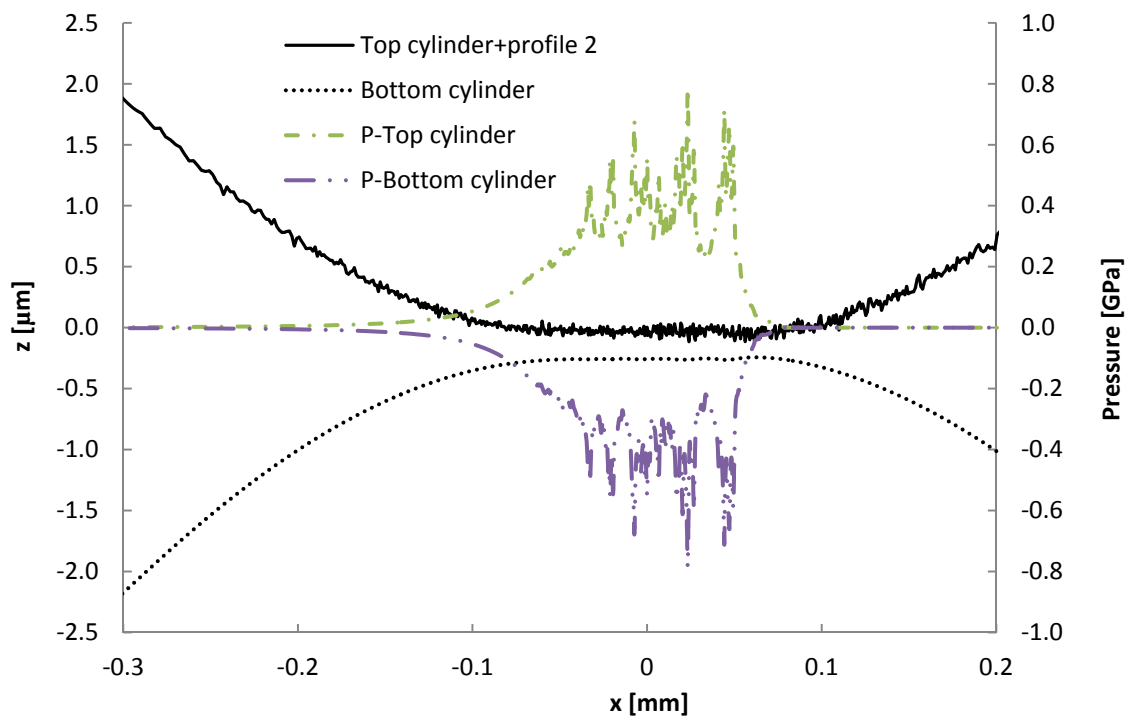


Figure 7-25: Effect of surface roughness when the top cylinder is rough (Profile 2).

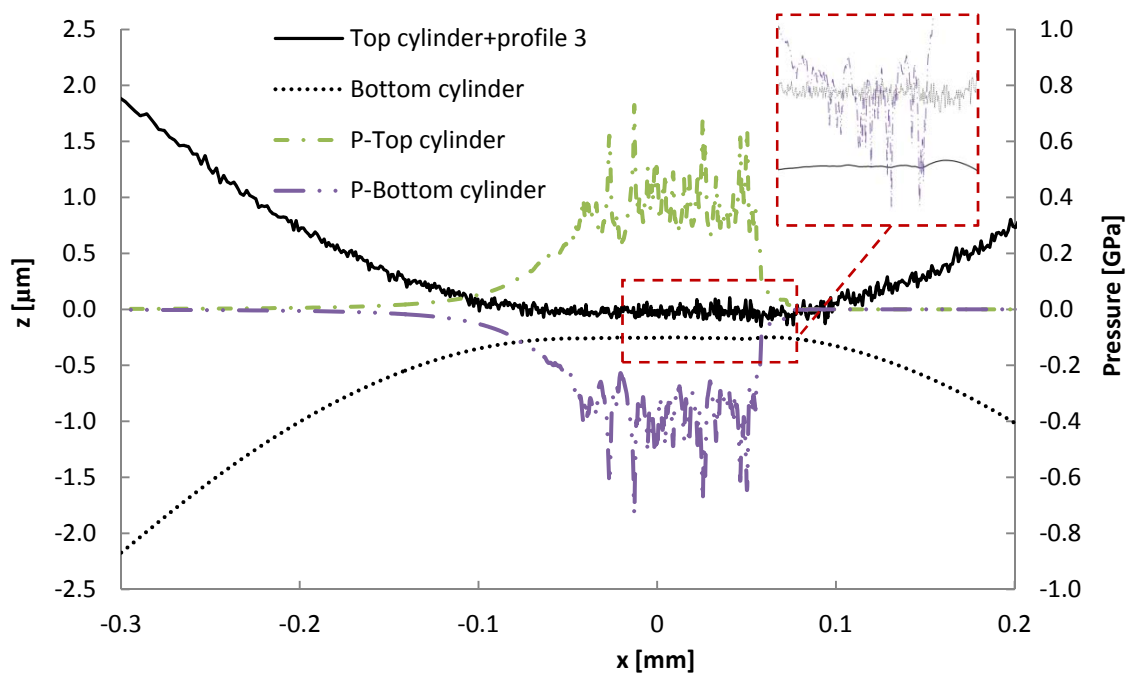


Figure 7-26: Effect of surface roughness when the top cylinder is rough (Profile 3).

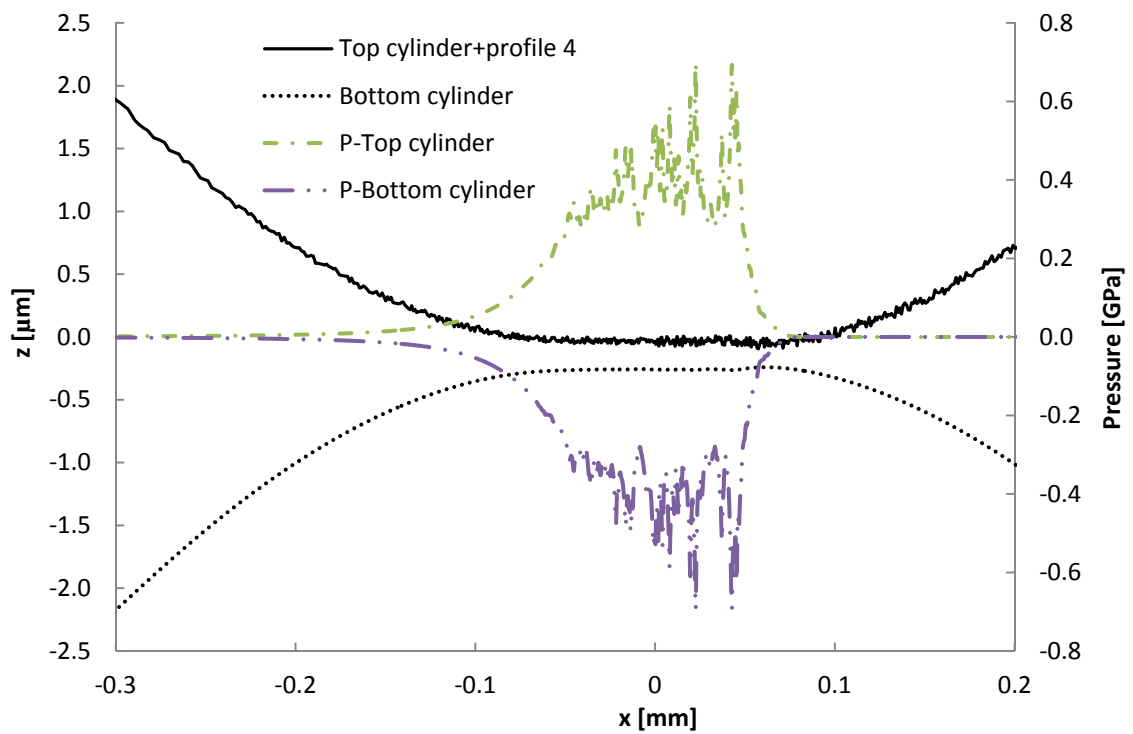


Figure 7-27: Effect of surface roughness when the top cylinder is rough (Profile 4).

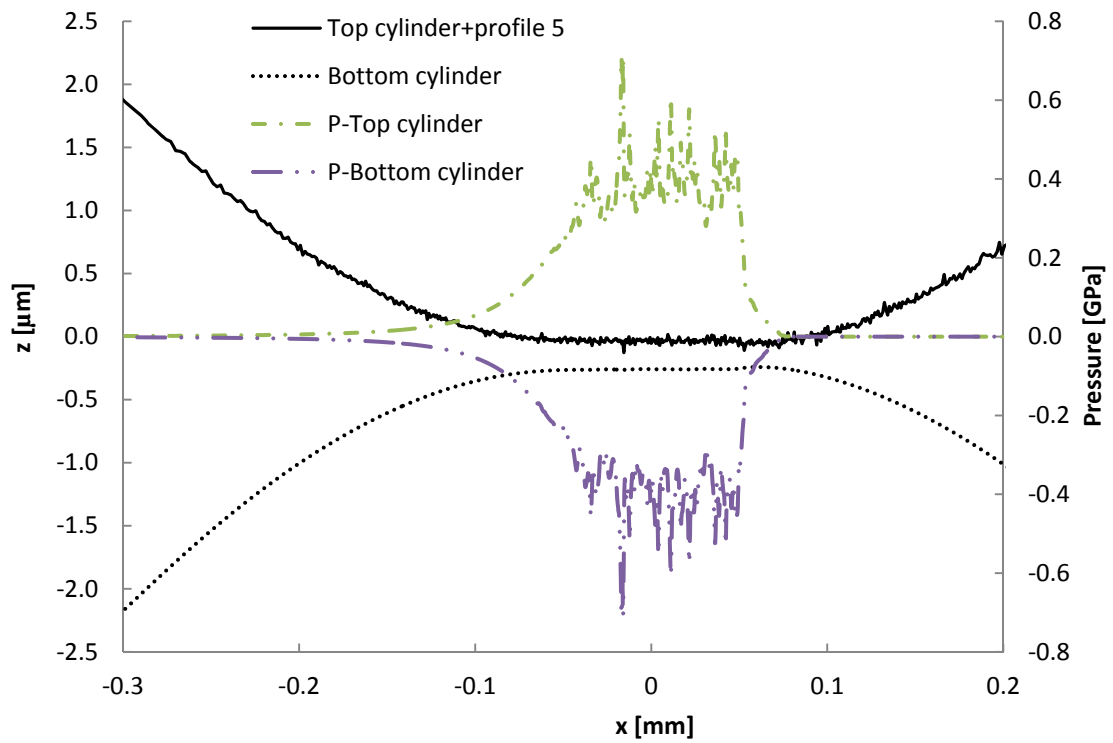


Figure 7-28: Effect of surface roughness when the top cylinder is rough (Profile 5).

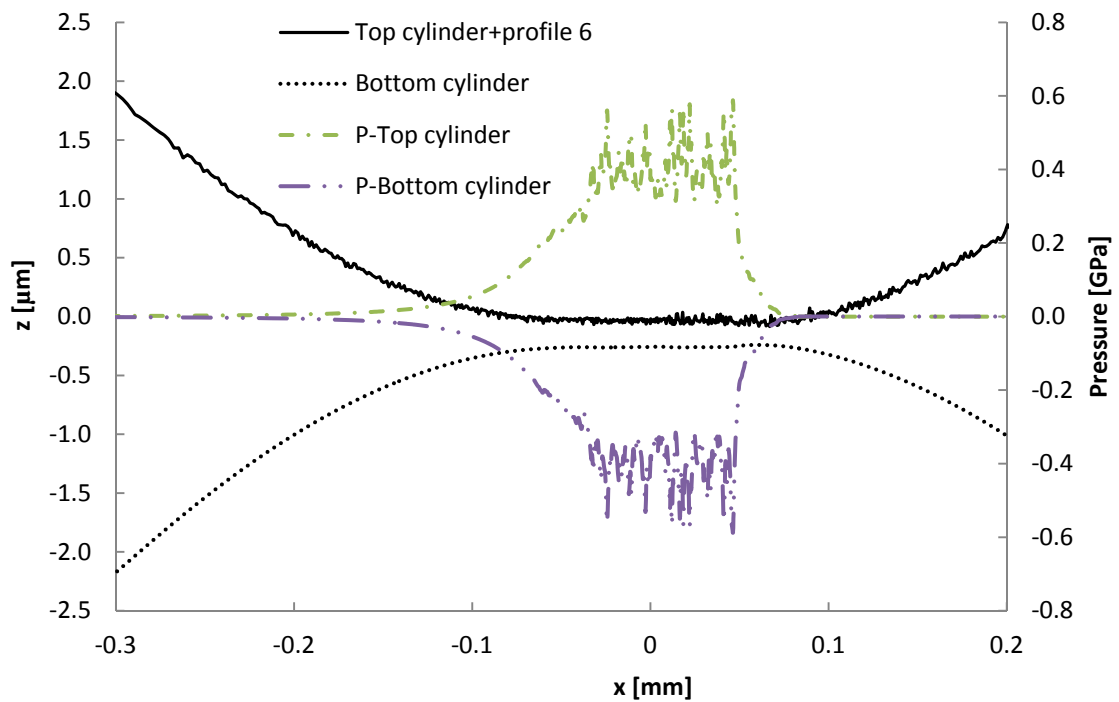


Figure 7-29: Effect of surface roughness when the top cylinder is rough (Profile 6).

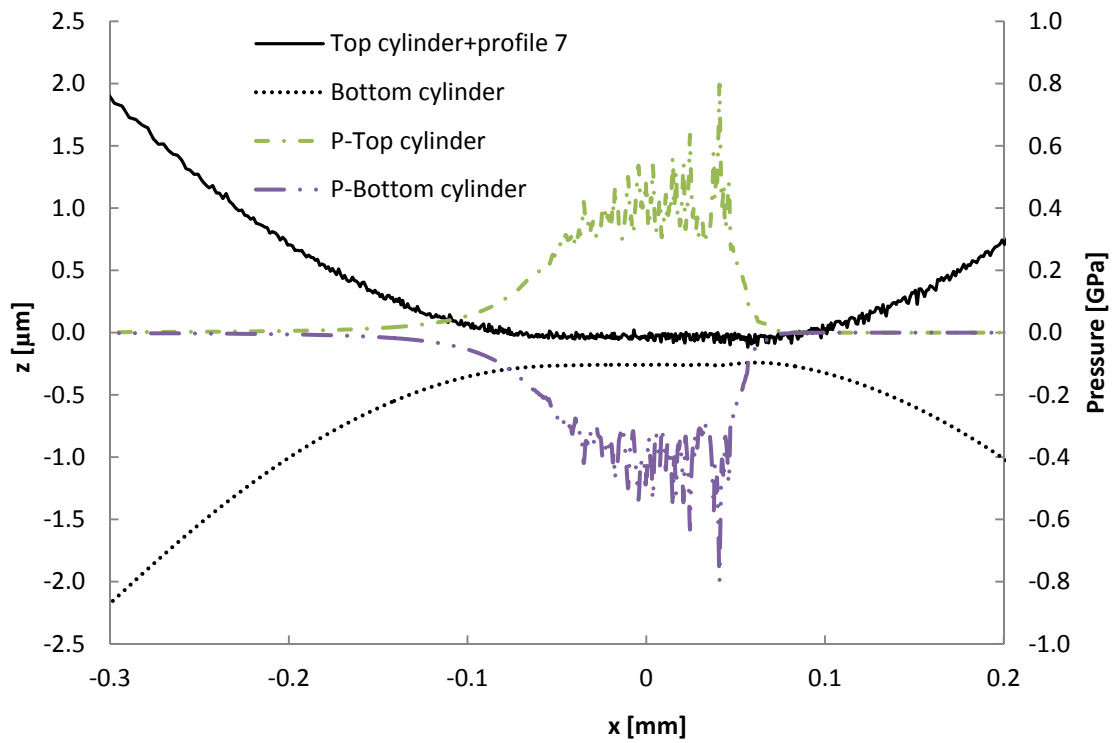


Figure 7-30: Effect of surface roughness when the top cylinder is rough (Profile 7).

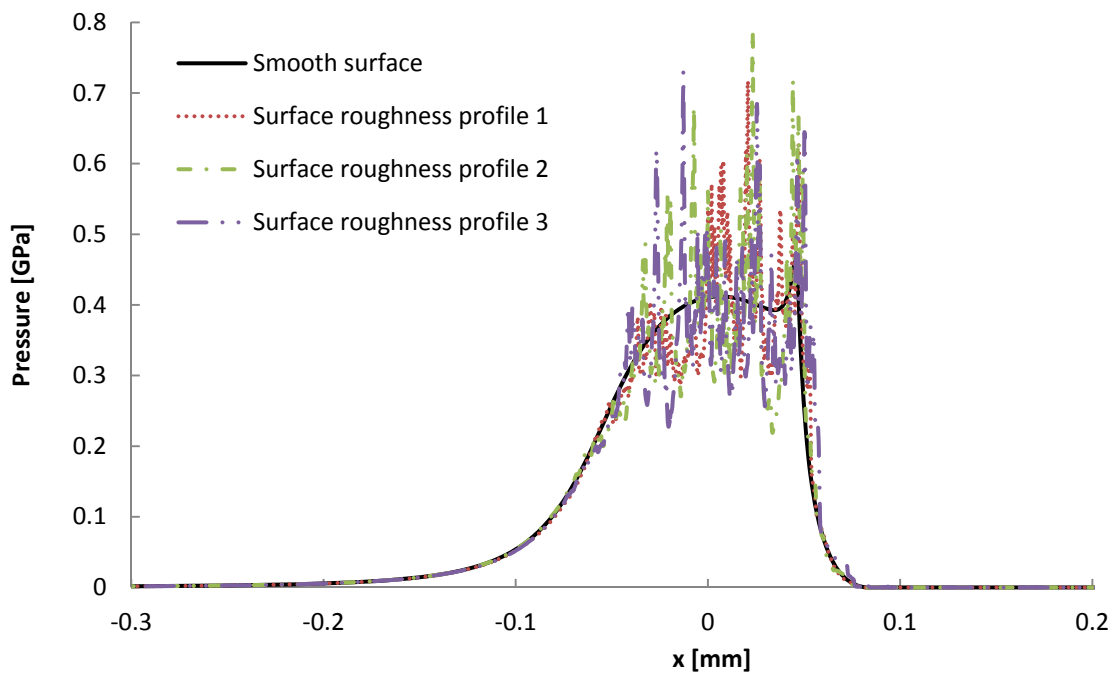


Figure 7-31: Effect of surface roughness on pressure distributions when the average roughness (R_a) is increased.

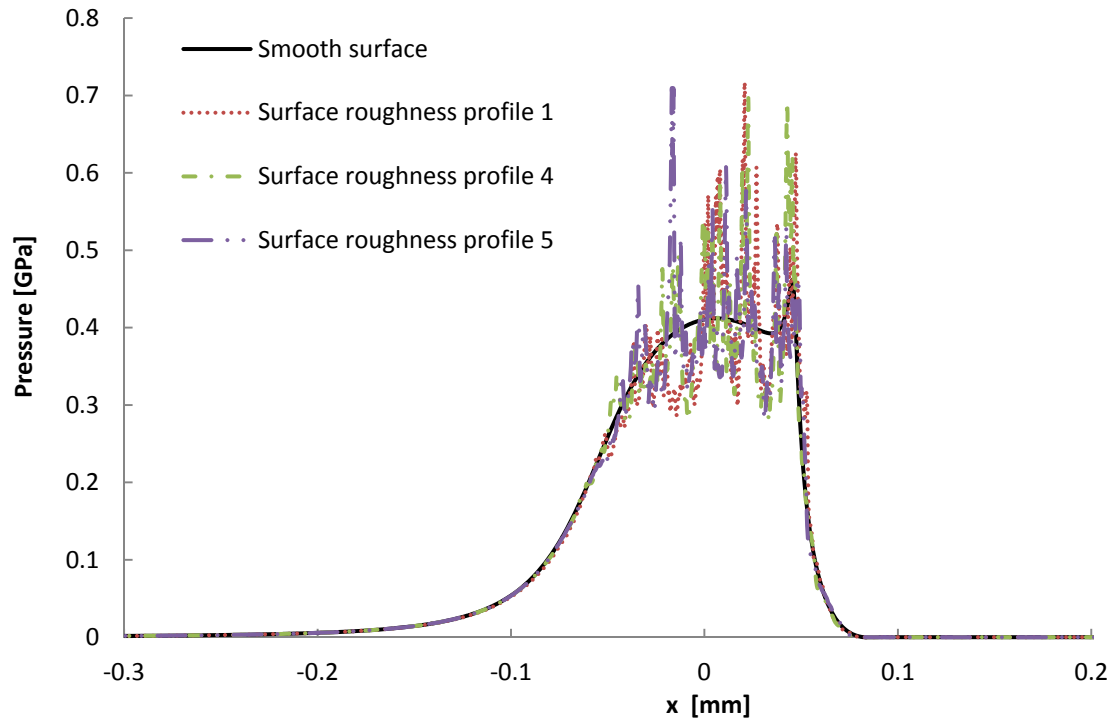


Figure 7-32: Effect of surface roughness on pressure distributions when the kurtosis (R_{ku}) value is varied ($R_{ku}=3$, $R_{ku}>3$ and $R_{ku}<3$).

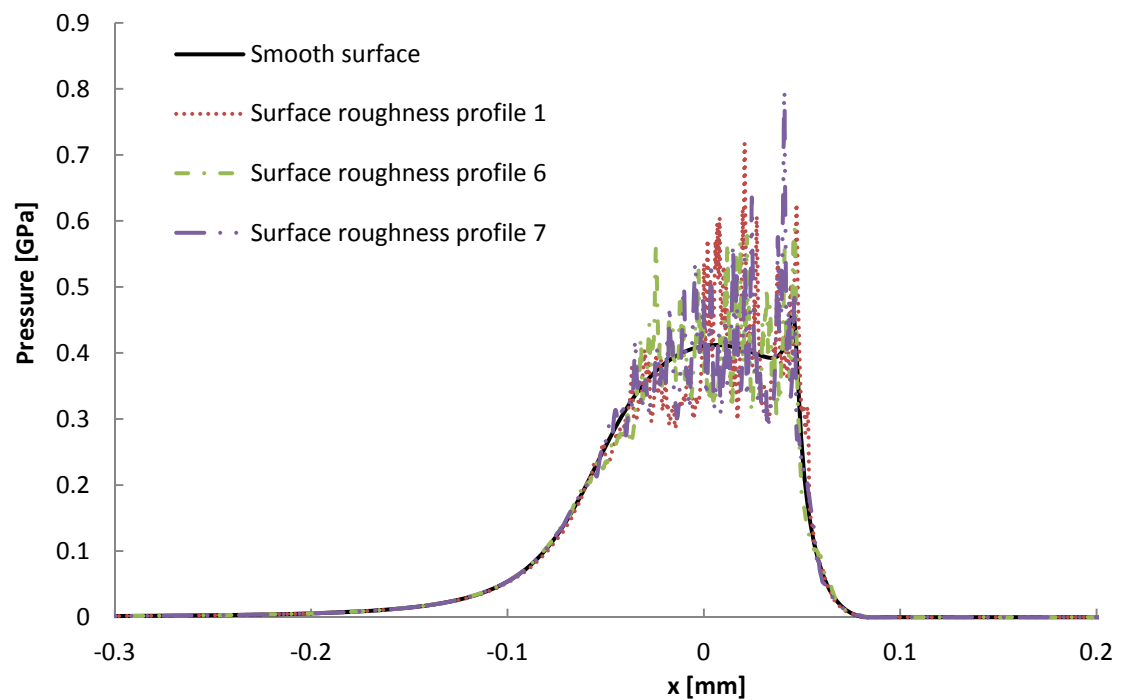


Figure 7-33: The effects of surface roughness on pressure distribution when the value of skewness is 0, -0.70 and 0.72, respectively.

Table 7-4: The average oil film thickness and friction coefficient

Cases	Oil film thickness (μm)	Friction Coefficient	Details
Smooth surface	15.8955	0.00274	$R_a=0.0$
Roughness profile 1	15.8978	0.01519	$R_a=0.02$, $R_{ku}=3$, $R_{sk}=0$
Roughness profile 2	15.9062	0.01922	$R_a=0.04$
Roughness profile 3	15.9130	0.02019	$R_a=0.05$
Roughness profile 4	15.8998	0.01551	$R_{ku}<3.0$
Roughness profile 5	15.8991	0.01466	$R_{ku}>3.0$
Roughness profile 6	15.8987	0.01511	$R_{sk}<0$
Roughness profile 7	15.8994	0.01583	$R_{sk}>0$

The results of the effect of the average surface roughness (R_a) parameter on the EHL problem (Figure 7-24, Figure 7-25, and Figure 7-26) show that the pressure fluctuates according to the surface roughness profile. It seems that the amplitude of the pressures fluctuations increases when R_a increases, as shown in Figure 7-31. The average oil film thickness in the Hertzian contact zone for $R_a = 0.2 \mu\text{m}$, $0.4 \mu\text{m}$, and $0.5 \mu\text{m}$, are $15.9067 \mu\text{m}$, $15.9032 \mu\text{m}$, and $15.9130 \mu\text{m}$ respectively, i.e. the average oil film thickness and the magnitude of pressure fluctuation are directly correlated to the R_a value. In addition, the generated pressure in the fluid film also affects the elastic deformation of the bottom cylinder, especially in the high R_a case, as presented in Figure 7-26. The R_a values affect not only the oil film thickness and the fluctuated pressure but also influence the friction coefficient of the top cylinder. Table 7-4 shows that the friction coefficient is directly correlated to the R_a value.

Figure 7-24, Figure 7-27 and Figure 7-28 show the influence of the kurtosis parameter (R_{ku}) on the pressure distribution and on the surface profile of the cylinders. The kurtosis parameter evidently plays an important role in determining the pressure distribution and the cylinder surface deformation. If the kurtosis is lower than 3, the surface roughness profile will not have several deep valleys or high peaks, as shown in Figure 7-22. When considering the influence of the rough profile with a kurtosis less than 3 on the pressure distribution, it was observed in Figure 7-27 that the generated pressures fluctuate according to the rough profile and that the average oil film thickness is more close to that in a smooth surface contact. For $R_{ku} > 3$, Figure 7-28 shows that the pressure fluctuation amplitude is higher than in the previous case, as shown in Figure 7-32, but the average oil film thickness is lower than the case where $R_{ku} < 3$. It is found that the friction coefficient is inversely correlated to the kurtosis values. This may be due to the fact that the peaks of the rough profile can help reduce the area of contact. The results of this study are consistent with the simulation results of Tayebi and experiment results of Polycarpou [154] and experiments of Sedlaček [155].

Figure 7-24, Figure 7-29, and Figure 7-30 depict the influence of the skewness parameter on the pressure distribution and on the surface profiles of the cylinders. It was found that the skewness values significantly affect the pressure distribution. Negative skewness has less influence on the pressure distribution in the Hertzian contact zone than positive skewness. These effects are more clearly seen by comparing the pressure distributions on the same graph, as shown in Figure 7-33. The skewness parameter also affects the friction coefficient, which increases when the skewness is positive, as shown in Table 7-4.

From the effects of the surface roughness parameters on the EHL problem, it can be concluded that average roughness, kurtosis, and skewness parameters play important roles in the behaviour of the EHL problem. The effects of the surface roughness parameters on pressure distribution and the friction coefficient can be summarised as follows:

- The average surface roughness parameter (R_a) is positively correlated to the magnitude of the pressure fluctuation, the average oil film thickness, and the friction coefficient.
- If kurtosis $R_{ku} < 3$, the average oil film thickness is similar to the one from the smooth contact case. However, if $R_{ku} > 3$, the average oil film thickness and the friction coefficient are reduced.
- A positive skewness value (R_{sk}) will have greater influence on pressure distribution and the friction coefficient than that in the negative skewness case.

Thus, when designing the bearing parts it is necessary to control and minimize the average surface roughness. At the same time, the kurtosis value should be lower than three. In addition, the skewness value of the surface texture should be negative in order to minimize the probability of machinery breakdown caused by surface roughness.

7.4 Thermal effects

The previous chapter showed that the thermal effect plays an important role in the EHL problem. At the same time, the material effect on the elastic deformation of solid parts is also significant. It is evident that the heat transfer rate depends on the fluid and solid properties used in the CFD models, as described in section 6.7. As the materials of the cylinder and plate used in the previous study were the same (mild steel), the influence of the type of material and of the heat generated on the EHL problem will be studied together in this section. In addition, the CFD model for the two cylinders contact (Model 3) will be used in this study instead of the plate and cylinder contact (Model 1).

The aim of this section is to understand the complex characteristics of the thermal effect on the EHL problem when the material of the top and bottom cylinders is different and the surfaces of both cylinders are considered to be rough. The materials used for the top and bottom cylinders are ceramic and brass respectively, as a significant elastic deformation was observed in such contacts. The material properties of ceramic and brass applied to the CFD

model are listed in Table 6-1. The viscosity model used is the non-Newtonian fluid and the lubricant properties presented in Table 6-3 will be used in this study. The pure sliding contact condition ($SRR = 2$) is chosen to simulate the CFD model because the heat generated within the fluid film at the contact zone can be clearly seen in this condition. Furthermore, the surface roughness profiles that were used in section 6.7 are also used in this section.

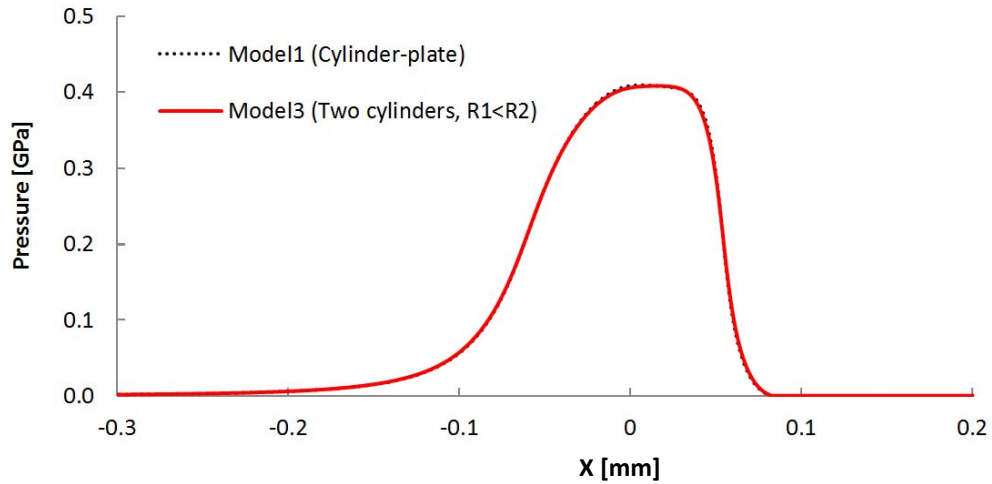


Figure 7-34: Comparison of pressure distributions between models 1 and 3.

Figure 7-34 shows the pressure distributions in the fluid film at the contact area between the CFD models 1 and 3. It can be observed that the profiles of these pressure distributions differ from Figure 7-16 as both results are simulated in different condition; the predicted results in Figure 7-16 are simulated under $SRR = 0$ and isothermal condition, while the results obtained in Figure 7-34 are simulated under $SRR = 2$ with thermal effect. Both pressure profiles in Figure 7-34 are quite similar, but the maximum pressure in the Hertzian contact zone predicted by the CFD model 1 is slightly lower than that the one from predicted by model 3. The pressures generated in the thin fluid film of both models are slightly different, as the elastic deformation of model 3 is different from that of model 1.

The influence of the type of material and of the temperature distribution on the characteristics of the EHL problem is shown in Figure 7-35. Figure 7-35a shows that the maximum temperature at the surface of the top cylinder is 299.5 K,

while the maximum temperature at the surface of the bottom cylinder is 301 K. It can be seen that the temperature at the bottom cylinder surface is higher than that of the top cylinder surface since the bottom cylinder is being rotated and this motion does work on the fluid. This affects viscosity at both surfaces - the viscosity at the surface of the bottom cylinder is lower than that of the top cylinder, as shown in Figure 7-35c. Furthermore, surface roughness has a significant effect on the velocity distribution at the contact area. The maximum velocity of the lubricant increases from 4.4 m/s to 5.3 m/s when surface roughness is considered. The viscosity and the temperature in the fluid film are increased due to the shear stress increase with a rough surface compared to a smooth surface.

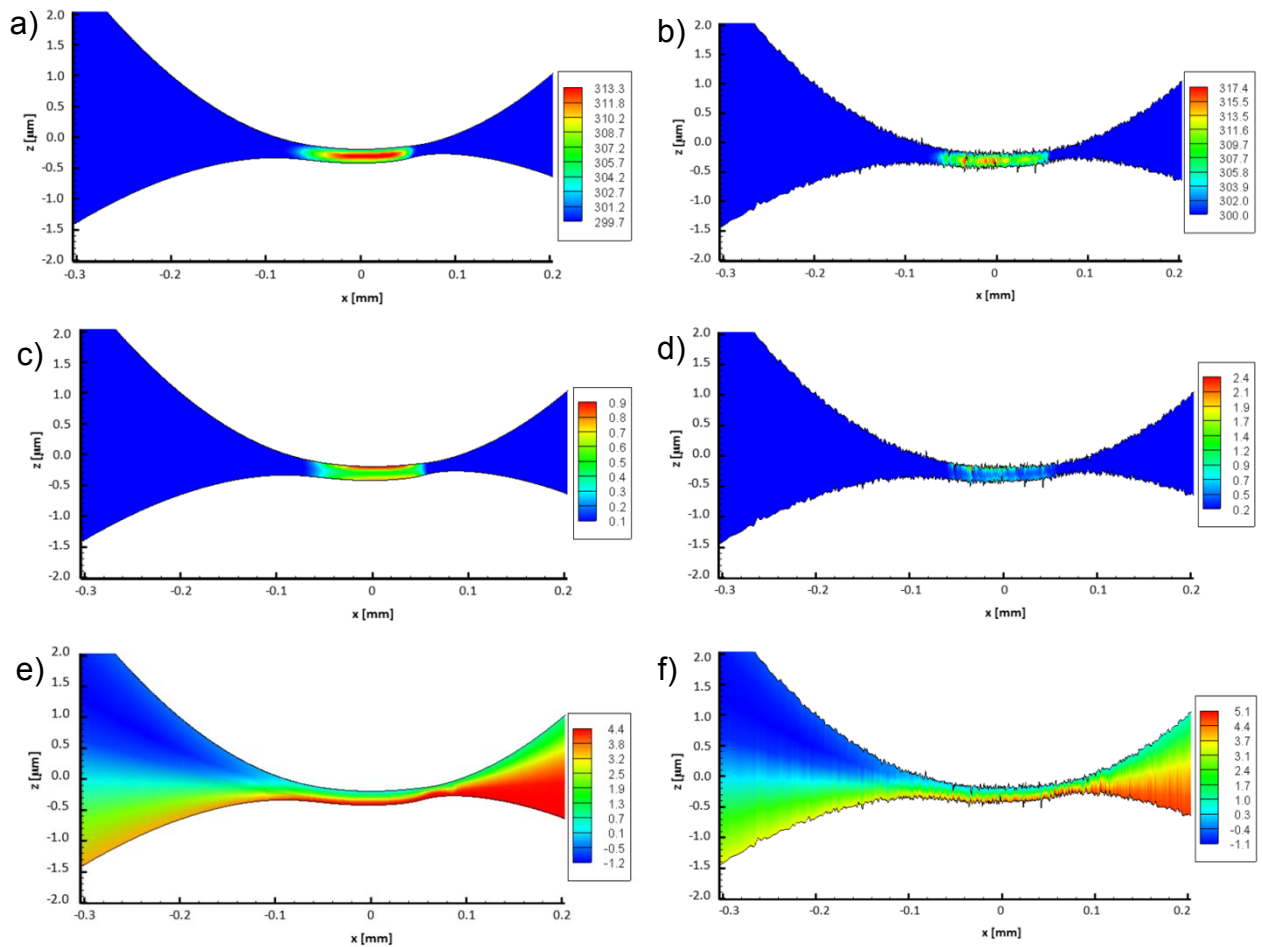


Figure 7-35: Comparison of (a-b) temperature distribution (K), (c-d) viscosity (Pa·s), and (e-f) velocity (m/s) between smooth (left) and rough surfaces (right).

Chapter 8

Conclusion and Future Work

8.1 Conclusion

The developed CFD model can be used to predict the influence of the surface roughness on the EHL line contact problem. Many conditions and parameters are studied using the CFD model, which leads to the following conclusions:

1. The study of the influence of non-Newtonian viscous effects has found that the non-Newtonian fluid model can solve the EHL problem in the case of high shear strain rate with better numerical stability than the Newtonian model, especially in the case of a pure sliding contact. While the pressure spike in the case of the non-Newtonian fluid is lower than in the Newtonian fluid case, the deformation of the cylinder in the case of the non-Newtonian fluid is less than in the Newtonian fluid case.
2. The viscosity of the lubricant plays an important role in the oil film thickness build up. If the viscosity of lubricant increases, the oil film thickness is also increased. On the contrary, the influence of the surface roughness is inversely correlated to the oil film thickness as the pressure fluctuation induced by the surface roughness in the thick film is lower than in the thin film case.
3. The applied load significantly affects the pressure distribution and the deformation of the solids. The pressure distribution and the deformation of the cylinder are directly correlated to the applied load. The effect of surface roughness on the pressure distribution fluctuation amplitude is increased when the applied load increases.

4. Thermal effects on the EHL problem are more significant when the SRR value increases, as the shear strain rate in the oil film increases with a higher SRR value. Thermal effects play an important role on the viscosity of the lubricant, as the viscosity decreases when the temperature increases. Furthermore, the influence of surface roughness is increased when the temperature increases, due to the reduction in viscosity that reduces the film thickness as at this condition. It was also found that the surface roughness is inversely correlated to the change of the SRR values.
5. The velocity significantly influences the film thickness. This relationship is similar to the influence of viscosity, in that the oil film thickness increases with the angular velocity of the cylinder. The influence of surface roughness is reduced when the velocity increases.
6. The influence of the material properties on the deformation of the solids is also significant. The results of the cylinder-plate contact shows that the minimum deformation occurs in the contact between hard materials such as iron and ceramic. This contact also produces the highest pressure. In contrast, the contact with materials of low hardness, for example brass and iron, leads to the higher deformation of the softer material. The CFD model for the contact of two cylinders is also created to predict the EHL problem. The obtained results are similar to the cylinder and plate contact, but the pressure distribution of the cylinder and plate contact is slightly different from the two cylinders contact. The pressure distributions of all CFD models are similar, but the cylinder surface profiles are entirely different. Particularly in the contact between ceramic and brass cylinders, the deformation of both cylinders (CFD model 3) are totally different from the deformation of the plate and the cylinder (CFD model 1).
7. Seven profiles of surface roughness are generated with different combination of R_a , R_{sk} , and R_{ku} parameters using the Pearson distribution function. The surface roughness profiles are applied to the CFD models to predict the influence of surface roughness on the EHL problem and the results are sorted into three groups:

- The average roughness parameter, R_a , influences the maximum pressure and the friction coefficient. The magnitude of fluctuated pressure, average oil film thickness and friction coefficient are directly correlated to R_a value.
- When the kurtosis R_{ku} is above 3, the pressure fluctuation is increased by the frequent occurrence high peaks in the roughness profile. In contrast, when the kurtosis is lower than 3, the average oil film thickness is similar to that of the smooth surface contact case.
- The skewness parameter R_{sk} is very important to the design of a bearing and machine parts, as rough surfaces will have greater influence on the pressure distribution in the Hertzian contact zone if the skewness value is positive.

The above information demonstrates that the developed CFD models can successfully predict the characteristics of the EHL line contact problem. It can be concluded that the surface roughness most affects the EHL in the case of thin fluid film contact, high load, high velocity, low viscosity, high temperature, and high elastic modulus. In addition, the influence of surface roughness is high in the case of a high average surface roughness, the kurtosis being higher than 3, and the skewness value being positive.

8.2 Further research recommendations

This thesis focuses on the development of CFD models for the EHL line contact problem with rough surfaces. The CFD models can be used to predict the characteristics of the fluid flow under smooth and rough surfaces.

However, the developed CFD model becomes numerically unstable and develops negative cell volumes when the film thickness is either very small and or zero, as the CFD model cannot account for dry contact. The pressure distribution will be close to that of the maximum contact pressure (Hertz's contact pressure) when the applied load is greater than what the lubricant film can carry. This will lead to direct contact between solid parts. This generates, a

mixed EHL lubrication case instead of an EHL problem. Therefore, further research on the mixed lubrication case with consideration of surface roughness using CFD techniques should be developed. In order to improve the CFD model for mixed lubrication, some UDF codes are required as follows:

- Some peaks of the roughness profiles will be deformed or eroded after contacting with other surfaces [156-162]. Thus the UDF code for the contact and wear mechanism is needed for the CFD model.
- The UDF code for the pressure balance equation must be modified in the starved lubrication case. The contact load ratio must be taken into consideration when calculating the total force [163, 164].
- The UDF code for the particulate transport of wear debris after the direct contact and wear has occurred [165-167] is also required.
- The UDF code for solving the dynamic mesh has to be modified to remove the negative volume problem when both surfaces are in contact by introducing a non-penetration condition between the solid boundaries.

Furthermore, the results obtained in chapter 7 show significant deformations for the two cylinders contact configuration. It would be interesting if the contact mechanics between solid parts and the fluid are compounded and solved for the whole system, for example, the contact between gears or rollers with lubrication. This idea can be designed by combining the solid mechanics and the fluid mechanics problems together [168]. Figure 8-1 demonstrates the concept of combining the fluid film problem and the solid mechanic problem together.

According to the results of this study, the surface roughness significantly affects the pressure distribution, so the surface of the rollers, as shown in Figure 8-1, should be modelled as rough. The model for solid and fluid interaction may take a long time to compute as the parameters, such as the pressure distribution and temperature rise, will be transferred between the fluid film and the solid parts at every iteration of the calculation.

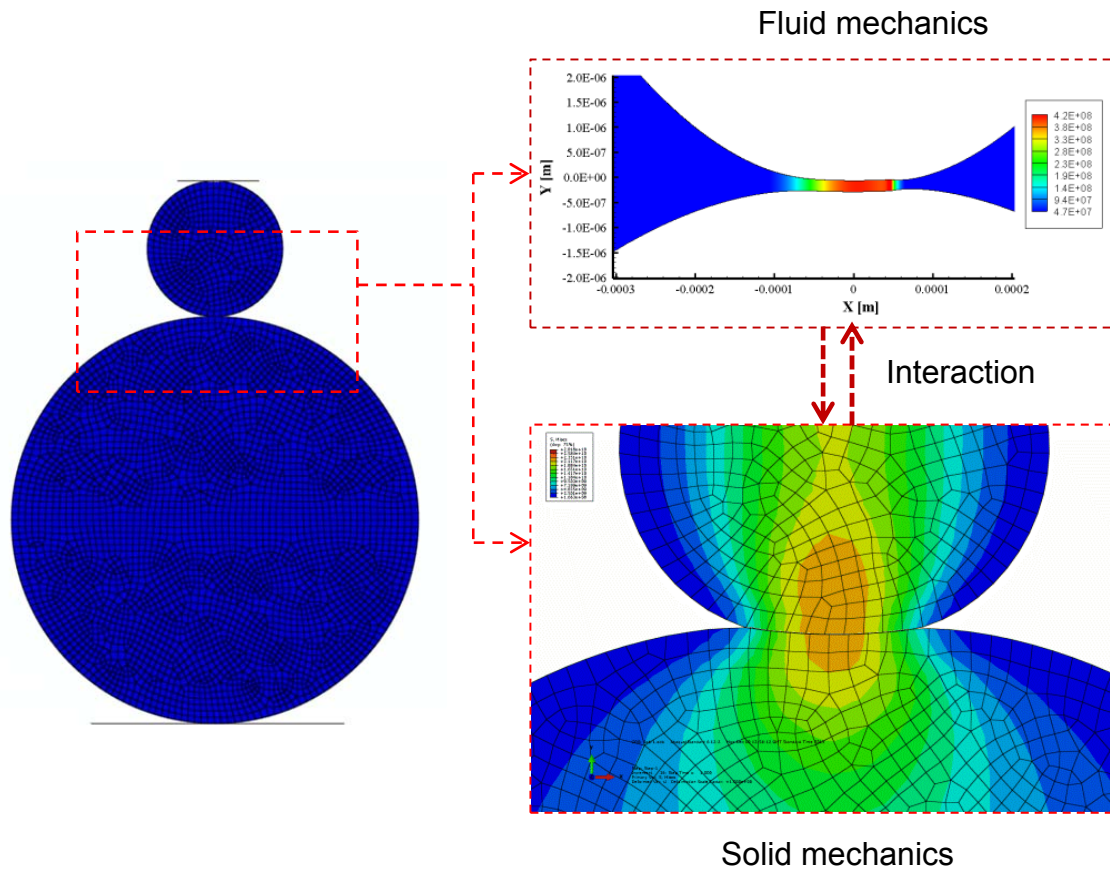


Figure 8-1: Schematic simulation between fluid and solid mechanics

Typically, the finite element method (FEM) is employed to solve solid mechanic problems. This should be linked to the CFD model for solving the complex, stress, strain, and fatigue equations in the solid parts [169-171] . There are many commercial softwares that can be employed to solve this problem, such as ANSYS, Abaqus, and NASTRAN. It is expected that more realistic results could be achieved by using the proposed combination of the solid mechanics and fluid mechanics simulations.

Appendices

Appendix 1	List of published papers
Appendix 2	UDF codes for CFD model parameters
Appendix 3	Numerical solver for the Reynolds equation
Appendix 4	Temperature at the solid surfaces
Appendix 5	Flow charts for the Reynolds equation and the CFD model

Appendix 1: List of published papers and papers on process.

This section of the thesis provides a list of the published papers during the project period. Some parts of this thesis as presented in Chapter 5 and Chapter 6 have been published in the proceedings and journals;

Published papers

- Paper I **Srirattayawong, S. and Gao, S.,** A CFD Study of the EHL Line Contact Problem with Consideration of the Surface Roughness under Varied Loads, *International Conference on Heat Transfer, Fluid Mechanics and Thermodynamics*, pp. 723-729, 2012.
- Paper II **Gao, S., and Srirattayawong, S.,** CFD Prediction of the Effects of Surface Roughness on Elastohydrodynamic Lubrication under Rolling/Sliding Conditions, *Applied Mechanics and Materials*, vol. 184-185, pp. 86-89, 2012.
- Paper III **Srirattayawong, S. and Gao, S.,** A Computational Fluid Dynamics Study of Elastohydrodynamic Lubrication Line Contact Problem with Consideration of Surface Roughness, *Computational Thermal Sciences*, 5(3): pp. 195–213, 2013

Appendix 2: UDF codes for CFD model parameters

```

/*****
/*      The UDFs for calculating the film thickness, Eq. (2.17)      */
*****/

#include "udf.h"
#include "dynamesh_tools.h"
#include "stdlib.h"
#define pi 3.1415926535897932384626433832795

DEFINE_GRID_MOTION(top_cylinder, domain, dt, time, dtime)
{
    Thread *tf = DT_THREAD (dt)      ;
    face_t f      ;
    Node *node_p      ;
    FILE *fr,*fw,*fk,*fs,*fd,*fx,*rg,*ft      ;
    double ho=0.0000001      ; /*      minumum gap, meters      */
    double R=0.02      ;
    double W=0.00002, ratio=0.7      ;
    double
xxx,yyy,Ph,Ho,xx,yy,b,force1,by,cj,pmax,fraction,Er,hmin,Coe_f,sumshear,E      ;

/***** Steel      E= 210,v= 0.30      *****/
/***** Brass      E= 130,v= 0.33      *****/
/***** Ceramic      E= 450,v= 0.15      *****/

    double v1=0.15,E1=4.5E11,load=50000.0      ;
    double *p_array,*deformation,*X,*Y,*deform,v,*deg      ;
    double (*x_array)[ND_ND]      ;
    float hon,iter,iter1,rei,time1=CURRENT_TIME,*rx,*rx1,*rx2,xold      ;
    real NV_VEC (A)      ;
    double aa,bb,sump,dxj,def,force,defect,hs,hom,cont,defectabs,a,al      ;
    int n_faces,j,i,n,ic,k,kn,nu,dr,e,num,ii,Nt,Dt,kk      ;
    double dx=0.00000025,u1=2.5      ;

    n_faces=THREAD_N_ELEMENTS_INT(tf)      ;
    Nt=n_faces+1      ;
    kn=2*n_faces      ;
    deformation=(real * )malloc(Nt*sizeof(double))      ;
    deform=(real * )malloc(Nt*sizeof(double))      ;
    p_array=(real * )malloc(Nt*sizeof(double))      ;
    x_array=(real (*)[ND_ND])malloc(ND_ND*Nt*sizeof(double))      ;
    X=(real * )malloc(Nt*sizeof(double))      ;
    Y=(real * )malloc(Nt*sizeof(double))      ;
    rx=(real * )malloc(Nt*sizeof(float))      ;
    rx1=(real * )malloc(Nt*sizeof(float))      ;
    rx2=(real * )malloc(Nt*sizeof(float))      ;
    deg=(real * )malloc(n_faces*sizeof(double))      ;

    Er=pi/((1.0-v1*v1)/E1)      ;
    E=2.0/((1.0-v1*v1)/E1)      ;

    W=load/(E*R)      ;
    b=4.0*R*sqrt(W*7.0/(2.0*22.0))      ;

    Ph=E*sqrt(W/(2.0*pi))      ;
    Ho=ho/(b*b/R)      ;
    by=b      ;

    fr=fopen("data.txt","r+")      ;
    fscanf(fr,"%E",&hon)      ;
    fclose(fr)      ;

    fx=fopen("iterate.txt","r+")      ;
    fscanf(fx,"%E",&iter1)      ;

```



```

iter=iter1
fclose(fx)

force=0.
pmax = 0.
sumshear=0.
force=0.
fs=fopen("rough_top.txt","r")
ft=fopen("X_top.txt","r+")

begin_f_loop(f, tf)
{
    p_array[f] = F_P(f, tf)
    f_node_loop (f, tf, n)
    {
        node_p = F_NODE(f, tf, n)
        X[f]=(NODE_X(node_p))
        Y[f]=(NODE_Y(node_p))

        if (Y[f]<Y[f-1])
        {
            hmin=Y[f]
            ic=f
        }

        F_AREA(A,f,tf)
        force += F_P(f,tf)*NV_MAG(A)
        sumshear += NV_MAG(F_STORAGE_R_N3V(f,tf, SV_WALL_SHEAR))
        fscanf(ft,"%E",&xold)
        X[f]=xold
    }
end_f_loop(f, tf)
fclose(ft)
Coe_f = sumshear/force

for (i=0;i<n_faces+1;i++)
{
    fscanf(fs,"%E\n",&rei)
    rx[i]=rei
}

fclose(fs)

if (time<3*dtime){
    sump=0.0;
    for(j=1;j<n_faces;j++)
    {
        aa=X[ic]-X[j]
        cj=(X[j]-X[j-1])/2
        sump=sump+(p_array[j]/Er)*(4*cj*log(2*by)+(aa-
cj)*log((aa-cj)*(aa-cj))-(aa+cj)*log((aa+cj)*(aa+cj))) ;
    }
    ho=Y[ic]-X[ic]*X[ic]/(2*R)-sump*0.5 ; }
else
{
    W=force/(E*R)
    by=4.0*R*sqrt(W*7.0/(2.0*22.0))
    ho=hon
}

/*****/

dr=ul*time1/dx

for (i=0;i<n_faces+1;i++)
{
    ii=i+dr
    if (ii>n_faces)
    {

```

```

        ii=ii%n_faces          ;
        rx1[i]=rx[ii]          ;
    }
    else
    {
        rx1[i]=rx[ii]          ;
    }

    ii=ii+1                    ;
}
kk=n_faces+1                  ;
for (i=0;i<n_faces+1;i++)
{
    rx2[i]=rx1[kk]            ;
    kk=kk-1                    ;
}

fs=fopen("rough_top.txt","w+") ;
    for (i=0;i<n_faces+1;i++)
    {
        v=rx2[i]              ;
        fprintf(fs,"%E\n",v)   ;
    }
fclose(fs)                    ;

defect=force-load              ;
defectabs=abs(force-load)      ;

if (iter<1)
{
    cont=0                      ;
    iter=iter+1                 ;
}
else
{
    cont=1E-13                  ;
    iter=0                      ;
}

if(defect>0)
    {defect=cont*defect          ;}
else
    {defect=-(cont)*defect       ;}

ho=ho+defect                    ;
Message ("hon = %E, ho= %E\n",hon,ho) ;
fw=fopen("data.txt","w+")      ;
fprintf(fw,"%E",ho)            ;
fclose(fw)                      ;
fx=fopen("iterate.txt","w+")    ;
fprintf(fx,"%E",iter)          ;
fclose(fx)                      ;

/*****/

SET_DEFORMING_THREAD_FLAG (THREAD_T0 (tf)) ;
if (! Data_Valid_P())
return ;
fk=fopen("data2.txt","a+")      ;
fprintf
(fk,"Time=%f,P=%E,force=%f,Load=%f,defect=%E,ho=%E,Y=%E,Hmin=%E,Friction_coef.
=%f\n",time,p_array[ic],force,load,defect,ho,Y[ic],hmin,Coe_f);
fclose(fk)                      ;

for(i=0;i<n_faces;i++)
{
    deg[i]=atan(abs((R-Y[i])/X[i])) ;
    if (X[i]<0&&(Y[i]-R)<0) {deg[i]=deg[i]+180 ;}
    if (X[i]>0&&(Y[i]-R)<0) {deg[i]=deg[i]+270 ;}
}

```

```

        if (i==0)
            {deformation[i]=Y[i]                ;}
        if ((i>0)&&(i<n_faces))
            { sump=0.0                            ;
              for(j=1;j<n_faces;j++)
              {
                  aa=X[i]-X[j]                    ;
                  cj=(X[j]-X[j-1])/2              ;
                  sump=sump+(p_array[j]/Er)*(4*cj*log(2*by)+(aa-
cj)*log((aa-cj)*(aa-cj))-(aa+cj)*log((aa+cj)*(aa+cj))) ;
              }

deformation[i]=ho+X[i]*X[i]/(2*R)+sump+ratio*sin(deg[i])*rx[i]    ;
            }
        if (i==n_faces)
            {deformation[i]=Y[i]                ;}
    }

begin_f_loop (f, tf)
{
    f_node_loop (f, tf, n)
    {
        node_p = F_NODE (f, tf, n)                ;
        yyy= NODE_Y (node_p)                        ;
        xxx= NODE_X (node_p)                        ;
        if (Y[f]==yyy)
        {
            if (NODE_POS_NEED_UPDATE (node_p))
                NODE_POS_UPDATED (node_p)          ;
            NODE_Y (node_p)=deformation[f]          ;
            NODE_X (node_p)=X[f]+ratio*rx[f]*cos(deg[f]) ;
        }
    }
}
end_f_loop (f, tf)

free(p_array)      ;
free(x_array)      ;
free(deformation)  ;
free(X)            ;
free(Y)            ;
free(rx)           ;
free(rx1)          ;
free(rx2)          ;

}

```

```

-----
/*****
/* The UDFs for calculating the viscosity of lubricant, Eq. (2.21) */
/*****
#include "udf.h"
#include "mem.h"
DEFINE_PROPERTY (cell_viscosity, cell, thread)
{
    double viscosity,viscosityn,alfa,no,bb,z,pv,aa ;
    double pressure=C_P(cell,thread) ; /* pressure, Pa */
    no=0.01 ; /* Absolute viscosity, p=0, Pa-s */
    pv=13.4010e-9 ; /* pressure-viscosity coef., 1/Pa */
    alfa=log(no)+9.67 ;
    z=pv/((5.1e-9)*(alfa)) ;
    aa=1.0+pressure*5.1e-9 ;
    bb=-1.0+pow(aa,z) ;
    viscosity=no*exp(alfa*bb) ;
    viscosityn=0.5*viscosity+0.5*C_MU_L(cell,thread) ;
    return viscosityn ;
}
-----

```

```

/*****
/* The UDFs for calculating the viscosity of lubricant, Eq. (2.23) */
*****/

#include "udf.h"
DEFINE_PROPERTY(cell_viscosity, cell, thread)
{
float viscosity,const1,no,z,pv,To,gram ;
float P = C_P(cell,thread); /* pressure, Pa */
float T = C_T(cell,thread);
no = 0.01 ; /* Absolute viscosity, p=0, Pa-s */
pv = 13.4010E-9 ; /* Pressure-viscosity coef., 1/Pa */
const1 = log(no)+9.67 ;
To = 298.15 ; /* Inlet temperature, K */
Gram = 0.0476 ; /*Temperature-viscosity coefficient,1/K */
Z = pv/((5.1E-9)*(const1)) ;
Viscosity = no*exp(const1*(-1.0+pow(1.0+P*5.1E-9,z))-gram*(T-To));
Viscosity = 0.5*viscosity+0.5*C_MU_L(cell,thread) ;
return viscosity ;
}

-----

/*****
/* The UDFs for calculating the viscosity of lubricant, Eq. (2.35) */
*****/

#include "udf.h"
#include "mem.h"
DEFINE_PROPERTY(cell_viscosity, c, t)
{
Double
viscosity,viscoroe,viscarreau,const1,n,bb,z,pv,To,shear,gram,shear0,value,asinh,S0,shearmin,const2,viscohoup,no ;
double P=C_P(c,t) ; /* Pressure, */
double T = C_T(c,t) ; /* Temperature, */
no=0.01 ; /* viscosity at low shear strain rate,p=0, Pa-s */
pv=13.4010E-9 ; /* pressure-viscosity coef., 1/ */
To=298.15 ; /* Inlet temperature, K */
gram=0.0476 ; /* thermo viscos constant., 1/K */
shear0=5.0E6 ; /* temperature-viscosity coefficient of lubricant, 1/K */
const1=log(no)+9.67 ;
z=pv/((5.1e-9)*(const1)); /* Roelands' P-viscosity index */
S0=gram*(To-138.0)/ ;
const2=const1*pow((1+(P*5.1E-9)),z)*(S0/(To-138.0)) ;
viscohoup=no*exp(const1*(pow(1.0+P*5.1E-9,z)-1)*(T-138.0)/(To-138.0))-const2*(T-To) ;
shearmin=1.0e-8 ;
shear=sqrt(2*(pow(C_DUDX(c,t),2)+pow(C_DVDY(c,t),2))+pow(C_DUDY(c,t)+C_DVDX(c,t),2)+pow(C_DUDZ(c,t),2)+pow(C_DVDZ(c,t),2)) ;
if (shear>=shearmin)
{
value=viscohoup*shear/shear0 ;
if (value>0)
{asinh= log(value+sqrt(value*value+1.0)) ;}
else
{asinh= -log(-value+sqrt(value*value+1.0)) ;}
viscosity=(shear0/shear)*asinh ;
}
else
{
viscosity=viscohoup ;
}
}

```

```

viscosityn=0.5*viscosity+0.5*C_MU_L(cell,thread)      ;
return viscosity      ;
}

-----
/*****
/* The UDFs for calculating the density of lubricant, Eq. (2.36) */
/*****
#include "udf.h"
#include "mem.h"
DEFINE_PROPERTY(cell_density,c,t)
{
double density,den,densityn      ;
double P = C_P(c,t)      ;
/* To define the density of lubricant at atmospheric pressure */
den=850.0      ;
density=den*(1.0+(P*0.59e-9)/(1.0+P*1.7e-9))      ;
densityn=0.5*density+0.5*C_R(c,t)      ;
return densityn      ;
}

-----
/*****
/* The UDFs for calculating the density of lubricant, Eq. (2.37) */
/*****
#include "udf.h"
DEFINE_PROPERTY(cell_density,c,t)
{
double density,den,densityn,beta,To      ;
double P = C_P(c,t)      ;
double T = C_T(c,t)      ;
To=298.15      ; /* Inlet temperature of lubricant, K */
den=850.0      ; /* Inlet density of lubricant, kg/m^3 */
beta=4.5e-4      ; /* Coefficient of thermal expansion, 1/K */
density = den*(1.0+(P*0.59E-9)/(1.0+P*1.68348E-9))*(1.0-beta*(T-To));
density=0.5*density+0.5*C_R(c,t)      ;
return density      ;
}

-----
/*****
/* The UDFs for calculating the heat source, Eq. (4.8) and Eq. (4.9)*/
/*****
#include "udf.h"
#include "mem.h"
DEFINE_SOURCE(heat_source, c, t, dS, eqn)
{
double Qshear,Qcomp,source      ;
double viscosity,den,beta,C1,Dden      ;
den=846.0      ; /* Inlet density of lubricant, kg/m^3 */
beta=4.5e-4      ; /* Coefficient of thermal expansion, 1/K */
C1=2.0*(pow(C_DUDX(c,t),2)+pow(C_DVDY(c,t),2))+pow(C_DUDY(c,t)+C_DVDX(c,t),2)+pow(C_DUDZ(c,t),2)+pow(C_DVDZ(c,t),2)-(2.0/3.0)*pow(C_DUDX(c,t)+C_DVDY(c,t),2)      ;
viscosity=C_MU_L(c,t)      ;
Qshear=viscosity*C1      ;
Dden=den*beta      ;
comp=(C_T(c,t)/C_R(c,t))*Dden*(C_U(c,t)*C_P_G(c,t)[0]+C_V(c,t)*C_P_G(c,t)[1])      ;
source=Qshear+Qcomp      ;
return source      ;
}
-----

```

```

%***** %
%   The MATLAB code for generating a surface roughness %
%   by using the Pearson function with mean, standard deviation, %
%   skewness and kurtosis. %
%***** %
clear ;
% Input the surface roughness parameters %
Rq=0.0315 ;
Rsk= -0.7 ;
Rku= 3.000 ;
n=978 ;
dx=0.0005 ;
L= 0.0 ;
MINB=-0.1 ;
MAXT=0.03 ;
% [r,type]= pearsrnd(Mean,Standard deviation,Skewness,Kurtosis) %
%   Type 0: Normal distribution (Gaussian,Rku=3, Rsk=0 ) %
%   Type 1: Four-parameter beta %
%   Type 2: Symmetric four-parameter beta %
%   Type 3: Three-parameter gamma %
%   Type 4: Not related to any standard distribution. Density %
%   proportional %
%   to (1+((x-a)/b)^2)^(-c) * exp(-d*arctan((x-a)/b)). %
%   Type 5: Inverse gamma location-scale %
%   Type 6: F location-scale %
%   Type 7: Student's t location-scale %
Ra=0.02 ;
fName = 'output.txt' ;
fid=fopen('output.txt','w' ) ;
[r,type]= pearsrnd(Ra,Rq,Rsk,Rku,n,1) ;
sprintf('Pearson type= %2.0f',type)
for j=1:n
    T(j)=r(j) ;
    Y5(j)=L ;
    L=L+dx ;
end
fprintf(fid,'%5.8f\r\n', r) ;
fclose(fid) ;

Ra1=sum(abs(T(:)))/n ; % Average roughness
Rq1=sqrt(sum(T(:).^2)/n) ; % RMS roughness
Rsk1=sum(T(:).^3)/(n*Rq1^3) ; % Skewness
Rku1=sum(T(:).^4)/(n*Rq1^4) ; % Kurtosis

Ra2=mean(T) ; % Average roughness
Rq2=std(T) ; % RMS roughness
Rsk2=skewness(T) ; % Skewness
Rku2=kurtosis(T) ; % Kurtosis

ErRa=abs(Ra-Ra1)*100/Ra ;
ErRq=abs(Rq-Rq1)*100/Rq ;
ErRsk=abs(Rsk-Rsk1)*100/Rsk ;
ErRku=abs(Rku-Rku1)*100/Rku ;
Error=(ErRa+ErRq+ErRsk+ErRku)/4.0 ;
sprintf('Input parameters')
sprintf('Ra= %7.4f, Rq= %7.4f, Rsk= %7.4f, Rku= %7.4f',Ra,Rq,Rsk,Rku)
sprintf('The parameters of generated roughness')
sprintf('Ra1= %7.4f, Rq1= %7.4f, Rsk1= %7.4f, Rku1= %7.4f',Ra1,Rq1,Rsk1,Rku1)
sprintf('The statistical parameters of generated roughness')
sprintf('Ra2= %7.4f, Rq2= %7.4f, Rsk2= %7.4f, Rku2= %7.4f',Ra2,Rq2,Rsk2,Rku2)

```

```

***** Expanding the rough profile by 2 space*****%
for j=1:n
    R1(2*j-1)=T(j) ;
    if (j==n)
        R1(2*j)=T(j) ;
    else
        R1(2*j)=(T(j)+T(j+1))/2.0 ;
    end
end

m=2*n ;
fid=fopen('new_2rough.txt','w') ;
L=0 ;
dx=0.0005/2.0 ;
for k=1:m
    fprintf(fid,'%f \r\n',R1(k)) ;
    H0(k)=R1(k) ;
    Y1(k)=L ;
    L=L+dx ;
end
fclose=(fid) ;

Ra3=sum(abs(R1(:)))/m ; % Average roughness
Rq3=sqrt(sum(R1(:).^2)/m) ; % RMS roughness
Rsk3=sum(R1(:).^3)/(m*Rq3^3) ; % Skewness
Rku3=sum(R1(:).^4)/(m*Rq3^4) ; % Kurtosis

sprintf('Ra3= %7.4f, Rq3= %7.4f, Rsk3= %7.4f, Rku3=
%7.4f',Ra3,Rq3,Rsk3,Rku3)
***** Expanding the rough profile by 3 space*****%

for j=1:n
    if (j==n)
        Lx=T(j-1)-T(j) ;
        dx3=Lx/3.0 ;

        RN(3*j-2)=T(j)-2.0*dx3 ;
        RN(3*j-1)=T(j)-dx3 ;
        RN(3*j)=T(j) ;
    else
        Lx=T(j+1)-T(j) ;
        dx3=Lx/3.0 ;

        RN(3*j-2)=T(j) ;
        RN(3*j-1)=T(j)+dx3 ;
        RN(3*j)=T(j)+2.0*dx3 ;
        RN(4*j)=T(j+1) ;
    end
end
v=3*n ;
fid3=fopen('new_3rough.txt','w') ;
L=0 ;
dx=0.0005/3.0 ;
for k=1:v
    fprintf(fid3,'%d \r\n',RN(k)) ;
    H1(k)=RN(k) ;
    Y2(k)=L ;
    L=L+dx ;
end
fclose=(fid3) ;

```

```

%***** Expanding the rough profile by 4 space*****%

for j=1:m
    R2(2*j-1)=R1(j) ;
    if (j==m)
        R2(2*j)=R1(j) ;
    else
        R2(2*j)=(R1(j)+R1(j+1))/2.0 ;
    end
end

t=2*m ;
fid4=fopen('new_4rough.txt','w' ) ;
L=0 ;
dx=0.0005/4.0 ;
for k=1:t
    fprintf(fid4,'%f \r\n',R2(k)) ;
    H2(k)=R2(k) ;
    Y3(k)=L ;
    L=L+dx ;
end
fclose(fid4) ;

subplot(3,1,3) ;
plot(Y3,H2,'LineWidth',0.4,'Color',[.6 0 0])
title('Surface roughness profile, space=dx/4') ;
xlabel('X (mm)') ;
ylabel('Y (micrometre)') ;

node =50 ;
for k=1:node
    G(k)=T(k) ;
    G0(k)=H0(k) ;
    G1(k)=H1(k) ;
    G2(k)=H2(k) ;
end
figure(1) ;
subplot(4,1,1) ;
plot(G,'-bx','LineWidth',0.4,'Color',[.6 0
0],'MarkerEdgeColor','k','MarkerFaceColor','g','MarkerSize',5);
title('Space=Dx') ;
ylabel('Y (micrometre)') ;

subplot(4,1,2) ;
plot(G0,'-bx','LineWidth',0.4,'Color',[.6 0
0],'MarkerEdgeColor','k','MarkerFaceColor','g','MarkerSize',5);
title('Space=Dx/2') ;
ylabel('Y (micrometre)') ;

subplot(4,1,3) ;
plot(G1,'-rx','LineWidth',0.4,'Color',[.6 0
0],'MarkerEdgeColor','k','MarkerFaceColor','g','MarkerSize',5);
title('Space=Dx/3') ;
ylabel('Y (micrometre)') ;

subplot(4,1,4) ;
plot(G2,'-gx','LineWidth',0.4,'Color',[.6 0
0],'MarkerEdgeColor','k','MarkerFaceColor','g','MarkerSize',5);
title('Space=Dx/4') ;
ylabel('Y (micrometre)') ;

```



```

figure(2)                                ;
subplot(3,1,1)                            ;
plot(Y5,T,'LineWidth',0.4,'Color',[.6 0 0])
title('A generated surface roughness') ;
ylim([-0.2 0.2])                          ;
xlabel('X (mm)')                          ;
ylabel('Y (micrometre)')                  ;

subplot(3,2,3)                            ;
histfit(T,20)
title('Histogram and a Normal distribution') ;
xlim([-0.2 0.2])                          ;
subplot(3,2,4)                            ;
ksdensity(r,'width',0.01)                  ;
title('A probabilitlity density estimate') ;
xlim([-0.2 0.2])                          ;

%***** Bounded the maximum and the minimum data *****%

for k=1:m
    if (Rl(k)>MAXT)
        Rc(k)=MAXT                        ;
    end

    if (Rl(k)<MINB)
        Rc(k)=MINB                        ;
    end
    if ((Rl(k)>=MINB)&(Rl(k)<=MAXT))
        Rc(k)=Rl(k)                      ;
    end
end
figure(3)                                ;
subplot(3,1,1)                            ;
plot(Rc,'LineWidth',0.4,'Color',[.6 0 0])
ylim([-0.2 0.2])                          ;
title('A generated surface roughness') ;
xlabel('X (mm)')                          ;
ylabel('Y (micrometre)')                  ;

Ra6=sum(abs(Rc(:)))/m                      ;           % Average roughness
Rq6=sqrt(sum(Rc(:).^2)/m)                  ;           % RMS roughness
Rsk6=sum(T(:).^3)/(m*Rq6^3)                ;           % Skewness
Rku6=sum(T(:).^4)/(m*Rq6^4)                ;           % Kurtosis

subplot(3,2,3)                            ;
histfit(Rc,40)
title('Histogram and a Normal distribution') ;
xlim([-0.2 0.2])                          ;
subplot(3,2,4)                            ;
ksdensity(Rc,'width',0.01)                  ;
title('A probabilitlity density estimate') ;
xlim([-0.2 0.2])                          ;

```

```

%%%%%%%%%%%%%%%%%%%%%%%%%%%%%%%%%%%%%%%%%%%%%%%%%%%%%%%%%%%%%%%%%%%%%%%%
% The code for filtering a surface roughness (Gaussian filter).      %
% The equations used are the algorithm for evaluation that was        %
% derived by Krytek [85].                                           %
%%%%%%%%%%%%%%%%%%%%%%%%%%%%%%%%%%%%%%%%%%%%%%%%%%%%%%%%%%%%%%%%%%%%%%%%
clear                                ;
eps=1^-3                            ;
alpha=0.46971863934982566688 ;
lc=0.25                             ; % cut-off value (mm)          %
dx=0.0005                           ; % spacing of data point (mm) %
y = xlsread('rough1.xls');           % Primary roughness profile (micrometre) %
n=1600                              % Number of data points        %
s=dx/(lc*alpha)                     ;
s0=dx/(lc*alpha)                    ;
g=sqrt(log(s/(dx*eps))/pi)/s+1      ;
m=int16(g)
d=exp(-pi*s*s)                      ;
b=d*d                               ;
for i=m:n-m
    z(i)= s*y(i)                    ;
end
for k=1:m-1
    sum=0                           ;
    s=s*d                           ;
    d=d*b                           ;
    for i=m:n-m
        z(i)=z(i)+s*(y(i-k)+y(i+k)) ;
    end
end
for p=m:n-m
    r(p)=y(p)-z(p)                  ;
end
figure(1)                           ;
subplot(2,1,1)                      ;
plot(z,'red')                       ;
title('Primary roughness and waviness') ;
xlabel('points')                    ;
ylabel('Y (micrometre)')           ;
hold on
plot(y)                             ;
subplot(2,1,2)                      ;
plot(r)                             ;
title('Roughness profile after filtering') ;
xlabel('points')                    ;
ylabel('Y (micrometre)')           ;

```

Appendix 3: Numerical solver for the Reynolds equation

The discretized equation of the equation (2.15) is

$$F_i = \frac{1}{\Delta X} \left[\left(\frac{\varepsilon_{i+1} + \varepsilon_i}{2} \right) \left(\frac{P_{i+1} - P_i}{\Delta X} \right) - \left(\frac{\varepsilon_{i-1} + \varepsilon_i}{2} \right) \left(\frac{P_i - P_{i-1}}{\Delta X} \right) \right] - \frac{1}{\Delta X} (\bar{\rho}_i H_i - \bar{\rho}_{i-1} H_{i-1}) \quad (\text{A3-1})$$

$$- \frac{1}{\Delta t^*} [\bar{\rho}_i H_i - \bar{\rho}_i^0 H_i^0]$$

where

$$\varepsilon = \frac{\bar{\rho} H^3}{\bar{\eta}} \left(\frac{p_H b}{12 \eta_o \bar{u}} \right), \quad \bar{u} = \frac{u_1 + u_2}{2}$$

Then the applied Reynolds equation can be solved by using the Newton Raphson method as the following;

$$\left[\frac{\partial F_i}{\partial P_j} \right] [\Delta P_i] = -[F_i]$$

where

$$\frac{dF_i}{dP_j} = \frac{1}{\Delta X} \left[\left(\frac{\varepsilon_{i+1} + \varepsilon_i}{2} \right) (\delta(i+1, j) - \delta(i, j)) + \frac{1}{2} (P_{i+1} - P_i) \cdot \left(\frac{\partial \varepsilon_{i+1}}{\partial P_j} + \frac{\partial \varepsilon_i}{\partial P_j} \right) \right]$$

$$- \frac{1}{\Delta X} \left[\left(\frac{\varepsilon_i + \varepsilon_{i-1}}{2} \right) (\delta(i, j) - \delta(i-1, j)) + \frac{1}{2} (P_i - P_{i-1}) \cdot \left(\frac{\partial \varepsilon_i}{\partial P_j} + \frac{\partial \varepsilon_{i-1}}{\partial P_j} \right) \right]$$

$$- \frac{1}{\Delta X} \cdot \left[\frac{\partial}{\partial P_j} (\bar{\rho}_i H_i) - \frac{\partial}{\partial P_j} (\bar{\rho}_{i-1} H_{i-1}) \right] - \left(\frac{1}{\Delta t^*} \right) \cdot \frac{\partial}{\partial P_j} (\bar{\rho}_i H_i)$$

$$\frac{\partial \varepsilon_i}{\partial P_j} = k \left\{ \eta_i \cdot \left[3 \bar{\rho}_i H_i^2 \left(\frac{\partial H_i}{\partial P_j} \right) + H_i^3 \left(\frac{\partial \bar{\rho}_i}{\partial P_j} \right) \right] - (\bar{\rho}_i H_i^3) \cdot \frac{\partial \eta_i}{\partial P_j} \right\}, \quad k = \frac{p_H b}{12 \eta_i^2 \eta_o \bar{u}}$$

$$\frac{\partial}{\partial P_j} (\bar{\rho}_i H_i) = \bar{\rho}_i \left(\frac{\partial H_i}{\partial P_j} \right) + H_i \left(\frac{\partial \bar{\rho}_i}{\partial P_j} \right)$$

$$\frac{\partial \bar{\rho}_i}{\partial P_j} = \left(\frac{p_H \times 0.6 \times 10^{-9}}{(1 + 1.7 \times 10^{-9} p_H P_i)^2} \right) \cdot \delta(i, j)$$

$$\frac{\partial \eta_i}{\partial P_j} = \exp \left\{ (\ln \eta_o + 9.67) \left[-1 + (1 + 5.1 \times 10^{-9} p_H P_i)^Z \right] \right\} \cdot (\ln \eta_o$$

$$+ 9.67) (Z) (1 + 5.1 \times 10^{-9} p_H P_i)^{Z-1} (5.1 \times 10^{-9} p_H) \cdot \delta(i, j)$$

$$\frac{\partial H_i}{\partial P_j} = -\left(\frac{\Delta X}{2\pi}\right) \delta(i, j) \cdot \ln \left\{ \left\| \frac{X_{i+1} - X_i}{2} - X_j \right\| \left\| \frac{X_i - X_{i-1}}{2} - X_j \right\| \right\}$$

$$H_i = H_o + \frac{X_i^2}{2} - \frac{\Delta X}{2\pi} \sum_{j=1}^N P_j \ln \left\{ \left\| \frac{X_{i+1} + X_i}{2} - X_j \right\| \left\| \frac{X_i + X_{i-1}}{2} - X_j \right\| \right\}$$

$$\delta(i, j) = \begin{cases} 0 & \text{if } i \neq j \\ 1 & \text{if } i = j \end{cases}$$

Appendix 4: Temperature at the solid surfaces

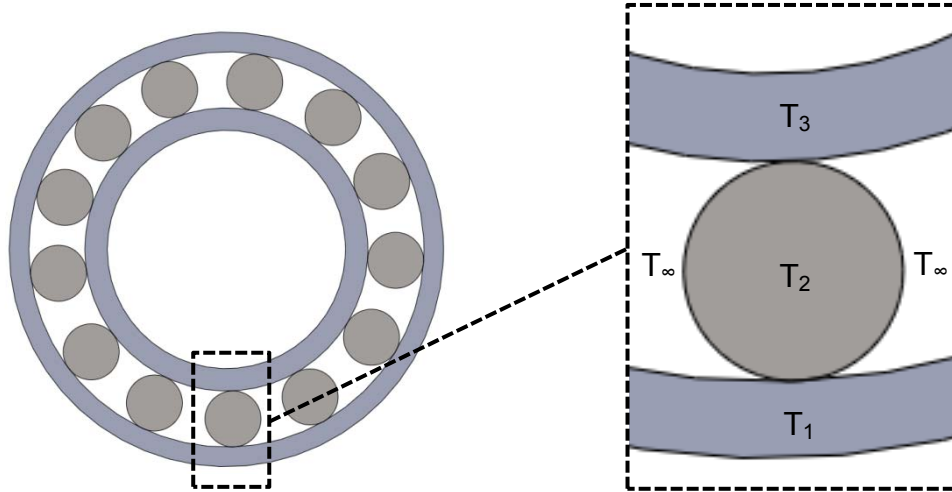


Figure A-1: Schematic picture of roller bearing (left) and section of temperature capture (right).

Usually, the temperature at the fluid film between the roller and the outer ring or roller and inner ring is only investigated as presented in Figure A-1. To simplify the EHL problem, the behaviour of fluid flow between the contact of inner ring and roller is assumed to be the same as the contact between roller and the outer ring. Thus, the contact between roller and the outer ring is only presented in this study.

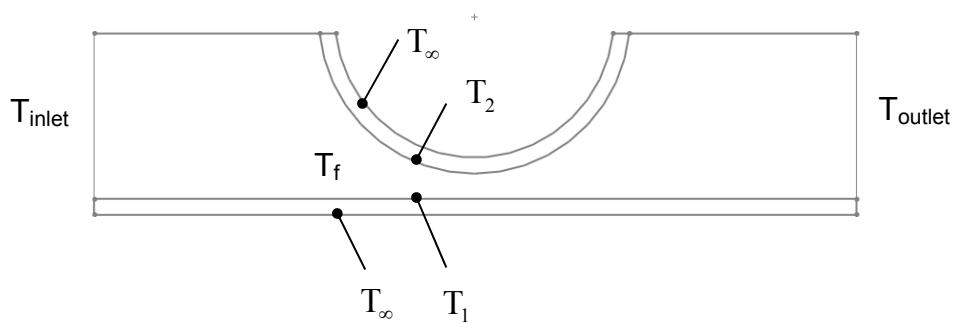


Figure A-2: Thermal boundary conditions for CFD model.

Figure A-2 shows the boundary conditions for calculating the temperature effect on EHL line contact problem using the CFD model. The temperature at the surface of the roller and plate can be directly calculated from the heat fluxes that transfer from fluid to solid parts [34]. Thus, the thermal boundary condition at the walls can be expressed as:

$$T_{\text{inlet}} = T_{\infty} = 298.15 \text{ K}$$

$$T_{\text{outlet}} \rightarrow \frac{\partial T}{\partial x} = 0$$

$$T_{\text{plate}} \rightarrow -k_f \left(\frac{\partial T}{\partial n} \right)_f = -k_1 \left(\frac{\partial T}{\partial n} \right)_1$$

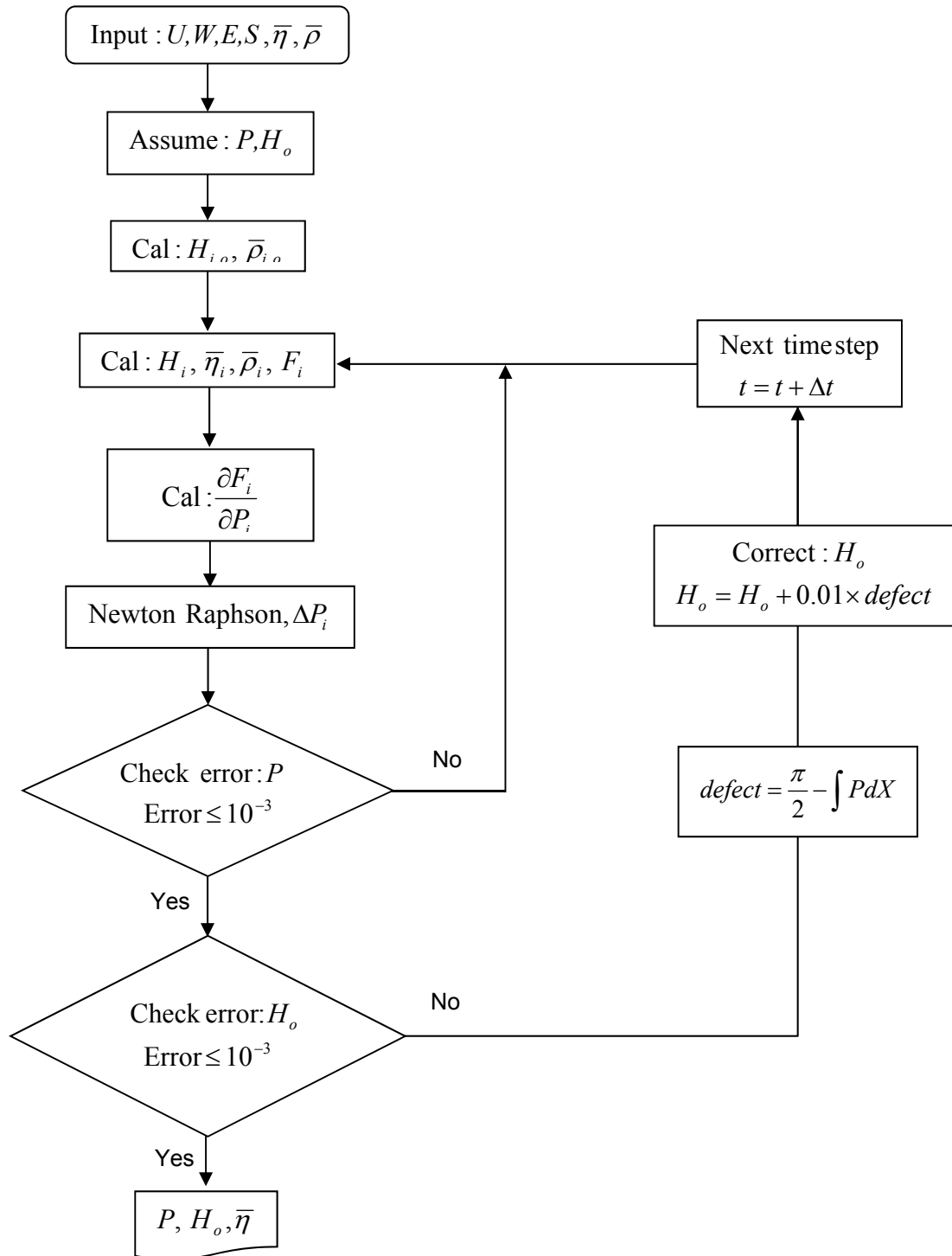
$$T_{\text{roller}} \rightarrow -k_f \left(\frac{\partial T}{\partial n} \right)_f = -k_2 \left(\frac{\partial T}{\partial n} \right)_2$$

where the subscript 1, 2 and f refer to bottom plate, top roller, and fluid, respectively.

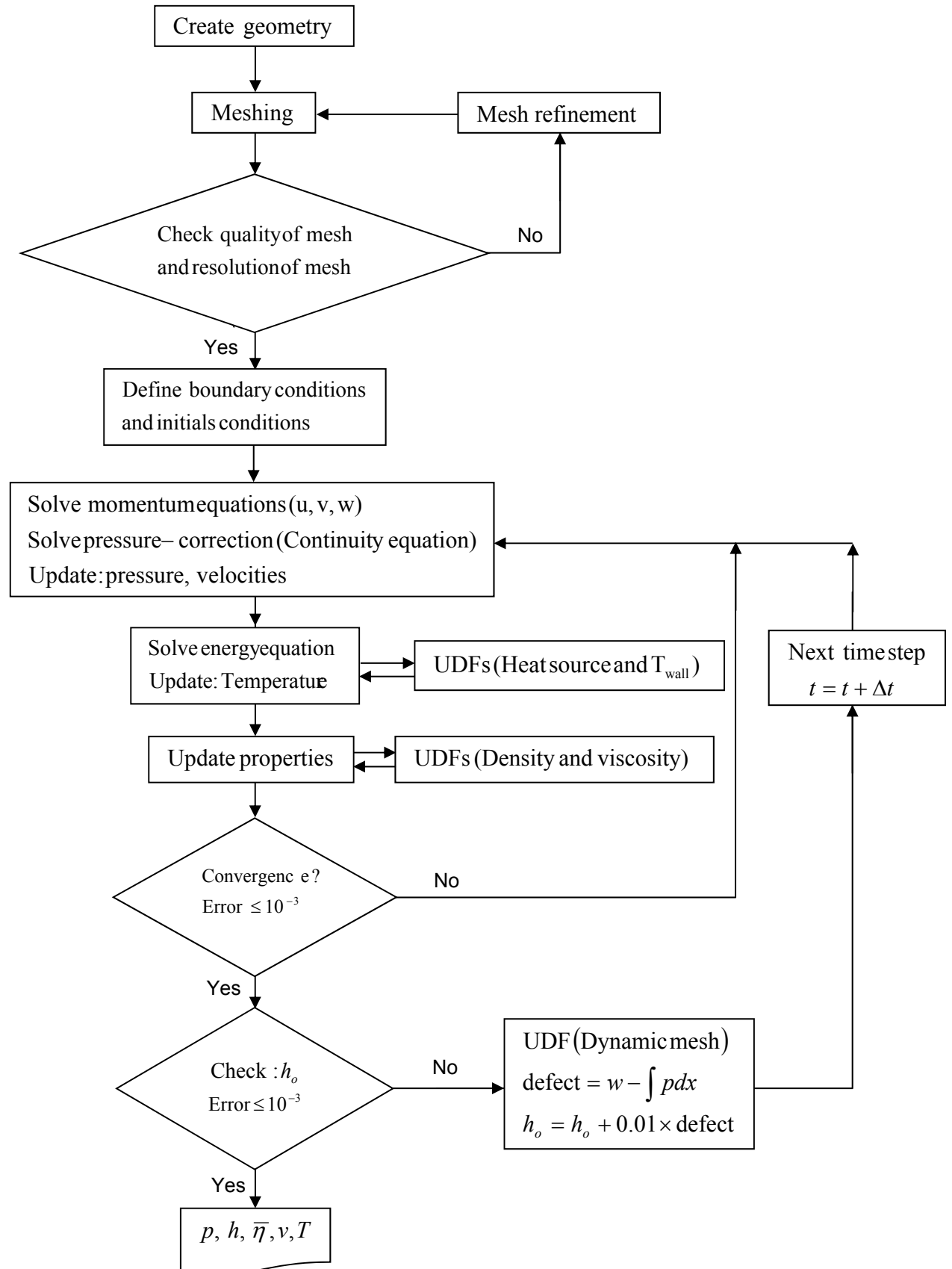
To simplify the problem, the solid part is assumed to have the same temperature as the ambient temperature in this study. According to the Figure A-2, if the wall is assumed to be very thin, then the temperatures at the solid surfaces (T_1 and T_2) are nearly uniform and equal to the ambient temperature T_{∞} of 298.15 K.

Appendix 5: Flow charts for the Reynolds equation and the CFD model

1. Flow chart for calculating the Reynolds equation (Dimensionless)



2. Flow chart to simulate the EHL problem using the CFD model



References

- [1] M. Kalin, I. Velkavrh, and J. Vižintin, The Stribeck curve and lubrication design for non-fully wetted surfaces, *Wear*, vol. 267, pp. 1232-1240, 2009.
- [2] A. Almqvist, *Rough surface elastohydrodynamic lubrication and contact mechanics*, Thesis (PhD), Luleå University of Technology, 2004.
- [3] T. R. Thomas, *Rough surfaces*, London: Imperial Collage Press, 1999.
- [4] O. Reynolds, On the theory of lubrication and its application to Mr. Beauchamp Tower's experiments, including an experimental determination of the viscosity of olive oil, *Philosophical Transactions of the Royal Society of London*, vol. 177, pp. 157-234, 1886.
- [5] D. Dowson and G. R. Higginson, *Elastohydrodynamic Lubrication: The Fundamentals of Roller and Gear Lubrication*, Oxford: Pergamon Press., 1966.
- [6] C. J. A. Roelands, *Correlational Aspect of Viscosity-Temperature-Pressure Relationships of Lubricating Oils*, Thesis (PhD), Delft University of Technology The Netherlands, 1966.
- [7] H. S. Cheng, *Calculation of Elastohydrodynamic Film Thickness in High Speed Rolling and Sliding Contacts*, USA: Defense Technical Information Center Press, 1967.
- [8] H. Martin, Lubrication of gear teeth, *Engineering, London*, vol. 102, pp. 199-200, 1916.
- [9] H. Hertz, The contact of solid elastic bodies [Über die Berührung fester elastischer Körper], *Journal für die reine und angewandte Mathematik*, vol. 92, pp. 156-171, 1881.
- [10] K. L. Johnson, *Contact mechanics*. Cambridge: Cambridge University Press, 1985.
- [11] A. Meldahl, Contribution to the Theory of the Lubrication of Gears and of the Stressing of the Lubricated Flanks of Gear Teeth, *Brown Boveri Review*, vol. 28, pp. 374-382, 1941.
- [12] E. McEwen, The effect of variation of viscosity with pressure on the load carrying capacity of oil films between gear teeth, *Journal of the Institute of Petroleum*, vol. 38, pp. 646–650, 1952.

- [13] A. M. Ertel, Hydrodynamic lubrication based on new principles, *Izv. Akad. Nauk. SSSR (OTN)*, vol. 3, pp. 41-52, 1939.
- [14] A. N. Grubin, *Investigation of the contact of machine components*, Moscow: Central Scientific Research Institute for Technology and Mechanical Engineering, 1949.
- [15] A. I. Petrusevich, Fundamental conclusions from the contact-hydrodynamic theory of lubrication, *Izv. Akad. Nauk. SSSR (OTN)*, vol. 2, pp. 209-223, 1951.
- [16] D. Dowson and G. R. Higginson, A numerical solution to the elastohydrodynamic problem, *Journal of Mechanical Engineering Science*, vol. 1, pp. 6-15, 1959.
- [17] A. Dyson, H. Naylor, and A. Wilson, The Measurement of Oil-Film Thickness in Elastohydrodynamic Contacts, *Proceedings of the Institution of Mechanical Engineers, Conference Proceedings*, pp. 119-134, 1965.
- [18] D. Dowson, A generalized Reynolds equation for fluid-film lubrication, *International Journal of Mechanical Sciences*, vol. 4, pp. 159-170, 1962.
- [19] D. Berthe, D. Dowson, and C. M. Taylor, *Fluid Film Lubrication - Osborne Reynolds Centenary*, New York: Elsevier Science, 1987.
- [20] B. J. Hamrock and D. Dowson, Isothermal elastohydrodynamic lubrication of point contacts. Part 1- Theoretical formulation, *Journal of tribology - Transactions of the ASME*, vol. 98, pp. 223-229, 1976.
- [21] H. Okamura, A contribution to the numerical analysis of isothermal elastohydrodynamic lubrication, *Proc. 9th Leeds-Lyon Symp. on Tribology*, pp. 313-320, 1983.
- [22] A. A. Lubrecht, T. N. W.E., and R. Bosma, Multigrid, an alternative method of solution for two-dimensional elastohydrodynamically lubricated point contact calculations, *Trans. ASME. Journal of Tribology*, vol. 109, pp. 437-443, 1987.
- [23] A. A. Lubrecht, *Numerical solution of the EHL line and point contact problem using multigrid techniques*, Thesis (PhD), University of Twente, Enschede, The Netherlands, 1987.
- [24] C. H. Venner, *Multilevel Solution of the EHL Line and Point Contact Problems*, Thesis (PhD), University of Twente, Enschede, The Netherlands, 1991.

- [25] K. F. Osborn and F. Sadeghi, Time Dependent Line EHD Lubrication Using the Multigrid/Multilevel Technique, *ASME, Journal of Tribology*, vol. 114, pp. 68-74, 1992.
- [26] H. Christensen, Stochastic Models for Hydrodynamic Lubrication of Rough Surfaces, *Proceedings of the Institution of Mechanical Engineers*, vol. 18, pp. 1013-1026, 1969.
- [27] N. Patir and H. S. Cheng, An Average Flow Model for Determining Effects of Three-Dimensional Roughness on Partial Hydrodynamic Lubrication, *ASME, Journal of Lubrication Technology*, vol. 100, pp. 12-17, 1978.
- [28] C. H. Venner and W. E. Ten Napel, Surface Roughness Effects in an EHL Line Contact, *ASME, Journal of Tribology*, vol. 114, pp. 616-622, 1992.
- [29] D. Zhu and Y. Hu, Effects of Rough Surface Topography and Orientation on the Characteristics of EHD and Mixed Lubrication in Both Circular and Elliptical Contacts, *Tribology Transactions*, vol. 4, pp. 391-398, 2001.
- [30] T. Almqvist and R. Larsson, The Navier-Stokes approach for thermal EHL line contact solutions, *Tribology International*, vol. 35, pp. 163-170, 2002.
- [31] T. Almqvist, A. Almqvist, and R. Larsson, A comparison between computational fluid dynamic and Reynolds approaches for simulating transient EHL line contacts, *Tribology International*, vol. 37, pp. 61-69, 2004.
- [32] T. Almqvist and R. Larsson, Thermal transient rough EHL line contact simulations by aid of computational fluid dynamics, *Tribology International*, vol. 41, pp. 683-693, 2008.
- [33] M. Hartinger, M. L. Dumont, S. Ioannides, D. Gosman, and H. Spikes, CFD modeling of a thermal and shear-thinning elastohydrodynamic line contact, *Journal of Tribology*, vol. 130, pp. 179-180, 2008.
- [34] V. Bruyere, N. Fillot, G. E. Morales-Espejel, and P. Vergne, Computational fluid dynamics and full elasticity model for sliding line thermal elastohydrodynamic contacts, *Tribology International*, vol. 46, pp. 3-13, 2012.
- [35] R. Gohar, *Elastohydrodynamics*, England: Ellis horwood limited, 1988.
- [36] R. C. Bhattacharjee and N. C. Dast, Power law fluid model incorporated into elastohydrodynamic lubrication theory of line contact, *Tribology International*, vol. 29, pp. 405-413, 1996.

- [37] A. Harnoy, *Bearing Design in Machinery: Engineering Tribology and Lubrication. Eastern Hemisphere Distribution*, Switzerland: Marcel Dekker, Inc., 2003.
- [38] D. Dowson and G. R. Higginson, *Elastohydrodynamic Lubrication*, Oxford: Pergamon Press, 1996.
- [39] G. E. Forsythe and W. R. Wasow, *Finite-difference methods for partial differential equations: Applied Mathematics Series*, New York: Wiley, 1960.
- [40] G. D. Smith, *Numerical Solution of Partial Differential Equations: Finite Difference Methods*, Oxford: Oxford University Press, 1985.
- [41] B. Bhushan, *Modern Tribology Handbook vol. One*, Florida: CRC Press, 2000.
- [42] M. Hartinger, *CFD Modelling of Elastohydrodynamic Lubrication*, Thesis (PhD), The University of London and Diploma of Imperial College, 2007.
- [43] J. Williams, *Engineering Tribology*, London: Cambridge University press, 2006.
- [44] S. Timoshenko, S. Timoshenko, and J. Goodier, *Theory of Elasticity*, Singapore: McGraw-Hill Book Company, 1951.
- [45] H. A. Barnes, J. F. Hutton, and K. Walters, *An introduction to rheology vol. 3*, Oxford: Elsevier, 1989.
- [46] W. G. Stachowiak and W. A. Batchelor, *Engineering Tribology*, Oxford: Elsevier, 2001.
- [47] I. M. Hutchings, *Tribology Friction and Wear of Engineering Materials*, London: Cambridge University press, 1992.
- [48] S. Srirattayawong, *Effect of Surface Roughness on Elastohydrodynamic Lubrication of Two Surfaces in Line Contact*, Thesis (Master), KMITL, 2005.
- [49] J. B. Hamrock, *Fundamental of Fluid Film Lubrication*, New York: McGraw - Hill, Inc, 1994.
- [50] C. Barus, Isopiestic and Isometrics Relative to viscosity, *American Journal of Sciences*, vol. 45, pp. 87-96, 1893.
- [51] P. S. Y. Chu and A. Cameron, Pressure Viscosity Characteristics of Lubricating Oils, *Journal of the Institute of Petroleum*, vol. 48, pp. 147-155, 1962.

- [52] C. Cioc, S. Cioc, L. Moraru, A. Kahraman, and T. G. Keith, A Deterministic Elastohydrodynamic Lubrication Model of High-Speed Rotorcraft Transmission Components, *Tribology Transactions*, vol. 45, pp. 556-562, 2002.
- [53] L. Houpert, New results of traction force calculations in ehd contacts, *Trans. ASME, J. Lub. Tech.*, vol. 107, pp. 241-249, 1985.
- [54] G. Astarita and G. Marrucci, *Principles of non-Newtonian fluid mechanics*, USA: McGraw-Hill Inc, 1974.
- [55] P. J. Carreau, Rheological equations from meolecular network theories, *Trans. Soc. Rheol.* , vol. 16, pp. 99-127, 1972.
- [56] K. L. Johnson and J. L. Tevaarwerk, The shear behaviour of elastohydrodynamic oil films, *Proc. R. Soc. London*, vol. A. 356, pp. 215-236, 1977.
- [57] H. Eyring, Viscosity, plasticity, and diffusion as examples of absolute reaction rates, *The Journal of Chemical Physics*, vol. 4, pp. 283-291, 1936.
- [58] S. Bair, J. a. Jarzynski, and W. O. Winer, The temperature, pressure and time dependence of lubricant viscosity, *Tribology International*, vol. 34, pp. 461-486, 2001.
- [59] S. Bair, Actual Eyring Models for Thixotropy and Shear-Thinning: Experimental Validation and Application to EHD, *Journal of Tribology*, vol. 126, pp. 728-732, 2004.
- [60] D. Dowson, G. Higginson, and A. Whitaker, Elasto-hydrodynamic lubrication: a survey of isothermal solutions, *Journal of Mechanical Engineering Science*, vol. 4, pp. 121-126, 1962.
- [61] F. Hirano and N. Kuwano, Observation of solidification of oils under high pressure, *Proc. JSLE int. Tribology Conference*, pp. 841-845, 1985.
- [62] W. Habchi, P. Vergne, S. Bair, O. Andersson, D. Eyheramendy, and G. E. Morales-Espejel, Influence of pressure and temperature dependence of thermal properties of a lubricant on the behaviour of circular TEHD contacts, *Tribology International*, vol. 43, pp. 1842-1850, 2010.
- [63] Z. Dong and W. SHI-ZHO, A full numerical solution for the thermoelastohydrodynamic problem in elliptical contacts, *Journal of tribology*, vol. 106, pp. 246-254, 1984.

- [64] B. Sternlicht, P. Lewis, and P. Flynn, Theory of lubrication and failure of rolling contacts, *Journal of Basic Engineering*, vol. 83, pp. 213-222, 1961.
- [65] A. Olver, Testing transmission lubricants: the importance of thermal response, *Proceedings of the Institution of Mechanical Engineers, Part G: Journal of Aerospace Engineering*, vol. 205, pp. 35-44, 1991.
- [66] M. Ghosh and B. Hamrock, Thermal elastohydrodynamic lubrication of line contacts, *ASLE transactions*, vol. 28, pp. 159-171, 1985.
- [67] Y. Peiran and W. Shizhu, A generalized Reynolds equation for non-Newtonian thermal elastohydrodynamic lubrication, *Journal of tribology*, vol. 112, pp. 631-636, 1990.
- [68] H. Carslaw and J. J. C. Jaeger, *Conduction of heat in solids*, London: Oxford University Press, 1959.
- [69] J. Jaeger, Moving sources of heat and the temperature of sliding contacts, in *J. and Proc. Roy. Soc. New South Wales*, pp. 203-224, 1942.
- [70] H. Cheng and B. Sternlicht, A numerical solution for the pressure, temperature, and film thickness between two infinitely long, lubricated rolling and sliding cylinders, under heavy loads, *Journal of Basic Engineering*, vol. 87, pp. 695-704, 1965.
- [71] *Engineering Handbook, Reference Tables -- Surface Roughness Table, Edition, 2004-2006.*
- [72] E. P. DeGarmo, J. T. Black, and R. A. Kohser, *DeGarmo's materials and processes in manufacturing*, USA: John Wiley & Sons, 2011.
- [73] S. Whitehead, A. Shearer, D. Watts, and N. Wilson, Comparison of methods for measuring surface roughness of ceramic, *Journal of Oral Rehabilitation*, vol. 22, pp. 421-427, 1995.
- [74] Digital Metrology Solutions, *Measuring Surfaces*, 2007, Available: <http://www.digitalmetrology.com/SurfaceFinishIn3Steps.htm> [Access on 12 October 2013].
- [75] B. Bhushan, *Principles and Applications of Tribology, Second ed.* USA.: John Wiley & Sons. Ltd, 2013.
- [76] J. B. P. Williamson, J. Pullen, and R. T. Hunt, Shape of Solid Surfaces, *Trans. ASME Journal of Surface Mechanics*, pp. 24-35, 1969.

- [77] N. Tayebi and A. A. Polycarpou, Modeling the effect of skewness and kurtosis on the static friction coefficient of rough surfaces, *Tribology International*, vol. 37, pp. 491-505, 2004.
- [78] E. J. Abbott and F. A. Firestone, Specifying surface quality: a method based on accurate measurement and comparison, *Mechanical Engineering*, vol. 55, pp. 569-572, 1993.
- [79] L. Mummery, *Surface texture analysis: the handbook*, Singapore: Hommelwerke GmbH, pp. 24-33, 1990.
- [80] G. Stachowiak and A. W. Batchelor, *Engineering tribology*, Butterworth-Heinemann, 2013.
- [81] Z. Lipa and D. Tomanícková, Utilisation of Abbott-Firestone Curves Characteristics for the Determination of Turned Surface Properties, *Annals of the Faculty of Engineering Hunedoara-International Journal of Engineering*, vol. 9, pp. 223-226, 2011.
- [82] T. Hobson, *Understanding the Abbott-Firestone Curve*, 2002.
- [83] R. Laheurte, P. Darnis, N. Darbois, O. Cahuc, and J. Neauport, Subsurface damage distribution characterization of ground surfaces using Abbott–Firestone curves, *Optics express*, vol. 20, pp. 13551-13559, 2012.
- [84] M. Tomov, M. Kuzinovski, and N. Trajcevski, Function on Gaussian and 2RC filters to determine the roughness profile in real non-periodic and periodic surfaces, *14-th International Research/Expert Conference*, pp. 9-12, 2010.
- [85] M. Krystek, A Fast Gauss Filtering Algorithm for Roughness Measurements, *Precision Engineering*, vol. 19, pp. 198-200, 1996.
- [86] I. J. Schoenberg, Spline functions and the problem of graduation, *Proceedings of the National Academy of Sciences of the United States of America*, vol. 52, 1964.
- [87] C. H. Reinsch, Smoothing by spline functions, *Numerische mathematik*, vol. 10, pp. 177-183, 1967.
- [88] T. Goto, J. Miyakura, K. Umeda, S. Kadowaki, and K. Yanagi, A Robust Spline Filter on the basis of L2-norm, *Precision Engineering*, vol. 29, pp. 157-161, 2005.
- [89] American National Standards Institute, *B46.1: Surface texture (surface roughness, waviness, and lay)*, USA, 1995.

- [90] J. Raja, B. Muralikrishnan, and S. Fu, Recent advances in separation of roughness, waviness and form, *Precision Engineering*, vol. 26, pp. 222-235, 2002.
- [91] H. Czichos, *Geometrical Product Specifications (GPS) – Surface Texture: Profile Method -- Metrological Characteristics of Phase Correct Filters*, Geneva: International Organization for Standardization USA: Springer, 1996.
- [92] T. Hobson, *Surtronic 3+ : Operating Instructions*, UK, 2004.
- [93] The optical society, *The Reflection of Light*, America, 2013, Available: <http://www.optics4kids.org/home/teachersparents/articles/the-reflection-of-light/> [Access on 3 June 2013].
- [94] Zygo Methodology Solution Divisions, *Optical profiling: how optical profilers work*, 2013, Available: <http://zometrics.com/optical-profilers-about.shtml> [Access on 5 May 2013].
- [95] S. A. Whitehead, A. C. Shearer, D. C. Watts, and N. H. F. Wilson, Comparison of two stylus methods for measuring surface texture, *Dental Materials*, vol. 15, pp. 79-86, 1999.
- [96] R. I. San, *Surface Finish Equipment*, 2013, Available: <http://surfacefinishequipment.com/b%20&%20s%2090G.htm> [Access on 14 November 2013].
- [97] A. Peters, *Surface Finish Measurement Basics*, 2008, Available: <http://www.qualitymag.com/articles/84505-quality-101-surface-finish-measurement-basics>
- [98] G. T. Smith, *Industrial metrology: surfaces and roundness*, Singapore: Springer, 2002.
- [99] NTN Bearing Corporation, *Cylindrical Roller Bearings*, 2013, Available: <http://www.ntnamericas.com/en/products/cylindrical-roller-bearings>, [Access on 14 January 2013].
- [100] D. B. Thomas, W. Luk, P. H. Leong, and J. D. Villasenor, Gaussian random number generators, *ACM Computing Surveys (CSUR)*, vol. 39, pp. 11:1-11:38, 2007.
- [101] P. Ranganath Nayak, Random process model of rough surfaces, *J. Lubric Technol Trans ASME*, vol. 93, pp. 398-407, 1971.

- [102] V. Kachitvichyanukul and B. W. Schmeiser, Binomial random variate generation, *Communications of the ACM*, vol. 31, pp. 216-222, 1988.
- [103] F. A. Haight and F. A. Haight, *Handbook of the Poisson distribution*, 1967.
- [104] L. Devroye, Sample-based non-uniform random variate generation, *Proceedings of the 18th conference on Winter simulation*, pp. 260-265, 1986.
- [105] A. M. Law, W. D. Kelton, and W. D. Kelton, *Simulation modeling and analysis vol. 2*, New York: McGraw-Hill, 1991.
- [106] N. L. Johnson, S. Kotz, and N. Balakrishnan, *Continuous univariate distributions 2 ed.*, New York: John Wiley, 1994.
- [107] M. Steyvers, *Computational Statistics with Matlab*, 2010.
- [108] W. H. Press, S. A. Teukolsky, W. T. Vetterling, and B. P. Flannery, *Numerical Recipes : The Art of Scientific Computing*, Hong Kong: Cambridge University Press, 2007.
- [109] T. Altiok and B. Melamed, *Simulation modeling and analysis with Arena*, USA: Academic Press, 2010.
- [110] E. Weisstein, *Pearson System*, 2013, Available: <http://mathworld.wolfram.com/PearsonSystem.html> [Access on 18 November 2013].
- [111] T. A. Spedding, T. G. King, W. Watson, and K. J. Stout, Pearson System of Distributions: Its Application to non-Gaussian Surface Metrology and a Simple Wear Model, *Journal of lubrication technology*, vol. 102, pp. 495-500, 1980.
- [112] Y. Nagahara, A method of simulating multivariate nonnormal distributions by the Pearson distribution system and estimation, *Computational Statistics & Data Analysis*, vol. 47, pp. 1-29, 2004.
- [113] Y. Nagahara, Non-Gaussian Filter and Smoother Based on the Pearson Distribution System, *Journal of Time Series Analysis*, vol. 24, pp. 721-738, 2003.
- [114] M. Kaneta, Effects of surface roughness in elastohydrodynamic lubrication, *JSME International Journal, Series 3: Vibration, Control Engineering, Engineering for Industry*, vol. 35, pp. 535-546, 1992.
- [115] X. Ai and H. S. Cheng, A Transient EHL Analysis for Line Contacts With Measured Surface Roughness Using Multigrid Technique, *Journal of Tribology*, vol. 116, pp. 549-556, 1994.

- [116] H. G. Elrod, Thin-Film Lubrication Theory for Newtonian Fluids with Surfaces Possessing Striated Roughness or Grooving, *JNL. LUBRICATION TECHNOL., TRANS. ASME*, vol. 95, SERIES F, 1973.
- [117] D. Zhu and Q. J. Wang, Effect of roughness orientation on the elastohydrodynamic lubrication film thickness, *Journal of Tribology*, vol. 135, 2013.
- [118] P. M. Gerhart, R. J. Gross, and J. I. Hochstein, *Fundamentals of fluid mechanics*, MA: Addison-Wesley Reading, 1985.
- [119] M. Y. Okiishi, *Fundamentals of Fluid Mechanics*, John Wiley & Sons, 2006.
- [120] O. GÜNDÜZ, *Derivation of Flow Equations*, in *ENV5056 Numerical Modeling of Flow and Contaminant Transport in Rivers*, Dokuz Eylul university, 2011.
- [121] *ANSYS FLUENT Theory Guide*, Canonsburg, PA 15317, 2011.
- [122] R. B. Bird, W. E. Stewart, and E. N. Lightfoot, *Transport phenomena*, USA: Wiley, 2007.
- [123] D. A. John, *Computational Fluid Dynamics*. Singapore: McGraw-hill , 1995
- [124] A. R. Mitchell, *The finite difference method in partial differential equations*, Chichester Wiley, 1980.
- [125] O. C. Zienkiewicz and R. L. Taylor, *Finite Element Method vol. 1*, Elsevier Butterworth-Heinemann, 2000.
- [126] T. Chung, *Computational Fluid Dynamics*, London: Cambridge university press, 2010.
- [127] B. Andersson, R. Andersson, and L. Håkansson, *Computational Fluid Dynamics for Engineers*, London: Cambridge University Press, 2011.
- [128] C. P. Hong, *Computer Modelling of Heat and Fluid Flow in Materials Processing*, UK: MPG Book Ltd., 2004.
- [129] H. K. Versteeg and W. Malalasekera, *An introduction to computational fluid dynamics- The Finite volume method*, Englands: Longman Group Ltd, 1995.
- [130] G. Gasni, M. K. Wan Ibrahim, and R. S. Dwyer-Joyce, Measurements of lubricant film thickness in the iso-viscous elastohydrodynamic regime, *Tribology International*, vol. 44, pp. 933-944, 2011.

- [131] A. K. Singhal, M. M. Athavale, H. Li, and Y. Jiang, Mathematical Basis and Validation of the Full Cavitation Model, *Journal of Fluids Engineering*, vol. 124, pp. 617-624, 2002.
- [132] P. Zwart, M. Scheuerer, and M. Bogner, Numerical modelling of free surface and cavitating flows, *VKI Lecture. Series: Industrial Two-Phase Flow CFD*, pp. 1-25, 2005.
- [133] W. Hackbusch, *Multi-grid methods and applications vol. 4*, Berlin: Springer-Verlag, 1985.
- [134] H. Versteeg and W. Malalasekera, *Introduction to Computational Fluid Dynamics, An: The Finite Volume Method*, UK: Pearson Education, 2007.
- [135] S. V. Patankar and D. B. Spalding, A calculation procedure for heat, mass and momentum transfer in three-dimensional parabolic flows, *Int. J. Heat Mass Transfer*, vol. 15, pp. 1787-1982, 1972.
- [136] R. I. Issa, Solution of the implicitly discretised fluid flow equations by operator-splitting, *Journal of computational physics*, vol. 62, pp. 40-65, 1986.
- [137] M. Hartinger, D. Gosman, S. Ioannides, and H. Spikes, CFD modelling of elastohydrodynamic lubrication, *Washington, D.C.*, pp. 531-532, 2005.
- [138] Ansys Fluent, *User Manual (ANSYS ICEM CFD 12.1)*, Available: <http://www.ansys.com> [Access on 2 January 2013].
- [139] Fluent Incorporation, *Fluent Software Training: UDFs For Moving/Deforming Mesh*, 2006, Available: <http://aerojet.engr.ucdavis.edu/fluenthelp/html/ug/node444.htm> [Access on 6 March 2013].
- [140] ME469B/6/GI: *User Programming & Automation*, Stanford University, Available: <http://www.stanford.edu/class/me469b/handouts/programming.pdf>, [Access on 8 January 2013].
- [141] Fluent Incorporation, *FLUENT 6.3 UDF Manual*, 2006. Available: <http://aerojet.engr.ucdavis.edu/fluenthelp/pdf/udf/fludf.pdf> [Access on 25 January 2013].
- [142] Fluent Incorporation, *Macros for Accessing FLUENT Solver Variables*, 2005, Available: [http://cdlab2.fluid.tuwien.ac.at/LEHRE/TURB/Fluent.Inc/fluent 6.2/help/pdf/udf/chp05.pdf](http://cdlab2.fluid.tuwien.ac.at/LEHRE/TURB/Fluent.Inc/fluent%206.2/help/pdf/udf/chp05.pdf) [Access on 25 January 2013].
- [143] Fluent Incorporation, *ANSYS FLUENT UDF Manual*, USA: SAS Press, 2011.

- [144] L.-M. Chu, H.-C. Hsu, J.-R. Lin, and Y.-P. Chang, Inverse approach for calculating temperature in EHL of line contacts, *Tribology International*, vol. 42, pp. 1154-1162, 2009.
- [145] I. Krupka, S. Bair, P. Kumar, M. M. Khonsari, and M. Hartl, An Experimental Validation of the Recently Discovered Scale Effect in Generalized Newtonian EHL, *Tribology Letters*, vol. 33, pp. 127-135, 2009.
- [146] Z. Fu, F. Guo, and P. L. Wong, Non-classical Elastohydrodynamic Lubricating Film Shape Under Large Slide-roll Ratios, *Tribology Letters*, vol. 27, p. 8, 2007.
- [147] I. Krupka, P. Kumar, S. Bair, M. M. Khonsari, and M. Hartl, The Effect of Load (Pressure) for Quantitative EHL Film Thickness, *Tribology Letters*, vol. 37, p. 9, 2011.
- [148] SKF, *Ceramic Bearing*, 2013, Available: http://www.skf.com/portal/skf_id/home/products?contentId=192009, [Access on 9 September 2013].
- [149] B. S. A. Komi, *091018 material properties*, 2008, Available: <http://www-bsac.eecs.berkeley.edu/~mccoy/files/091018-material-properties-efunda-v02.pdf> [Access on 11 September 2013]
- [150] J. R. Calvert and R. A. Farrar, *An Engineering Data Book*, New York: PALGRAVE, 1999.
- [151] T. Sperrfechter and R. Haller, Elastohydrodynamic Lubrication Between Rolling and Sliding Ceramic Cylinders: An Experimental Investigation, *Journal of Tribology*, vol. 122, pp. 721-724, 2000.
- [152] MathWorks Inc., *MATLAB (R2013b)*, 2005, Available: http://www.mathworks.co.uk/academia/student_version/learnmatlab_sp3.pdf [Access on 5 June 2012].
- [153] MathWorks Inc., *Pearson system random numbers: Pearsrnd*, 2014, Available: <http://www.mathworks.co.uk/help/stats/pearsrnd.html> [Access on 10 January 2014].
- [154] N. Tayebi and A. A. Polycarpou, Modeling the effect of skewness and kurtosis on the static friction coefficient of rough surfaces, *Tribology International*, vol. 37, pp. 491-505, 2004.
- [155] M. Sedlaček, B. Podgornik, and J. Vižintin, Correlation between standard roughness parameters skewness and kurtosis and tribological behaviour of contact surfaces, *Tribology International*, vol. 48, pp. 102-112, 2012.

- [156] B. K. Prasad, A. K. Patwardhan, and A. H. Yegneswaran, Wear characteristics of a zinc-based alloy compared with a conventional bearing bronze under mixed lubrication conditions: Effects of material and test parameters, *Canadian Metallurgical Quarterly*, vol. 40, pp. 193-210, 2001.
- [157] B. K. Prasad, Investigation into sliding wear performance of zinc-based alloy reinforced with SiC particles in dry and lubricated conditions, *Wear*, vol. 262, pp. 262-273, 2007.
- [158] Y.-R. Jeng and S.-R. Peng, Contact Behavior of Surfaces Containing Elliptical Asperities with Gaussian and Non-Gaussian Height Distributions, *Journal of Tribology*, vol. 129, pp. 743-753, 2007.
- [159] A. I. Vakis, Asperity interaction and substrate deformation in statistical summation models of contact between rough surfaces, *Journal of Applied Mechanics, Transactions ASME*, vol. 81, p. 041012 (1:10), 2014.
- [160] P. Pawlus and W. Zelasko, The importance of sampling interval for rough contact mechanics, *Wear*, vol. 276, pp. 121-129, 2012.
- [161] B. Bhushan, Contact mechanics of rough surfaces in tribology: Multiple asperity contact, *Tribology Letters*, vol. 4, pp. 1-35, 1998.
- [162] S. Andersson, A. Söderberg, and U. Olofsson, A random wear model for the interaction between a rough and a smooth surface, *Wear*, vol. 264, pp. 763-769, 2008.
- [163] Y.-Z. Hu and D. Zhu, A Full Numerical Solution to the Mixed Lubrication in Point Contacts, *Journal of Tribology*, vol. 122, pp. 1-9, 1999.
- [164] J. I. McCool, Comparison of models for the contact of rough surfaces, *Wear*, vol. 107, pp. 37-60, 1986.
- [165] S. M. Jhurani and C. Fred Higgs Iii, An elastohydrodynamic lubrication (EHL) model of wear particle migration in an artificial hip joint, *Tribology International*, vol. 43, pp. 1326-1338, 2010.
- [166] C. Q. Yuan, Z. Peng, X. P. Yan, and X. C. Zhou, Surface roughness evolutions in sliding wear process, *Wear*, vol. 265, pp. 341-348, 2008.
- [167] X. Ai and H. P. Nixon, Fatigue Life Reduction of Roller Bearings Due to Debris Denting: Part I — Theoretical Modeling, *Tribology Transactions*, vol. 43, pp. 197-204, 2000.

- [168] W. Habchi, D. Eyheramendy, P. Vergne, and G. Morales-Espejel, A Full-System Approach of the Elastohydrodynamic Line/Point Contact Problem, *Journal of Tribology*, vol. 130, pp. 1-10, 2008.
- [169] X. U. Gang, F. Sadeghi, and M. Hoeprich, Residual stresses due to debris effects in EHL contacts, *Tribology Transactions*, vol. 40, pp. 613-620, 1997.
- [170] A. C. Urzică, M. R. D. Bălan, and S. S. Crețu, Pressures distributions and depth stresses developed in concentrated contacts between elements with non-Gaussian rough surfaces, *ASME 2012 11th Biennial Conference on Engineering Systems Design and Analysis*, vol. 4, pp. 547-554, 2012.
- [171] F. Sadeghi, B. Jalalahmadi, T. S. Slack, N. Raje, and N. K. Arakere, A review of rolling contact fatigue, *Journal of Tribology*, vol. 131, pp. 1-15, 2009.